The University Of Sheffield.

Department Of Mechanical Engineering

PhD Mechanical Engineering

Investigation of the Effects of Soot on Friction and Wear Characteristics of Polymers (Elastomers and Thermoplastics) Engine Components

Nur Fathiah MOHD NOR

Supervisors:

Prof Roger Lewis

Dr Tom Slatter

Thesis submitted to the Department of Mechanical Engineering, University of Sheffield in fulfilment of the requirements for the degree of PhD

Summary

Over recent years, there has been an increase in the level of soot in an engine attributing to the friction and wear of engine components. This has caused challenges to the automotive industries to develop advanced lubrication or use other materials for engine components that can withstand friction and wear problems in order to increase the performance of an engine. The cause of the increase of soot levels in an engine is the technological development that requires a decrement of pollutants emitted to the air in respect to the emission policy; as well as the need to reduce the maintenance costs by extending service intervals. Many previous research studies have been conducted to see the effect of soot on ferrous materials, using laboratory specimens and real engine components. And there is vast research on nonferrous materials using abrasive particles; however; the effect of soot on nonferrous materials is still lacking.

This study aims to investigate the effect of soot on nonferrous material such as polymers. Nonferrous materials are seeing increased use in engines so it is important to understand how they behave with soot as abrasive particles. To achieve this, the working performance of different material specimens particularly O-rings has been evaluated using ball-on-flat and block-on-ring test rigs. This specific component is chosen to mimic the valve stem O-ring contact condition inside an engine. Different surface analysis techniques such as 3D contact profilometry, 2D profilometry, optical microscopy and scanning electron microscopy (SEM) were used to understand the effects of soot on the wear of elastomer/thermoplastics materials.

Results obtained in this work indicate that the major wear mechanism for all materials is abrasion with respect to increasing of carbon black content inside the lubricant with some material removal due to fatigue cracking for thermoplastics materials and signs of deformation and particles embedment in elastomers ones. It can be said that the friction and wear is dominated by material properties for elastomer materials while for thermoplastics materials; the friction and wear is affected by the lubricant, soot and other contact parameters such as load and temperature.

This work also complements previous research on the hardness of soot whereby most research claim that the soot/carbon black is harder than ferrous material. From this study, it is known that the roughness of the indentation from the load test are higher for both particles, thus it could be concluded that the soot/carbon black particles are harder than ferrous material.

A new approach using an ultrasound technique to determine oil film thickness (OFT) for elastomer/polymer materials in contact with steel is presented in this study. The trends seen show that outcomes of these measurements are promising, but improvements and further tests are needed to improve reliability and validate the results.

Acknowledgements

I would like to express my sincere gratitude to my supervisor; Prof Roger Lewis who is highly supportive which he always showed by going through all of my submissions and giving positive comments and pushing me harder when I was near my limit which I really appreciate. This became a source of encouragement for me to finish my research. Dr. Tom Slatter, my second supervisor, was also helpful and consistently gave valuable suggestions and comments when necessary. Through all 4 years working with both of them has become enormously rewarding.

I also would like to thank Dave Butcher and Luke Callaghan, technicians in the Leonardo Centre for Tribology, for their skills, knowledge and help whenever needed. Also not forgotten, Scott Beamish who has helped me in a part of my research. Without Scott, one of the most important part of my research could have been missed.

I am also thankful towards Universiti Teknikal Malaysia Melaka for giving me consent to pursue my PhD here in Sheffield. Without their consent, I would not have been able to meet great knowledgeable people and experience doing research here in Sheffield, Thanks also to my funding scholar (Ministry of Education, Malaysia) for sponsoring me throughout 3 years of my PhD journey here.

Last but not the least, my sincere appreciation to my loving husband Faiz, who was willing to let go of his career and experience the loss of a loved one in order to take care of my loving children (Fahim, Maryam and Marissa) and home affairs here in Sheffield. I would also like to thank my Mom for sacrificing her time to take care of my new-borns while I was in confinement, and also the entire family members and friends in Malaysia and Sheffield for their prayers and support which they have given to me and my small family.

Table of Contents

List of Figures

List of Tables

Nomenclature

Terms	Definition	Units
a, b	Major and minor radius	m
HSp	Scratch hardness number	-
C	Speed of sound	m/s
E	Young's modulus	MPa
E'	Reduced Young's modulus	MPa
f	Resonant frequency	Hz
F	Force	N
G	Non-dimensional material parameter	-
H_{min}	Non-dimensional minimum film parameter	-
H_c	Non-dimensional central film parameter	-
h_{min}	Minimum film thickness	m
h_c	Central film thickness	m
k	Non-dimensional ellipticity parameter	-
P	Load	N
p_o	Maximum contact pressure	GPa
p_{mean}	Mean Average contact pressure	GPa
r	radius	m
R_q	(R.M.S) surface roughness	m
R_a	Average surface roughness	m
T	Torque	N/mm
U	Non-dimensional speed parameter	-
L	Stroke length	m
W	Non-dimensional load parameter	-
w_n	Width of the wear scar	m
R	Curvature of O-ring	m
z	Acoustic impedance of a material	$Pa.s/m^3$
Z	Viscosity-pressure index	-
α	Pressure viscosity coefficient	GPa^{-1}
η	Absolute viscosity	cP or Pa.s
T	Temperature	°C
ϑ	Kinematic viscosity	cSt
λ	Lambda ratio	-
μ	Friction coefficient	-
υ	Poisson's ratio	-

Chapter 1 Introduction

This chapter outlines the instigation of this research along with its main aims and objectives. The developing engine technology trends with increased in global energy challenges are highlighted here as well as the regulations introduced relating to current automotive trends.

1.1 Global energy challenges

In an engine, a substantial amount of energy is lost through friction between moving parts that converts the energy to heat which is then dissipated through the environment. Thus keeping an engine well lubricated will help to reduce the losses. Figure 1.1 shows the categorization of energy losses in an engine where it shows that the higher peak cylinder pressure, the friction mean effective pressure (FMEP) will also increases. The piston group contributes the highest friction loss followed by valve train and bearings [1]. From this, it is known that friction and lubrication have a substantial influence on the efficiency and lifespan of automotive components and on the global economy.

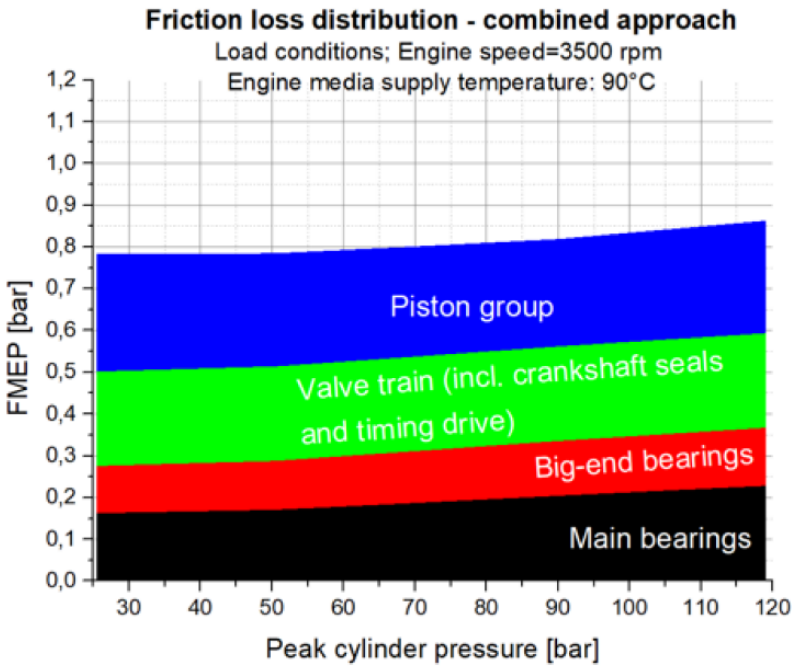

Figure 1.1 Friction loss distribution in an engine [1]

With the increase in demand for automobiles, in the automotive industries, more research is being done on advanced lubrication and transmission technology to cater for the higher demand for high efficiency automobiles. Automotive manufacturers are now frequently trying to prolong the lifetime of their internal combustion engines (ICEs)

in order to reduce the maintenance cost and environmental effects [2]. This, however will affect the lubrication oil, where soot products which are harmful to the tribological contacts, will infiltrate the lubrication oil [3][4] and produce many other pollutants. In order to comply with the Euro standard, the automotive manufacturers are investigating a few models to reduce these emissions. Exhaust gas emissions consist of carbon monoxide (CO), nitrogen oxide (NOx), sulphur dioxide (SO_2), unburned hydrocarbons (UHC) and particulate matter (PM) where the majority of the PM (64%) content is soot. Added to this is the fact that exhaust gas recirculation (EGR) is being widely used to reduce NOx emissions in complying with the stringent emissions regulations. The EGR recirculates and returns part of the combustion products into the engine combustion system thus increasing the level of soot product in the lubricating oil where there is already soot contamination. The implication of this is that EGR does reduce the NOx emission, but at the same time soot also increases in the lubricating oil; a sort of trading soot for NOx as shown in Figure 1.2 [5]. Figure 1.2 shows where the soot goes inside an engine. Having less efficient combustion means more fuel goes out unburned and that's what we call as soot. Half of the soot goes back into the intake and inside the combustion chamber and blows by and ends up in the lubrication oil as shown by the red arrow and black sprays which represents the soot. The presence of increased levels of soot in the engine has led to increased wear of engine parts such as cylinder liner, piston rings, valve train system and bearings [6].

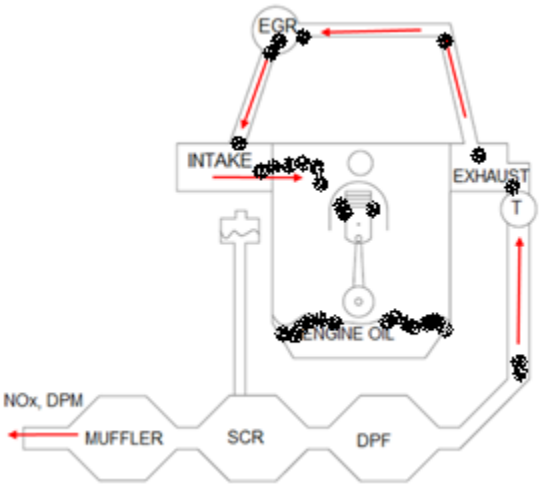

Figure 1.2 Schematic diagram of an engine with the use EGR, SCR and DPF to reduce emission pollutants

Soot formation which is mainly in fuel-rich regions in the combustion, is due to an insufficient amount of oxygen that converts all carbon into carbon dioxide. It can also be formed due to cold-start and warm-up phases where a very rich fuel–air ratio is needed for ignition and combustion processes. The combustion process in a diesel engines is heightened by the fuel distribution dis-homogeneity with air-fuel mixing processes where incomplete combustion occurs [7]. In SI engines, it is known that the SI engine operates close to a stoichiometric air-fuel ratio, thus the soot emissions from these engines are insignificant, particularly with the use of unleaded fuel. Hence the study and investigation of combustion and soot inside a diesel engine has been

conducted by researchers via experiment and simulation in order to design them to conform to the rules and regulations of the Euro standard [8].

The European vehicle emission standard plays a major role in controlling the regulations of exhaust emissions that are permitted. European emission standards have a stringent emissions policy that governs the EU member automobile exhaust emissions. Figure 1.3 [9] illustrates the evolution of European emission standards from Euro 2 to Euro 6 for diesel and gasoline engines. US limits are also shown here for comparison.

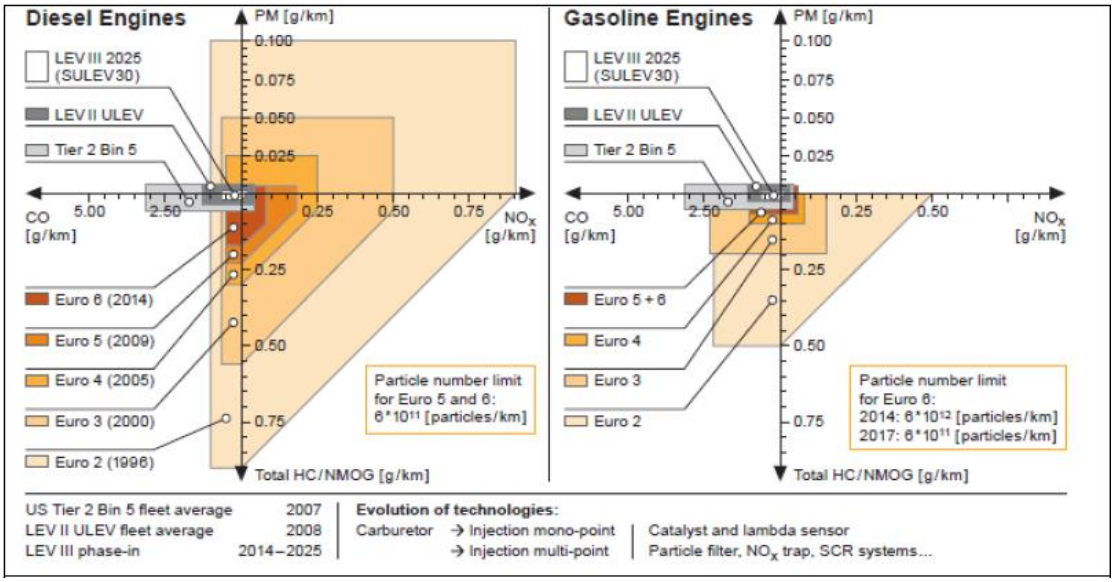

Figure 1.3 Evolution of European emissions standards [9]

1.2 Regulation-induced relating to automotive trends

Starting in September 2017, the EU Legislative acts introduced Real Driving Emission (RDE) tests to further the stringent regulations that automotive manufacturers should comply to. The tests were conducted in real-time using Portable Emission Measurement Systems (PEMS). This will show intrinsically high variability in emission results which then will be defined by a conformity factor for each pollutant and Euro 6 limit. Vlachos [10] stated that the procedure, which is a novel approach for controlling the global emissions, has been very effective in vehicle emission control.

	Gasoline (positive ignition)			Diesel (compression ignition)		
Limit values for type 1 test	**All Cat. M and N1 Ref. mass ≤ 1305 kg**	All Cat. N1 1305 kg < RM ≤ 1760 kg	All Cat. N1 1760 kg < RM and Cat. N2	**All Cat. M and N1 Ref. mass ≤ 1305 kg**	All Cat. N1 1305 kg < RM ≤ 1760 kg	All Cat. N1 1760 kg < RM and Cat. N2
Mass of carbon monoxide (CO)	**1000 mg/km**	1810 mg/km	2270 mg/km	**500 mg/km**	630 mg/km	740 mg/km
Mass of total hydrocarbons (THC)	**100 mg/km**	130 mg/km	160 mg/km			
Mass of non-methane hydrocarbons (NMHC)	**68 mg/km**	90 mg/km	108 mg/km			
Mass of oxides of nitrogen (NO_x)	**60 mg/km**	75 mg/km	82 mg/km	**80 mg/km**	105 mg/km	125 mg/km
Combined mass of hydrocarbons and oxides of nitrogen (THC + NO_x)				**170 mg/km**	195 mg/km	215 mg/km
Mass of particulate matter (PM)	**4.5 mg/km** (only direct injection)	4.5 mg/km	4.5 mg/km	**4.5 mg/km**	4.5 mg/km	4.5 mg/km
Number of particles (PN)	**$6\,10^{11}$ #/km** (only direct injection)	$6\,10^{11}$ #/km	$6\,10^{11}$ #/km	**$6\,10^{11}$ #/km**	$6\,10^{11}$ #/km	$6\,10^{11}$ #/km

Figure 1.4 Euro 6 standards showing the limits that WLTP and RDE must comply [9]

This test aimed to determine the test pollutants in real driving conditions, as it was determined that actual driving conditions of vehicles on the road produced more pollutants than laboratory tests. In order to conform to the new guidelines, the test procedure with EGR incorporated is known to aggravate the soot level development in the engine.

Lower viscosity lubricants are now introduced to comply with the demand of more efficient automotive engines, through reduced friction. However, this will have an effect on the tribological contacts due to thin film thickness being formed between the engine contacts thus causing wear to the components [11].

1.3 Aims and objectives

The lack of wear models for lubricated engine components causes problem to the engine designers to understand the problems in engine lubrication. Therefore, wear models and design tools for engine components are required to increase the understanding and reduce wear. The study will be focused on investigating the influence of increasing soot levels in oil on valve train component interface friction and wear and understanding the wear mechanisms that occur within the contaminated contact zone. This will be done for a range of different materials and contact conditions. At the same time, a test set-up will be developed to help understand the results from wear and friction tests that will allow measurement of the film thickness of each contact. This will be achieved by completing the following objectives:

- To compare and validate the wear and friction mechanisms that occur within a soot contaminated metal-to-metal contact with previous research with EN24 steel using simple ball-on-flat specimen test rig.
- To determine the effects of increasing soot levels to wear and lubrication of valve train components in simple specimen non-conformal point contact for metal-to-metal contact and metal-to-non-metal contact.
- Designing and producing a new holder for the Plint TE77 reciprocating test rig to study the effects of soot on O-rings (simulating a valve stem and seal contact).
- Characterising the fundamental aspects of soot wear effects by varying contact parameters on different materials using the Plint TE77 test rig.
- Designing and producing a new holder for a block-on-ring test rig to study the effects of soot on O-rings in a point contact.
- Studying the effects of soot on simple component non-conformal contacts (using the Block-on-O-ring).
- Developing a novel test set-up that allow measuring oil film thickness for different test specimen materials of a contact using ultrasound techniques to help understand the results from wear and friction tests.

1.4 Contributions of the study

The contributions of this study are outlined below:

- The study was focused on real engine contacts simulated in a laboratory based specimen tests, rather than testing in a common laboratory test (e.g. four ball test).
- The design and development of an O-ring holder for the use of a ring-on-flat reciprocating test rig which simulates the contact between a cylinder and a seal.
- The design and development of an O-ring holder for the use of block-on-ring test rig which simulates non-conformal contact between O-ring and block.
- The study and understanding of soot wear effects on elastomer/polymer O-rings materials for both point and line contact simulating movement in an engine.
- The design and development of an ultrasonic test methodology to measure sooty-oil film thickness on different materials.

1.5 Thesis outline

A thorough review of fundamental theories and literature, experimental techniques employed in this research; results and discussion are presented in this thesis. The thesis outline is as follows:

- Chapter 2: This chapter describes the fundamental theories and concepts of tribology, mainly on wear, friction and lubrication which are related to this study. Wear mechanism classifications are also discussed mainly for the soot induced wear in internal combustion engines (ICE)

- Chapter 3: The basic definition of soot is described here; where it goes and what problems it will cause to parts of an internal combustion engine (ICE). It also includes earlier research works that have been conducted on automotive soot with the effects on lubricant and materials. A paper grading methodology is also presented here to identify gaps that can be explored in this study.

- Chapter 4: The soot characterisation and hardness of carbon black and used engine oil is investigated in this chapter.

- Chapter 5: This chapter discusses non-conformal ball-on-flat experiments (metal-on-metal) in order to replicate previous studies done by another researcher and to build confidence in conducting experiments using different materials.

- Chapter 6: This chapter explores soot wear effects on elastomers/polymers used in non-conformal Plint TE77 experiments. Details of the test-rig and the test procedures, specimens used and theoretical equations are presented here.
- Chapter 7: A detailed non-conformal reciprocating sliding investigation test using real engine components (O-rings) is presented in this chapter. Details of specimens, testing methods and results obtained are discussed here.

- Chapter 8: This chapter outlines the non-conformal elliptical contact test using a BICERI rig (Block-on-ring). Details of test rig, specimens, testing method and results are analysed and presented.

- Chapter 9: This chapter discusses the oil film thickness measurement using ultrasound for carbon black contaminated lubricant. Details of the test procedures, specimens used, analysed results are presented here.

- Chapter 10: This chapter gives an in-depth discussion on the studies conducted.

- Chapter 11: This chapter summarised the conclusions and future works of the study that could be explore thoroughly.

Chapter 2 Theoretical Characteristics of Tribology

This chapter discusses the characteristics of tribology, namely: wear, friction and lubrication. Each term related to this study is discussed here. The contact mechanics which relate to the stress in the interfaces that were caused by contact between two bodies is discussed in each chapter, according to its contact condition.

2.1 Introduction to tribology

"Tribology" is derived from the Greek word "Tribos" that means "rubbing", and "ology" which refers to "field of study". This scientific term focuses on friction, wear and lubrication of interacting surfaces [12]. Despite the importance of tribology in engineering, the subject of tribology is still unclear to the wider community. This could be due to the poor availability of tribology to the broader engineering community.

2.2 Friction

Friction is the resisting force occurring when one object moves in the opposite direction with respect to other object. Several parameters such as contact surface (materials), surface roughness, lubrication, contact geometry, load (contact pressure), temperature and sliding speed could influence friction of a body. In engine design, low friction is required to have an efficient operation and low energy loss. The majority of power loss is generated by the subassemblies of the piston group, crankshaft journal bearing, valve train, timing drive and shaft seals [1]. Figure 2.1 (a) shows that the piston ring assembly is the major contribution to the mechanical losses distribution in a diesel engine with half of the friction loss comes from the piston ring as shown in Figure 2.1 (b).

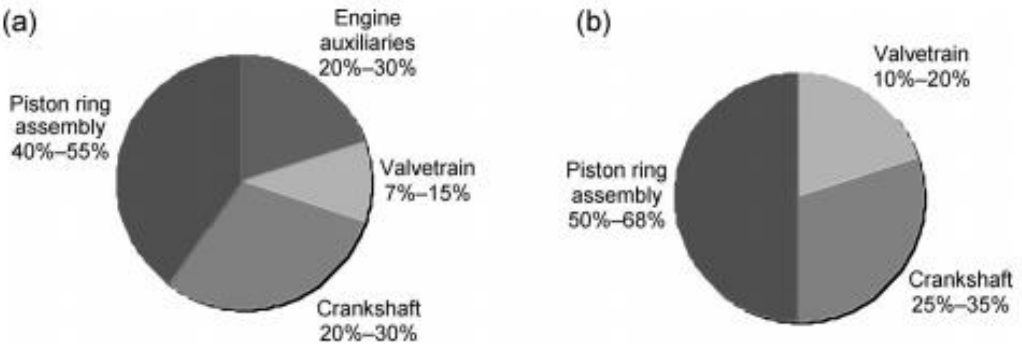

Figure 2.1 Distribution of (a) mechanical losses and (b) friction in a diesel engine [13]

2.3 Lubrication

Lubricant is a thin low-shear-strength layer of gas, solid or liquid protecting the surface between two contacting solid bodies from friction and wear during rubbing action of the surfaces. In an engine lubrication, a liquid base stocks lubrication is used. Three main base stocks are used in lubricant formulation, which are mineral oil based, synthetic and bio-based.

2.3.1 Mineral oil based lubrication

Mineral oils which are produced by the refining process of crude oil is the most common lubricant used in the automotive industry and it can be classified into three sub-groups based on its chemical structure; paraffinic (straight and branched hydrocarbons), naphthenic (cyclic carbon molecules) and aromatic oils (benzene type compounds). The physical properties of the lubricants are influenced by the different molecule structure in the oils such as the viscosity-temperature characteristics between paraffinic and naphthenic oils are significantly different [12].

2.3.2 Synthetic oil based lubrication

Commercial synthetic mineral engine oils undergoes complex chemical modifications reacting it with different chemical compounds of low molecular weight such as poly-α-olefins (PAOs) and polyalkylene glycols (PAGs) to form high molecular weight compounds [14]. Synthetic oils which are more expensive in comparison to mineral oils applications are limited which require high performing lubricants. While semi-synthetic oils (blend of mineral oil and PAOs) are cheaper and more commonly used in automotive applications.

2.3.3 Bio-based lubrication

Bio-based lubrication that are derived from vegetable oils such as palm oil and soybean oil consists of triacylglycerol structure derived from glycerol and fatty acid chains are desired in boundary lubrication as their ability to adhere to metallic surfaces while creating a monolayer that can reduce friction and wear [15]. Vegetable oil is widely used as a bio-based lubrication due to its high viscosity index, high flash point, high biodegradability and a reduced friction coefficient [16]. However, vegetable oil also has some disadvantages in terms of oxidation stability, low thermal stability, and a comparatively high wear rate. Thus to overcome this problem, various techniques is implied such as blending with polyalphaolefin and oleates, esterification and transesterification [17].

2.3.4 Additives

Additives are chemicals that are added to base oils to improve the lubricating properties, suppress unwanted properties and introduce new features to the base oil. Fully formulated oil typically contains between five and fifteen different additives depending on application demand. There are several types of additives commonly found in diesel oils. Some additives perform multiple functions in the lubricant such as ZDDP and dispersants. Most of the studies done use antiwear additives (ZDDP) and dispersants to protect the engine surface. Others use base oil protection such as MoDTC (molybdenum compounds).

The dispersant additive's function is to suspend oil insoluble contaminants and degradation products. Basic dispersants are very effective at ensuring soot particles remain dispersed in the oil and cause less soot mediated oil thickening. These additives prevent corrosion, oil thickening, sludge and deposition on metal surfaces.

Antiwear additives prevent damage and wear to parts experiencing boundary lubrication. Antiwear additives react with metal surfaces at elevated temperatures to form a tribochemical protection layer that prevents direct contact between sliding surfaces. Zinc dialkyldihtiophosphates (ZDDP or also known in terms as ZDTP, ZnDTP or ZDP) are most widely used antiwear additive in lubricating oils. Metal dithiocarbamates, such as molybdenum dithiocarbamnate (MODTC) are one antiwear additive that can enhance antiwear properties when used in combination with ZDDP [18].

2.3.5 Lubrication regimes – Stribeck curve

Lubrication is also related to wear of the rubbing surfaces under an applied load. The film thickness is determined in order to define which lubrication regime a system is operating in. The form of lubrication depends on the contact parameters such as load, speed, temperature and materials (surface conformity). This is shown in the Stribeck Curve, where the coefficient of friction is displayed against viscosity, speed and load. The curve shows four lubrication regimes as shown in Figure 2.2. The curve shows the coefficient friction is higher at boundary lubrication where solid contact occurs, to hydrodynamic lubrication where CoF are lower; this is because at this point a full film occurs in the contact. at the end of the hydrodynamic lubrication regime, the CoF starts to increase because of the viscous drag effects increasing either due to high viscosity of the lubrication or due to high oil film thickness. The ideal lubrication is normally operated in between mixed regime and hydrodynamic lubrication where the surface is separated by the oil film thickness; however, some asperity contact may still occur which cause plastic deformation [19].

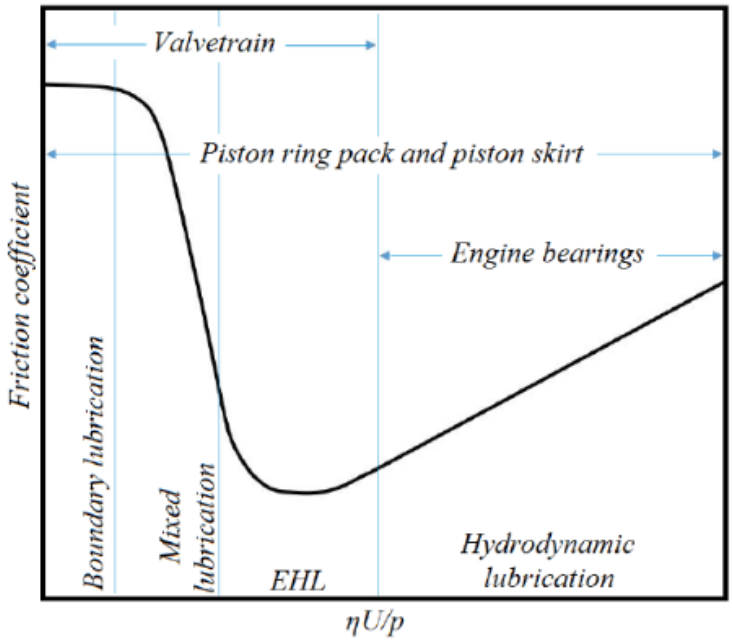

Figure 2.2 Stribeck curve [20]

- Boundary lubrication (BL)
  The asperity interaction between surfaces becomes significant whereby severe wear could occur. When soot content increases with increase in temperature, higher wear is observed on the contact [21]. This could cause failure by adhesive and corrosive wear. In this regime, the chemical properties of the contact are vital than the physical properties of the lubricant [22].

- Mixed lubrication
  Here the asperities in contact are not fully separated, but interact somewhat in between. Here, surface roughness plays a vital role on the contact surface. The operating regime is between hydrodynamic and boundary lubrication. At mixed lubrication regime, the increase in soot content generates lower friction, but will still lead to an increase of wear on the surface contact [21].

- Elastohydrodynamic lubrication (EHL)
  The surfaces are separated by a thin layer of fluid film lubrication. At higher load and low speed, physical interactions occur between surface asperities where pressure is high which result in elastic deformations of the surfaces [22]. In hydrodynamic lubrication, soot loaded oils generate a friction coefficient similar to fresh oil and this increases when soot level rises, thus increasing the wear of the contact [21].

- Hydrodynamic lubrication (HL)
  This regime is also called full film lubrication, is the most looked-for lubrication. Here, the surfaces of the two bodies are fully separated such that there is no asperity-to-asperity contact thus the resistance to motion, friction force, is dependent on the viscosity of the lubricant [12].

The Stribeck curve is a useful tool for either designing lubrication system in which the oil film thickness can be obtained from the Stribeck curve or using analytical solutions. In hydrodynamic regime, lower load increases the CoF and vice versa. While in mixed lubrication, the load is supported by the pressure of the fluid and some asperity contact. When load increases, the solid contact increases too. Increased in fluid pressure will also increase the CoF. High load is preferable in hydrodynamic lubrication as it gives thinner oil film thus lowering the CoF.

In hydrodynamic regime, the temperature also plays a role in reducing the CoF; whereby an increase in temperature will lowered the viscosity of oil and the viscous drag effects thus reducing the oil film thickness. While in mixed regime, when the temperature increases, the CoF increases. The increase in CoF is due to the reduction in viscosity where it is unable to provide sufficient protection to the surfaces coming into contact. the speed between contacting surfaces is the dominant factor in lubrication regimes to which it must be sufficient to allow oil entrainment into the contact where a fluid film could be created [19].

2.3.6 Oil film thickness

The role of lubrication is to provide a fluid film between two bodies which means the lower the lubricant viscosity, the thinner the fluid film thus severe wear could occur. The lubrication regime is determined by the lambda ratio (ʎ) where it is defined as the ratio of film thickness to the surface roughness, and it helps to determine the lubrication regime. As shown in the Stribeck Curve (Figure 2.2), viscosity is the most important parameter when in full film lubrication (no-asperity contact); shear stability of the lubricant is essential in minimising shear-related viscosity losses.

2.4 Surface roughness

The surface roughness also plays a vital role in assessing tribological contacts [23]. Besides the use to compare minimum film thickness in estimating lubrication regime, it is also use to indicate the contact reduction of the nominal contact are a due to the peaks and valleys of the surface [24].

The surface roughness is also vital when aiming to increase the efficiency of the energy system. This will require automotive engines to work under increasingly extreme conditions such as thin film thickness (lubrication).

2.5 Wear

The damage due to the movement of contacting surfaces between solid bodies is attributable to the lubrication film failure. The effect of the film failure is severe wear. Material degradation occurs due to increasing wear damage to the surfaces of

contacting bodies. The consequence of changes in surface properties and topography due to the material removal is reduction of the mechanical component performance [25]. Many researchers have investigated the wear and its mechanisms. Prominent wear mechanisms are explained here:

2.5.1 Abrasive wear

There are two types of abrasive wear known as “two-body” abrasive wear and “third-body” abrasive wear where in “third-body” abrasion, particles formed during abrasion or the presence of particles in the system causes abrasive wear while in “two-body” one of the materials plays the role of the abrasive. A simple chart is presented in Figure 2.3 that shows the elements involved in an abrasive process [26].

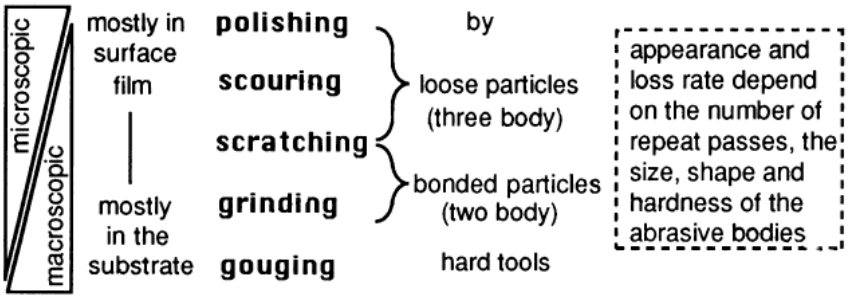

Figure 2.3 Abrasive process chart [26]

2.5.2 Adhesive wear

Severe wear can occur due to two contacting bodies adhering to each other through asperity contact. It involves material loss between contacting bodies at higher friction. Adhesive wear normally take place in boundary and mixed lubrication regimes, where there is insufficient lubrication as a result of starvation. This could result in material transfer between contacting surfaces. Figure 2.4 shows a schematic illustration of the wear mechanism.

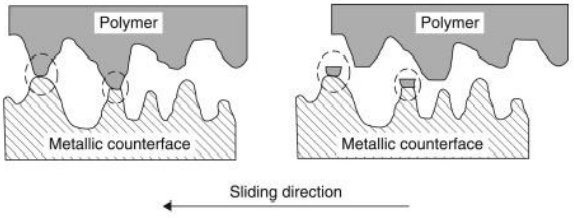

Figure 2.4 Schematic illustration of adhesive wear

2.5.3 Fatigue wear

Fatigue wear is commonly found on elastomers where a rubber, which is highly elastic, moves relatively to a rigid and blunt surface under a certain load and continuous cyclic sliding, which will then produce repeated compression and expansion within the surface layers [27]. The surface of the rubber layers will wear through under the action of compressive, tensile and shear deformations leading to crack formation and propagation, delamination and small cavities, which are the root cause of material failure after cyclic sliding. Fatigue wear could also take place in lubricated contacts when repeated high stress are exerted in cyclic sliding or rolling [12].

2.6 Polymers wear and friction problems

2.6.1 Abrasion

Abrasive wear on elastomers/thermoplastics is caused by the abrasive action of the asperities on the harder counterpart which in turn ploughs into the rubbing surface of the polymer and removes the material [28] due to the deformation of the materials that is related to viscoelastic effects. Sometimes the wear of elastomer materials such as rubber may not appear to be abrasive, this could be the result of the removal of chemically unaltered molecular chains of the elastomer material [26].

2.6.2 Adhesion

Adhesive wear occurs when polymers slide in contact with metals. When two bodies are sliding relative to each other, a force is needed to shear the adhesive bonds formed at the interface where the interface bonds are stronger than the cohesive bonds in weaker materials. Polymer films will transfer to the metal surface, where shear takes place in the polymer due to its weaker cohesive bonds [29]. During sliding of polymer-metal contacts, more wear particles from the soft materials are formed than the harder counterpart due to the shearing process.

The mechanical properties and chemical interaction of sliding bodies influences the adhesion strength of the interface. This could be reduced by the use of lubricant where it is easier to shear a fluid film than solid-solid contact and also reduce friction [30]. Briscoe & Sinha [31] reported that the reduction in contact area due to film formation, changes of shear properties and adhesion properties and polymer plasticisation is due to the effects of lubricants. It is also reported that the effects of lubrication of polymers is different to metals, where it is suggested that the lubricant is able to penetrate into the bulk of material and change its mechanical properties or the lubricant effects the shear and adhesion properties of the transfer film.

2.6.3 Hysteresis friction

Hysteresis is known as a component of friction occurs in viscoelastic materials at the elastic limit due to hysteresis losses. Hysteresis losses occurs when a viscoelastic material (polymer) is stressed in and out during sliding and continues as the point of contact moves on. Elastic energy is used to stress the volume of the element and when stress is removed, the energy is released where a part of it is released as heat as a result of elastic hysteresis loss (Figure 2.5). The energy losses are large especially for elastomers, but for metals the energy loss is approximately less than 1% in the elastic region.

Thermoplastics, which are different from elastomers, are not perfectly elastic, therefore the total energy loss is related to the input and energy and loss of material properties depending on the temperature, pressure and deformation process. For thermoplastic material, the material will experience delay in recovery or will deformed permanently due to softening of the material when subjected to mechanical interactions and adhesion. The chains will reallocate to different orientation when subjected to sliding action and consequently micro-crack will appear under the surface and particles of polymer materials are removed from the surface [32]. But for elastomers, the deformation of the material occurs when the material experience delay in recovery; this is called the hysteresis friction [30]. After sliding occur, part of the energy, heat is released to the ambient, and the molecule structure will returned back to its original shape.

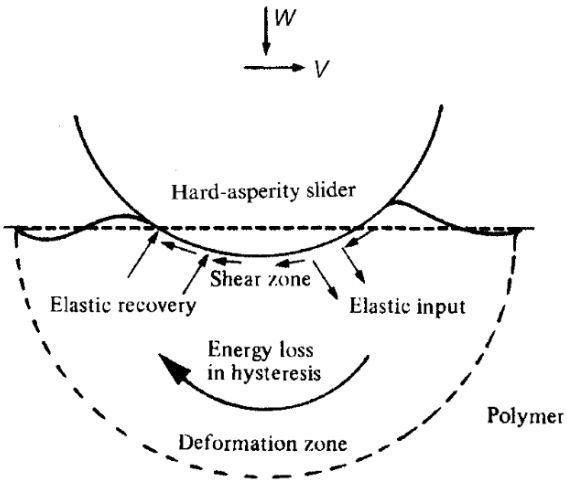

Figure 2.5 Sliding of rough hard sphere over a polymer [30]

2.6.4 Deformation

During sliding of two dissimilar materials, in this case metal-thermoplastics; a macroscopic interaction occurs where the asperities from the harder material either plough through the surface of the softer material via plastic deformation or tear the material thus producing wear particles/debris. In the case of elastomer materials, the deformation is related to the hysteresis friction loss that is caused by the delayed recovery of the material after indention of hard material into the rubber material [30].

2.7 Summary

In this chapter, a significant amount of information and overview of tribology has been discussed here. The types of lubrication and wear that normally occur in rubbing surfaces were also explained here. Wear and friction effects on polymers are also discussed, however the interactions with the presence of soot in oil and the wear mechanism from it will be discussed in detailed in Chapter 3.

Chapter 3 Soot Review

In this chapter, an in-depth review on soot and the problems it creates within the engine will be provided. The review continues by examining all of the earlier research that has been conducted on soot effects on machine element contact tribology and also wear of different materials, followed by current wear testing methods and standards. A paper grading methodology is also discussed in this chapter. The results from this grading allow a quick visualisation of where data is available and of what "quality". The identified gaps are then highlighted in this chapter.

3.1 Introduction to soot

Soot is a carbonaceous particle, which is produced as a result of incomplete combustion of either gasoline or diesel fuels. It is comprised of carbon, ash and unsaturated (unburned) hydrocarbons as shown in Figure 2.1 [6]. Measurements from elemental analysis have shown that engine soot typically contains 88.3% carbon, 4.9% oxygen and 2.6% hydrogen with the remainder consisting of nitrogen, sulphur and traces of metals (Figure 3.1) [33][34].

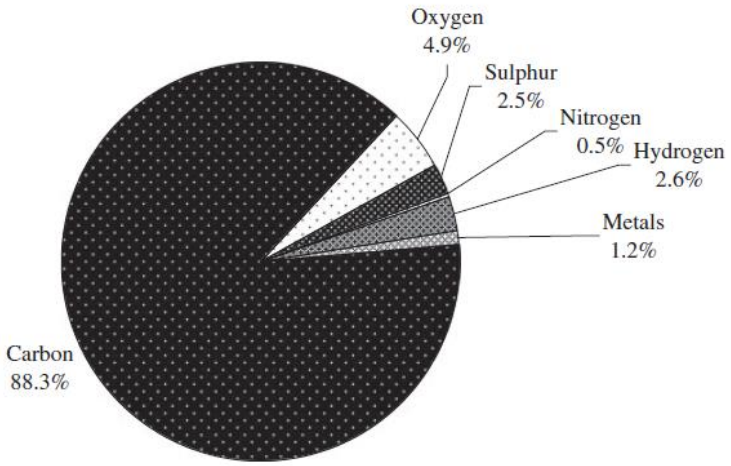

Figure 3.1 Elemental composition of diesel particulate matter [34]

The soot carbon will agglomerate up to 500nm in size due to its colloidal properties, with an average of the agglomerates of 200nm size where the primary soot particles were measured to be approximately 40nm in size [33] (see Figure 3.2).

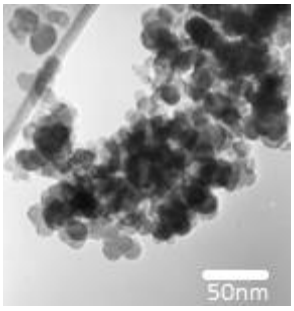

Figure 3.2 Image of engine soot agglomeration [33]

Research has shown that engine soot and exhaust soot emitted from the exhaust pipe are quite different in terms of their element composition. Exhaust soot is a heterogeneous material with a highly oxidised surface compared to engine soot. It is also known that soot particles are harder than steels as has been investigated by Li [35]. As for exhaust soot, the carbon content can be 50% lower and the oxygen 30% higher. This could probably occur due to the oxidation processes the combustion products experience. It has also been noticed that the concentration of volatile contents also significantly increases in the exhaust soot [36].

3.2 Where does it go?

In internal combustion engines, mainly diesel engines, 29% of soot produced in an engine is ejected to the atmosphere from the cylinder through the exhaust pipe [37]. 68% of the remainder of the soot produced is deposited back through the cylinder walls and piston crown in the lubricating oil, 3% is due to blow-by gases, the rest results from soot on piston rings which ends up in the sump [2]. The soot content accumulated in the crankcase increases during time between services, degrading the lubricant performance and forming deposits of carbonaceous material that wear the engine parts [37].

Throughout the valve train in an engine, there are numerous component interfaces, which all have different geometry and motion. There are sliding, rolling-sliding and reciprocating contacts as shown in Figure 3.3. Because of varying motion and loads at each contact, different regimes of lubrication will also be apparent. As marked in Figure 3.3, the contacts that develop varying motion are the elephant’s foot to valve tip interface which exhibits reciprocating motion; the rocker arm/cam interface exhibits rolling/sliding motion; the valve stem/valve guide exhibits sliding motion and the rocker arm contact exhibits reciprocating motion.

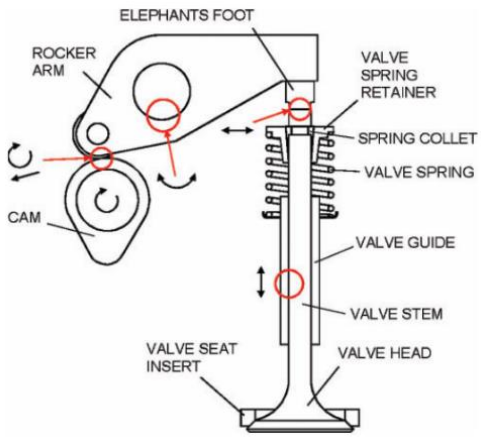

Figure 3.3 Valve Train Component Contacts [2]

Chinas-Castillo and Spikes [38] stated that the soot particles penetrate into the lubrication contact by cohering and piling up onto the surfaces until they form an inhomogeneous boundary film which influences the wear rate when soot particles are larger than the film thickness. They also found that the film thickness increases when soot concentration increases where these soot particles had penetrated the elasto-hydrodynamic film.

3.3 Where is it a problem?

The increase in soot and solid particulate content in the engine oil may result in accelerated abrasive wear of critical engine components. Elemental analysis has shown that soot also contains hydrogen, oxygen and sulphur. The increase in the oil acid content (sulphuric acid) is expected to increase corrosive wear of lubricated surfaces [5]. Figure 3.4 shows component wear data from engine tests with increasing levels of EGR thus gives an impact on the increase of soot as proved by Nagai [4]. In the figure it shows that wear is worse in the valve train components. The cam nose was shown to have greater wear followed by rocker arm. Cylinder liner and piston rings are also contacts that are vulnerable to wear. Other valve train components with visible wear are the valve guides and stems.

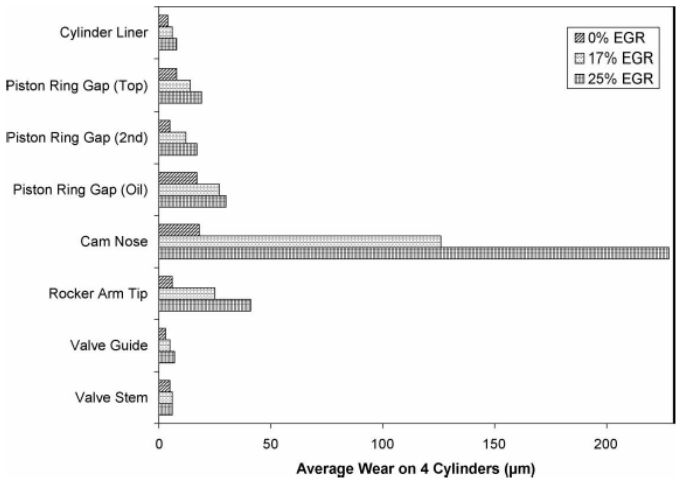

Figure 3.4 Average engine wear data for tribological components in a 4-cylinder engine [4]

3.4 Wear testing methods

Real engine tests are difficult to execute due to the issues in controlling many test parameters to provide good wear measurements. However, standard engine tests can be designed that allow soot wear studies to be carried out.

Tribological testing can be conducted at different levels. The complexity decreases with the move down from field tests to specimen tests where greater control of the parameters can be achieved and the tests are also more repeatable. It is necessary in a bench laboratory test when testing involves contaminant, that the geometry, loading and contact motion is achieved. This is because, the contact parameters will influence the entrainment of contaminants and it helps to determine which wear process may actually occur in real components.

3.4.1 Test apparatus

Many research works have used the four-ball approach method in which various soot contaminated lubricant formulations have been tested [37][39]. Other methods used are a high frequency reciprocating wear tester [36]; three body wear machine [40]; pin-on-disc [41][42] and ball-on-flat sliding apparatus [43][44]. These methods are limited to specimen tests. It is necessary to test the level of wear using real engine components of an engine so as to obtain the real wear results using real component contact conditions. This work has been done by Green et al. by investigating wear on the tips of valves and the rocker pads with which they make contact [43][44].

The use of optical microscopes or for a more definite analysis on the wear scar, Scanning Electron Microscopy (SEM) is used to understand the wear mechanisms produced on the surface after each test. Wear measurement is usually achieved through wear scar profilometry and determining wear depth or wear scar volume [45].

3.4.2 Sources of soot for testing

In research regarding soot wear, there are three options for the test materials for soot. These are:

- Ageing oil / extracted used oil
- Extracted engine soot blend with new engine oil
- Carbon black blend with new engine oil

The first can only be generated by running an engine over an extended period under certain conditions. This method is expensive and time consuming and it would be hard to produce the same soot each time.

The second method is by extracting soot from a used lubricant in a diesel engine and mixing it with chosen test lubricant. This test method requires less time, but it is more expensive than the first method. The disadvantage is that it is hard to maintain consistency in soot samples.

The final method is by using carbon black as a soot surrogate. This method has been used widely to replace real diesel soot to access the level of wear due to soot contamination [45]. It is easier to obtain and inexpensive. The disadvantage of using carbon black as a surrogate is that although it is found to be similar to engine soot, it is not engine soot and the results of wear using carbon black have been questioned as to whether the results produced are comparable to using real diesel soot.

For example, investigations have shown that carbon black can act as a surrogate in replacing soot by comparing soot extracted from diesel engine oils with various commercial carbon blacks. Findings show that there is a similarity in their primary particle sizes (between 30 and 50 nm) using electron microscopes. It is believed that diesel soot and carbon black have greater similarity at the nanometre scale [33].

Another study concluded that certain grades of carbon black such as Regal 250R can be useful surrogate of diesel soot in the presence of polymeric lubricant additives. Similar data on fractal morphologies, grain sizes and density can be obtained for carbon black and diesel soot when using copolymer dispersants [46].

3.4.3 Soot effects on wear and friction of metals

Early research suggested that the anti-wear additives in the lubricant could be adsorbed by soot and later found that the major wear mechanism was caused by abrasion [47][48]. Berbeizer [47] found that carbon black particles with a 20nm diameter produced a lower wear rate than particles of 300nm.

Gautam [6][39] using data from three-body wear tests, higher wear was caused by soot contaminated lubricant than uncontaminated oils and it was determined that abrasion wear is the wear mechanism that causes increased of wear in contacts. Green [3] had observed from a ball-on-flat reciprocating test that the wear mechanism in lubricated metal-to-metal sliding (Figure 3.5) was abrasion and starvation due to the carbon black particles blocking the lubricant from flowing into the contact.

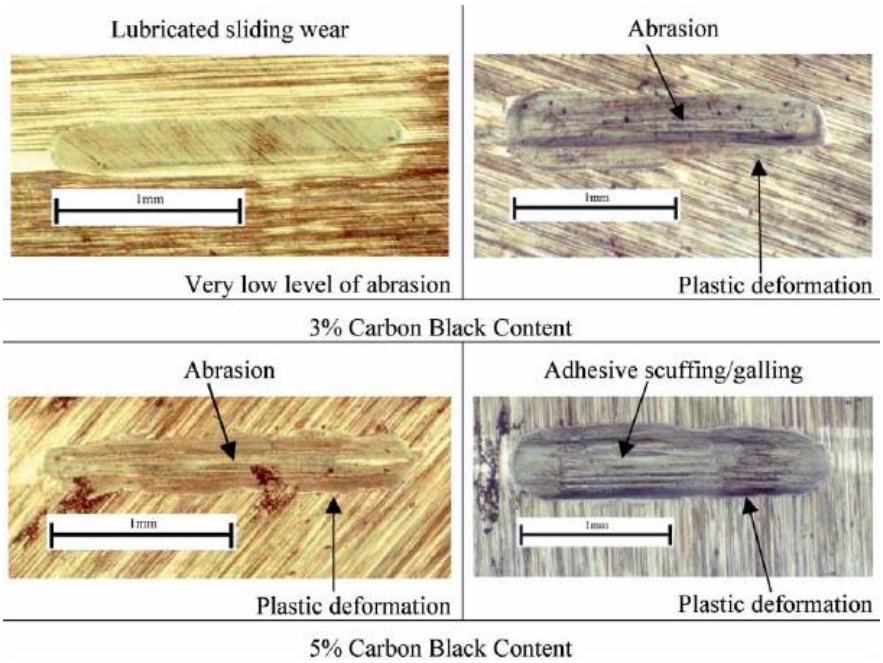

Figure 3.5 Images of abrasion mechanism at 3% and 5% carbon black content [3]

Green & Lewis [2], also discovered that using blended carbon black with base oil increases the wear volume significantly at higher temperature as shown in Figure 3.6.

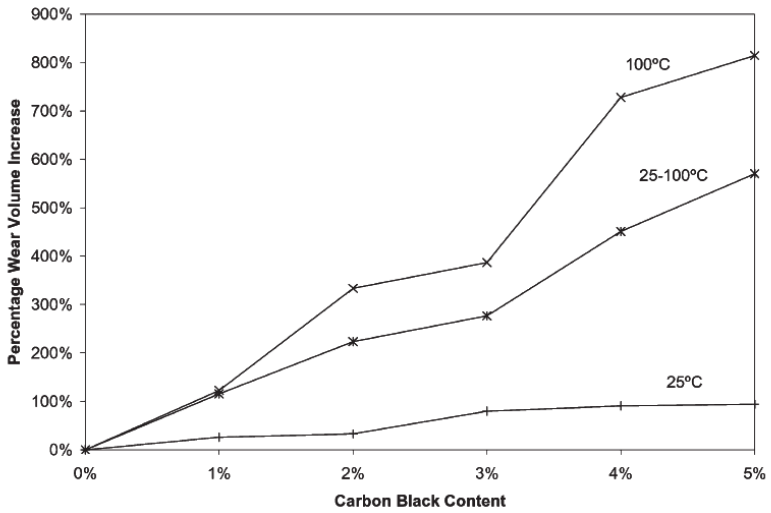

Figure 3.6 Percentage wear volume at different temperatures and different levels of carbon black content [2]

3.5 The effects of soot on lubrication

3.5.1 Friction

Through follower and cam testing, it has been shown the friction fluctuates and increases with the lapse of the time in the case of contaminated oil with soot [49], however Antusch [42] had used a pin-on-disc (PoD) tribometer in his study, and discovered that the increase in soot content decreases the CoF. Ramkumar's [50] work on effects of diesel engine oil on friction using a PoD tribometer also shows that friction increases with increased in level of contamination. Green and Lewis [44], using a ball-on-flat reciprocating wear tester, also found similar trends with increasing carbon black content in engine oil. However, Liu et al. [51] found different results when measuring the friction coefficient with different lubricants with various soot contamination levels. It showed that the friction decreased with the presence of soot in the lubricant.

3.5.2 Viscosity

Truhan [52] also stated that concentration levels of soot in oil is about 9.3% by weight. This is proof from the measurement conducted by George [53] of eight oil test blends which showed that the viscosity of the oil samples increased with increase in soot at both 40°C and 90˚C. The analysis indicated a nonlinear behaviour of viscosity as the amount of soot increased at 40˚C, whereas there was a linear variation at 90˚C. The statistical analysis results at 40°C and 90˚C showed that the effect of base stock and ZDP levels were negligible at 40˚C, whereas the dispersant level and soot level influenced the viscosity of the oil samples at both temperatures.

Increasing soot content in an engine clearly shows the adverse effect on fuel consumption as stated by Carvalho [54]. Green's results on viscosity measurements shows that at higher soot levels, the effects of soot in the contact are most trivial [44].

3.5.3 Starvation

Starvation is caused due to blockage of lubricant to enter a contact. The soot tends to absorb additives and oil molecules to form mixtures and agglomerates. The agglomerated soot prevents fresh oil from entering the contact thus resulting in starvation therefore causing unlubricated sliding wear.

Aldajah and Sato [5][55] stated that agglomeration of soot inside the lubricant will cause starvation if the lubricant fluid film thickness is smaller than the diameter of soot agglomerates. However, Enzhu [56] discovered that the fluid film thickness increases when the agglomerated soot increases thus preventing fresh oil from entering the contact thus resulting in starvation.

However, Enzhu [56] discovered that the carbon black particles played a part in the wear and friction properties of the lubricants used in his studies. It was found that the simulated soot absorbed additives and oil molecules to form mixtures and agglomerates. The agglomerated soot prevented fresh oil from entering the contact thus resulting in starvation. This can be verified from the oil film thickness where the oil film thickness increased with the increase of the oil viscosity.

3.5.4 Lubrication degradation

The effectiveness of lubricants is degraded during use by contamination and thermal degradation. As it degrades, the lubricant functions less efficiently, until it must finally be replaced to maintain engine performance and prevent damage to components. During use, the oil can be contaminated by soot, unburned fuel, metallic particles, water and acid by products of fuel combustion or lubricant degradation. Before contaminants reach critical levels, the oil must be drained and engine refilled with fresh oil.

Exhaust product (soot) that is returned to the diesel engine combustion chamber will accelerate the degradation of the lubrication oil by increasing the total acid number (TAN), increasing soot content due to incomplete combustion and also increasing the viscosity [5]. As soot particles are highly acidic, the acids that contaminate oils are the source of many lubricant related problems in diesel engines. During normal engine operation, lubricant is exposed to combustion and blow-by gases containing nitrogen, sulphur and carbon-based acids. Severe problems can occur if these acids remain in the oil and are not neutralized. Weak organics acids build up in an oil can cause detrimental effect to the engine such as fouling of engine components and lubricating films due to engine wear and corrosion. It shows that soot tends to cause lubricant deterioration by lowering the TBN number.

The additives in a lubricant helps in reducing further ageing of the oil while the dispersants function is to retain the soot particles inside the lubrication in order to reduce engine wear. When soot level and wear debris increases inside the lubrication, the dispersants will be depleted. Soot is entrained in the oil and harmlessly suspended until active additive components become depleted. This condition causes the soot particles to agglomerate into larger particles thus resulting in lubricant failure as it degraded.

3.6 The effects of soot on different materials

3.6.1 Steel

All investigations on soot wear using steel shows that abrasive wear is the major wear mechanism occur for all specimens/component from a low level of soot/carbon black content in the lubricant and start to starve at higher soot concentration [3][42][44][57][58]. Figure 3.7 shows that the scratches shown on the ball with respect

to the sliding direction indicate abrasive wear. Meanwhile Kaneta [57] discovered that soot particles adhered to a soft steel roller surface to protect its surface against wear, but brings wear to the hard steel roller surfaces. Although friction is reduced, the wear volume is higher when soot concentration increases [5][59].

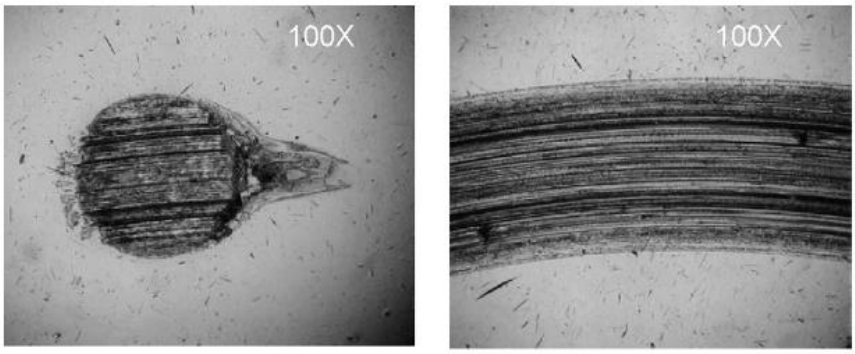

Figure 3.7 Optical micrographs for ball wear tracks showing abrasive wear [5]

3.6.2 Cast iron

The research on soot wear for cast iron also shows signs of abrasive wear when soot increases [40][35][52][60], as shown in Figure 3.8. In a study done by Li [35], it was found that soot is harder than ferrous material, thus the soot is hard enough to abrade metal engine parts. It is also learned that the groove width discovered on the surface is larger than the soot size. It is suggested that carbides are also found as one of the abrasive particles that abrade the metal. Li and Kuo [35][45] suggested that the carbides are possibly inherent to the carburized cast iron microstructure. While friction decreases due to the additives in the engine oil. Kuo [45] discovered that there are differences in the wear of crosshead and rocker arms of two different materials. It appears that the rocker arm wear pattern exhibits more cracks than the crosshead, due to the inhomogeneity of the rocker arm microstructure.

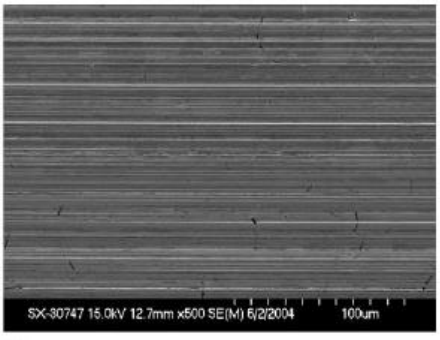

Figure 3.8 SEM image of abrasive wear scar of the flat cast iron specimen [52]

3.7 Wear in seals

Elastomers is a general term for the group of polymers with common characteristics such as viscoelasticity and high elasticity [61]. Seals used in reciprocating engine applications are made from elastomers/polymers such as rubber, polyurethane elastomers and PEEK. Seals are components which prevents leakage of fluids or gas from machine equipment. Seals may be divided into static or dynamic seals depending on their application. Examples of static seals are gaskets and O-rings while reciprocating and rotating seals are classified as dynamic seals. Elastomers are prone to wear under contact sliding conditions and this is known to be the cause of failure for dynamic seals. Abrasion, compression, chemical and thermal degradation are a few process of failure occurs in seals. Most of the papers reviewed concluded that the abrasive particles inside the lubricants are the causes to the abrasive wear of seal lips [62][63][64].

In most of the research done in lubricated tests, the oil was injected into the counterface using a syringe. Results from tests show that the abrasive wear of elastomers in lubricated condition is higher than in dry conditions due to the weakening of the elastomer by the lubricant. The presence of lubricant in the contact prevented the particles from aggregating, therefore more particles can come into the contact with the surface of the elastomer and contribute to the abrasive wear [65]. Other tests used ball-on-flat disk sliding apparatus to investigate the wear characteristics of the rubber seal material (Figure 3.9). Park [64] showed that the rubber as plastically deformed by a ploughing mechanism (Figure 3.10) caused by the abraded particles. And the particles were embedded in the surface of the rubber. When the particles were removed from the surface, craters were formed at the surface.

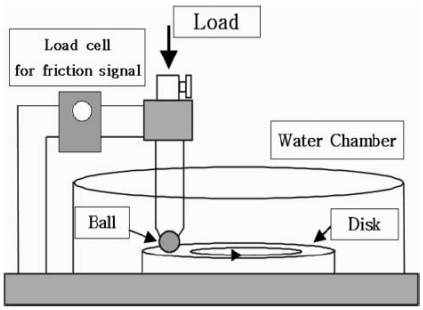

Figure 3.9 Schematic diagram of a sliding wear tester [63]

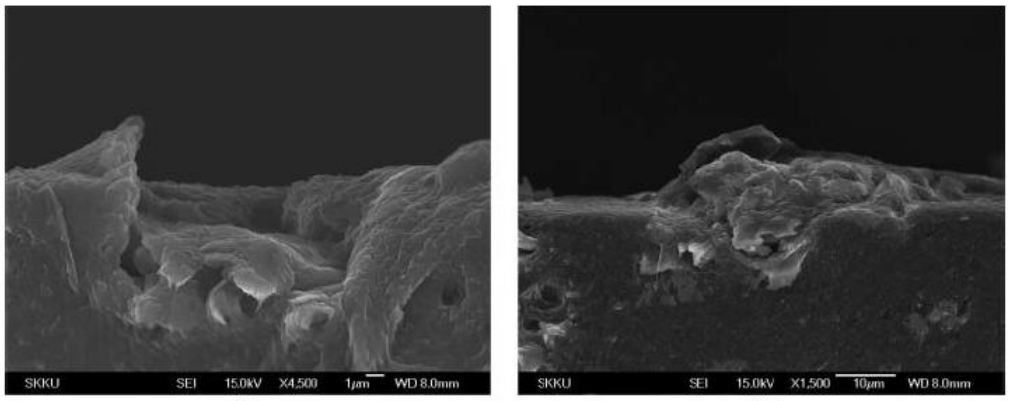

(a) (b)

Figure 3.10 SEM Images of rubber seal and steel ball (a) wear crater due to particle (b) particle embedded into rubber [63]

Lee [62] used a pin-on-plate reciprocating tribotester for the wear tests. The rubber was used as the pin that slides against a flat stainless steel surface. Lee discovered that the wear scars were mostly found at the centre region of the specimen thus the centre region was expected to be at high contact pressure. Alumina particles were added to the lubricant to increase the probability of wear. It was found that a similar wear pattern to that for the normal wear test was reproduced.

All of the research mentioned above used abrasive particles to assess the wear of seal materials, however there is no research yet that has been done to see the effects of soot on seals that are made of polymers.

Based on these findings, the proposed hypothesis in the present studies shows that although soot particles do produce abrasive wear on steel and cast iron, it is known that abrasive particles do wear polymers. However, the interactions between soot particles and polymers still remain unclear.

3.8 Paper grading methodology

A paper grading system on the status of the current research on soot effects in IC engines has been created. The grading system is constructed to allow quick visualisation of where data is available and related to this research by scoring each reference according to a set of criteria. The methodology has been used previously by Harmon & Lewis [66] in reviewing wheel interface rail tribology. Each referenced paper in this research is also assigned to a primary and secondary group according to the main focus of the research, whereby this methodology could help in identifying the research gaps and unknowns for this study. The grading of the papers is separated into 4 areas that is related to soot effects which are shown in Figure 3.11.

The relevancy of the document is then assessed according to the criteria as listed below:

- Is the document peer reviewed?
- Is the theory of the document supported by testing?
- Are the conclusions in the document evidenced within the data?
- Does the document contain a small-scale specimen testing?
- Does the document contain component laboratory testing?
- Does the document contain a full-scale engine testing?

The research was evaluated against either having met (score of 1) or not met (score of 0) each criterion to generate a mark out of 6 (engine testing, component testing and small-scale testing are treated as separate criteria). Papers were then ranked as Not related (1-2), Related (3-4) and Highly Related (5-6). The evaluation results were then plotted in map of knowledge to highlight the extent and quality of available information on soot and its effect in engine contacts. This grading was referenced with papers mainly on soot research for metal-to-metal contacts and wear in elastomers/thermoplastics. The timeframe when searching for related papers was done for 2 years beginning 2015 till 2017. This grading is quite focused which means that it will score highly for some of the evaluation criteria, but low for others. Even where information on small scale test is highly available, critical pieces of information are missing, for example there are very few records on the full-scale engine test. This grading system for this research is not a criticism of the research, but to highlight the availability of information and the current status of this research according to the criteria mentioned above. The maps of knowledge displaying the results of the grading are shown in Figure 3.11. From the map it is obvious that most of the research is ranked as “Related” with only four papers ranked as “Highly Related”. The small number of papers ranked as “Highly Related” is mainly because they had conducted full-scale tests that helped to validate the research. According to the paper grading method, there has been less research done to study the effects of soot on wear and friction using full-scale tests. Although a full-scale engine test is preferable due to the more realistic results that will be produced, results from bench specimen testing are displaying similar results which is reliable. A large variety of test rigs have been used to try to understand the wear created by soot contaminated lubricants [67].

Another map displaying results of the grading is shown in Figure 3.12. This chart shows the wear of materials by abrasive particles. This shows that only a few papers investigated the wear of polymers using abrasive particles and no research yet on sooty oil. The difference between these two charts clearly shows that there is a large gap in the research found. This shows that work should be done to determine the effects of soot on different materials other than steel and cast iron that are generally used in an IC engines [67].

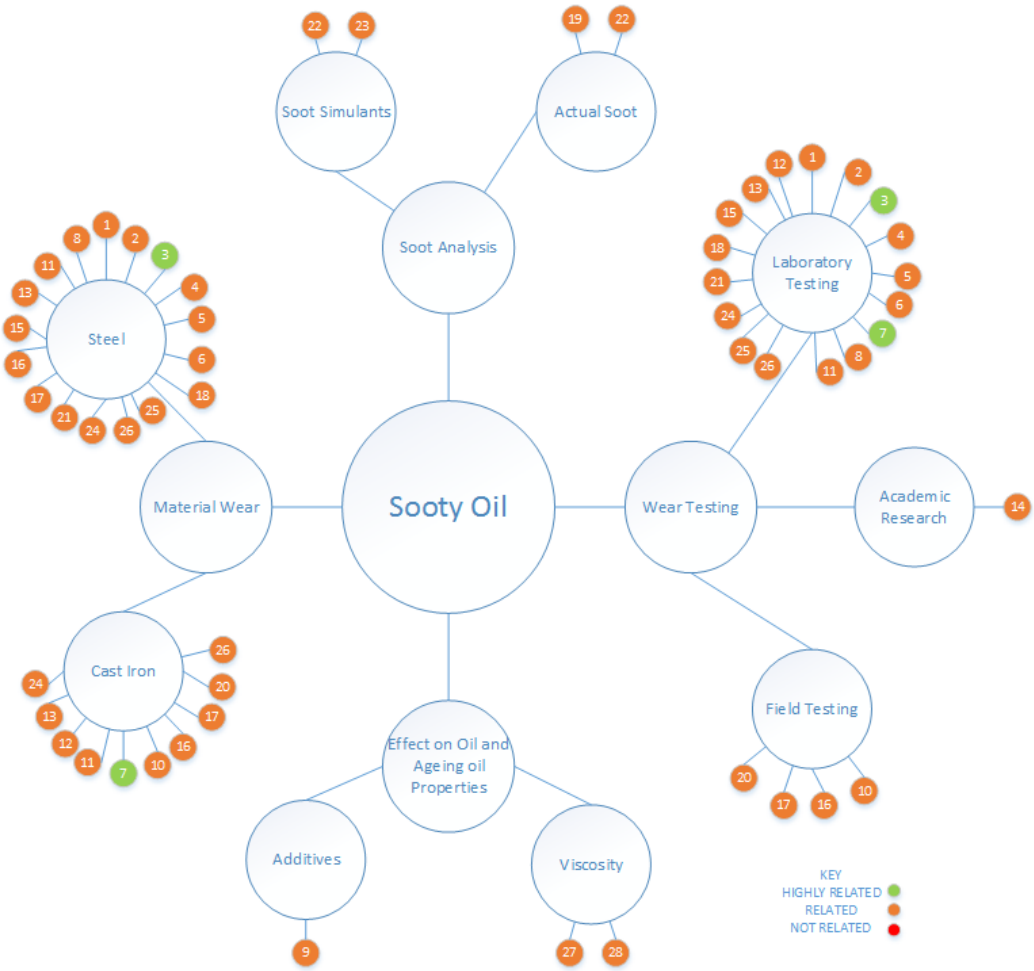

Figure 3.11 Knowledge map for soot effects on engine contacts [67]

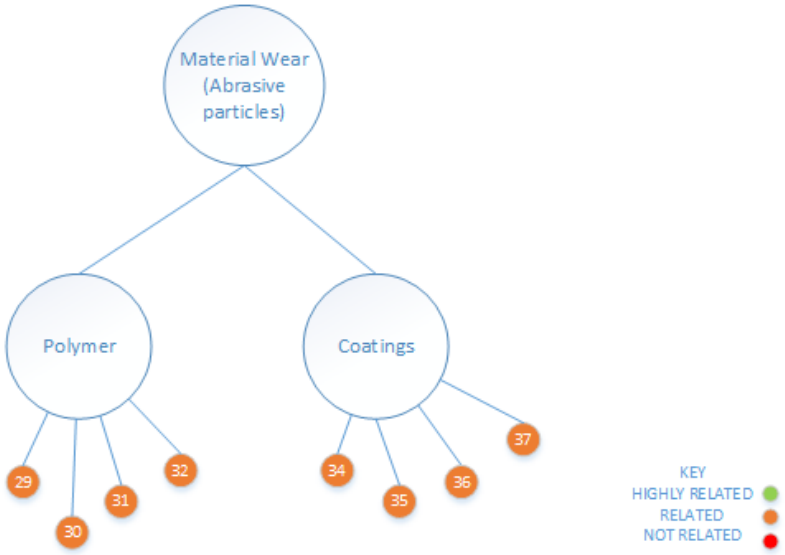

Figure 3.12 Knowledge map on material wear with particles [67]

3.9 Discussion

3.9.1 Paper grading

According to the paper grading method, there has been less research done to study the effects of soot on wear and friction using full-scale component tests. Although a full-scale engine test is preferable due to the more realistic results that will be produced, results from bench specimen testing are displaying similar results which are reliable. A large variety of test rigs have been used to try to understand the wear created by soot contaminated lubricants [67].

From the paper grading method, a “map of knowledge” plot was developed from the outputs evaluated from each paper. Only 35 papers are related to the effect of soot on wear of engine contacts. Most of the wear testing shows bench specimen testing is used and only 4 papers exist that mostly investigate the soot wear effects using full-scale component tests. Generally, there are no papers in the literature that are related to the effects of soot wear on different materials such as polymers or coatings. There is also a lack of work on wear of polymers with a lubricant present. This shows that work should be done to determine the effects of soot on different materials other than steel and cast iron [67].

3.9.2 Testing, wear and friction

From the literature review, to create a test standard for investigating soot wear, the oil contaminated mixture method, test specimen preparation, test method and wear and friction procedure and analysis should be determined. The lubricants that most of the researchers have used are base oil and formulated oil. Base oil is used to determine the wear that occurs when no additives are present and formulated oil is used to determine the wear that occurs when additives are present and the wear when the additives start to deplete. Investigating wear by using aged oil should also be done as aged oil may have traces of soot inside the oil thus comparison can be made between three different lubricants. Real engine soot extraction blended with fresh lubricant is the best soot simulant, however, due to various issues with such particles, carbon black is the next best option. The mixing method of carbon black shows that heating and ultrasonic agitation of the mixture is proven to be the best method. From the literature, it also known that there is a lack of data on soot properties. This is because probably due to the size of the soot which is relatively very small and thus is hard to measure its properties.

A large number of investigations have used test specimens to investigate the wear of soot contaminated contacts. A replication of the real engine condition in a test contact is most required whereby the specimens should be comparable in terms of material composition and dimensions while having similar contact pressure or at least a similar lubrication regime. Most researchers used SEM and optical microscopes for wear scar imaging while profilometry is used to measure the wear scars profile. The majority of the research discovered that the abrasive wear is the major wear mechanism that is

caused by increased of level of soot in engines, while other authors referred to such wear as polishing. Abrasive and polishing wear is clearly seen using a microscope and visualisation directly from the eye.

From the wear mechanisms that occur, Chinas-Castillo and Spikes [38] had found that soot particles entrained into an elastohydrodynamic lubricated contact, where it adheres into the surface and influences the behaviour of the contact. It is found that the soot particle size is larger than the film thickness, thus penetrating the contact where abrasive wear occur [35][45][41]. Other researchers also suggested that starvation may occur when the agglomerates are much larger than the oil-film thickness thus severe wear occurred in engine components [3][55].

There is very little research done on visualisation of the entrainment of soot into a contact. This technique will improve understanding on how soot enters a contact and how it behaves inside the contact thus starving it of lubricant. The visualisation of soot entrainment to a contact will help in understanding the results from wear and friction test.

Soot wear is mostly found in engine valve trains due to its reciprocating motion where they often operate with inadequate lubrication. Wear is found to be worse in the engine valve train, but in-cylinder there is also significant wear due to soot contamination. All major components of the engine suffer soot related wear, and in this current research there is vast research on wear of seals due to abrasive particles. Seals are components that prevent leakage of fluids or gas from machine equipment. Most of the papers reviewed show that the cause for abrasive wear of seal lips is mainly abrasive particles deposited as contaminants in the lubricant such as sea water and oil, however there are no research yet that has been done to see the effects of soot on seals that are made of polymers.

3.10 Summary

From this review, a significant amount of information and research on soot contaminated lubricants and related soot wear in engines has been gathered. It is also known that lubricants are designed to work well with steel-on-steel contacts, but not on non-ferrous materials. It is shown that the soot production increases significantly at higher load engine operating conditions. The generated soot particles within the engine are expelled to the atmosphere from the cylinder through the exhaust pipe while the remainder will remain inside the lubricant oil. The soot will then tends to agglomerate due to high temperature thus blocking the lubricant from entering a contact.

Presence of soot inside the lubricants has been shown to increase wear of numerous engine components, mostly on ferrous materials. The valve train has proven to be the most susceptible to wear due to the thinning of oil film thickness. Most researchers used ball-on-flat sliding apparatus; a four-ball approach method; a high frequency reciprocating wear tester; three body wear machine and pin-on disc apparatus which

are limited to small scale specimens. From the paper grading method, it is known that most researchers had investigated the effects of soot on wear using small scale specimens in order to understand the fundamentals of soot wear and they discovered that abrasion is the major wear mechanism, but other researchers also suggest that starvation wear mechanism is also one of the causes of soot wear in engine components.

Hence, further testing is required especially with different materials and contact conditions. Seals which are non-ferrous materials are one of the engine components that need to be investigated to see the wear effects on the materials. First tests to understand the fundamental of wear effect on non-ferrous materials will be done using ball-on-flat apparatus and to address the issues on scaling of test, testing should also be done on component scale to see the comparisons with small scale to obtain the real wear results. An oil film thickness test is also attributable to the understanding of how or whether the sooty oil gives an effect to the surface of the materials tested.

Chapter 4 Soot Characterisation

Soot characterisation testing was developed to study the characteristics in terms of roughness affects and indentation patterns of soot when loaded onto a polished steel surface using a Universal Mechanical Testing (UMT). The tests were run under pure engine soot extraction and blended carbon black with engine oil extraction by centrifugation in order to differentiate the characteristics of each soot.

4.1 Experimental details

4.1.1 Sample preparation

The materials used as test specimens were cast iron plates that were polished to a surface finish of 0.05µm Ra using wet polishing with abrasive ceramic media as shown in Figure 4.1 and Figure 4.2. The lubricant used was from 12% carbon black blended with engine oil and from used engine oil from which soot was extracted using a centrifugation process.

Figure 4.1 “Mirror” surface finished cast iron plate

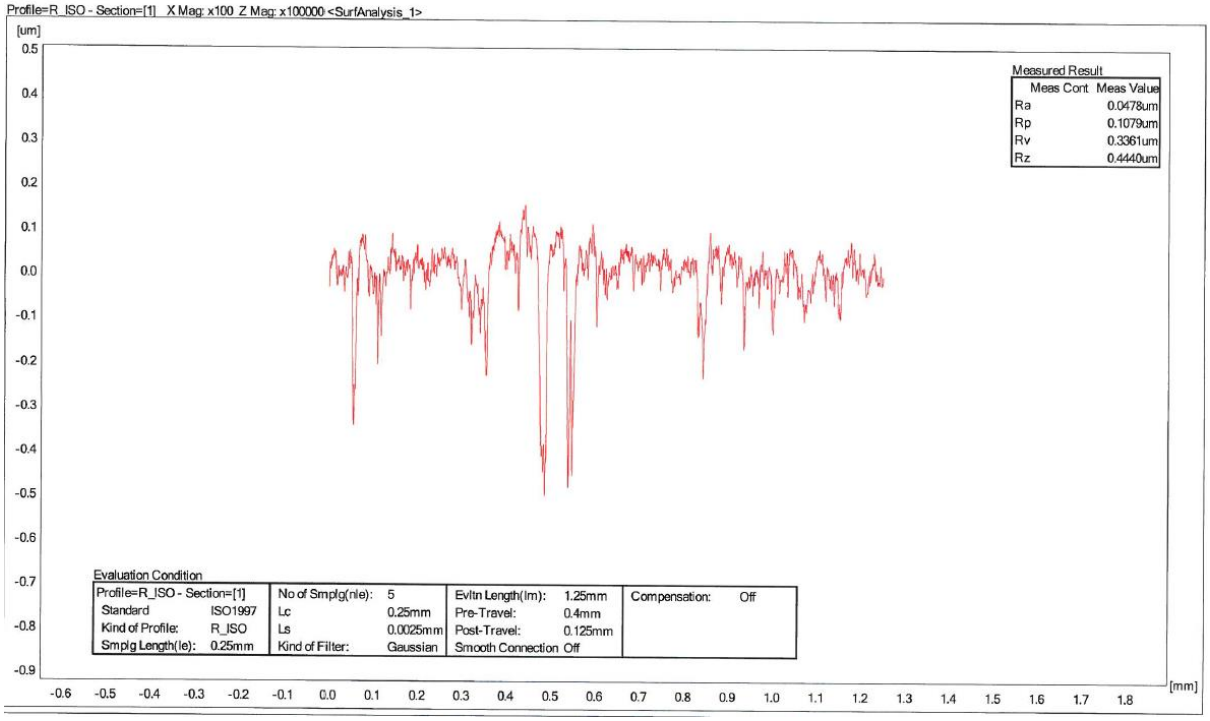

Figure 4.2 Polished plate surface roughness 0.05µm

4.1.1.1 Centrifugation process

For centrifugation of soot particles, a centrifuge (*Pico 17 Thermo Fischer*) was used in order to extract soot/carbon black from used engine oil/engine oil. Used engine oil and carbon black blended with engine oil was centrifuged at 12000rpm for 60 minutes. The used engine oil was equally diluted with heptane at ratio 1:1. This procedure was repeated three times to make sure the oil was separated. After centrifuging, the supernatant is discarded and soot particles are collected (Figure 4.3). The particles are then dried in a vacuum oven at 60°C overnight (Figure 4.4). The centrifugation and drying procedure was repeated using mixture of carbon black at 12% (carbon by weight) with engine oil (Shell Helix-HX5 15W40). The extracted soot was then used in a compression test in order to measure the roughness and hardness of the soot on a polished steel surface.

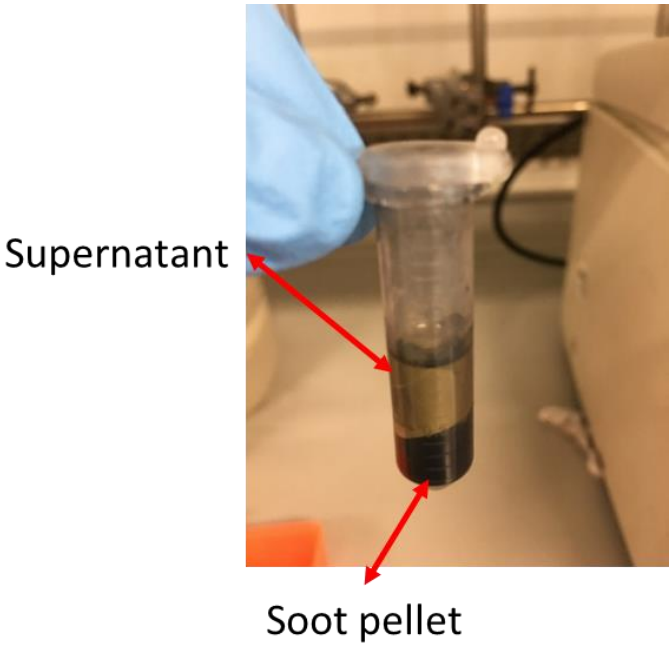

Figure 4.3 Soot particles after centrifugation process

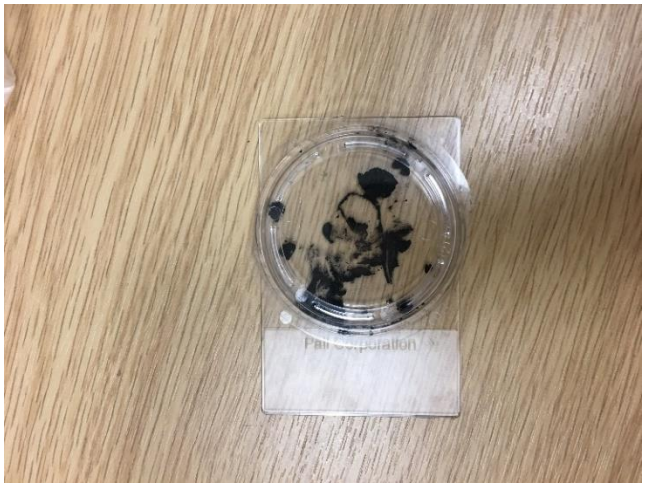

Figure 4.4 Dried soot particles after drying in a vacuum oven at 60°C for 24hours

4.2 Experimental procedures

4.2.1 Compression test

The dried soot particles obtained were then dispersed in chloroform and homogenized for 10 minutes. A small amount of solution was then dropped onto the polished plate and allowed to dry. Using a Bruker Universal Mechanical Tester (UMT) the upper

specimen was pushed towards the bottom specimen (which has the solution) at 40N for 5 minutes and retracted back to the normal position as shown in Figure 4.5. The polished flat plate was then measured under an Alicona 3D surface profile to measure the roughness and surface morphology of the flat plate. The tests were continued using dried soot particles obtained from carbon black blended with engine oil.

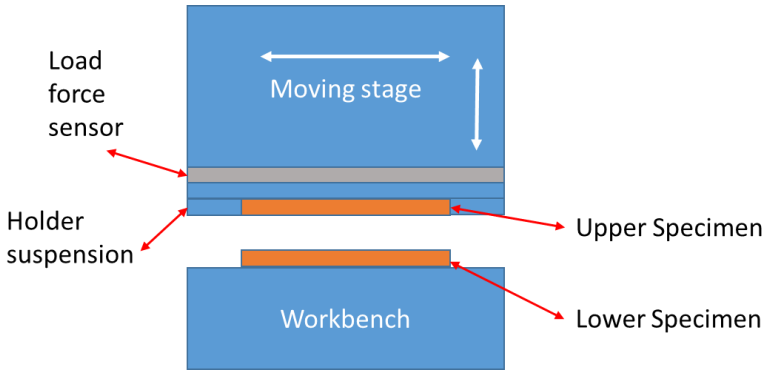

Figure 4.5 Schematic diagram for the compression test

As the particles did not spread uniformly using the application describe above, another load test was conducted on the polished flat plate by smearing the dropped solution onto the polished plate and allowing it to dry. This is to break the coagulated dried pellet even though it has been sonicated before to promote a better dispersion. Using the same method mentioned above, an upper specimen was pushed towards the lower specimen (with the solution) at 40N for 5 minutes and then retracted back to the normal position. The surface morphology and the roughness of the polished plate was then measured using an Alicona 3D surface profiler and compared with the first test (non-smearing test). The tests were also continued using a dried soot pellet from carbon black blended with engine oil.

4.3 Experimental results

4.3.1.1 Surface morphology analysis

An Alicona 3D optical profilometer and optical microscope was utilised to analyse the surface structure for the carbon black/soot particles for both test methods. The microscope image and profile of the indentation caused by the “blobs” obtained from the surface with the solution applied were measured as seen in Figure 4.6 - Figure 4.9(a) and for the upper specimen in Figure 4.6 - Figure 4.9(b). The profile shows that the estimated size of the particles here is 72-76µm (carbon black) and 150-220µm (soot) which is larger than the findings from other researchers [33] while the depth of the indent blobs are 9-15µm (carbon black) and 5-7µm (soot) of the surface. This could be because the agglomerated particles are not well dispersed after homogenization is done. The depth of the indentation is used to quantify whether the soot is harder than

steel. This is difference with the approached used by Li [35] in measuring the hardness of soot.

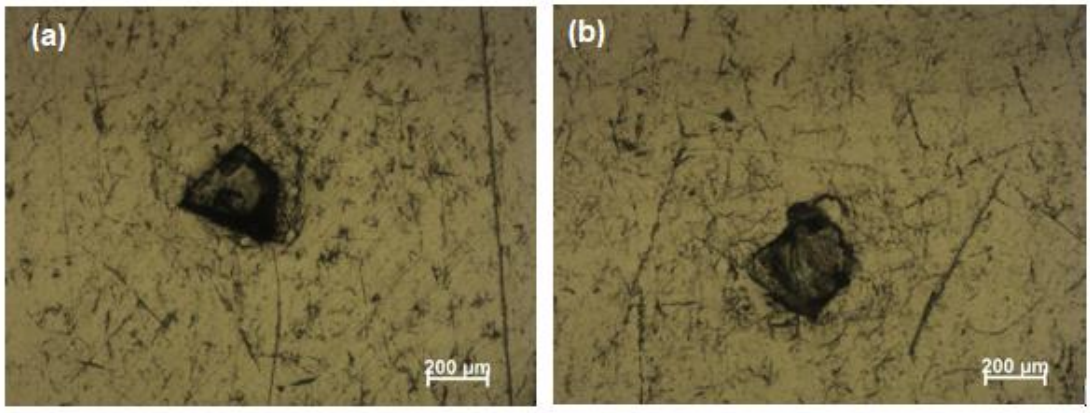

Figure 4.6 Microscope image showing an identation from a carbon black particle blob on a steel surface

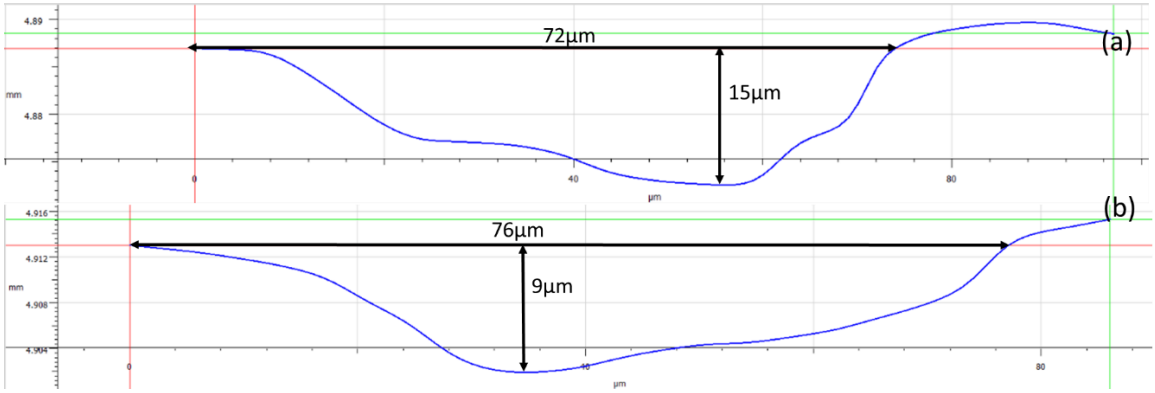

Figure 4.7 Profile image showing an indentation from a carbon black particle blob on a steel surface

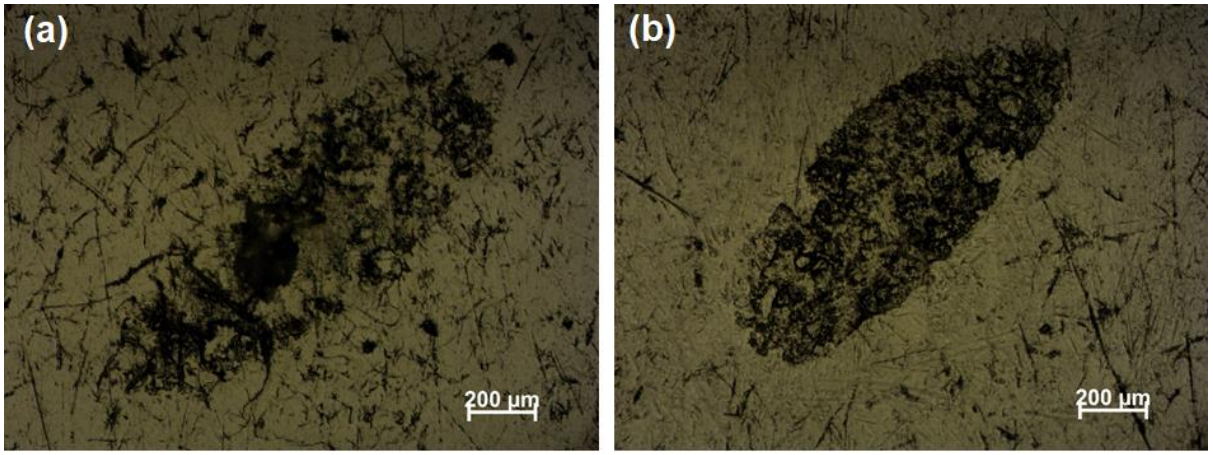

Figure 4.8 Microscope image showing an identation from a soot particle blob on a steel surface

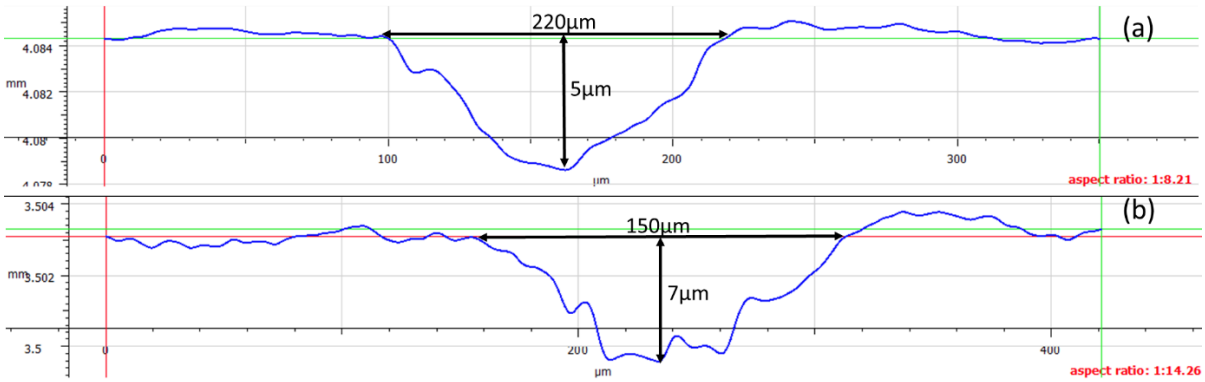

Figure 4.9 Profile image showing an identation from a soot particle blob on a steel surface

While for the test method where the carbon black/soot is smeared first before load test is conducted, the microscope image and profile of the indentations obtained from the surface of the bottom specimen were measured as shown in Figure 4.10-Figure 4.13 (a) and for upper specimen in Figure 4.10-Figure 4.13 (b). The indentations from smeared carbon black/soot particles after the test were found to be 75-150µm (carbon black) which is similar to the previous test and 60-110µm (soot) which is smaller before smearing. They are still larger than the estimated size of indentations found by others [33]. While the depths of the indentations are 0.2-1µm which is smaller than the depth of carbon black without smearing.

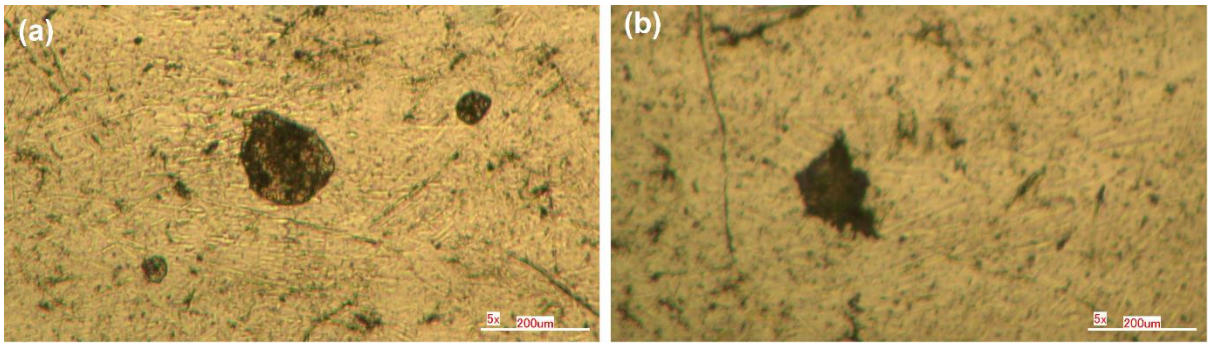

Figure 4.10 Microscope image showing an identation from a carbon black particle blob (after smearing) on a steel surface

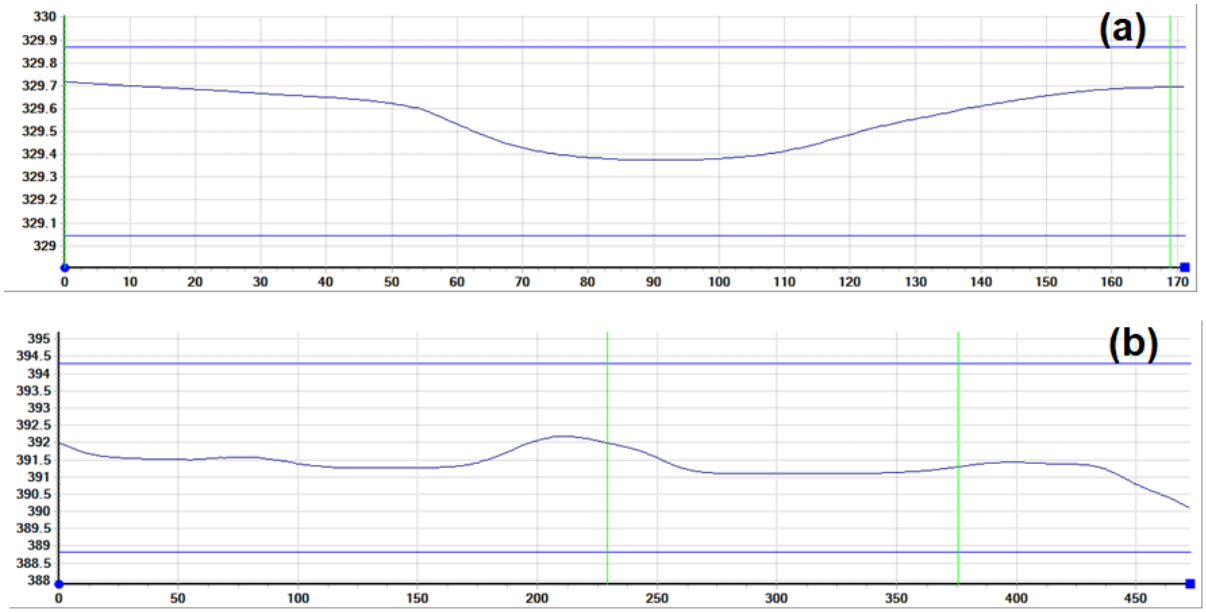

Figure 4.11 Profile image showing an identation from a carbon black particle blob (after smearing) on a steel surface

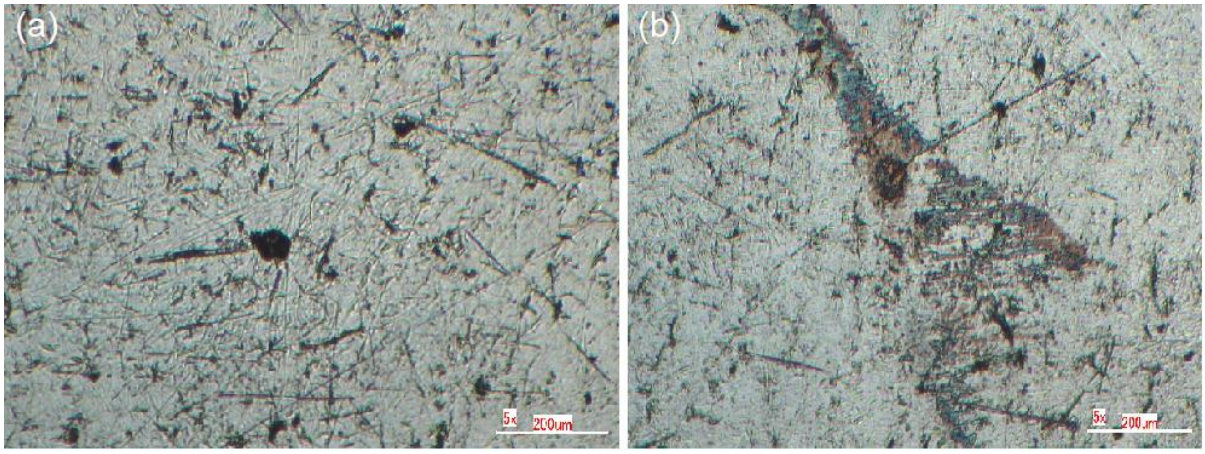

Figure 4.12 Microscope image showing an identation from a soot particle blob (after smearing) on a steel surface

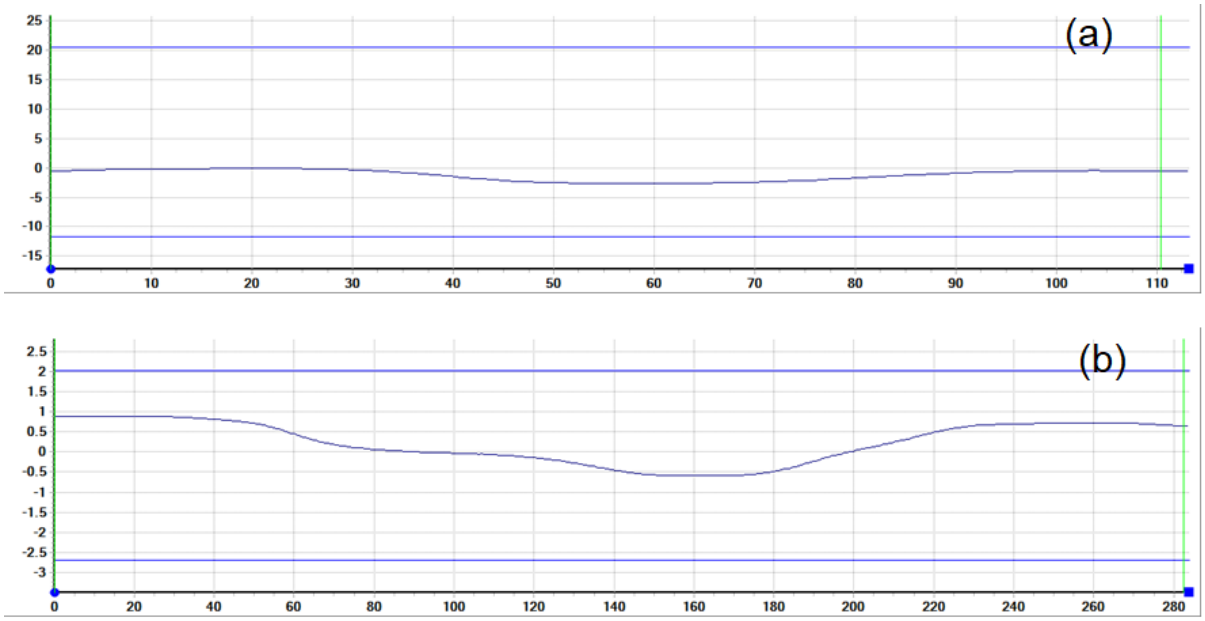

Figure 4.13 Profile image showing an indentation from a soot particle blob (after smearing) on a steel surface

4.3.1.2 Post-test roughness analysis

For further assessment of the morphological changes in the soot particle characterisation, the changes in the topography were analysed via surface roughness. The surface morphology and topography of the polished plate after the load test were characterized respectively using an Alicona 3D optical profilometer and an Optical Microscope with an objective of 5x. The topography was assessed via measurements of the roughness (Ra) and the root mean square roughness (Rq) of the indentation images over the surface for each specimen. Examples of the roughness after load the tests are depicted in Figure 4.14. Both polished plates showed an increase in roughness for engine soot and carbon black. Polished plates that had carbon black lubricant show higher values of roughness compared to the specimen plate that had engine soot solution applied. This could probably occur because of the hardness and size of the particles when indented onto the surface of the polished specimens. Such an increase in roughness for both lubricants can be attributed to the particles roughness on a contact when load is applied.

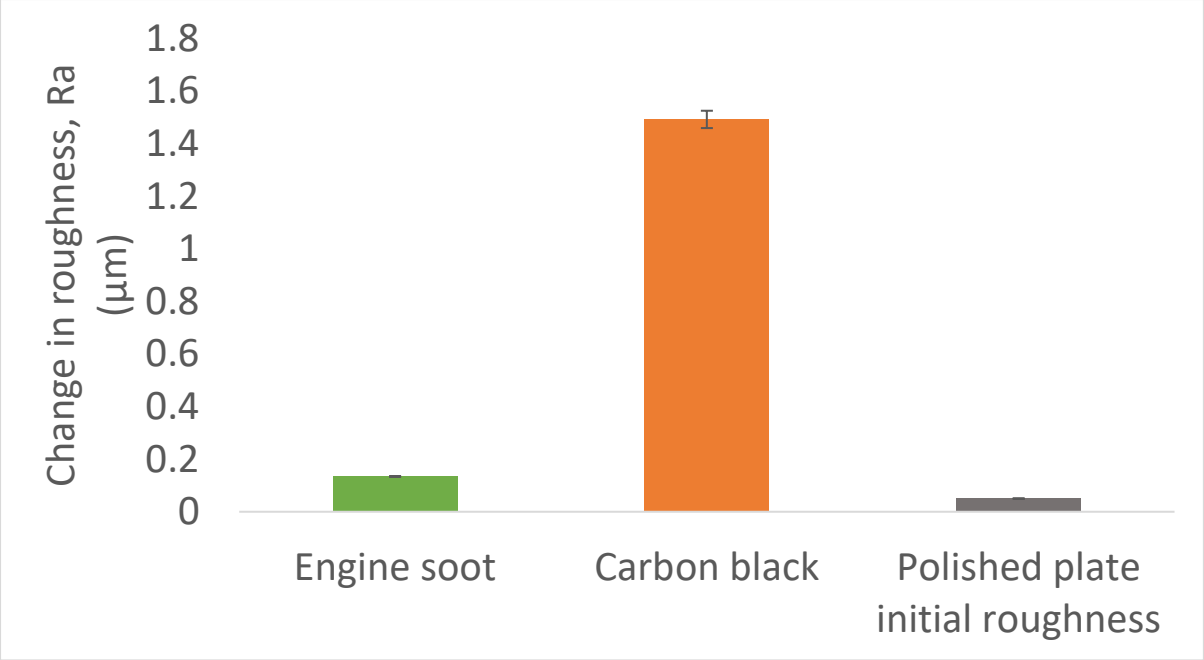

Figure 4.14 Surface roughness change of a polished plate after a load test (measured across the indentation)

4.4 Summary

The experimental research summarized in this chapter examines the characterisation of engine soot/carbon black particles in terms of roughness and indentation patterns from soot when it is loaded onto a polished steel surface using a UMT. More specifically, the experiments were designed to correlate with Li [35] who found soot to be harder than steel. From the results it can be concluded that:

- Soot is harder than steel whereby from the load test with engine soot and carbon black particles, the size and depth of the indentations found due to the particles indenting the surface of the polished plate when force is applied is larger than the particle size obtained from other researchers.
- The post-test roughness of the indentations was also higher for both particles; this may be due to the hardness and size of the particles indented into the polished specimens when force is applied.
- The limitations from this work is that Li [35] has measured the hardness of the soot by plasmon energy using low-loss electron energy-loss spectroscopy (EELS) which is proportional to the electron density which then correlates with carbon density and afterwards with carbon hardness. The hardness of the soot was measured in density, whereas here in the study the hardness were only measured by the depth the particles indented the metal specimen. In order to obtain a more realistic value of hardness for soot is by repeating the same procedures as what has been done by Li.

Chapter 5 Ferrous Material Wear

The wear and friction testing method was developed to understand the effect of increasing soot levels to the wear and lubrication of valve train component materials. In this chapter, a general overview on test specimens is given; the test lubricants, the methodology for the sooty oil mixing process and also test equipment used in this wear testing are explained in detail. The test procedure and test condition for the experimental study are also presented. In order to replicate some previous work that used ferrous materials, an initial test using a ball-on-flat test rig was conducted to obtain the fundamentals of soot wear effects behavioural patterns with various carbon black content level on the one hand, and build confidence in this test method on the other.

5.1 Test specimens

The materials used as test specimens were ferrous materials. The flat specimens used in these tests were EN1561 Grey Cast Iron and EN24 Steel. The EN1561 Grey Cast Iron contains 1.5-4.3% carbon and 0.3-5% silicone with manganese, sulphur and phosphorous as other chemical elements. The mechanical properties of this material show a moderate tensile strength and good wear resistance with excellent surface finish. This material is widely used in automobile components including cylinder heads, cylinder blocks, connecting road and gearbox cases. EN24 contains 1.3-1.8% nickel, 0.9-1.4% chromium and 0.2-0.35% molybdenum. The mechanical properties of this material show a good high tensile strength, ductility and wear resistance. This material is used in automobile components such as connecting rods, slide gears, slide cams and others.

The flat specimens were produced from bar steel according to the required size in the mechanical workshop, then acetone is used to clean the specimen thoroughly and dried with hot air before testing commenced. The ball specimens used for these tests were Chrome Steel EN31, with high carbon content and about 1.5% chromium content which are high in hardness, resistive to abrasion and also good in compressive strength. This material is used widely as bearings in the automotive sector. Table 5.1 shows the mechanical properties for ball and flat specimen. Table 5.2 shows the properties of the formulated mineral oil as lubricant (Shell Helix-HX5, 15W40) and carbon black.

Table 5.1 Mechanical properties of the ball and flat specimens for ferrous materials

	Ball Specimen	**Flat specimen**	
		Ferrous Material	
Material	**Chrome Steel EN31**	**Grey Cast Iron E1561**	**Steel EN24**
Tensile Strength (MPa)	750	250	850
Average Hardness (Hardness Vickers)	393	225	303
Young's Modulus, E (GPa)	215	103	207
Poisson's Ratio, υ	0.3	0.26	0.3
* Average Roughness - Ra (µm) - measured	0.05	0.52	0.6
*Dimension (mm)	ϕ6	66 x 25 x 4	66 x 25 x 4
*Source of information on above data were taken from respective supplier and compared with CES edupack	Steel Express, Wolverhampton, UK	Steel Express, Wolverhampton, UK	Steel Express, Wolverhampton, UK

Table 5.2 Test lubricant and carbon black

Substance	**Name**	**Description**
Lubricant	Shell Helix-HX5 15W40 (formulated mineral oil)	Kinematic viscosity @ 40˚C = 106.00 cSt Kinematic viscosity at 100˚C = 14.27 cSt Density at 15˚C = 865.8 kg/m^3
Carbon Black	N/A	Acetylene, 100% compressed, 99.9+% S.A 75 m^2/g, Bulk density 170 - 230 g/L, Particle Density @ 20˚C = 1.8 - 2.1 g/cm^3

5.2 Sooty oil mixing process

An ultrasonic bath (Camlab CamSonix C080T) with a digital overhead stirrer (SciQuip Pro-40) is used to blend the carbon black soot surrogate (at 0 – 12% carbon black/soot content level) with fresh formulated mineral oil (Shell Helix-HX5 15W40). The ultrasonic agitation is set to 60°C for 20 minutes. To homogenize the mixture, the speed of the stirrer was adjusted from 60 rpm to 100 rpm in 10 rpm steps after every 4 minutes. At 12% carbon black content, the sooty oil becomes very thick due to soot

agglomerations. This is due to the high carbon black concentration soot levels in an engine can reach these levels so they were kept in the test programme.

5.3 Wear test equipment

To study the wear and friction of the test specimens, a standard test rig was needed for the wear and friction measurements. A Cameron-Plint High Frequency Reciprocating Rig (TE77) was used for all tests to simulate wear and friction on the specimen using typical engine component interface conditions, while a Veeco Dektak 150 Profilometer was used to measure the wear depth and Optical Zeiss Microscope images were used to interpret the wear mechanism.

5.3.1 Cameron-Plint high frequency reciprocating rig (TE77)

A standard test approach for friction and wear measurement on a Cameron-Plint High Frequency Reciprocating Rig (TE77) was used for all the tests (Figure 5.1). Various researchers have used this tests in modelling and simulating different components of automotive engines [7][3][43][44].

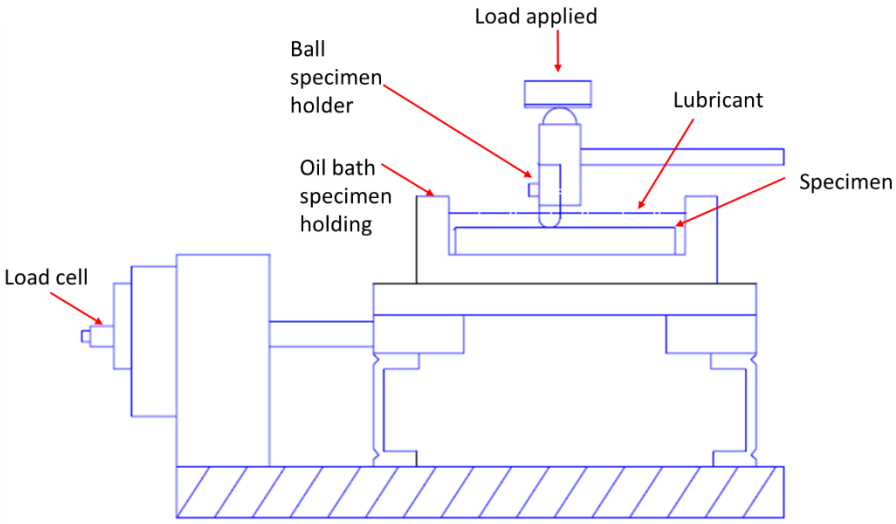

Figure 5.1 Schematic of Cameron-Plint High Frequency Reciprocating Rig (TE77)

This test uses reciprocating motion where the scotch yoke mechanism will convert the rotary motion to reciprocating motion. This machine has stroke length from 0.1mm to 15mm and a temperature range from room temperature to 600˚C maximum. The load range is from 10N to maximum of 250N with frequency range of 2.5Hz to 50Hz.

Before testing commenced, the operating conditions (temperature, speed and load) are pre-set into the programme for the specimen test. Then, the ball specimen is mounted onto the Plint head and lowered into the oil bath to make sure that the ball

specimen touches the flat specimen and clamped using the loading stirrup so the position of the ball remains unchanged during testing. Load is then applied via the lever.

The friction force of the oscillating contact is measured where the piezo-electric force transducer is placed in line with the contact by resisting the motion in the horizontal direction. The raw output data is then transferred to the data acquisition system and captured by the LabView Software as shown in Figure 5.2. These are then analysed afterwards using Microsoft Excel Software with an interval of 600 data points taken (1minute data) and the final average of the CoF is reported by using Equation 5.1 where the friction coefficient is determined.

$$\mu = \frac{f}{N} \tag{5.1}$$

where *f* is friction force and *N* is the applied normal force.

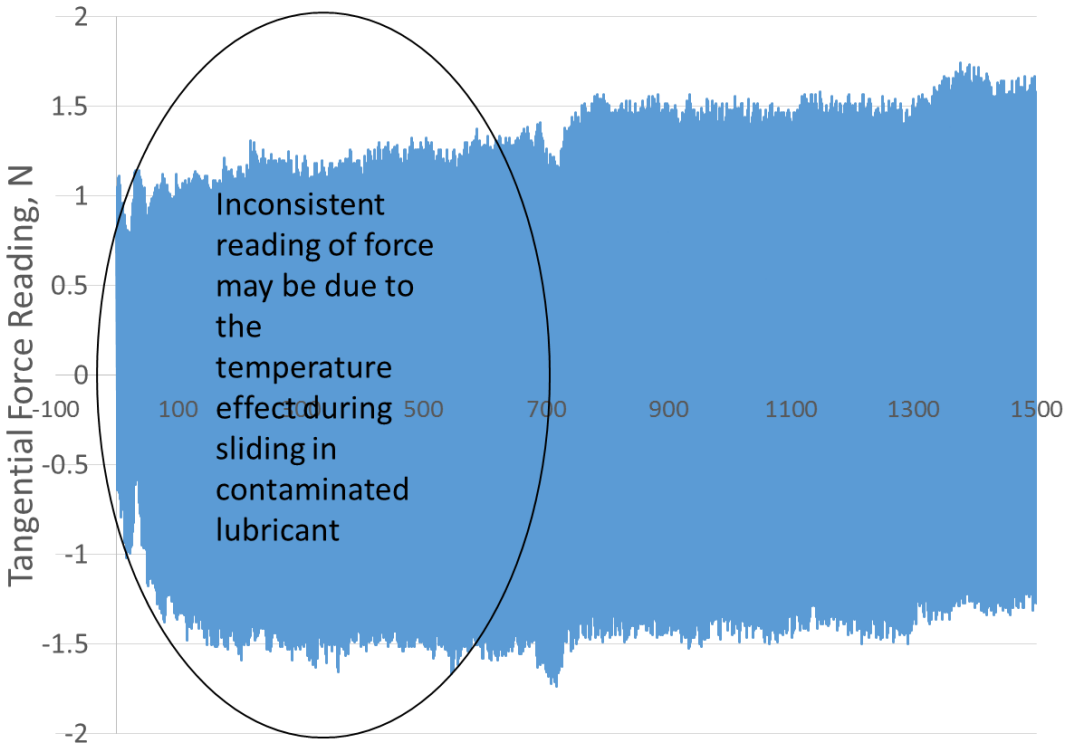

Figure 5.2 Example of raw data acquisition of friction from Plint TE77 test rig

5.3.2 Profilometer

The average surface roughness, and wear scar profiles for the flat specimens were measured using a Veeco Dektak 150 profilometer. The Dektak 150 is a surface profilometer that takes surface measurements using contact profilometry techniques. The wear volumes were measured using the profilometer.

Before a test is started, the tower is raised and the specimen is positioned in the centre of the stage right below the stylus. The parameters of the scan (length and duration) are set up before the test is conducted. The stylus tip was moved using the control button on the surfaces of the specimen where the location of the wear scar is located. The wear depth which is varied along the wear scar was measured using the profilometer and the depth measurements were recorded at 5 locations on the wear scar. The experimental average depth was determined from these points.

5.3.3 Zeiss microscope

Wear imaging was conducted using an Optical Microscope. All of the worn surfaces of the specimens were examined using a Zeiss Microscope in order to determine the characteristics of the wear produced with increased in carbon black content.

5.4 Experimental procedures

The lubricant used in ball-on-flat specimen contacts were in an uncontaminated condition and also mixed carbon black (soot surrogate) at varying percentages (3% and 12%) with fresh lubricant. The tests were carried out on ferrous materials: EN24 steel and cast irons. The oil temperature was set to 100°C during testing programme to simulate engine working condition. All of the tests were performed at least three times to ensure a statistically significant evaluation. The test conditions for ferrous material were as outlined in Table 5.3. These test conditions were chosen to compare with a previous study that used cast iron as it's specimens.

Table 5.3 General Test Conditions (Ferrous materials)

No.	**Parameter**	**Test Conditions**
1	Ball Specimen Radius (mm)	3
2	Temperature (℃)	100
3	Normal Force (N)	50
4	Stroke Length (mm)	2
5	Sliding Linear Speed (m/s)	0.14
6	Test Duration (min)	20
7	Lubrication	0%, 3% CB, 12% CB

5.4.1 Friction and wear tests at high temperature 100°C

The Plint TE77 machine was programmed by increasing the temperature to 100°C in 10 minutes, and the temperature is let to dwell at the same temperature for 50 minutes. The extra 30 minutes time is needed to stabilize the temperature to 100°C as the temperature will continue to increase and stabilizes back to 100°C. The ball specimen

is lowered onto the flat specimen in the first 15minutes minutes to ensure that the ball and flat specimen reaches the same temperature before testing commenced.

5.5 Hertzian contact pressure

The initial assumptions of the Hertzian contact pressures (maximum and mean) for point contact where the geometry of the contact is a ball on flat contact were calculated for ferrous material at 50N. The initial contact pressures are shown in Table 5.4. The calculations on contact pressure are included in Appendix A-1.

Table 5.4 Contact Pressures for various material and nominal loads

Specimen Materials	**Nominal Load, P (N)**	**Mean Contact Pressure p_m, GPa**	**Maximum Contact Pressure, p_o GPa**
Cast Iron	50	1.21	1.83
EN 24	50	1.63	2.45

The maximum contact pressure, p_0 can be determined by using Hertz's contact formulae for circular point contact [68]:

$$p_{0} = \frac{3P}{2\pi a^2} \tag{5.2}$$

Contact area dimension, *a* is given by:

$$a = \sqrt[3]{\frac{3PR}{E'}} \tag{5.3}$$

A schematic diagram of a ball-on-flat configuration with contact pressure area on the surface interface (a) and contact pressure increases from zero of the contact surface (where r = ±a) to a maximum value of p_0 at the axis of symmetry (r = 0) with an elliptical form of the contact distribution (b) is shown in Figure 5.3.

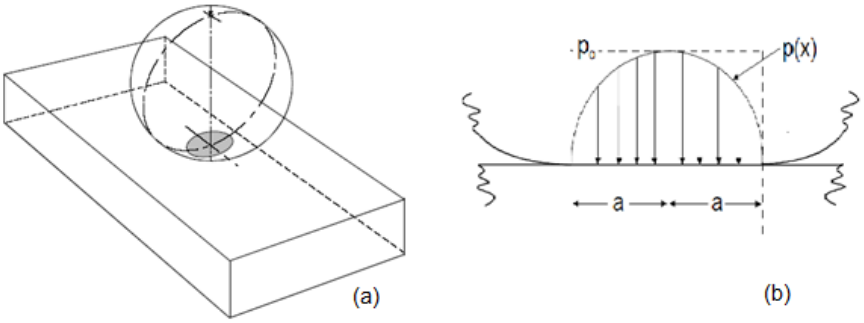

Figure 5.3 Schematic of (a) ball-on-flat surface interface (b) and contact pressure distribution [68]

5.5.1 Film thickness

The theoretical film thickness was determined to analyse the tribological behaviour of the surfaces. A standard equation is used in most of the literature for oil film thickness [12] as stated below, Equation 5.4, comprises of dimensionless load, *W*, speed, *U*, material paramaters, *G*, and elastic parameter, *k*.

$$H_{min} = 3.63U^{0.68}G^{0.49}W^{-0.073}(1 - e^{-0.68k}) \quad (5.4)$$

Where,

$H = \frac{h}{R_x}$

$U = \frac{\eta_o u}{E'R'}$

$G = \alpha E'$

$W = \frac{P}{E'R'^2}$

$k = \frac{a}{b}$

It was assumed that the values of viscosity and density for the sooty oil (Table 5.5) were the same as measured for the previous study [69]. The calculated minimum film thickness and lambda ratios are presented in Table 5.6. From the table, it can be seen that the film thickness and lambda ratio increase with carbon black content. The system is expected to operate under boundary lubrication from the indicator of the lambda ratios that show values lesser than one. The full calculations on film thickness are included in Appendix B-1.

Table 5.5 Kinematic Viscosity and Density of Sooty Oils [69]

Sooty oil	**Kinematic Viscosity @40°C (cSt)**	**Kinematic Viscosity @100°C (cSt)**	**Density at 15°C (g/cm^3)**
0%CB	106	14.27	0.866
3%CB	184.17	50.874	0.881
12%CB	1156.1	888.07	0.928

Table 5.6 Minimum film thickness and Lambda ratio of different material with sooty oils

Specimen Material	Sooty Oils	Minimum Film Thickness (μm)	Lambda Ratio, λ
EN24	0% CB	0.0035	0.005
	3% CB	0.0059	0.009
	12% CB	0.0126	0.019
Cast Iron	0% CB	0.0037	0.005
	3% CB	0.0062	0.009

5.5.2 Lambda ratio

Lambda ratio, ʎ, is used to determine the effects of asperity interactions in a lubricated sliding contact between minimum film thickness and the root mean square of the surface roughness as shown in Equation 5.5 and 5.6. The lubrication regime of the operating contact is determined by ʎ value. For ʎ>3, the lubrication is named as hydrodynamic as full film prevents both surfaces from contacting each other thus asperity contact is negligible. While for 1<ʎ<3, asperity contacts may occur thus the lubrication regime is termed as mixed or elastohydrodynamic. And for ʎ<1, there are significant asperity interactions between two surfaces which lead to a boundary lubrication regime [70].

$$\Lambda = \frac{h_{min}}{\sigma^*} \tag{5.5}$$

where, $$\sigma^* = \sqrt{R_{q1}^2 + R_{q2}^2} \tag{5.6}$$

where R_{q1} and R_{q2} are the root mean square surface roughness for object 1 and 2, $R_q = 1.25Ra$ is the root mean square surface roughness, m and R_a is the average surface roughness, m.

As mentioned in the literature review, the estimated size of soot particles is similar to the size of carbon black used in this study, which is between 0.2 μm and 0.5 μm. When this is compared to the film thickness calculated, it is expected that the carbon black particles (being larger) can abrade through the film thickness thus causing wear to the specimens.

5.6 Experimental results

5.6.1 Friction coefficient measurement

Using Equation 5.1, the coefficient of friction was determined from the friction force for every data point. A moving average was taken at an interval of 600 data points that represents one-minute data collected. Then a final average of CoF values were recorded. Figure 5.4 shows the graph of coefficient of friction against time for different carbon black contents.

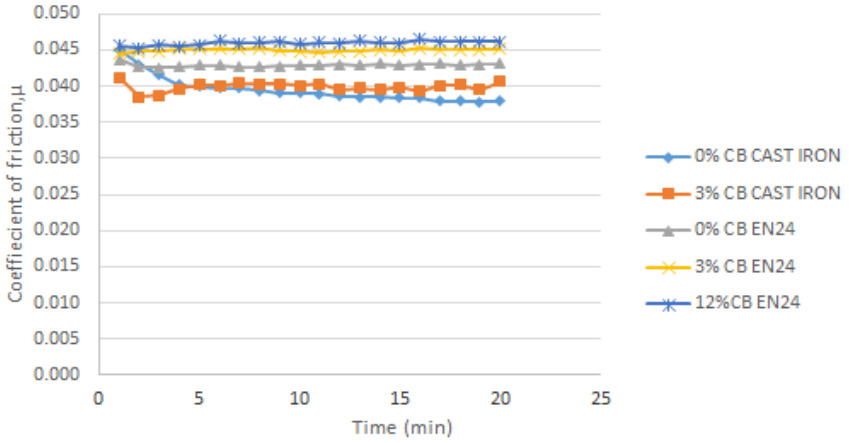

Figure 5.4 Results of coefficient of friction against time for ferrous materials at varying carbon black contamination1.83GPa (EN24 and Cast-Iron)

5.6.2 Wear analysis

5.6.2.1 Wear scar optical microscope images

The optical microscopie images for 0%CB and 3%CB presented in Figure 5.5 and Figure 5.6 show the wear scar microscopic images for 12% CB at 100°C for EN24. For cast iron the optical microscopic images are shown in Figure 5.7. The observed wear mechanisms move from lubricated sliding wear at 0%CB to mild metal-to-metal abrasion at 3%CB for both materials due to the lubricant blockage that causes abrasive wear with plastic deformation as carbon black content increases. Plastic deformation at the edges of the wear scar is also visible at 12%CB.

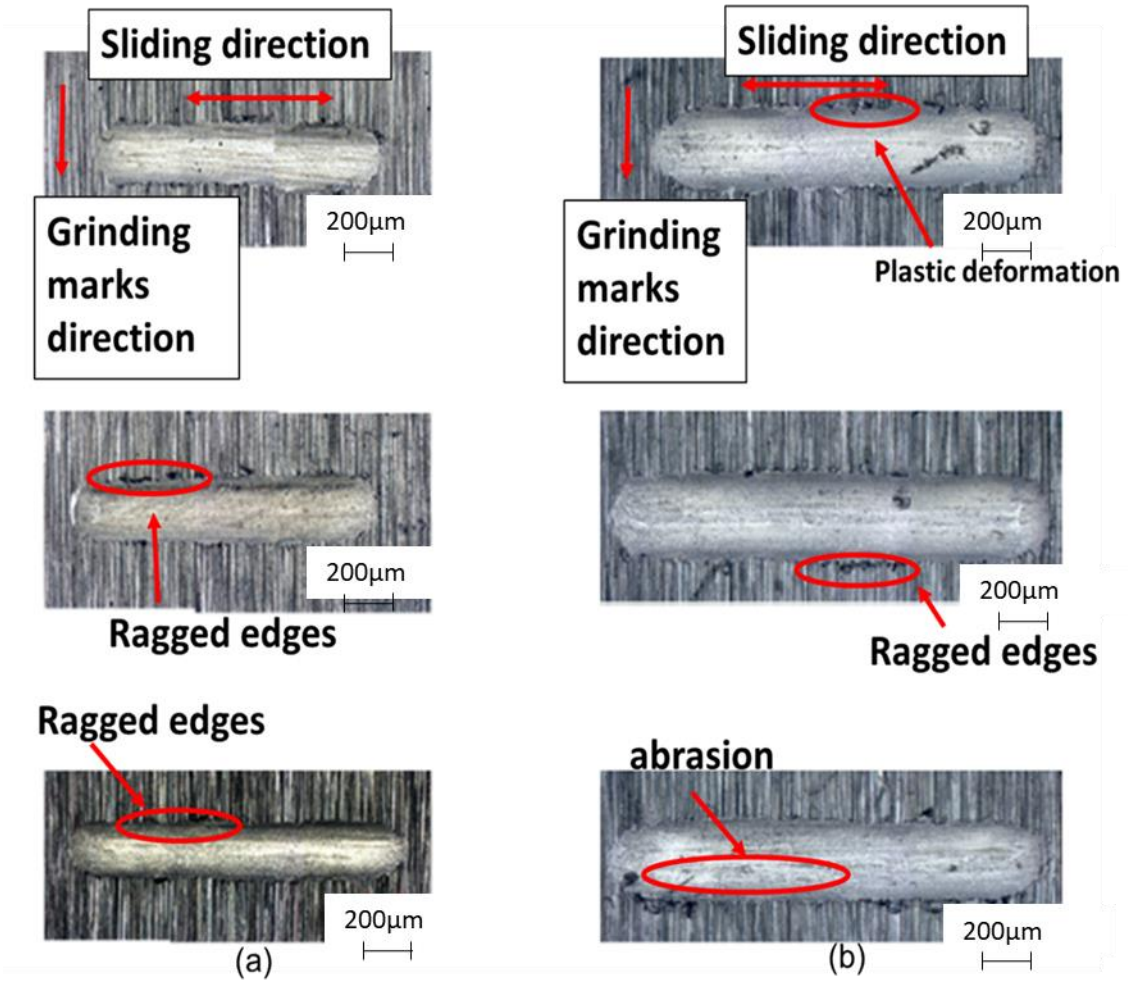

Figure 5.5 Optical microscope images of (a) 0% CB contents (b) 3% CB contents for 100°C at 2.45 GPa contact pressure (EN24 steel)

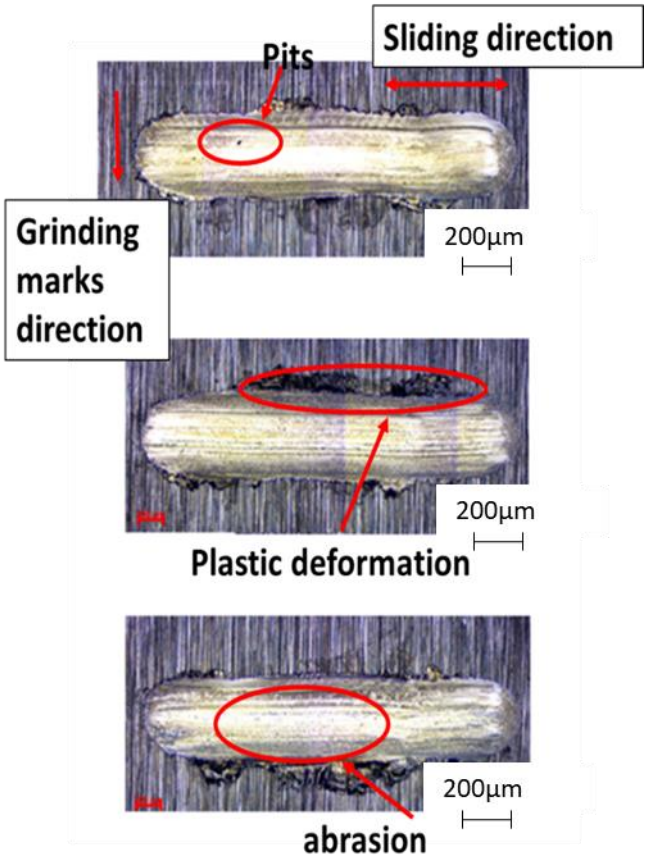

Figure 5.6 Optical microscope images of 12 % CB contents for 100°C at 2.45 GPa contact pressure (EN24 steel)

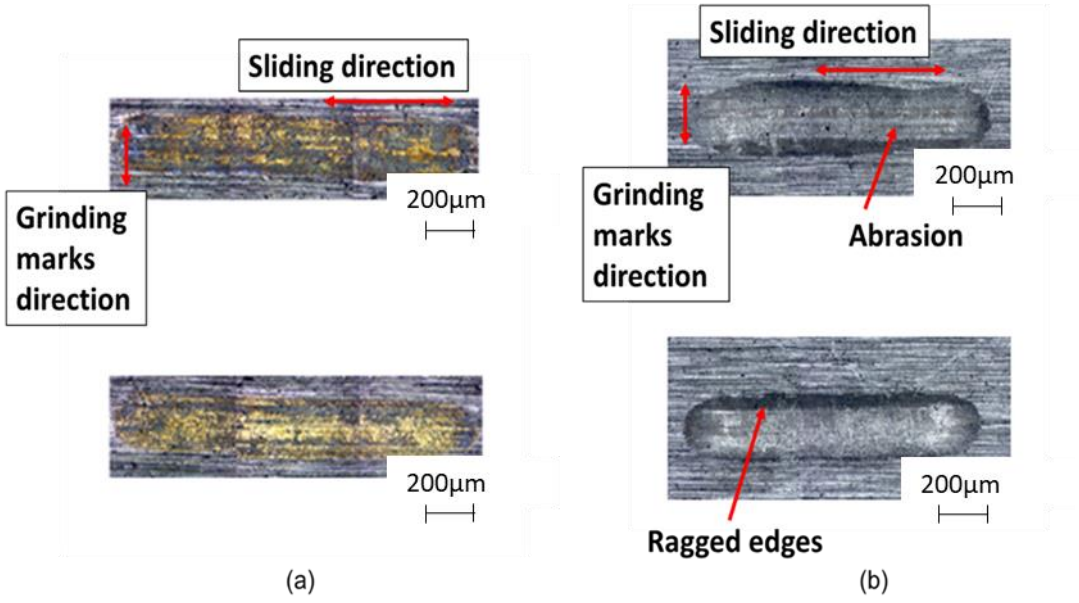

Figure 5.7 Optical microscope images of (a) 0% CB contents (b) 3% CB contents for 100°C at contact pressure of 1.83 GPa (cast iron)

5.7 Discussion

5.7.1 Coefficient of friction

The sliding friction results indicate that the coefficient of friction varies with carbon black content for both ferrous metals. The difference of coefficient of friction between 0% carbon black and 3% carbon black is small and both values became constant as test progressed where the level of conformity between the contacting surfaces increased. Based on previous research [69], the friction differs by 20% for cast iron while Green and Lewis [3][71] observed similar trends with lubricant oil blended with carbon black. This is due to the ability of the lubricant to retain and disperse the carbon black particles evenly. EN24 shows higher coefficient of friction compared to cast iron, however, the differences are small, and this could be because of its material properties whereby the roughness of EN24 is higher than cast iron resulting in higher friction.

Meanwhile, at higher carbon content, 12% carbon black contamination, the coefficient of friction increases. This is due to the increase of viscosity whereby the sooty oil thickens resulting in viscous shear of the lubricating film and asperities became severe. The reduced ability for the carbon black to disperse at higher concentration also increases the coefficient of friction due to the blockage of the carbon particles in the lubricant to flow into the contact.

5.7.2 Wear mechanisms

Abrasion wear is the major wear mechanism observed in these tests where at 0% carbon content, the contact was boundary lubricated with abrasive wear. The ball specimens which are harder than the flat specimen, results in two body abrasive wear as illustrated in Figure 5.8 where it can be seen that the particles are moving inside the lubricant. At a normal load of 50N with moderate to higher carbon black contents, 3% CB and 12% CB, the observed wear mechanism was three-body abrasive wear where the carbon black particles entrained into the contact causing the surface to experience plastic deformation and scratches due to starvation of lubricant caused by the agglomerates. The surface could also experience crack formation and propagation leading to scuffing at higher load, as had been predicted by Green and Lewis [71]. From this result, it shows that the carbon black content and temperature does influence the wear mechanisms on the rubbing surface.

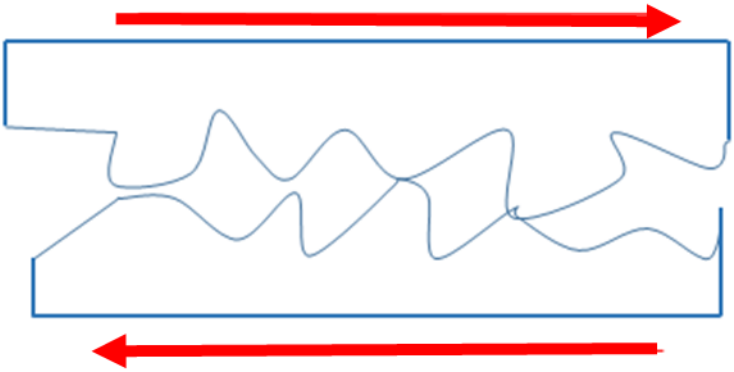

(a)

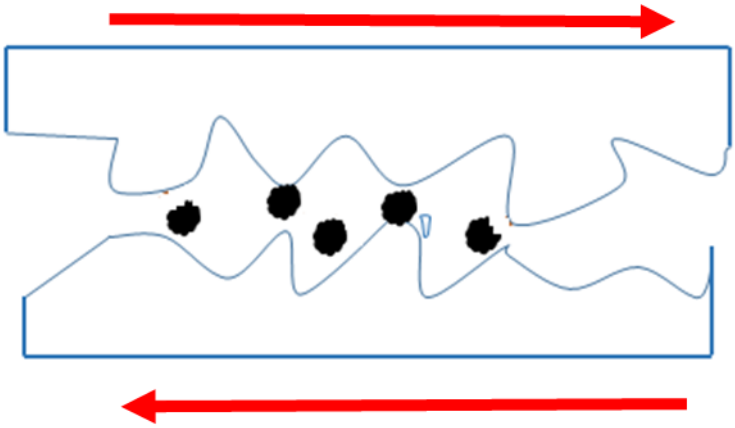

(b)

Figure 5.8 Illustration of abrasive wear mechanisms depicted from [72]

5.8 Summary

From the experiments carried out in this chapter, it is concluded that:

- The friction is expected to reduce with an increase in viscosity of the sooty oil as the carbon black content increases. Theoretical calculations of contact pressure and film thickness for both ferrous metal show that the sliding contact is expected to operate under a boundary lubrication regime. However, the fact that the coefficient friction increases with carbon black content, indicates that the viscosity of the lubrication played a major role in determining the regime that the tribosystem operates. At higher carbon black content, the viscosity increases with respect to thicker oil, thus the contact friction will also increase, which eventually decreases the performance of the automotive engine.

- The limitations on this study is that throughout this study only one commercial lubricant is used which were Shell Helix-HX5, 15W40 and blend with a percentage of carbon black to differentiate the wear effects of the contaminated oil. Thus, the viscosity of oil effects on the materials are limited. This could be improved by comparing also with based oil and other commercial lubricants as the additives packages are not the same for all commercial lubricants.

- Optical microscope images showed the wear mechanism progressing from lubricated metal contact sliding wear at 0% CB to three body abrasive wear with plastic deformation.

- These tests conducted conform to the previous results obtained [69]. This experiment also built the confidence and conformity to replicate the test method in order to study the effects of soot on non-ferrous materials.

Chapter 6 Polymers Wear

In this chapter, a wear and friction testing method was developed to determine the effect of increasing soot levels on the wear and lubrication of non-ferrous valve train components. The initial set of tests involved ball-on-flat specimens and was aimed to replicate some previous work that used ferrous materials to obtain the fundamentals of soot wear effects on non-ferrous materials with various carbon black content levels and build confidence in this test method.

6.1 Test equipment and specimens

The tests were performed using a Cameron-Plint High Frequency Reciprocating Rig (TE77) in a lubricated medium. The tester configuration has been explained in Chapter 5. The materials used as test specimens were non-ferrous. The flat specimens used in these tests were NBR, PEEK, PTFE and silicone. Nitrile Butadiene Rubber (NBR) is one of the most commonly used elastomers in automotive sealing applications including standard seals, O-rings and gaskets. NBR has good physical properties and chemical resistance to mineral oils, hydraulic oils and vegetable oils. It can withstand temperatures up to 100˚C [73].

Polyetheretherketone (PEEK) is an engineering thermoplastic that is used for applications where thermal, combustion and chemical properties are critical to performance. PEEK is commonly used for seals in power transmission in automotive industry. PEEK has high strength and toughness, outstanding chemical resistance and good wear resistance. It can withstand temperatures up to 343˚C with glass temperature of 143˚C [73].

Polyetrafluorethylene (PTFE) is an engineering thermoplastic that is commonly used for belting, gaskets and as lip seals in the automotive industry. PTFE contributes to low friction but mechanically it is quite weak. It can withstand temperatures up to 260˚C with glass temperature of 119˚C [73].

Silicone rubber is a synthetic elastomer that has certain advantages over natural rubber because of its stability and non-reactive properties that make it resistant to high temperature. It is commonly used in automotive components such as shaft seals, O-rings and gaskets. It can withstand temperatures up to 200˚C [73].

The ball specimens (Chrome Steel EN31) used for these tests were the same ball material used in Chapter 5. In order to obtain small flat specimens for the counterface, the test pieces were extracted from thin commercial available sheets of each material. The samples were cut into a rectangular shape with dimensions of 25mm x 66mm as shown in Figure 6.1. The mechanical properties of the materials are given in Table 6.1. The lubricant used in this study is the same lubricant used in Chapter 5 where fresh formulated mineral oil is blended with carbon black that act as soot surrogate.

Table 6.1 Mechanical properties of the ball and flat specimens

	Ball Specimen	**Flat specimen**			
		Nonferrous Material			
Material	**Chrome Steel EN31**	**NBR**	**PEEK**	**PTFE**	**Silicone**
Tensile Strength (MPa)	750	15	103	22	5.5
Average Hardness (HV – Hardness Vickers) and Shore Hardness A	63	70 (A)	28.5 HV	6.1 HV	62 (A)
Young's Modulus, E (GPa)	215	0.0049	3.95	0.5	0.005
Poisson's Ratio, υ	0.3	0.48	0.393	0.46	0.49
* Average Roughness, Ra (μm) - measured	0.05	2.23	11.45	7.75	15.28
*Dimension (mm)	ϕ6	66 x 25 x 4	66 x 25 x 4	66 x 25 x 4	66 x 25 x 4
*Source of information on above data were taken from respective supplier and compared with CES edupack	Steel Express, Wolverhampton, UK	Polymax	Direct plastics	Direct plastics	Polymax

*Measured values

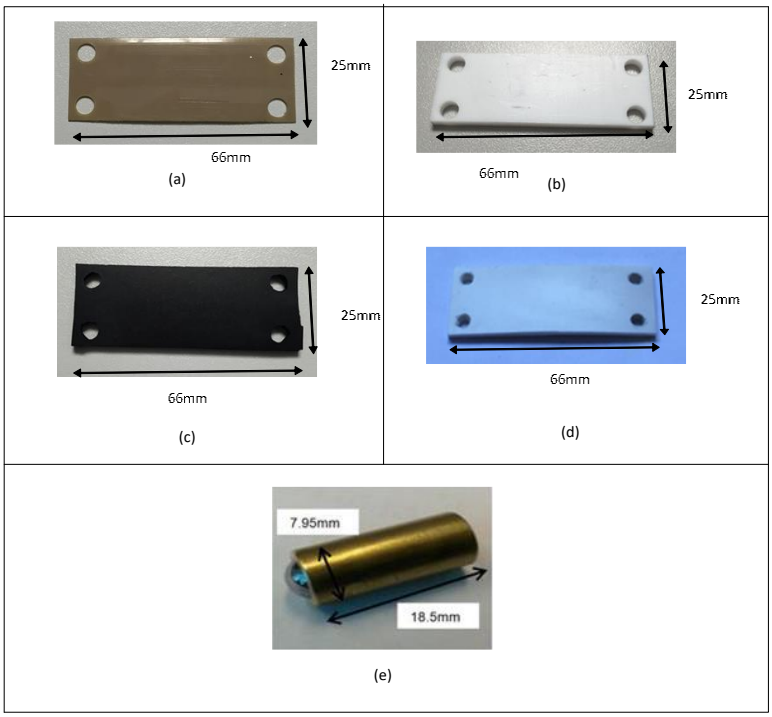

Figure 6.1 Graphic views of the specimens: (a) PEEK; (b) PTFE; (c) NBR; (d) Silicone and (e) ball

6.1.1 Hardness test with universal mechanical tester (UMT)

The Bruker Universal Mechanical Tester (UMT) was used to determine the hardness of all polymer specimens. The UMT is a unique test and measurement system that can be used for scratch testing that will determine the scratch hardness of the polymer specimens.

6.1.1.1 Scratch test

A scratch hardness test determines the resistance of a material to scratches and abrasion due to sliding from a sharp object. This test is applicable to the elastomer/polymer that were used in this tests. The scratch hardness test for elastomers/polymers materials using a diamond stylus was conducted with reference to ASTM standard (ASTM G171-03) [74]. A constant normal force was applied by the stylus to the specimens and a scratch track of length 10mm was formed by a sliding movement of the stylus against the specimen surface at a constant speed. The scratch width was measured using a profilometer. The test conditions are shown in Table 6.2.

Table 6.2 Test conditions for a scratch tests

No.	Parameter	Test Conditions
1	Normal Force (N)	50N
2	Temperature (℃)	23±2 (Room)
3	Stroke Length (mm)	10
4	Sliding Speed (mm/s)	5

By measuring the scratch width, the specimen scratch hardness can be determined using the following equation (6.1) [74]:

$$HSp = \frac{8P}{\pi W^2} \tag{6.1}$$

where *HSp* is the scratch hardness number, *P* is the normal force and *W* is the scratch width.

The measured scratch stroke width and calculated scratch hardness number (HS_p) are presented and compared in Table 6.3. The harder materials show different wear widths compared to softer materials, where the stroke width is smaller for harder materials thus giving higher value of hardness number. This result is in line with strength recorded in Table 6.1 where PEEK is tougher than other elastomers (NBR and silicone)

Table 6.3 Summary of scratch stroke width and scratch hardness number

Material	Scratch Stroke Width (μm)	HS_p (GPa)
PEEK	325	1.21
PTFE	642	0.31
Silicone	1044	0.12
NBR	1124	0.10

6.1.2 Wear test equipment

To study the wear and friction of the test specimens, a Cameron-Plint High Frequency Reciprocating Rig (TE77) was used for all tests to simulate wear and friction on the specimen using typical engine component interface conditions, while a Veeco Dektak 150 Profilometer was used to measure the wear depth and Optical Zeiss Microscope image were used to interpret the wear mechanism. The wear depth which is varied along the wear scar was measured using the profilometer and the depth measurements were recorded at 5 locations on the wear scar. The experimental average depth was determined from these points.

6.1.2.1 Profilometer

The average surface roughness and wear scar profiles for the flat specimens were measured using a Veeco Dektak 150 profilometer. The Dektak 150 is a surface profilometer that takes surface measurements using contact profilometry techniques. The wear volumes were measured using the profilometer.

Before a test is started, the tower is raised and the specimen is positioned in the centre of the stage right below the stylus. The parameters of the scan (length and duration) are set-up before the test is conducted. The stylus tip was moved using the control button on the surfaces of the specimen where the location of the wear scar is located. The wear depth which is varied along the wear scar was measured using the profilometer and the depth measurements were recorded at 5 locations on the wear scar. The experimental average depth was determined from these points.

6.1.2.2 Zeiss microscope

Wear scar imaging was conducted using an Optical Microscope. All of the worn surfaces of the specimens were examined using a Zeiss Microscope (Imager A2.M) to demonstrate the effects of wear produced changes with increasing carbon black content.

6.2 Calculation of contact parameters

6.2.1 Hertzian contact pressure

The initial Hertzian contact pressures (maximum and mean) were theoretically calculated for loads of 10N and 30N using equations for ball-on-flat configuration as shown previously in Equation 5.2 and 5.3. The contact pressures are shown in Table 6.4. Even though the nominal loads were the same for all materials, the contact pressure values are different due to their differing material properties. From these values it is known that the contact operates under soft elasto-hydrodynamic lubrication for rubber (NBR and silicone) where Bharat et al. [75] had stated that for soft elastohydrodynamics, the maximum pressure lies between 0.5 to 4MPa. While harder materials (PEEK and PTFE) shows value of contact pressure larger than the value for soft elastohydrodynamic condition, thus it could be said that the thermoplastic materials operates under hard elastohydrodynamics where the value of the contact pressure is more than that of soft elastohydrodynamics [75]. The values determined are the initial contact pressures although when contact area increases due to wear, the contact pressure is expected to decrease. A detailed calculation is shown in Appendix A-2.

Table 6.4 Contact pressures for various materials and nominal loads applied

Specimen Materials	Nominal Load, P (N)	Mean Contact Pressure p_m GPa	Maximum Contact Pressure p_o GPa
PEEK	10	0.113	0.169
PTFE	10	0.092	0.138
NBR	10	0.0005	0.0007
Silicone	10	0.001	0.002
	30	0.002	0.003

6.2.2 Film thickness

The film thickness of the sooty oil surrogates for specific materials is determined to analyse the tribological behaviour of surfaces in a lubricated contact. A film thickness equation for soft materials presented here is used in most of the literature for oil film thickness. The values of viscosity and density in Table 6.5 were taken from previous tests as it was assumed that the values of viscosity and density for the sooty oil were the same as measured for the previous study [69].

Lubrication regime was determined based on two methods which are the film thickness calculation, as represented by Equation 6.2 [76]; and identifying the regimes in the demarcated regimes map in terms of two non-dimensional variables, as represented by Equation 6.3 till 6.6 [77][78]. From the table, it can be seen that the film thickness increases with carbon black content. The fully detailed calculations are included in Appendix B-2.

The equation derived by Hamrock and Dowson for soft materials is as follows [76]:

i. Minimum film thickness, h_{min} is determined from:

$$h_{min} = 7.43(1 - 0.85e^{-0.31k})U^{0.65}W^{-0.21} \quad (6.2)$$

where U (non-dimensional speed parameter) is $U = \frac{\eta_0 u}{E' R'}$

W (non-dimensional load parameter) is and $W = \frac{P}{E' R'^2}$

k (non-dimensional ellipticity parameter) is $k = 1.034\left(\frac{R_y}{R_x}\right)^{2/\pi}$

ii. Non-dimensional central film thickness, H_c and minimum film thickness H_o for 4 different lubricant regimes:

Isoviscous-rigid, $H_{c/o} = 134$ (6.3)

Piezoviscous-rigid, $H_{c/o} = 5.35 g_v^{0.375}$ (6.4)

Isoviscous-elastic, $H_c = 5.08 g_E^{0.67}$, $H_o = 3.28 g_E^{0.67}$ (6.5)

Piezoviscoues-elastic, $H_c = 2.55 g_V^{0.53} g_E^{0.13}$, $H_o = 1.69 g_V^{0.49} g_E^{0.17}$ (6.6)

where $g_V = \frac{\overline{GW}^3}{\overline{U}^2}$, $g_{vE} = \frac{\overline{W}^{8/3}}{\overline{U}^2}$, and $\overline{U} = \frac{U\eta_o}{E' R'_x}$, $\overline{W} = \frac{W}{E' R'_x}$, $G = \alpha E'$

Table 6.5 Kinematic Viscosity and Density of Sooty Oils

Sooty oil	Kinematic Viscosity @40°C (cSt)	Kinematic Viscosity @100°C (cSt)	Density at 15°C (g/cm^3)
0%CB	106	14.27	0.866
5%CB	239.35	131.86	0.891
12%CB	1156.1	888.07	0.928

6.2.3 Minimum film thickness

The predicted minimum film thickness at 25ºC and 100ºC, using Equations 6.2 till 6.6, are presented in Table 6.6. It clearly shows that the film thickness increases with carbon black content. As mentioned in the literature review, the estimated size of soot particles are similar to the size of carbon black used in this study which is between 0.2 µm and 0.5 µm. When this is compared to the film thickness calculated in Table 6.6, it is expected that the carbon black particles (being larger) can abrade through the film thickness when at lower and higher temperature thus causing wear to PEEK and PTFE. However, the film thickness for NBR and silicone are higher compared to the size of the soot surrogates and thus they are less likely to influence the amount of wear on the specimens.

Table 6.6 Minimum film thickness for different materials with sooty oils at 10N

Specimen Material	Sooty Oils	Minimum Film Thickness at 25°C (μm)	Minimum Film Thickness at 100°C (μm)
NBR	0% CB	0.544	0.086
	5% CB	0.639	0.374
	12% CB	1.708	1.327
Silicone	0% CB	0.536	0.085
	5% CB	0.630	0.369
	12% CB	1.683	1.308
PEEK	0% CB	0.030	0.005
	5% CB	0.035	0.021
	12% CB	0.094	0.073
PTFE	0% CB	0.072	0.011
	5% CB	0.085	0.049
	12% CB	0.226	0.175

At higher load, it is obvious that soot particles influence the wear on all types of specimens as the minimum particle size is greater than the maximum film thickness obtained as shown in Table 6.7.

Table 6.7 Minimum film thickness for different materials with sooty oils at 30N, 100°C

Specimen Material	Sooty Oils	Minimum Film Thickness at 100°C (μm)
NBR	5% CB	0.297
Silicone	5% CB	0.293
PEEK	5% CB	0.016
PTFE	5% CB	0.039

6.2.4 Lubrication regime map

The regime map produced by Hamrock and Dowson [76] and further revisited by Esfahanian and Nigel [77][78] is a useful tool in determining the regime in which the non-comforming lubricated contact will operate [76][78] by determining the two non-dimensional variables. The value of the two non-dimensional variables gives an indication of the lubrication regime operational contact. All materials that have been mapped into the regime map show that they are expected to operate under a soft-isoviscous elastic lubrication regime often known as elastic-hydrodynamic lubrication

(EHL) (Figure 6.2 and Figure 6.3). The lubrication map regime conforms to the calculated predicted film thickness from four equations (6.3-6.6) where the thickest hydrodynamic film corresponds to the regime in which the contact will operate.

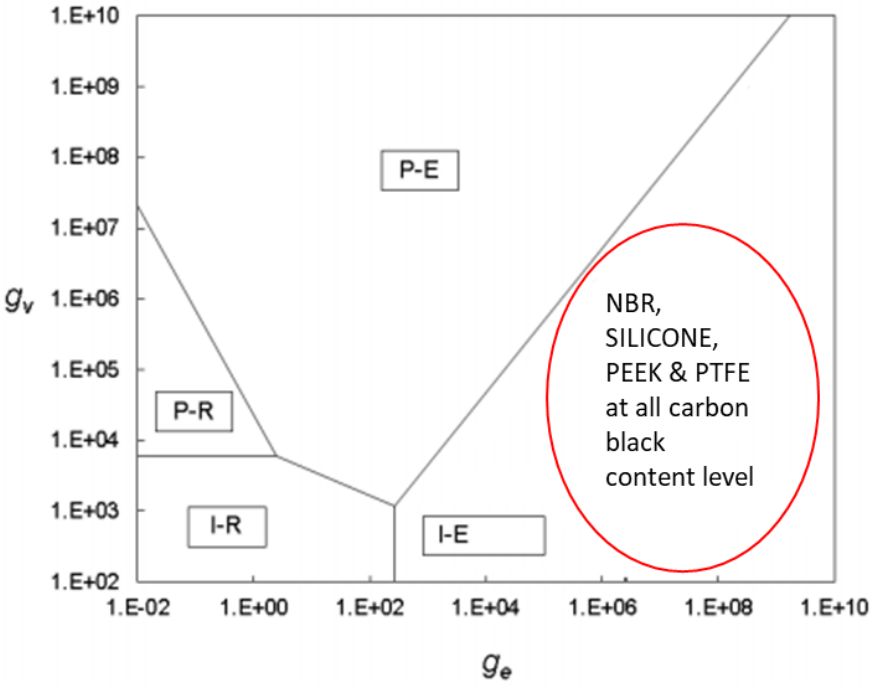

Figure 6.2 Hydrodynamic regime map for different materials with sooty oils at 100N, 25°C and 100°C adapted from [76][78]

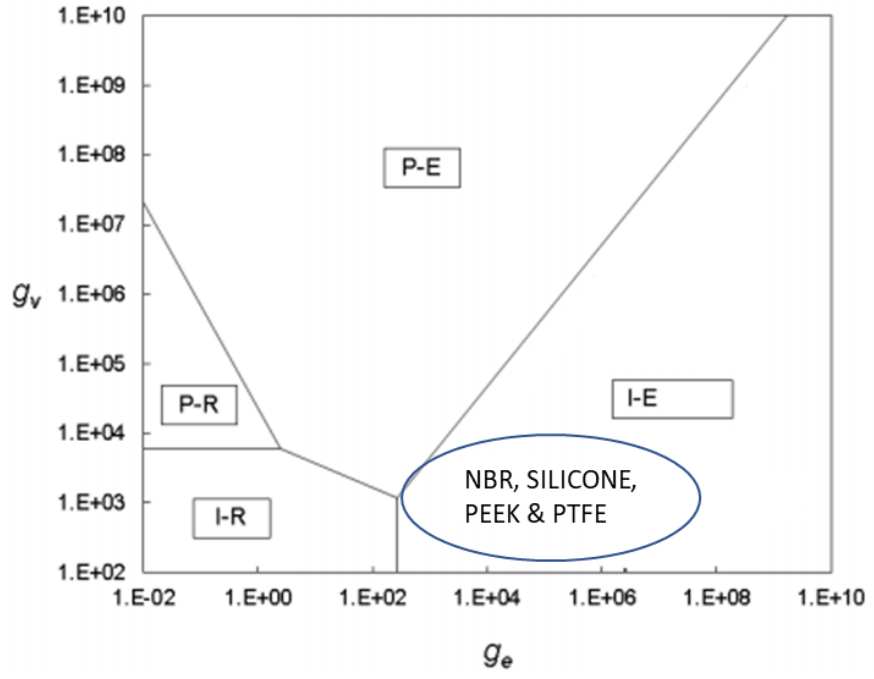

Figure 6.3 Hydrodynamic regime map for different materials with sooty oils at 30N, 100°C adapted from [76][78]

6.2.5 Contact temperature

When two solid bodies slide against each other, friction occurs. The friction force occurs at the real area of contact between the sliding bodies of the asperity level and through this process, the mechanical energy is transformed into heat which causes the temperature of the sliding bodies to increase. In polymers, the friction and wear behaviour is influenced by frictional temperature and contact temperature, this frictional heating and contact temperature plays an important role for the tribological behaviour of a polymer and should be considered when investigating the tribological mechanism between sliding components [79].

In sliding contacts, there are three levels of temperature which the highest contact temperature T_c (total contact temperature) occurs at the contact between asperities on the sliding surfaces [80]. Usually there are several flash temperature, T_f, rises at various spots within the nominal contact patch, $\Delta T_{nom.}$. Once the counterface moves from the sliding body (contact patch), the temperature will decrease to a bulk temperature T_b. The total contact temperature, T_c (6.7) at a given point is given by the three levels of temperature mentioned above [80]:

$$T_c = T_b + \Delta T_{nom} + \Delta T_f \tag{6.7}$$

For case involving stationary heat source on moving body (with circular region of radius, a), the maximum flash temperature can be estimated by using the following equation [80]:

$$\Delta T_{fmax} = \frac{2qa}{k\sqrt{\pi(1.273 + Pe)}} \tag{6.8}$$

Where, q = μPU is the rate of heat generated per unit area, (W/m^2), μ is the coefficient of friction, P is the contact pressure (N/m^2), a is the circular radius in m, k is the thermal conductivity (W/mK), P_e is the Peclet number = $\frac{Va}{2K}$, V is the velocity (m/s) and K = $\frac{k}{\rho c}$ is the thermal diffusivity (m^2/s).

The nominal temperature is measured when a heat source passes repeatedly over the same point on a surface. The nominal temperature rise for the moving body is estimated by [80]:

$$\Delta T_{nom} = q_{nom}\frac{lb}{k} \tag{6.9}$$

With $q_{nom} = q\frac{A_r}{A}$, A_r is the real contact area (m^2), A = πa^2 is the nominal contact area (m^2), $l_b = \frac{a}{\pi^{1/2}}\tan^{-1}\left[\frac{2\pi K}{aV}\right]^{1/2}$ is the effective diffusion length (m).

The estimated total contact temperature for a lubricated contact for every specimen is shown in Table 6.8. Values of coefficient of friction and contact pressure that were used in the calculations are based on the results from the Plint Test Rig and in Table 6.4. All contact temperatures were found to be below the melting temperature point for every specimen with an average standard deviation of 0.025 for all tests. From the table, it is found that the contact temperature for NBR and silicone is lower than PEEK and PTFE, even though the friction for the softer materials are higher than the harder materials. Due to the PV limit of the materials, the combination of high contact pressure and sliding velocity of the harder materials causes the surface temperature to increase. It also clearly shows that the contact temperature increases with presence of carbon black surrogate for all specimens. This is probably due to the fact that when sooty oil with carbon black content increases, it restricts the lubricant flow into contact therefore increasing the friction force between the rubbing surfaces, thus increasing the contact temperature of the contact area.

Table 6.8 Total contact temperature for different specimens and sooty oils at 10N

MATERIAL SPECIMENS	SOOTY OILS	COEFFICIENT of FRICTION, μ	CONTACT TEMPERATURE at 25 (°C)	COEFFICIENT of FRICTION, μ	CONTACT TEMPERATURE at 100 (°C)
NBR	0% CB	0.124	29	0.034	101
	5% CB	0.113	29	0.045	102
	12% CB	0.125	29	0.055	102
PEEK	0% CB	0.028	91	0.052	145
	5% CB	0.035	107	0.023	152
	12% CB	0.039	115	0.073	270
SILICONE	0% CB	0.103	34	0.060	105
	5% CB	0.101	34	0.060	105
	12% CB	0.101	34	0.071	106
PTFE	0% CB	0.022	74	0.034	175
	5% CB	0.027	85	0.053	215
	12% CB	0.031	92	0.068	248

For lubricated sliding at higher load, 30N (Table 6.9) the contact temperatures are seen to be higher for harder materials; PEEK and PTFE. PEEK and PTFE show higher contact temperature than NBR and silicone at higher load. An increase in temperature may lead to a higher tendency for initiation of wear. The wear images obtained indicate that PTFE shows signs of material removal and larger wear scar while PEEK shows signs of abrasion and starvation. This is probably due to the geometry and properties of the surface contacts of each specimen.

Table 6.9 Total Contact Temperature for Lubricated Contact (5% CB) at 30 N

MATERIAL SPECIMENS	SOOTY OILS	COEFFICIENT of FRICTION, μ	CONTACT TEMPERATURE at 100 (°C)
NBR	5% CB	0.140	105
PEEK		0.078	281
SILICONE		0.265	124
PTFE		0.148	422

6.3 Experimental procedures

The lubricant used in ball-on-flat specimen contacts are in uncontaminated conditions and also by mixing carbon black (soot surrogate) at varying percentages (5% and 12%) with fresh lubricant oil. The tests were carried out on non-ferrous materials: NBR, silicone, PTFE and PEEK. The oil temperature was selected to simulate real engine conditions which are room temperature 25°C and at high temperature 100°C were programmed inside the machine. All of the tests were performed at least three times to ensure a statistically significant evaluation. The test conditions for non-ferrous material were as outlined in Table 6.10. These test conditions were chosen to simulate engine operating conditions that are applicable to flat elastomer/polymer contacts to gain a fundamental understanding rather than performing a direct comparison. The speed was chosen according to the suggested in work on abrasive wear of seals [81]. Two different loads were selected in order to approach contact pressure lower than 1MPa since it represents the mean contact pressure in actual sealing [82]. The contact pressures were estimated by Hertz theory for a ball-on-flat contact (see the equations in Chapter 5). The other data such as elastic modulus was obtained from the material data sheets. For the elastomer/polymer materials, the same ball was used for three repeated test for each flat specimen where no damage occurred to the steel ball.

Table 6.10 General Test Conditions (Non-Ferrous materials)

No.	Parameter	Test Conditions
1	Ball Specimen Radius (mm)	3
2	Temperature (℃)	23±2 and 100
3	Normal Force (N)	10 and 30
4	Stroke Length (mm)	15
5	Sliding Linear Speed (m/s)	0.14
6	Test Duration (min)	25
7	Lubrication	Lubricated (0%, 5%, 12% CB)

6.3.1 Friction and wear tests at high temperature 100°C

The Plint TE77 machine was programmed by increasing the temperature to 100°C in 10 minutes, and the temperature is let to dwell at the same temperature for 50 minutes. The extra 30 minutes of time is needed to stabilize the temperature to 100°C as the temperature will continue to increase and stabilizes back to 100°C. The ball specimen is lowered onto the flat specimen in the first 15 minutes to ensure that the ball and flat specimen reaches the same temperature before testing is commenced.

6.3.2 Friction and wear tests at low temperature 25°C

The same programme was used for testing, the difference is that the temperature was ramped to room temperature. The Plint TE77 machine was programmed by increasing the temperature to 25°C in 10 minutes, then to dwell at that temperature for 60 minutes. The extra 35 minutes is needed to stabilize the temperature to 25°C as the temperature will continue to increase and stabilizes back to 25°C. The ball specimen is then lowered onto the flat specimen in the first 15 minutes to ensure that the ball and flat specimen reaches the same temperature before testing is commenced.

6.4 Experimental results

6.4.1 Friction coefficient measurement

The overall coefficient of friction for both low and high temperature at various carbon black contents is depicted in Figure 6.4. From these early results, it is obvious that the coefficient of friction is dominated by lubricant and soot for thermoplastic materials. While for elastomer materials it is dominated by the material properties at lower temperature, however, at high temperature, the friction value does not vary significantly for all materials, thus it can be said that the coefficient of friction is affected by both lubricant (mechanism in Figure 6.10) and material properties (mechanism in Figure 6.9). All polymers show higher friction at higher carbon content level. This is because the sooty oils thicken which results in increasing viscosity and larger sizes of carbon black agglomerate restricting lubricant flow into the contact thus increasing the coefficient of friction.

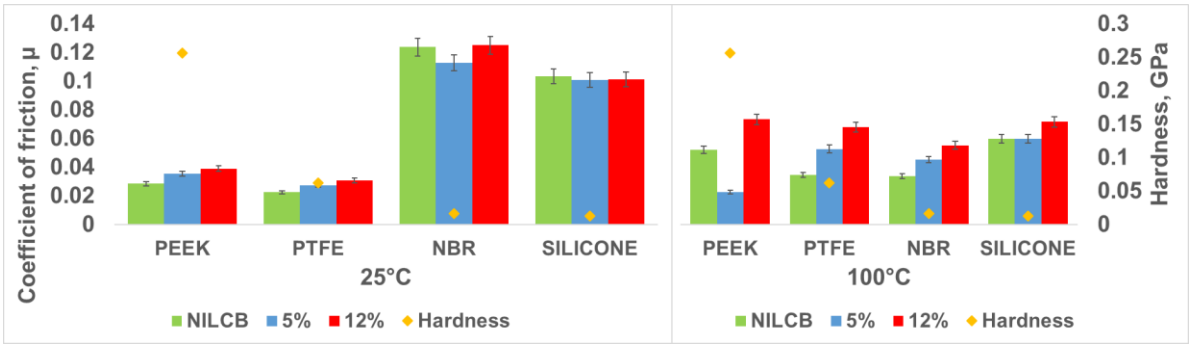

Figure 6.4 Coefficient of friction for all polymers at low and high temperature for various carbon black contents at 10N

The increase in viscosity and predicted film thickness at lower temperature when operating in elasto-hydrodynamic lubrication regime will increase the friction due to the viscous resistance to shear. At higher temperature, the coefficient of friction is found to be low. This is due to the low viscosity of the lubricant at higher temperature thus lowering the friction. The decrease in viscosity suggests that it is operating within the elasto-hydrodynamic lubrication regime thus decreasing the contact friction. This is demonstrated by the Stribeck curve as shown in Figure 6.5.

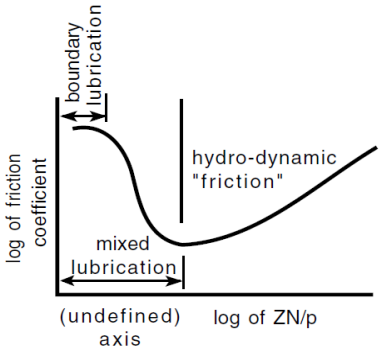

Figure 6.5 Stribeck curve [83]

Figure 6.6 shows the coefficient of friction for 5% carbon black content for all polymers at higher temperature and 30N. As expected, PEEK showed the lowest coefficient of friction while silicone shows the highest. The molecular construction of harder materials (PEEK and PTFE) helps the molecules to stretch easily in the direction of the shear force thus making it less resistant to shear [84]. Figure 6.7 and Figure 6.8 shows a better representation of how the molecules acts when forces applied on elastomers and thermoplastic materials.

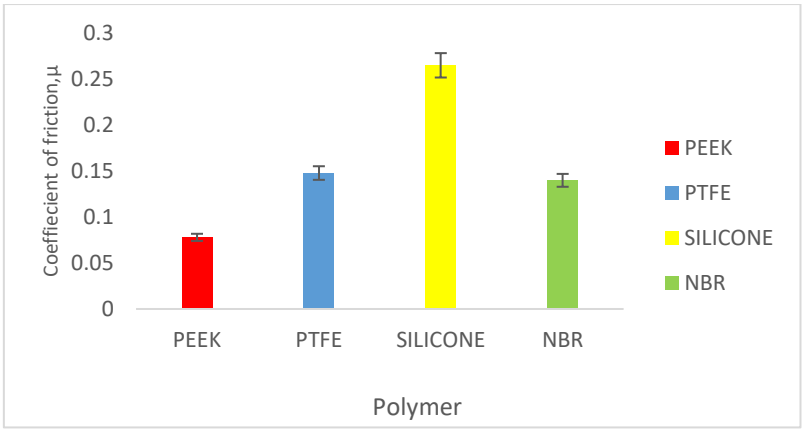

Figure 6.6 Coefficient of friction for all polymers at high temperature for 5% carbon black content at 30N

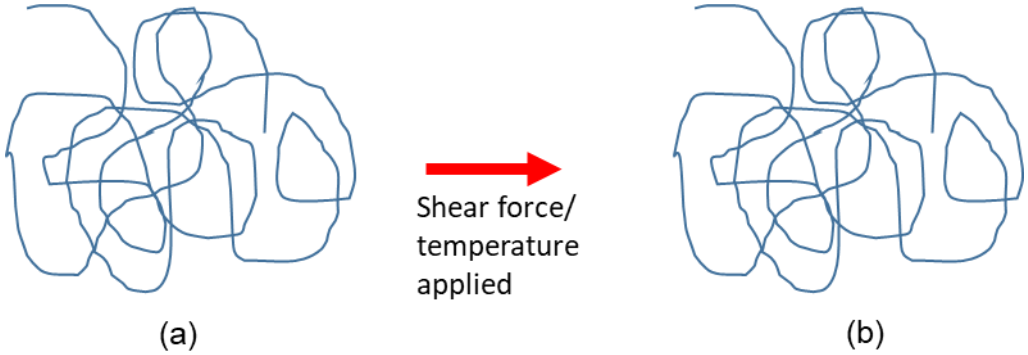

Figure 6.7 Morphology molecule structure of chain polymers for elastomers (a) before stress applied (b) after stress applied

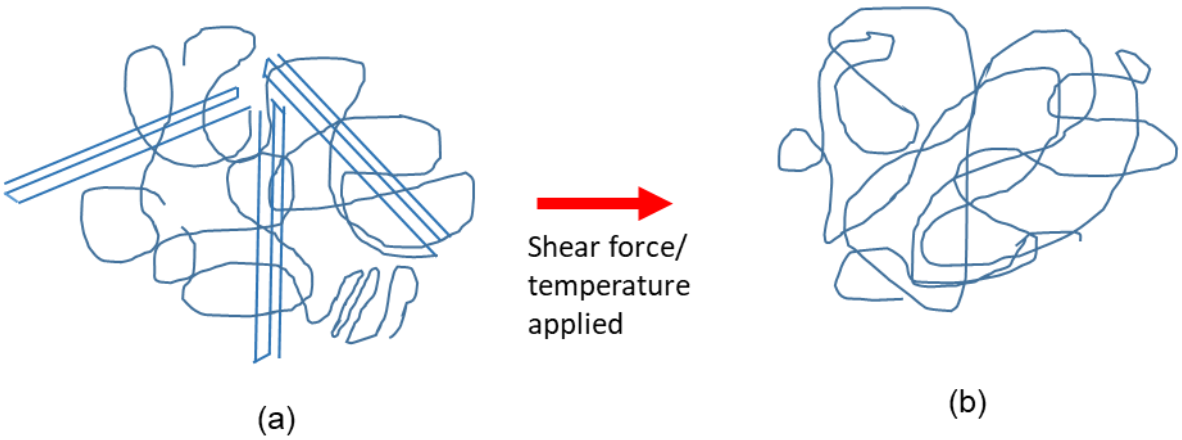

Figure 6.8 Morphology molecule structure of chain polymers for thermoplastics (a) before stress applied (b) after stress applied

Elastomers consists of polymer molecules chains have weak intermolecular forces with one another to keep the chains from disentangling. This results in a structure similar to rubber bands fold together as shown in Figure 6.7. When shear force and temperature is applied on the polymer, the molecules begins to untangle and when stress is removed, the molecules relax again and return to its original form. Figure 6.8 (a) shows the thermoplastics having more orderly arranged chain molecules. When subjected to shear force and temperature over time, the polymer chains are positioned further apart thus the chains can disentangle more easily as seen in (b) [85].

6.4.2 Wear analysis

Wear analysis was conducted using Veeco Dektak 150 Profilometry and a Zeiss Optical Microscope where the profilometry is used to generate data for analysis while microscopy is used to generate images for visual observation and to interpret the wear mechanisms.

6.4.2.1 Wear scar profile

With reference to the schematic shown in Figure 6.9 the ball indents the elastomers during sliding thus creating a larger contact area. For elastomer materials, it may experience constant deformation and for thermoplastic materials, the materials experienced fatigue cracking which formed on the surface as shown in Figure 6.10.

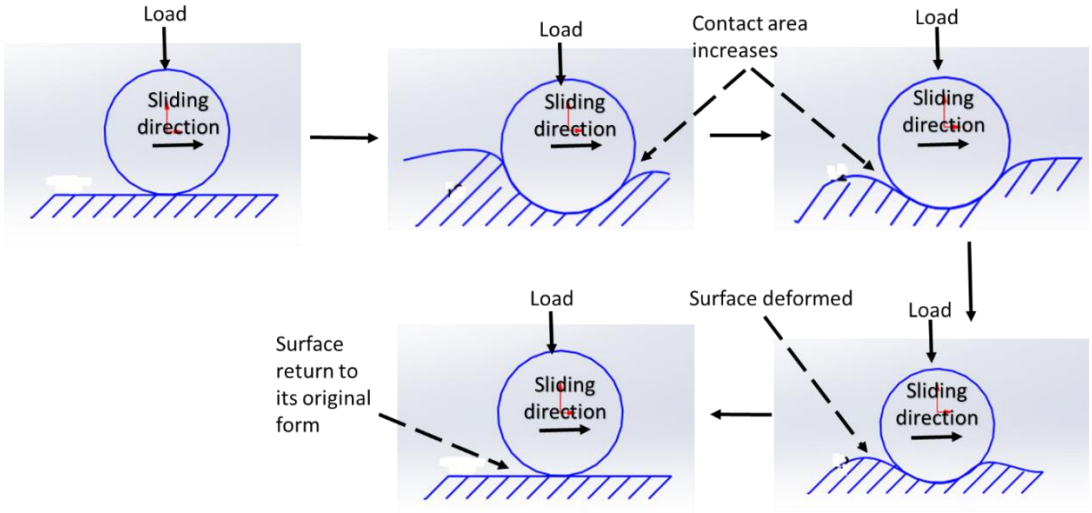

Figure 6.9 Steel ball pressing on an elastic material

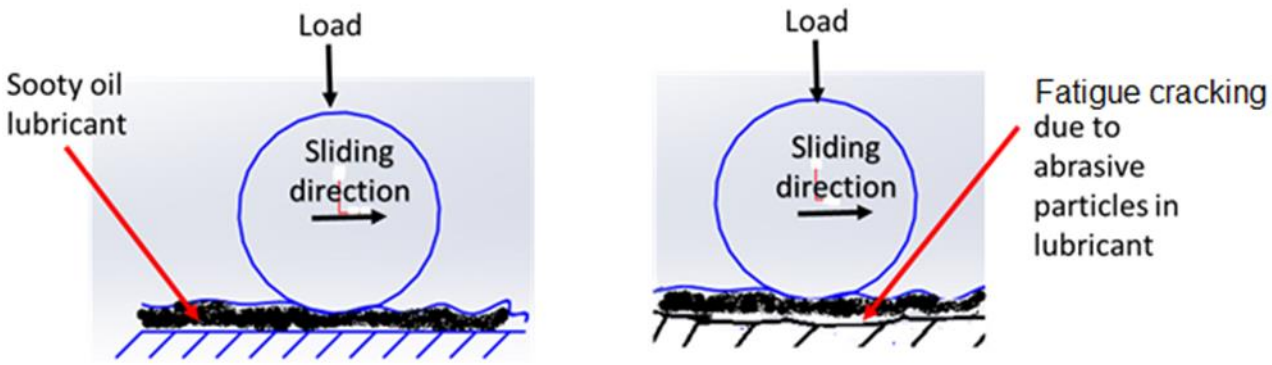

Figure 6.10 Steel ball sliding on a polymer material

The wear scar profiles were measured using a Veeco Dektak 150 profilometer to determine the geometry of the wear scars. This was done by moving the stylus perpendicular to the sliding direction. The geometry of the wear profiles such as the width, depth and surface area of the wear scar can be determined using the profilometry. The cross section of the wear track is the area of the material removed from the original flat surface. With this data, the volumes of the wear profiles were determined.

Examples of the wear scar profiles for all polymers are shown in Figure 6.11. For elastomer materials (silicone and NBR), it is known that the materials experience deformation. Even though silicone specimen profile images show higher wear volume than the thermoplastic materials, this is due to the to the indentation of the ball from the sliding force which the silicone flows to conform to the contour of the steel ball, however, the abrasive wear is insignificant for the elastomer material. The flowing action of the silicone generates higher friction, as has been shown in Figure 6.9, via hysteresis. For PTFE and PEEK, the wear profiles show signs of material removal due to abrasive wear for both temperatures. Other raw data can be seen in Appendix C.

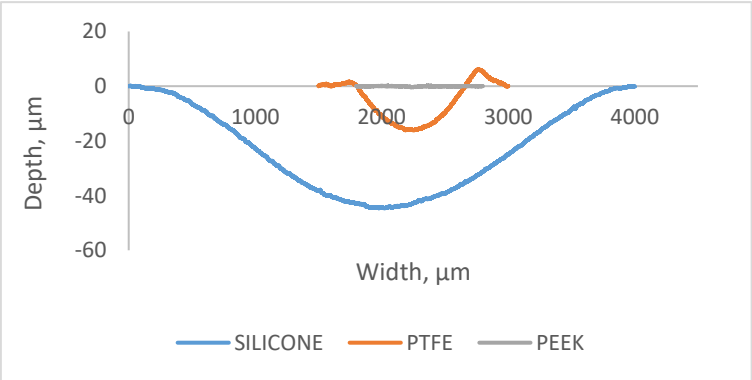

Figure 6.11 Wear scar profiles for silicone, PTFE and PEEK at 25°C, 10N

6.4.2.2 Wear scar volume measurement

The wear scar volumes were calculated using ASTM standard G133-05 (Standard Test Method for Linearly Reciprocating Ball-on-Flat Sliding Wear). The wear volume of the specimen is measured from the length of stroke and the surface area of the wear profile using Veeco Dektak 150 profilometer. The surface area of the wear and roughness profiles were taken at three different locations. The wear volume in mm^3 of the flat surface is calculated using the equation shown below (6.8).

$$V_{total} = A \times L \tag{6.8}$$

where *A* is average cross-sectional area of the wear track, (mm^2) and *L* is length of stroke, *(mm).*

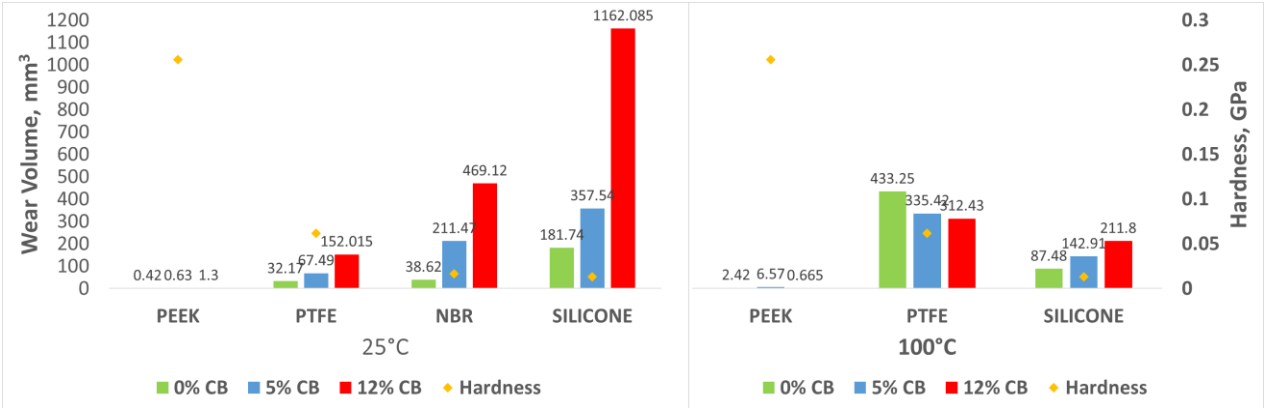

Figure 6.12 Wear volume of different polymers for various carbon black content at 25°C and 100°C at 10N

Figure 6.12 presents the wear volume of different polymers at various carbon black contents for temperatures of 25°C and 100°C. At room temperature (25°C), it shows that the volume increases with increasing carbon content. As expected PEEK has the lowest wear volume followed by PTFE compared to silicone and NBR due to its material properties as silicone is softer than PEEK thus the indentation depths of the steel ball sliding on elastomer materials are more significant than on thermoplastic polymers. While at higher temperature PTFE has a higher wear volume than silicone (Figure 6.12 and Figure 6.13). This is probably because at higher temperature, PTFE softens and the wear scar becomes larger. The glass transition temperature, *T*g for PTFE is 119°C whereby in Table 6.8 the contact temperature is above the *T*g value thus material starts to soften and melts. At higher temperature PEEK also demonstrates lower volume, probably because the indentation depth of the sliding ball is low due to its hardness and the ability to withstand higher temperature without melting. This correlates with the glass transition temperature, *T*g of PEEK is 143°C where in Table 6.8, the contact temperature is above the *T*g value and began to soften when reaching approximately 250°C. Test at 30N were only conducted for 5% CB

where it is assumed that the lubricant for 12% CB at higher load will give the same results.

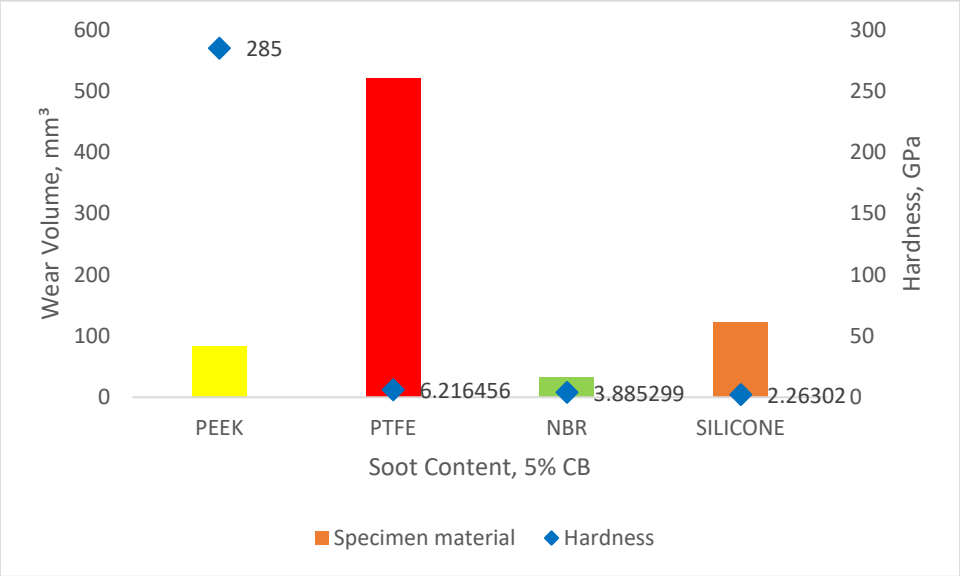

Figure 6.13 Wear volume of different polymers at 30N and 100°C and 5%CB

6.4.2.3 Final contact pressure

An initial Hertzian contact pressure for non-confomal contact configuration is normally used tribological contact. However, as a test progresses the contact area increases with development of wear or because of the deformation of the material which decreases the nominal contact pressure. The final wear contact pressure which shows an elliptical wear shape as shown in Figure 6.14 can be determined by using the final wear equation (Equation 6.9) as obtained from Ajayi and Erck [86].

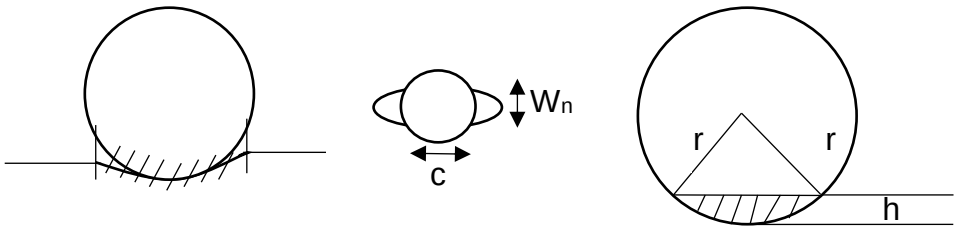

Figure 6.14 Schematic diagrams of conformal contact

$$P_n = \frac{P}{\pi ab} \tag{6.9}$$

where, P_n is the nominal contact pressure; P is the normal load, N; and a and b are the major and minor radius axes respectively, *(m)*

From Figure 6.14, the major axis is the wear scar width and the minor axis is the diameter of the ball segment embedded in the wear scar.

Therefore,

$$a = \frac{1}{2} w_n \tag{6.10}$$

$$b = \frac{1}{2}\, x\, c = \frac{1}{2}(2rh - h^2)$$

$$b = \sqrt{2rh - h^2} \tag{6.11}$$

where, w_n is the width of the wear scar; h is the depth of the wear scar; and r is the radius of the ball specimen.

The results of the final contact pressure using the above equations are presented in Figure 6.15. It can be seen that the final contact pressures obtained are higher than the initial contact pressures for PEEK and PTFE at room and high temperature and lower contact pressure for other materials as the contact area increases after sliding occurs. This correlates with finding from Ajayi and Erck [86], when the wear increase progressively due to increase in contact area, the contact pressure will reduce correspondingly. PEEK shows higher final contact pressure could probably because of its mechanical properties, which are higher in strength, thus lower contact area, correspond to its lower wear compare to other materials.

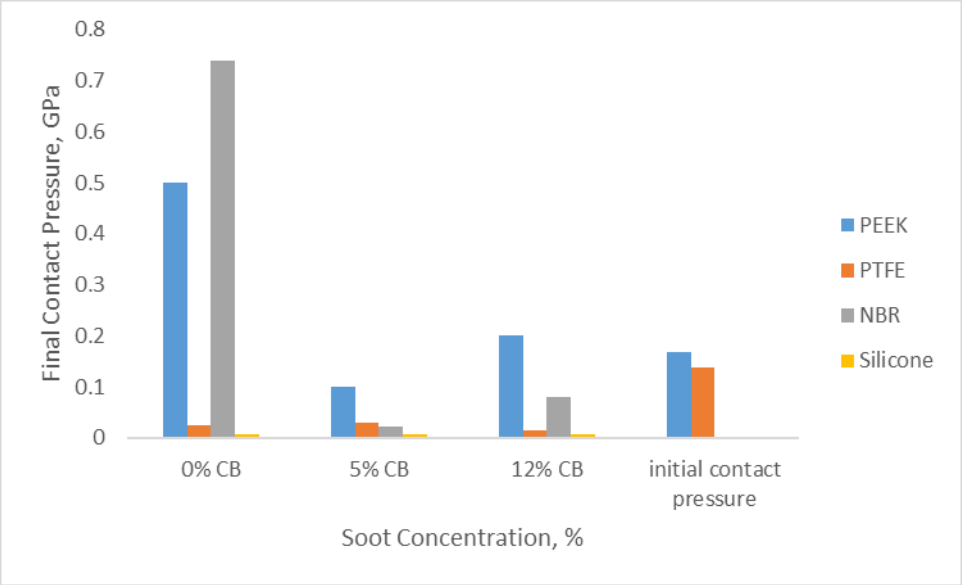

(a)

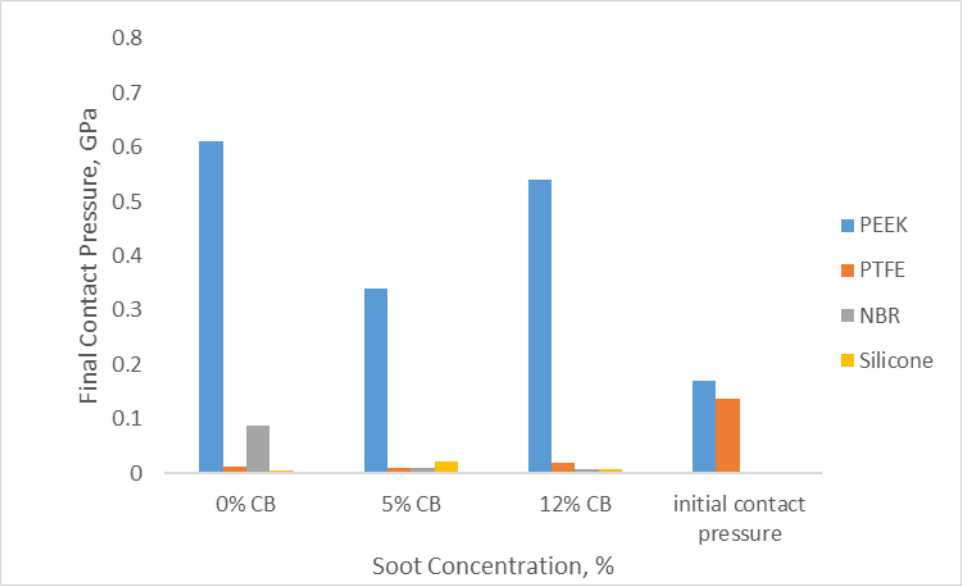

(b)

Figure 6.15 Final nominal contact pressure for (a) 10N at room temperature (b) 10N at 100°C

6.4.2.4 Wear scar optical images

The effects of the wear are demonstrated visually using an optical microscope. To understand the wear mechanisms, wear scar images of lubricated specimens with pure engine oil and sooty oils are presented in Figure 6.17 to Figure 6.19. Figure 6.16 shows the images of all tested polymers before a reciprocating sliding test.

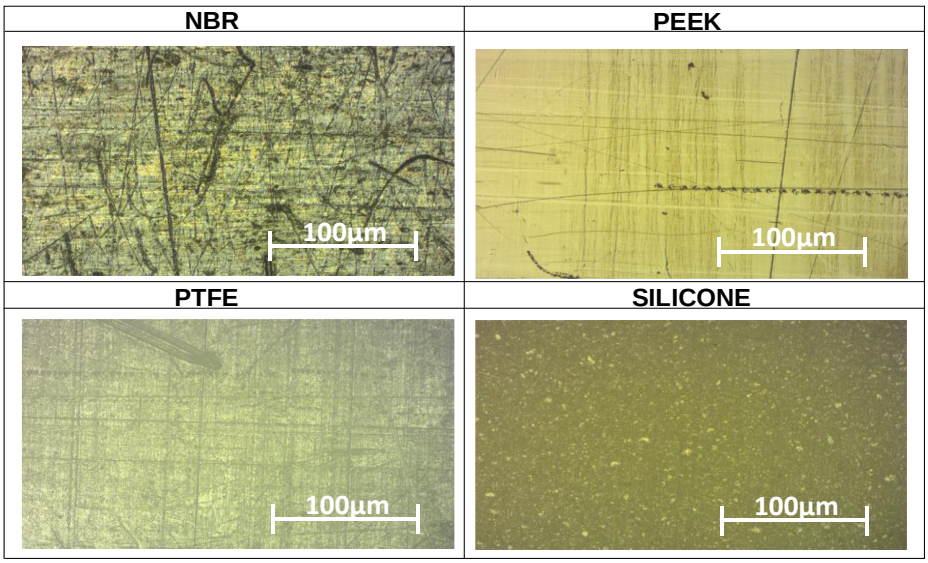

Figure 6.16 Images before reciprocating sliding tests

Figure 6.17 demonstrate the effect of increasing carbon black content to the characteristic of wear scar surface PEEK with respect to temperature. At low temperature, 25°C, very low signs of abrasion are shown in the images for 0% carbon black. For 5% and 12% carbon black content, the type of wear remains the same where low levels of abrasion and adhesion are shown at both end of the specimens. At 100°C, the wear scar images show high levels of abrasion when carbon black content increases. At 12% carbon black, the surfaces show signs of high levels of abrasion and polishing streaks due to possible starvation of lubricant from the contact.

Figure 6.18 shows the effect of increasing carbon black content to the characteristic of wear scar surface of PTFE when sliding at low and high temperature (25°C and 100°C respectively). It is observed that a low level of abrasion is found at low temperature and the evidence of machining marks are still running through the wear scar regions. At high temperature, scratch marks are observed at 0% carbon black content with some evidence of machining marks as well. And at 5% and 12% carbon black, high level of abrasion is found with carbon deposition at the start and end of stroke of the specimen. The wear scar width at high temperature for increasing soot levels was also found to be larger than at low temperature. This may be due to the material softening at higher temperature which can be seen through the profile as in Figure 6.11.

For silicone, the wear images in Figure 6.19 demonstrates little signs of abrasive wear for 0%, 5% and 12% carbon black for both low and high temperature, but the wear is not measurable. It also shows marks of soot deposition on the silicone which is noticeable for 12% carbon black content at higher temperature, this is due to the cleaning process after the reciprocating test. Carbon black tends to adhere to silicone because of its surface topography.

<table>
<tr><th colspan="2">0% Carbon Black</th></tr>
<tr><th>25°C</th><th>100°C</th></tr>
<tr><td> 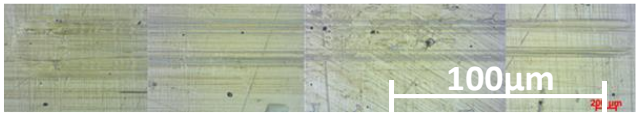

Very low level of abrasion</td><td> 

High level of abrasion</td></tr>
<tr><th colspan="2">5% Carbon Black</th></tr>
<tr><th>25°C</th><th>100°C</th></tr>
<tr><td>Low level of abrasion
 
</td><td>Abrasion
 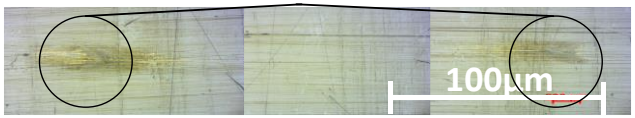
</td></tr>
<tr><th colspan="2">12% Carbon Black</th></tr>
<tr><th>25°C</th><th>100°C</th></tr>
<tr><td>Low level of abrasion
 
</td><td>Polishing streaks
High level of abrasion
 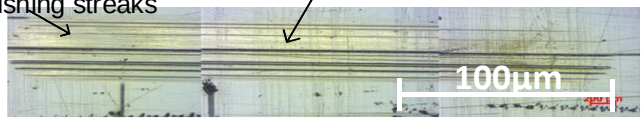
</td></tr>
</table>

Figure 6.17 Images of PEEK wear scars for 0%, 5% and 12% Carbon Black at 25°C and 100°C

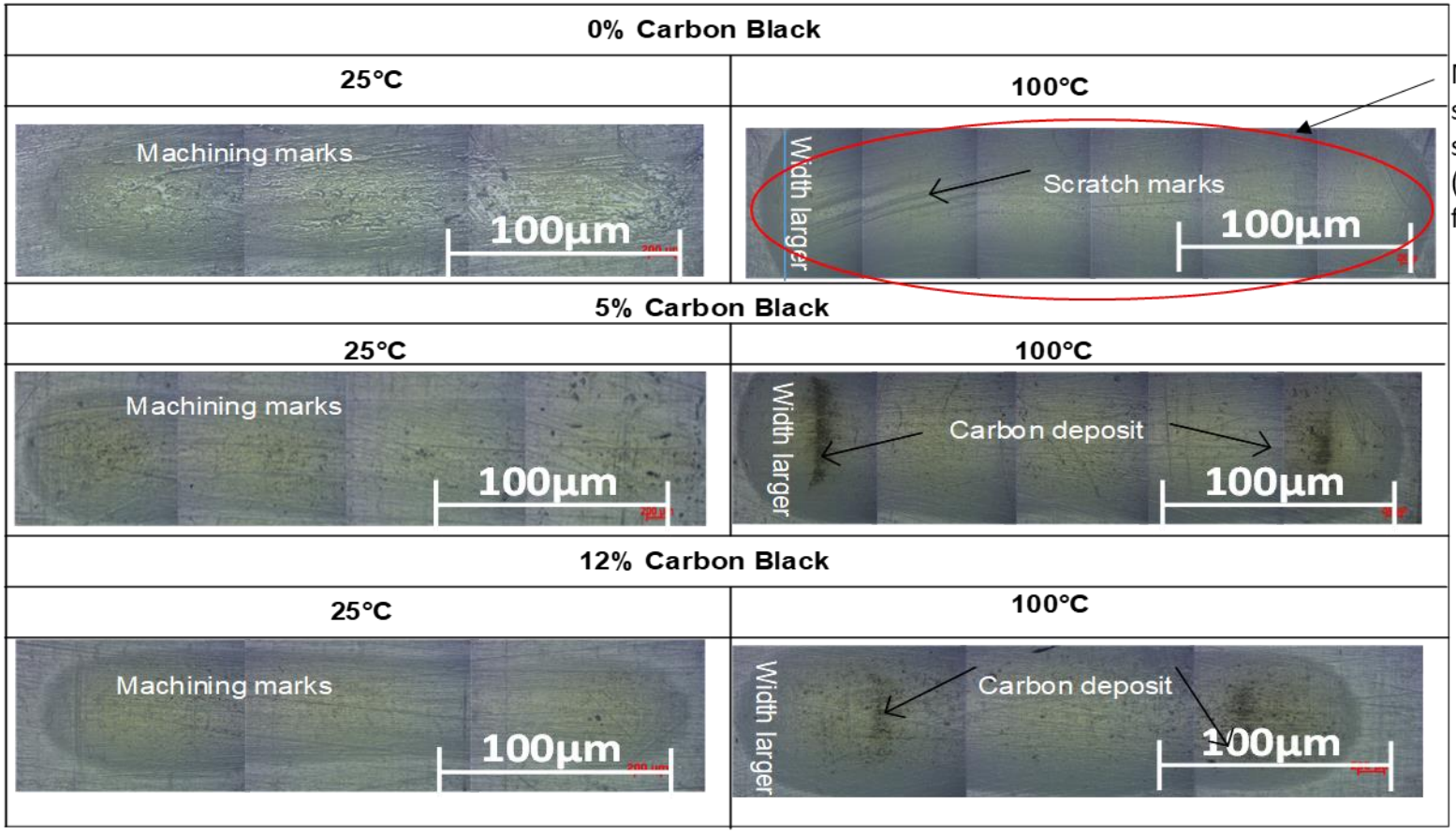

Figure 6.18 Images of PTFE wear scars for 0%, 5% and 12% Carbon Black at 25°C and 100°C

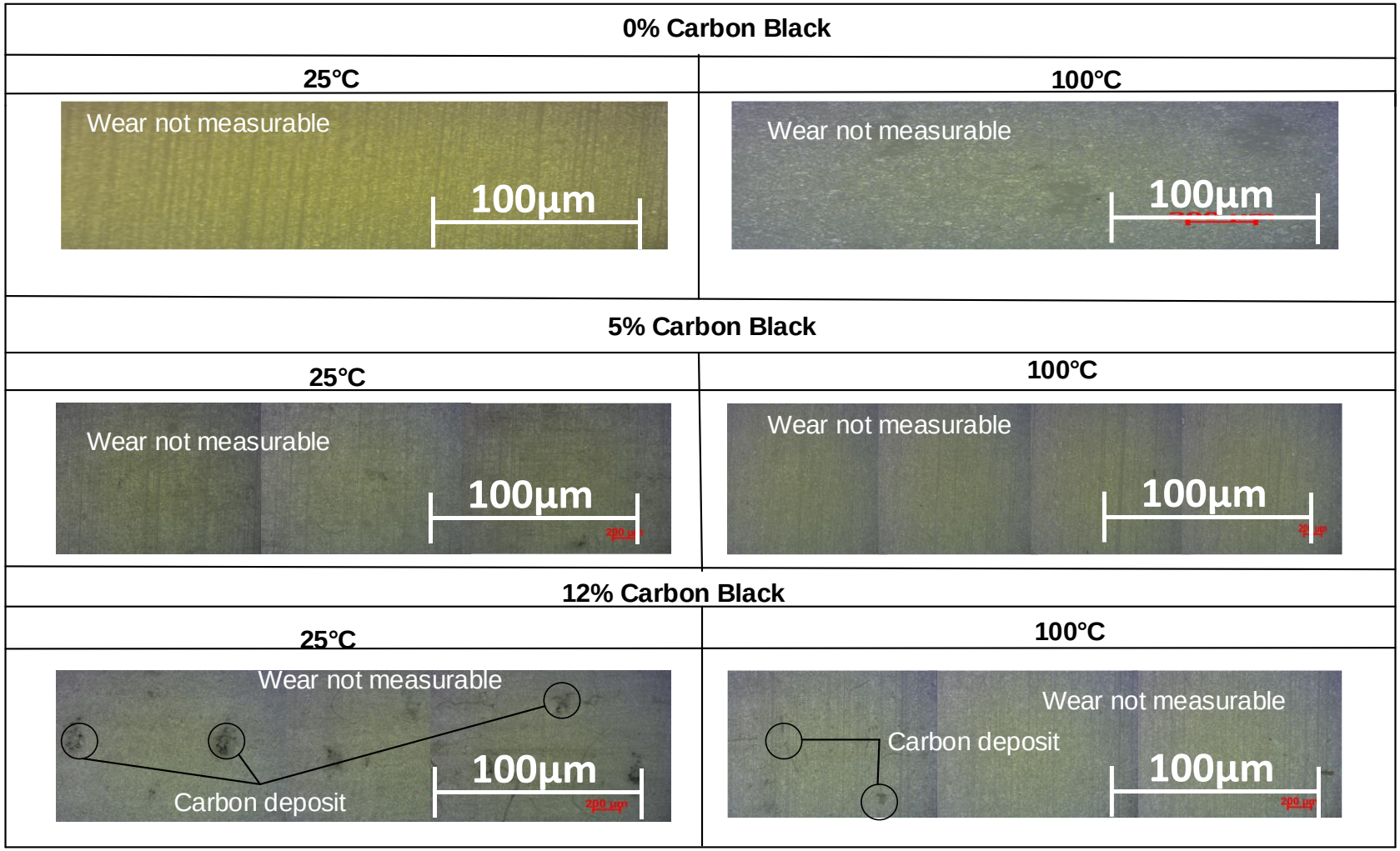

Figure 6.19 Images of Silicone wear scars for 0%, 5% and 12% Carbon Black at 25°C and 100°C

6.5 Discussion

6.5.1 Contact temperature

The contact temperature for elastomer materials is lower than for thermoplastic materials, even though the friction for the elastomer materials was higher than the thermoplastic materials. Due to the PV limit of the materials, the combination of high contact pressure and sliding velocity of the thermoplastic materials causes the surface temperature to increase. Polymers give high interface temperatures due to their low thermal conductivities. During sliding, the temperature generated is called the interface temperature which is a product of PV (pressure x velocity). By exceeding the PV limit, polymers will start to melt at moderate temperature and wear may increase [30], this can be seen from the results of PTFE where there are signs of material melting at high temperature and a high wear rate is obtained.

It also clearly shows that the contact temperature increases with carbon black content for all specimens. This is probably due to the fact that when sooty oil with carbon black content increases, it restricts the lubricant flow into contact therefore increasing the friction force between the rubbing surfaces and thus increasing the contact temperature of the contact area.

6.5.2 Contact pressure

The results obtained for the contact pressure clearly show that the contact pressure operates under soft elasto-hydrodynamic and high elasto-hydrodynamic regime related to the material properties where NBR and silicone are categorised as elastomer materials and PEEK and PTFE as thermoplastic materials. Soft elasto-hydrodynamic relates to low elastic materials such as rubber and the elastic properties predominate even at lower load. While hard elasto-hydrodynamic relates to high elastic modulus where the elastic and viscous effects are both important [75]. The area of contact influence the contact pressure, it is also known that the relationship between contact pressure and sliding speed also plays a role in defining the contact temperature for different polymers thus enhancing the ability to propose and predict the wear mechanisms that may occur in the test.

6.5.3 Coefficient of friction

The sliding friction results shows that the coefficient of friction varies with percentage of carbon black content. The difference was not that significant as the values for 5% carbon content and 12% carbon content were not that different. Overall, at higher

sooty levels, 12% carbon black contamination, the friction increases as expected. This is due to the sooty oil becoming thicker, higher in viscosity and size of the agglomerates are bigger thus restricting lubricant flow into the contact [2].

For elastomer materials, the coefficient of friction is higher than harder materials and it shows that the uncontaminated oil leads to higher friction than contaminated ones. Figure 6.20 shows that the specimens push the material during sliding thus restricting soot to enter, therefore the soot is able to abrade the surface of the material. But the material exhibits a loss of volume following the indentation force that is applied to the material and it deforms to a certain volume. Meanwhile for thermoplastic materials, PEEK and PTFE show low friction for both low temperature and high temperature. This is due to the in molecule construction that helps the molecules to stretch easily in the direction of the shear force thus making it less resistance to shear [84]. From the results in the test conducted, it can be concluded that the coefficient of friction effects (Figure 6.4) are dominated by lubricant and soot for thermoplastic materials while for elastomer materials it is dominated by the material properties.

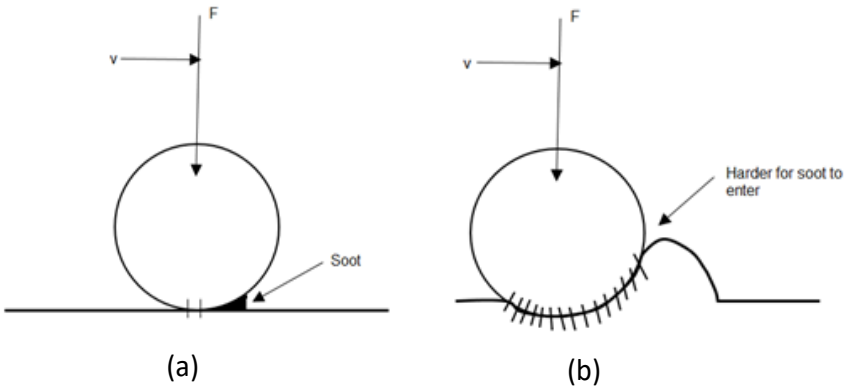

Figure 6.20 A schematic diagram of wear mechanism for softer material

6.5.4 Wear analysis

6.5.4.1 Wear scar volume

At different carbon black content levels at room temperature, the volume of wear scar increases. This is attributable to the lubricant film thickness and the amount of carbon black particles in the lubricant thus increasing the wear volume. The thermoplastic materials show the lowest wear volume due to their material properties where PEEK are categorised as hard material therefore the indentation depth of the sliding ball on the material is small.

As for high temperatures, PTFE shows a higher wear volume than silicone. This is probably because at high temperature, the temperature at the interface exceeds the PV limit thus PTFE softens and wear becomes larger [30]. Silicone, having the second

largest volume scar, is deformed due to hysteresis loss that is caused by the delayed recovery of the material after indention of harder material onto the rubber material. While NBR having the lowest volume wear followed by PEEK is probably because the indentation depth of the sliding ball is low due to its hardness and the ability to withstand higher temperature without melting.

6.5.4.2 Wear mechanisms

From the results outlined in the previous section, possible wear mechanisms can be proposed. The wear mechanisms are dependent on various factors including temperature (oil film thickness), carbon black content and the material properties. At lower temperature and zero content of carbon black, for all polymers, it is known that the wear is influenced by boundary lubricated metal-to-polymer contact due to lower wear. At higher temperature, for hard materials and zero content of carbon black, there are signs of mild abrasion for PEEK and PTFE, but with a larger volume scar for PTFE. At low and high temperature, silicone shows lower levels of wear for 5% carbon black content and it also shows marks of soot deposition on the silicone which is noticeable for 12% carbon black content at higher temperature. Silicone tends to adhere carbon black because of its surface topography. Silicone and NBR also shows signs of deformation and delayed recovery of the material after indentation of the ball during sliding.

PTFE shows signs of abrasion from carbon black particles penetrating into the film that produces scratch marks at 5% and 12% carbon black content. At higher temperature, PTFE shows more carbon black particles entrained at the beginning and end of the sliding wear scar, which may cause high level of abrasions and starvation due to particles blocking the contact region. It also shows a larger wear scar where the carbon might plough through the PTFE and destroy the transfer film from the counter face due to higher temperature [87].

While for PEEK, low levels of abrasion and adhesion wear [88] for 5% and 12% carbon black content is shown at both end of the specimens due to the scratching process that is caused by the hard asperities from the steel counter face and carbon black particles at low temperature. At 100°C, the wear scar images show a pronounced level of abrasion with respect to higher carbon black content. At 12% carbon black, the surfaces show signs of a high level of abrasion and polishing streaks due to possible starvation of lubricant from the contact. Through the film thickness calculations, it is demonstrated that formulated oil produces thicker oil films, giving a surface separation thus lower probability of wear of the polymers. But due to the combination of carbon black content in the lubricant where it agglomerates, it still can increase wear as it is bigger in size than the oil film thickness.

6.6 Summary

Experimental tests in order to see the effects of soot induced wear on non-ferrous material were conducted. The test replicated previous work using ferrous metals to study the fundamentals of soot wear with various carbon black content levels. From the results, it can be concluded that:

- The soot does influence the friction and wear properties of the flat polymer specimens, however, it does not have an effect on the friction. Different materials show different wear mechanisms relative to soot content and other parameters such as contact area and contact temperature. For harder materials, higher soot content accelerates its wear, where higher carbon black content restricts the lubricant flow thus increasing the friction force between the rubbing contacts resulting in material melting at higher contact temperatures. For elastomer materials, the wear is dominated by material properties where carbon black adheres on the surface of the specimen and deformation of the surface is high when the ball is sliding during the wear test.

- The friction and wear properties are dependent on load, applied temperature and also soot content levels for thermoplastic materials. While elastomer materials, material properties predominated. These valuable results help us to understand whether soot contents have implications for elastomer/thermoplastic seals in order to provide a fundamental basis to redesign them to aid in reducing wear.

- Wear volume here shows that at higher temperature and higher soot content material will be removed during sliding due to higher friction forces especially for thermoplastic materials with a low melting point. However, elastomer materials deform more and the delayed recovery of the deformation causes higher volume loss.

Chapter 7 Wear in Seals (Seal-on-flat reciprocating)

In order to fulfil an aim of this research, this chapter investigates how increasing soot level affects wear of valve train components especially for different types of materials on a non-conformal point contact. The test was conducted using a Cameron-Plint High Frequency Reciprocating Rig (TE77) in a lubricated medium at higher stroke (15mm) ball-on-flat contact condition; this was to reveal the behaviour of sooty-oil surrogate against an actual O-ring component in an engine. This study focused on the wear of O-rings from 4 different types of elastomers/polymers in a lubricated contact at different loads and temperatures.

7.1 Test equipment and specimens

The tests were performed using a Cameron-Plint High Frequency Reciprocating Rig (TE77) in a lubricated medium. The tester configuration has been explained in Chapter 4. For the specimens, a common O-ring that is used as a seal in an engine valve was chosen, from 4 different materials which were NBR, silicone VMQ, PTFE and PEEK. O-rings can be produced by using a number of techniques such as extrusion, injection moulding, compression moulding or machining. EN1561 Grey Cast Iron flat specimens with dimensions of 66mm x 25mm were used as the sliding counterface as shown in Figure 7.1.

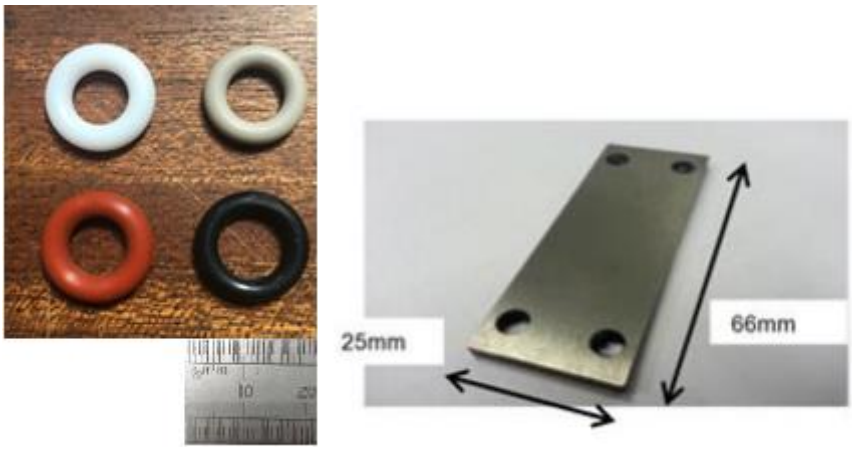

(a) (b)

Figure 7.1 Graphic view of the specimens (a) O-rings specimens (PTFE, PEEK, Slicone and NBR) (b) cast iron flat specimen

Figure 7.2 shows the schematic diagram of the O-rings sliding on flat specimen with the size of each O-rings were selected based on the size of the specimen holder of

the TE77 as shown in Figure 7.3. The dimensions and mechanical properties can be seen in Table 7.1.

Table 7.1 Mechanical properties of O-rings and flat specimens

Material	Cast-Iron	NBR	Silicone	PTFE	PEEK
Tensile Strength (MPa)	250	14	6.1	29.5	82.7
Young Modulus (GPa)	103	0.00102	0.05	3.075	4.2
Average Hardness (HV – Hardness Vickers) and Shore Hardness A	225 HV	76.1 (A)	95 (A)	6.1 HV	28.5 HV
Poisson's Ratio, υ	0.26	0.5	0.49	0.46	0.39
Dimension (mm)	66 x 25 x 4	8.5 ID x 3 CS	7.52 ID x 3.53 CS	7.52 ID x 3.53 CS	7.5 ID x 3 CS
*Source of information on above data were taken from respective supplier and compared with CES edupack	Steel Express, Wolverhampton, UK	Polymax	Polymax	Polymax	East Anglian Seals

*Sources of information on above data were taken from respective supplier

The O-ring specimen was fixed on a head that was specifically designed to fit with the existing tribometer (Plint TE77) as shown in Chapter 5. A block heating element was constructed below the bottom section of the oil bath to control the temperature of the test where the counterface specimen is located. Test load was manually applied through a lever.

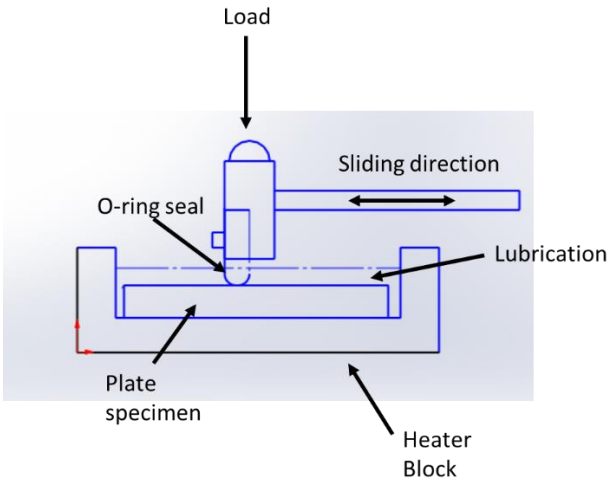

Figure 7.2 Schematic diagram for O-rings sliding on flat specimen

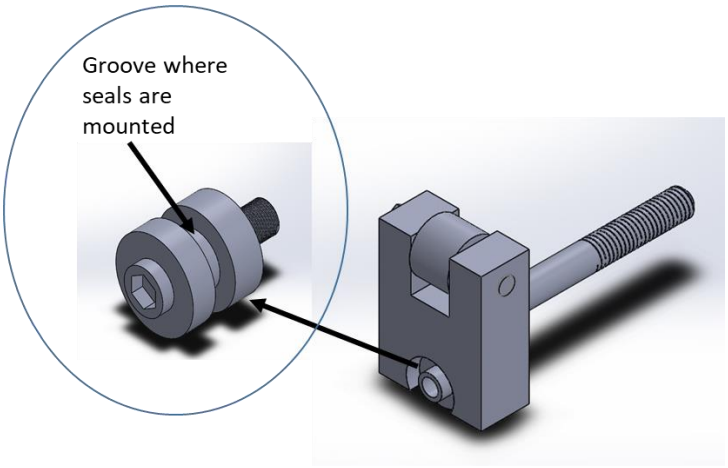

Figure 7.3 A specifically designed head to fix the O-rings to the tribometer

7.2 Calculation of contact parameters

7.2.1 Hertzian contact pressure

The initial contact pressure for O-rings sliding on flat steel specimens were estimated using equations 5.1 and 5.2. The contact pressures are shown in Table 7.2. The contact pressures for elastomer materials (NBR and Silicone) show lower values of hertzian pressure compared to thermoplastic materials (PEEK and PTFE) even at the same nominal speed and load, due to the varying material properties of each O-rings. The initial values of this contact pressures indicates that the contact operates under soft elasto-hydrodynamic for all materials where the maximum pressure lies between

0.5 to 4MPa for soft elasto-hydrodynamics lubrication [75]. However, these are only the initial contact pressure estimations. It is expected that the contact pressure will reduce with increase of contact area due to progressive wear.

Table 7.2 Contact Pressures for various material (O-rings) and nominal loads

Specimen Materials	**Nominal Load, P (N)**	**Mean Contact Pressure p_m (GPa)**	**Maximum Contact Pressure p_o (GPa)**
PEEK	30	0.0944	0.1416
NBR	30	0.0016	0.0024
PTFE	30	0.0233	0.0349
SILICONE	30	0.0049	0.0073

7.2.2 Film thickness

For the film thickness analysis, the procedure and equations are outlined in Chapter 6. The values for viscosity and density of the lubricant is are in Table 6.5 where all the data are assumed to be the same as measured in a previous study [69]. The predicted calculated minimum film thickness is presented in Table 7.3, the lubrication regime is determined from the mapping of the predicted film thickness on the regime map as presented in Figure 7.4.

Table 7.3 Minimum film thickness for O-rings specimens at 30N (Seal-on-flat wear test)

Specimen Material	**Sooty Oils**	**Minimum Film Thickness at 25°C (nm)**	**Minimum Film Thickness at 50°C (nm)**
NBR	0% CB	1681	756
	5% CB	1974	1617
	12% CB	5276	4818
Silicone	0% CB	843	379
	5% CB	991	812
	12% CB	2648	2418
PEEK	0% CB	44	20
	5% CB	52	42
	12% CB	138	126
PTFE	0% CB	52	23
	5% CB	61	50
	12% CB	162	148

From the results of expected film thickness, it can be seen that the film thickness increases with increased soot content in the lubricant. By comparing to the estimated size of soot particles which are between 0.2 µm and 0.5 µm, it is expected that the carbon black particles can abrade through the film thickness for both load and temperature of the thermoplastic materials (PEEK and PTFE). While the film thickness for elastomer materials (NBR and Silicone) show thicker films compared to the size of soot surrogates and thus might not be influenced by the wear of the specimens.

7.2.3 Lubrication regime map

By using equations from Hamrock & Dawson [76] (Equation 6.2); the value of the two non-dimensional variables gives an indication of the lubrication regime operational contact. All materials that have been mapped into the regime map show that they are expected to operate under a soft-isoviscous elastic lubrication regime often known as elastic-hydrodynamic lubrication (EHL) (Figure 7.4). The lubrication map regime conforms to the calculated predicted film thickness from four equations (6.3-6.6) where the thickest hydrodynamic film corresponds to the regime in which the contact will operate.

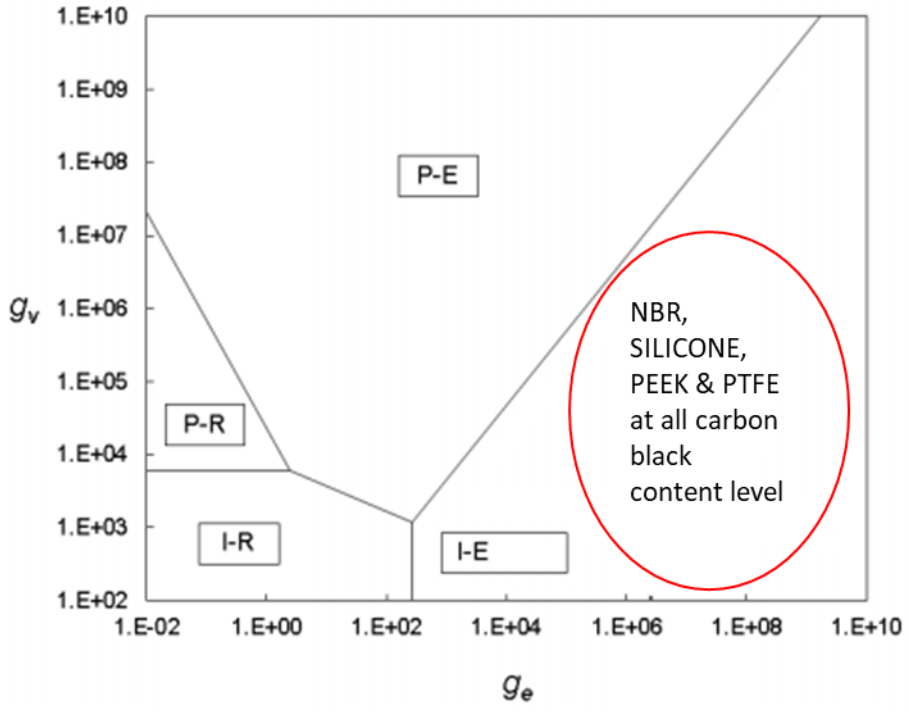

Figure 7.4 Hydrodynamic regime map for different materials with sooty oils at 30N, 25°C and 50°C adapted from [76][78]

7.3 Experimental procedures

The lubricant used in this test was similar to that used in Chapter 6 for the ball-on-flat configuration with 0% CB for uncontaminated oil and mixed with varying percentages (5 and 12%) of carbon black as a soot surrogate. Two temperature conditions were selected to simulate heat passing out through the valve guide respectively [89]. These test condition were chosen to approach the real environment of a valve guide interface O-rings seals and to investigate the effect of the sooty oil on elastomer/polymer specimens. The normal contact loads applied were chosen in order to achieve a contact pressure below 1MPa since it is the average contact pressure for seals and the sliding speed was selected to replicate the valve lift [75][90]. The duration for the sliding test was predetermined with several preliminary tests in order to generate wear on the surface of the O-rings. The test conditions for the sliding tests for all types of O-rings are shown in Table 7.4.

Table 7.4 General test conditions for O-rings

Parameter	**Test Conditions**		
Temperature [°C]	25	50	
Load [kN]	0.03		
Sliding velocity [m/s]	0.14		
Test Duration [min]	60		
Soot Concentration [%]	0	5	12

7.3.1 Friction coefficient measurement

The friction force of the oscillating contact is measured using the same method as described in Chapter 5 where the data is evaluated using Microsoft Excel Software and coefficient of friction can be estimated using Equation 5.1.

7.3.2 Wear analysis

A sequence of wear measurements before and after each test was conducted in examining the wear resulting from these tests by using Alicona 3D Profilometry and Scanning Electron Microscopy (SEM). In the wear analysis, the standard practice used to measure wear is gravimetric (mass loss) analysis. Nevertheless, the constraint in using this method is that the wear volume is very small for thermoplastic materials; and because of the effects of deformation on elastomer materials. Therefore, 3D surface profiling is used which is accurate and reliable, where data is generate for numerical analysis of the wear scar and scanning electron images were used to interpret the wear mechanisms for each O-rings. In order to measure the surface of the wear using Alicona and SEM, all O-ring were gold coated to provide a conductive layer to be able to measure the wear using an Emscope Gold Sputter (SC500).

7.3.2.1 Wear volume measurement method

A 3D confocal microscope (Alicona Infinite Focus SL) is used to measure the geometry wear scar of the O-rings since the weight loss of the specimen is insignificant to measured using a balance. The geometry of the wear scar was determined using Eq. (7.1), and the variables in this equation were acquired from the microscopy images as shown in Figure 7.5. Figure 7.6 shows an illustration of the wear volume quantifications of O-ring specimens that was used in determining the wear volume, where '*R*' is the curvature of the O-ring, '*r*' is the radius of the O-ring vertical cut section, and '*a*' is the radius of the elliptical wear surface [91].

$$V_{loss} = \frac{3\pi}{16}\frac{a^4}{R}\sqrt{\frac{r}{R}} \tag{7.1}$$

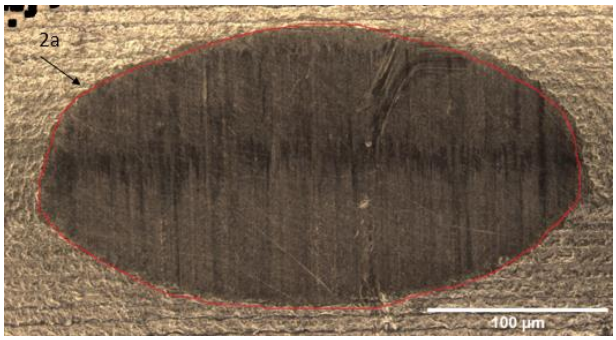

Figure 7.5 An example of micrograph acquired by confocal microscope used to estimate the elliptical wear scar semi-major diameter, '2a'

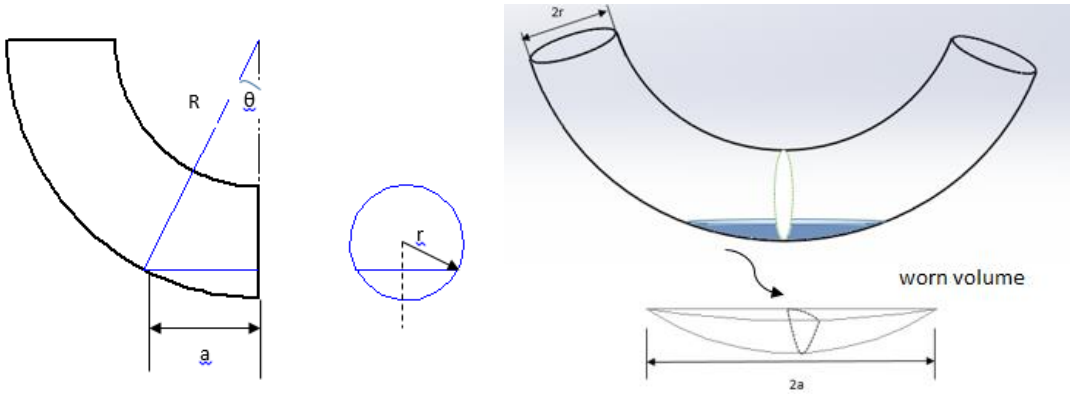

Figure 7.6 An illustration of wear volume quantification of O-ring specimens adapted from [92]

7.4 Experimental Results

7.4.1 Friction behaviour of O-rings as a function of soot concentration

The friction coefficient values for elastomer/thermoplastic O-rings sliding against cast-iron counterface ranged from 0.005 to 0.0065 for all soot concentrations at 30N as depicted in Figure 7.7 (a) and (b). These friction coefficient values were found to be lower than the friction coefficient values of metal-to-metal and steel ball on flat polymer sliding contacts. From these early results, it is apparent that the friction is pre-dominated by lubricant and material properties for elastomer/thermoplastic materials and does not change significantly with regards to temperature. All materials show that friction slightly increased with the presence of a higher percentage of soot concentration at room temperature and decreased slightly in friction at higher soot contents at high temperature.

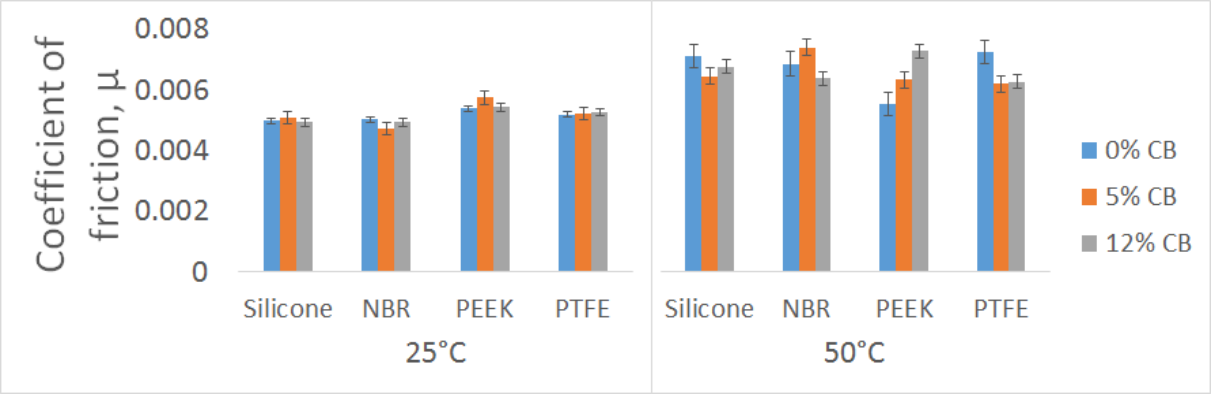

Figure 7.7 Friction coefficient of all O-rings with respect to temperature and soot content at 30N

7.4.2 Wear behaviour of O-rings as a function of soot concentration

The wear behaviour of the elastomer/thermoplastic O-ring varied significantly with regard to soot content; even though the friction coefficient values did not vary significantly with regard to soot content. After the friction test, it was found that a significant amount of wear was observed on the O-ring specimens using a table top scanning electron microscope (SEM, Hitachi TM3030) and no wear could be found on the counterface. This was expected as the hardness of cast-iron is much higher than the O-ring specimen. Figure 7.8 to Figure 7.11 shows SEM images of four different O-ring materials at different temperature and soot content. Debris, abrasion marks, cavities due to fatigue cracks, particles embedment were found on the O-ring surfaces. Adhesive wear is known to occur when an elastomer material slides against smooth and hard material [65][90].

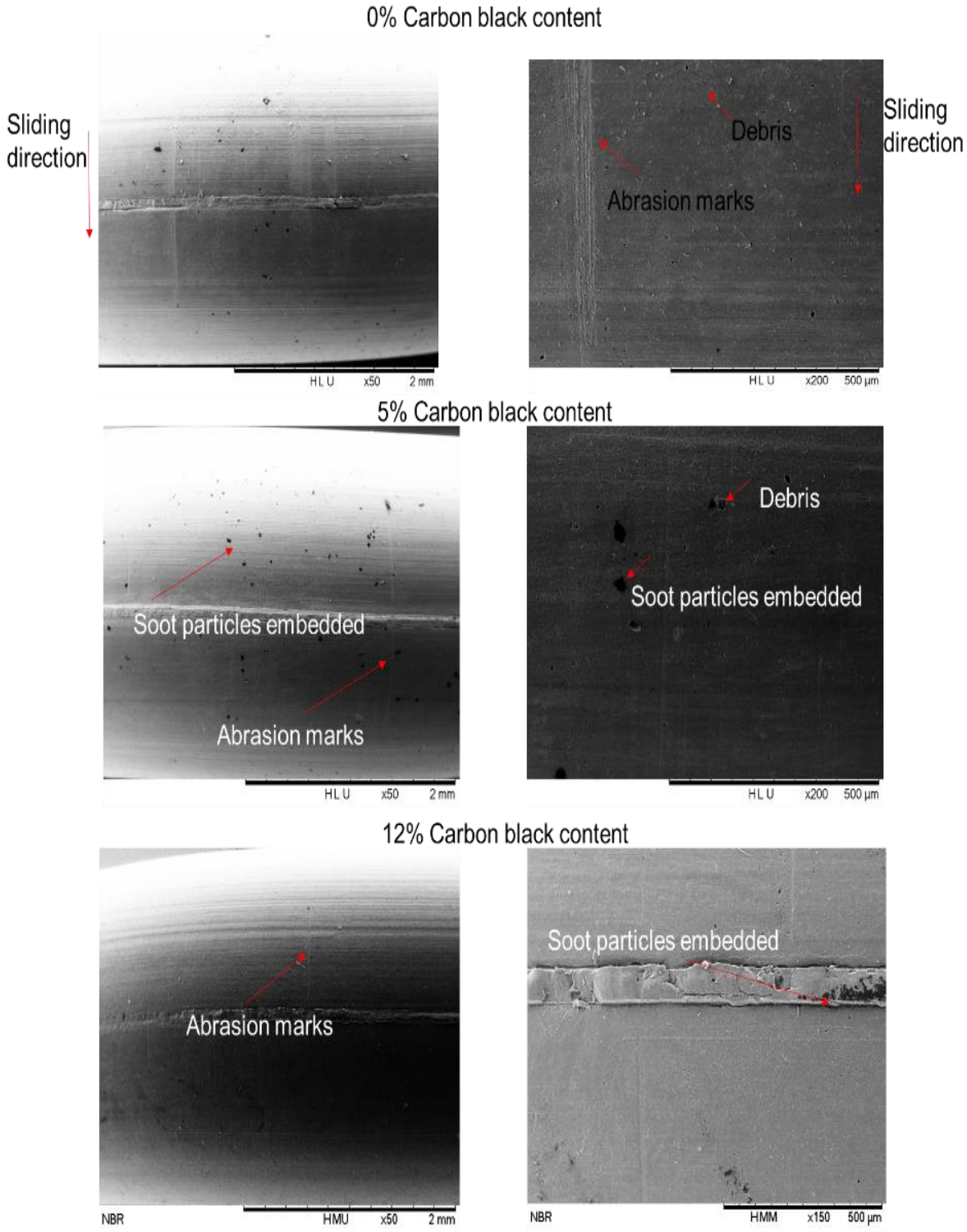
0% Carbon black content
Sliding direction
Debris
Abrasion marks
Sliding direction
HL U x50 2 mm
HL U x200 500 µm
5% Carbon black content
Soot particles embedded
Abrasion marks
Debris
Soot particles embedded
HL U x50 2 mm
HL U x200 500 µm
12% Carbon black content
Abrasion marks
Soot particles embedded
NBR HMU x50 2 mm
NBR HMM x150 500 µm

(a)

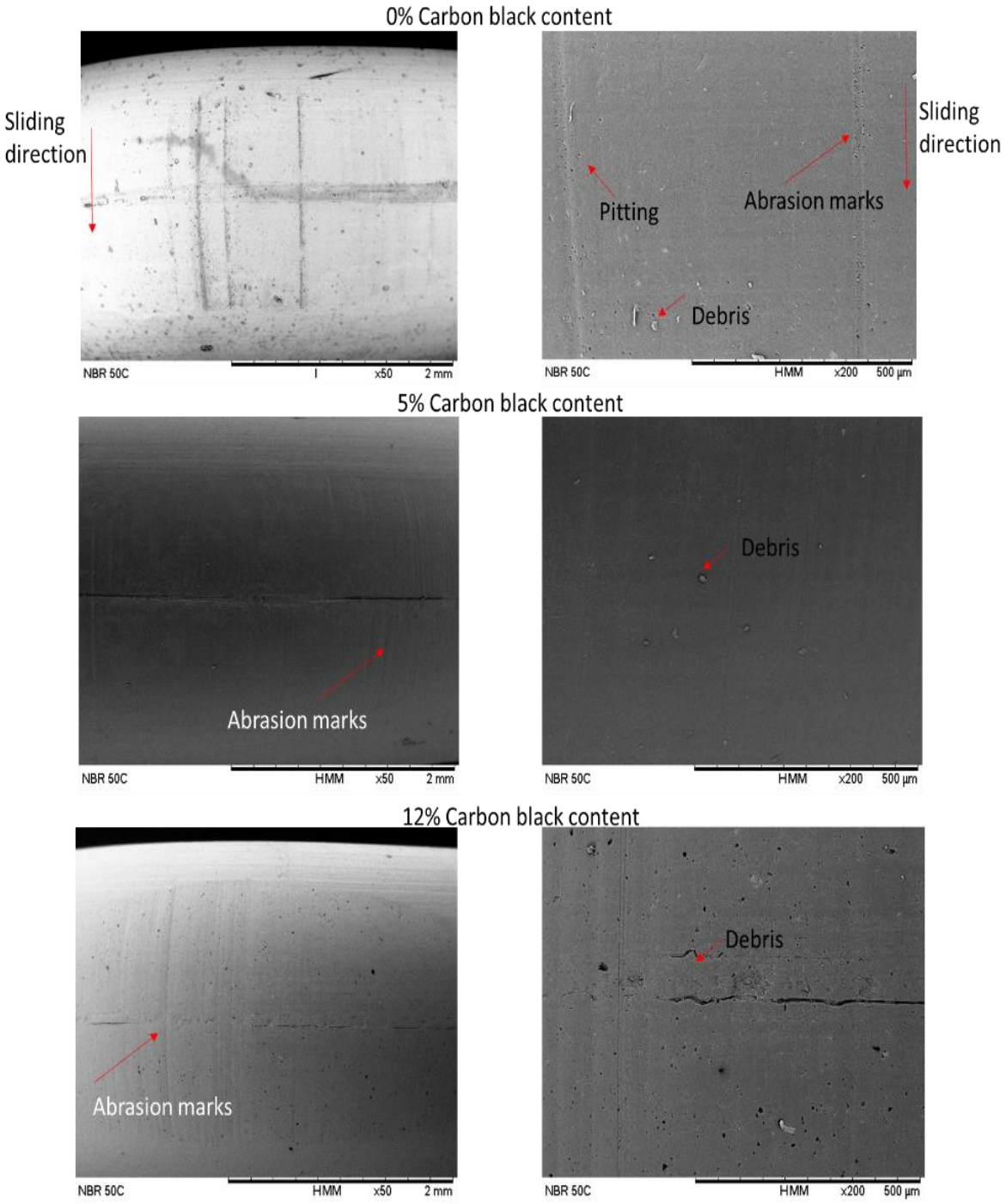

(b)

Figure 7.8 SEM images of wear surface of 0%CB (NBR O-rings) for (a) 25°C and (b) 50°C at 0.0024 GPa contact pressure

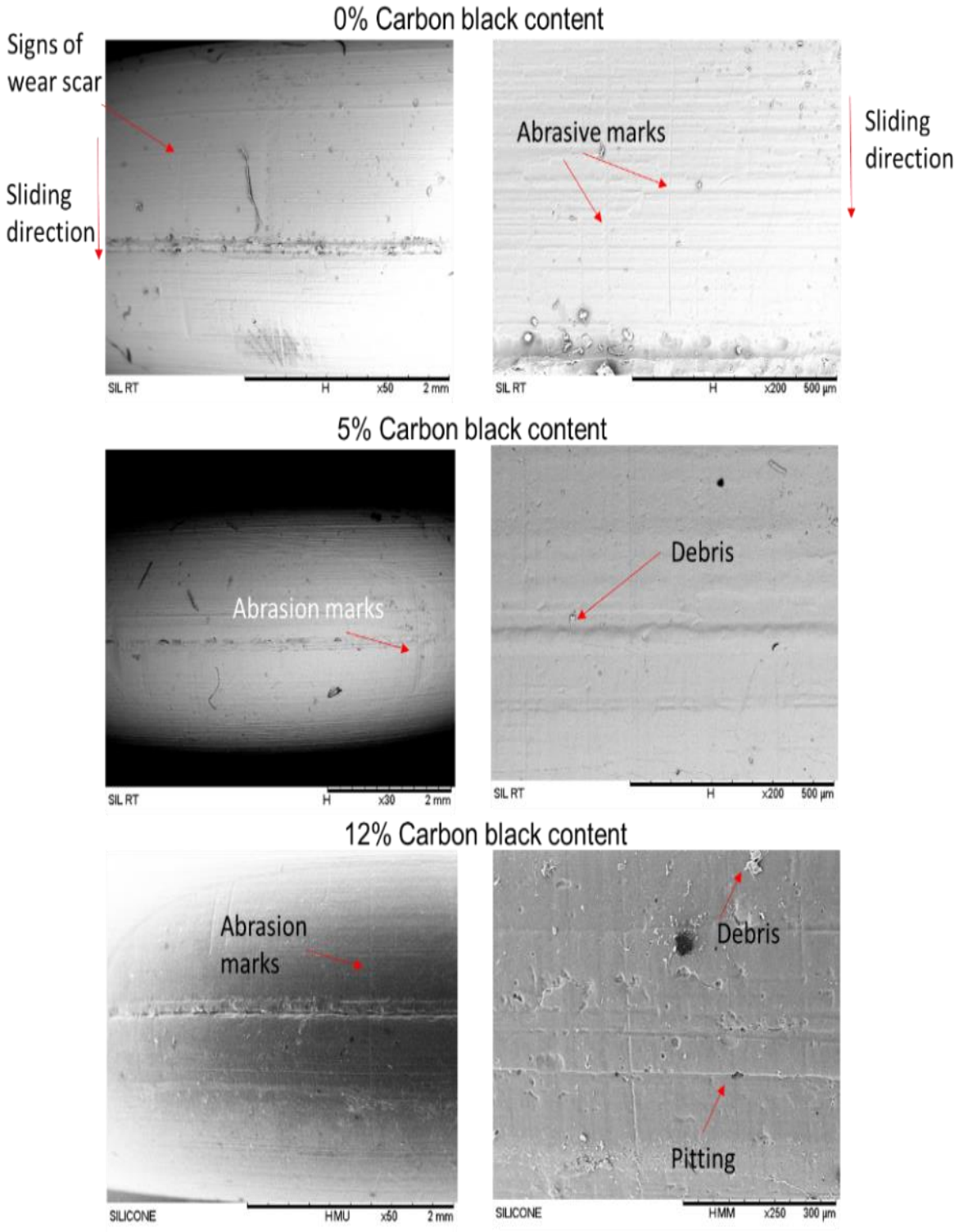
0% Carbon black content
Signs of wear scar
Sliding direction
Abrasive marks
Sliding direction
SIL RT H x50 2 mm
SIL RT H x200 500 µm
5% Carbon black content
Abrasion marks
Debris
SIL RT H x30 2 mm
SIL RT H x200 500 µm
12% Carbon black content
Abrasion marks
Debris
Pitting
SILICONE HMU x50 2 mm
SILICONE HMM x250 300 µm

(a)

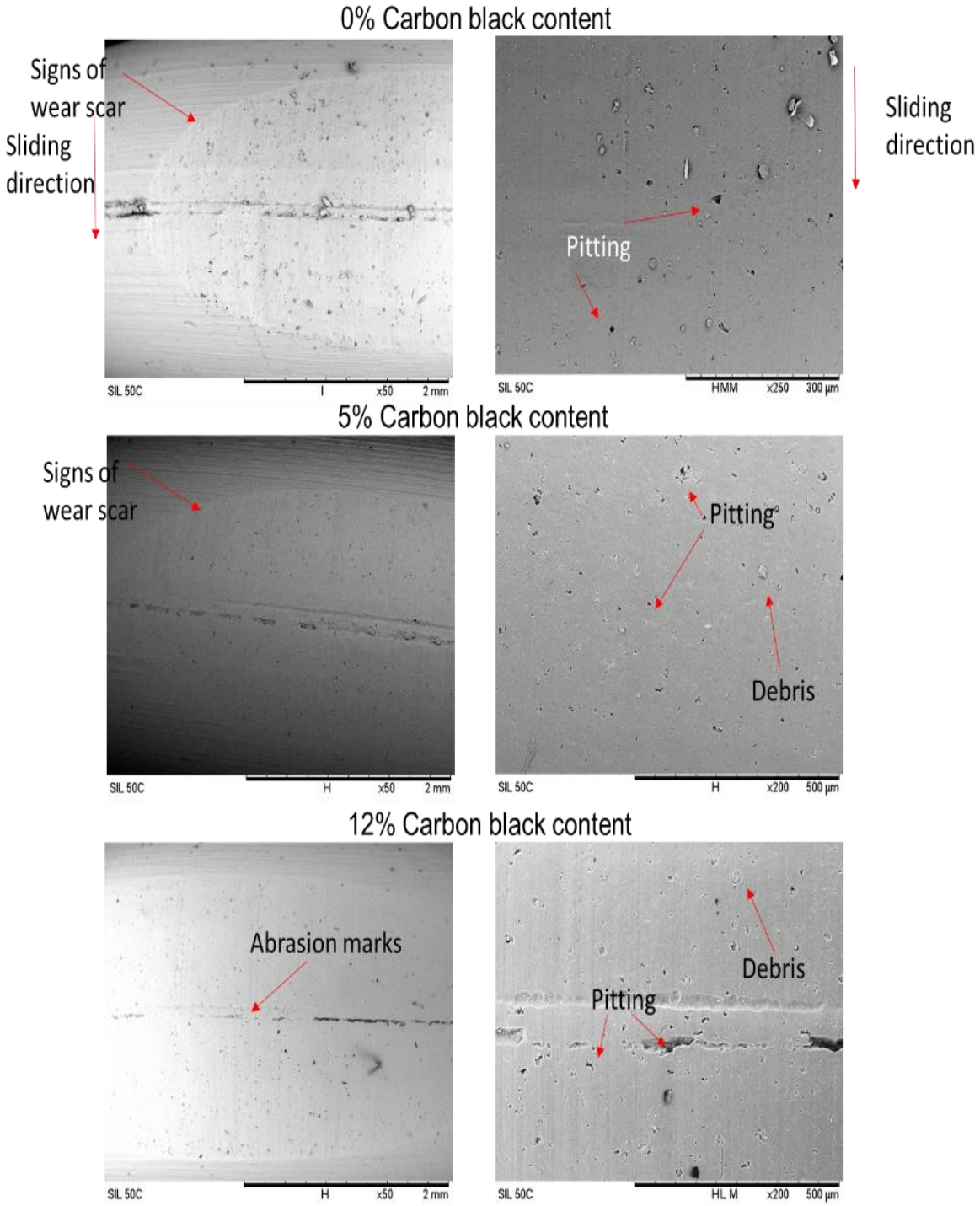

(b)

Figure 7.9 SEM images of wear surface of 0%CB (silicone O-rings) for (a) 25°C and (b) 50°C at 0.0073 GPa contact pressure

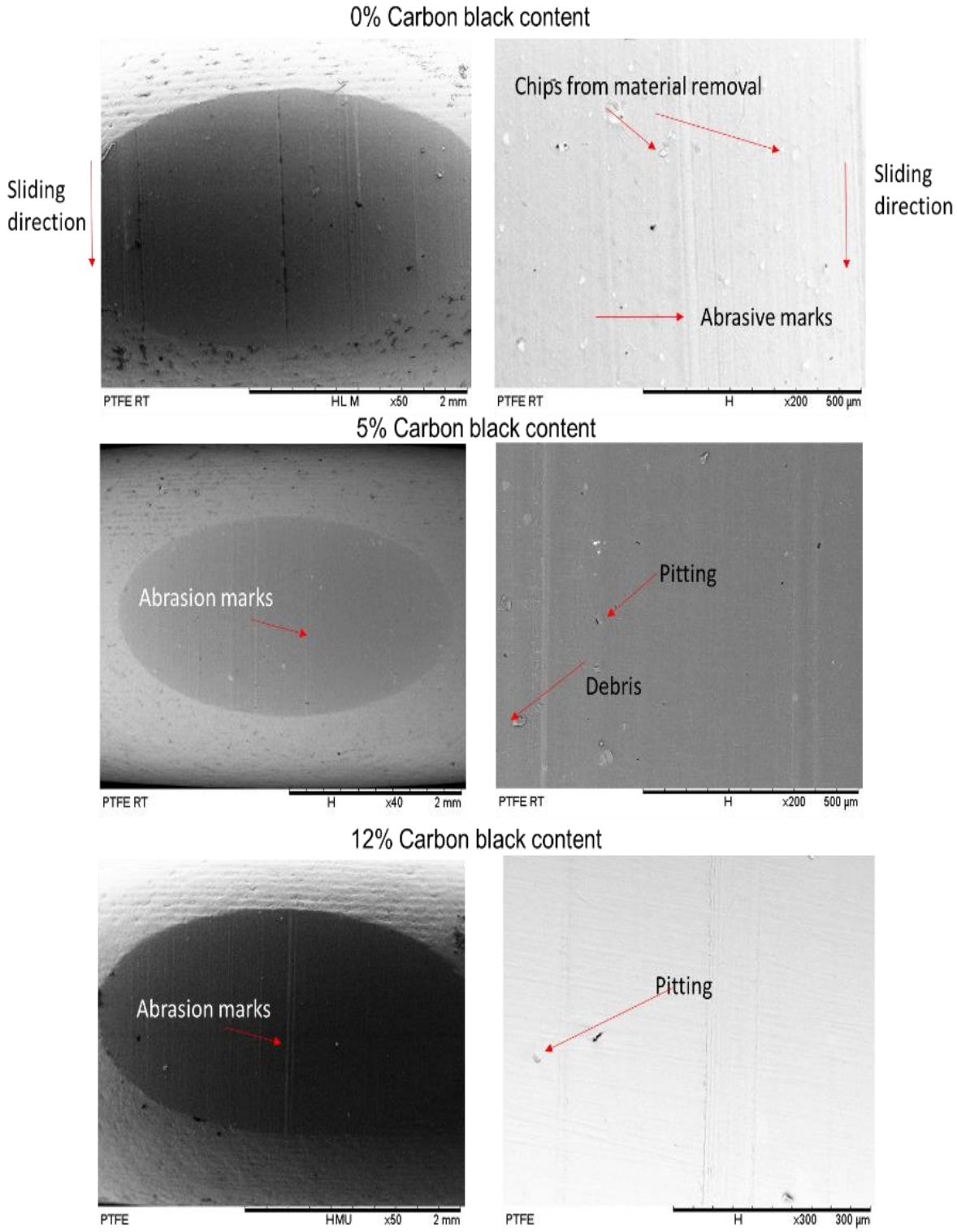
0% Carbon black content
Sliding direction
Chips from material removal
Sliding direction
Abrasive marks
PTFE RT HL M x50 2 mm
PTFE RT H x200 500 µm
5% Carbon black content
Abrasion marks
Pitting
Debris
PTFE RT H x40 2 mm
PTFE RT H x200 500 µm
12% Carbon black content
Abrasion marks
Pitting
PTFE HMU x50 2 mm
PTFE H x300 300 µm

(a)

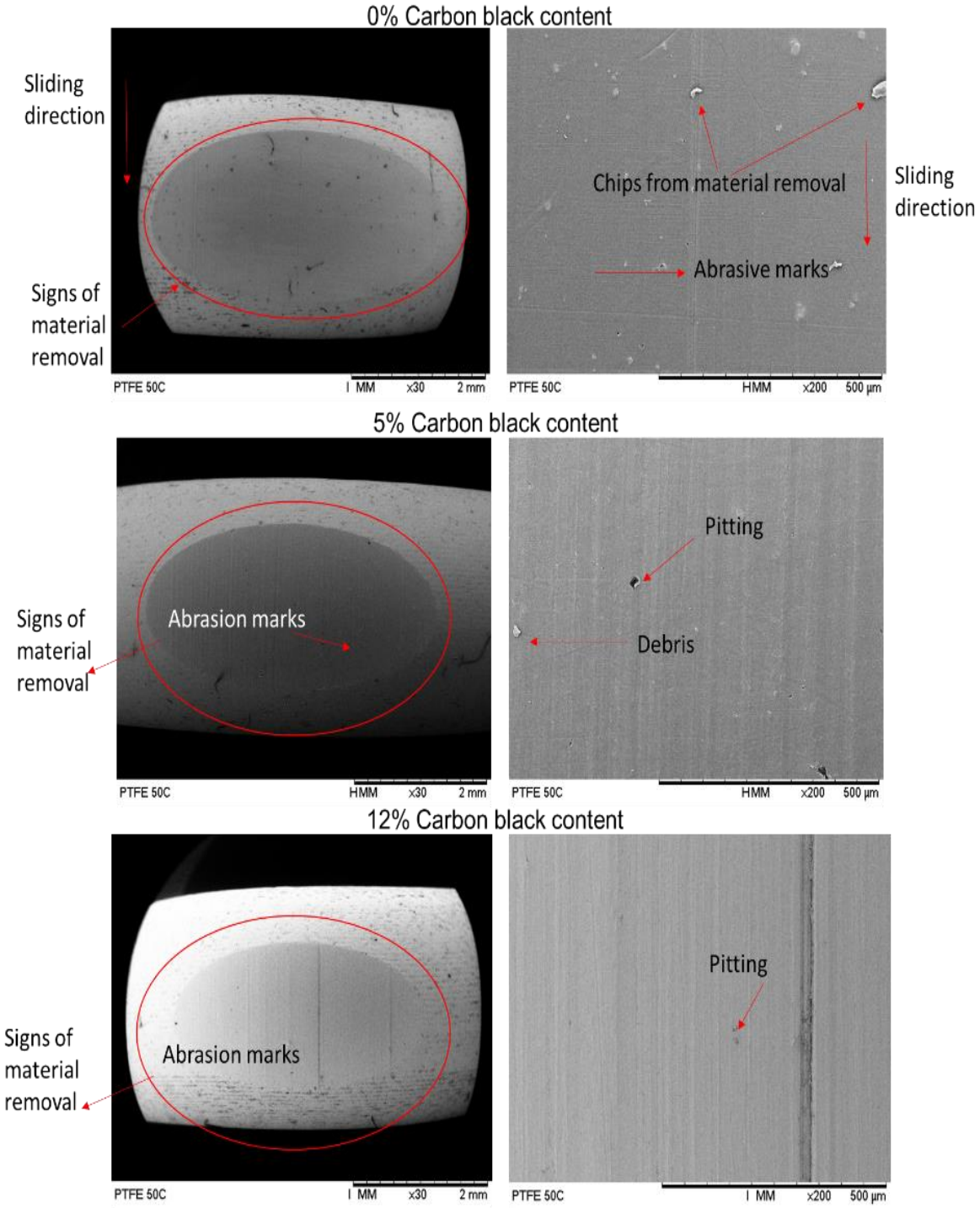

(b)

Figure 7.10 SEM images of wear surface of 0%CB (PTFE O-rings) for (a) 25°C and (b) 50°C at 0.0349 GPa contact pressure

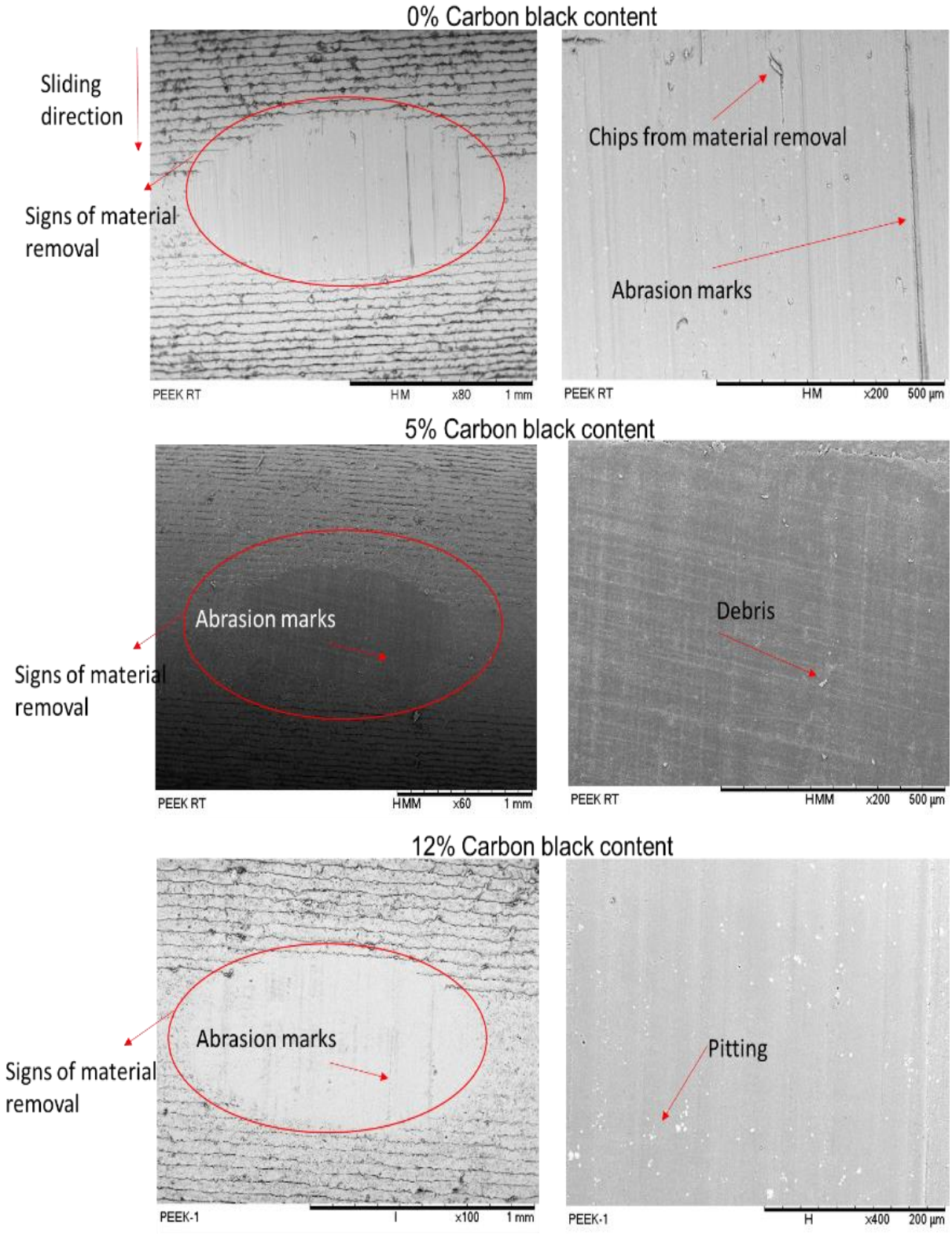
0% Carbon black content
Sliding direction
Signs of material removal
Chips from material removal
Abrasion marks
PEEK RT HM x80 1 mm
PEEK RT HM x200 500 µm
5% Carbon black content
Abrasion marks
Signs of material removal
Debris
PEEK RT HMM x60 1 mm
PEEK RT HMM x200 500 µm
12% Carbon black content
Abrasion marks
Signs of material removal
Pitting
PEEK-1 I x100 1 mm
PEEK-1 H x400 200 µm

(a)

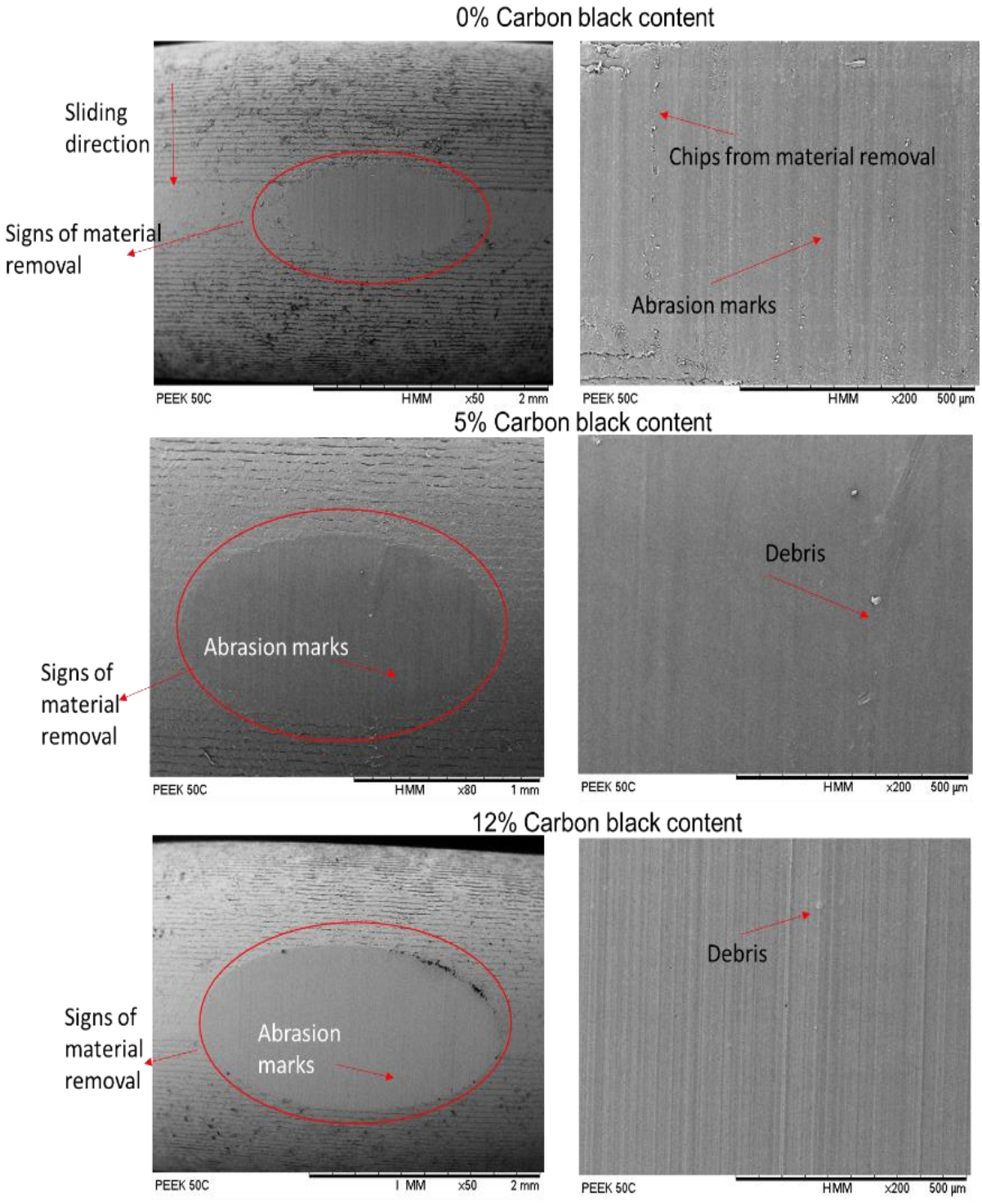

(b)

Figure 7.11 SEM images of wear surface of 0%CB (PEEK O-rings) for (a) 25°C and (b) 50°C at 0.1416 GPa contact pressure

7.4.3 Effects of load and temperature on the wear behaviour of O-rings

Load and temperature does play a significant role on the wear behaviour of the O-rings. Elastomer material showed a higher wear rate when temperature increased particularly for silicone. However, thermoplastic materials, particularly PEEK, exhibited lower wear rate than elastomer materials with respect to temperature and load increase. Elastomer materials wear rate is due to the deformation of the material itself with respect to load and temperature without any material removal occurring. This is because, elastomers which consist of polymer molecules have weak intermolecular forces with one another. When stress is applied, the molecules begins to untangle and when stress is removed, the molecules relax again and return to its coiled shape as shown in Figure 6.7 [85]. Moreover, due to its viscoelasticity behaviour the material tested is also generally insoluble and can swell in presence of lubricant. Therefore it can be said that the wear effects on elastomers are largely determined by the material properties.

However, for thermoplastic materials the wear rate is dominated by the material removal due to the frictional heating occurred at the interface. Theoretically, thermoplastics also behaves viscoelastic. When subjected to stress and increase temperature relatively to time, the polymer chains molecules which were arranged orderly (Figure 6.8) are positioned further apart where the chains can then disentangle more easily. In addition, when it reaches sufficient temperature *Tg*, the crystallinity results in softening and melts when it reaches melting point, *Tm*. From the results, it can be concluded that sliding friction does affect the wear behaviour where the heat generated during sliding causes material removal at the surface. For elastomer materials NBR/silicone, it also shows significant wear behaviour, however the wear scar shows deformation of the material itself due to hysteresis loss that is caused by delayed recovery of the material after sliding test.

7.4.4 Wear volume loss

The wear volume loss for elastomer/thermoplastic O-rings varied with regard to soot content and temperature effect. After the sliding test, it was found that a substantial amount of wear was found on the O-ring specimens using Alicona 3D profilometer analysis and minimal wear on the counterface could be found using microscope for elastomer materials. This was expected as the hardness of cast-iron is much higher than the O-ring specimen. Figure 7.12 shows the wear volume loss of four different O-ring materials at different temperature and soot content. Elastomer materials show high volume loss even though material loss is insignificant due to the material deforming back to its original condition. The volume loss shown here is by taking into account the wear scar measurement on the surface of the O-rings compared to thermoplastic material the wear scar does show sign of material removal thus the lower volume loss due to its material properties.

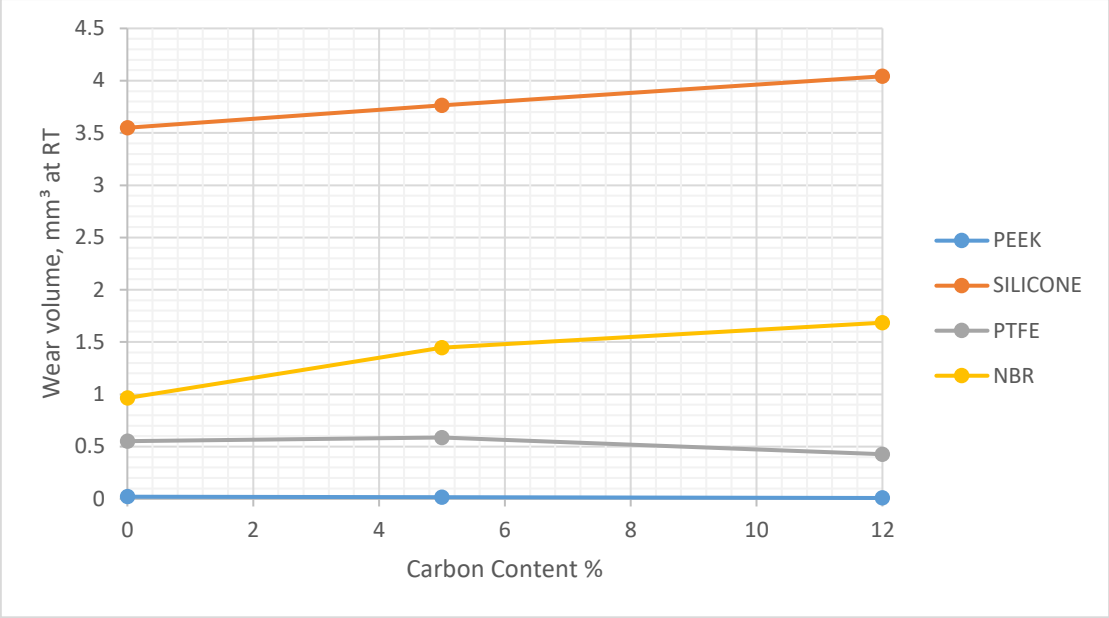

(a)

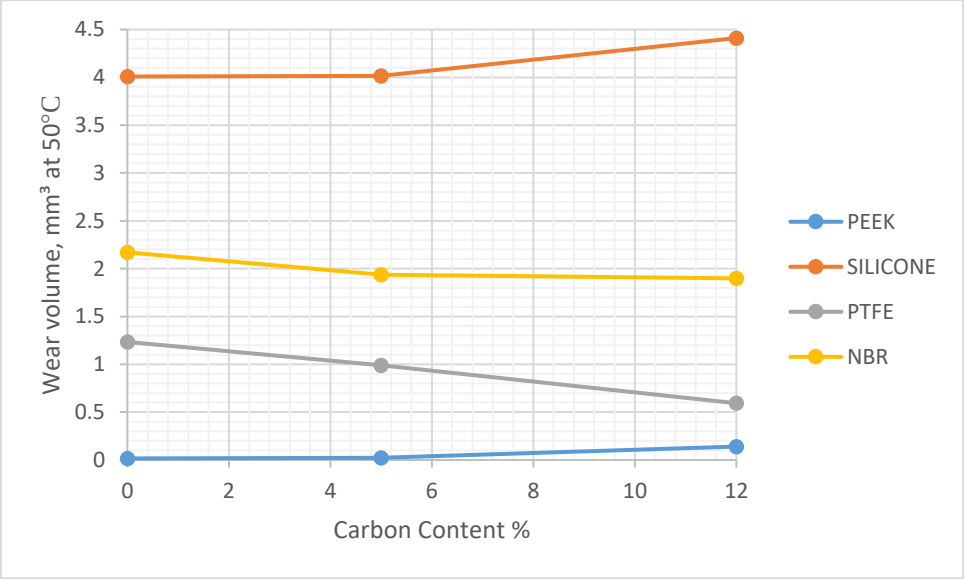

(b)

Figure 7.12 Wear volume loss for (a) 25°C and (b) 50°C at for all O-rings material

7.5 Discussion

7.5.1 Coefficient of friction

The sliding friction results show that the variation of coefficient with respect to temperature was not that significant as the values for 0-12% soot concentration were not that different. At higher soot concentration, 12% carbon content, the friction slightly increases as expected. This is due to the sooty oil becoming thicker at lower temperature, higher in viscosity and size of the agglomerates are bigger thus restricting lubricant flow into the contact. The increase in viscosity and predicted film thickness at lower temperature suggest that it is operating in an elasto-hydrodynamic lubrication regime thus increasing the friction because of visco-elastic response. The coefficient of friction is found to be low at higher temperature. This is because of the low viscosity of the lubricant at higher temperature thus lowering the friction. Due to the decrease in contact friction with respect to viscosity when at higher temperature, it is suggested that the sliding seals operate within the boundary lubrication regime.

7.5.2 Wear analysis

7.5.2.1 Wear mechanisms

From the results, possible wear mechanisms can be proposed. The wear mechanisms are dependent on various factors including temperature, carbon black content and the material properties. For thermoplastic materials experiencing material removal with respect to temperature, load and soot content, the volume wear is lower than for elastomer materials. However, these O-rings showed abrasion marks and debris due to the material removal as shown in the previous section (Figure 7.10). This could probably be because of the formation of carbon black clusters at increasing soot level concentrations thus restricting the lubricant to flow into the contact or blocking the lubricant into the contact region of the specimens. The profile of the thermoplastic O-rings in Figure 7.14 also shows the removal material after sliding test.

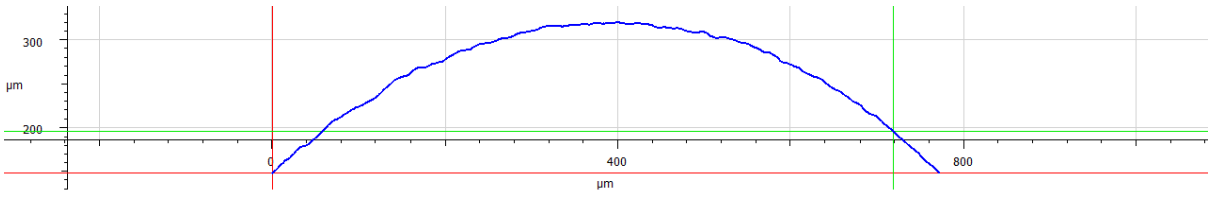

Figure 7.13 Profile of O-rings (PTFE) before reciprocating sliding wear

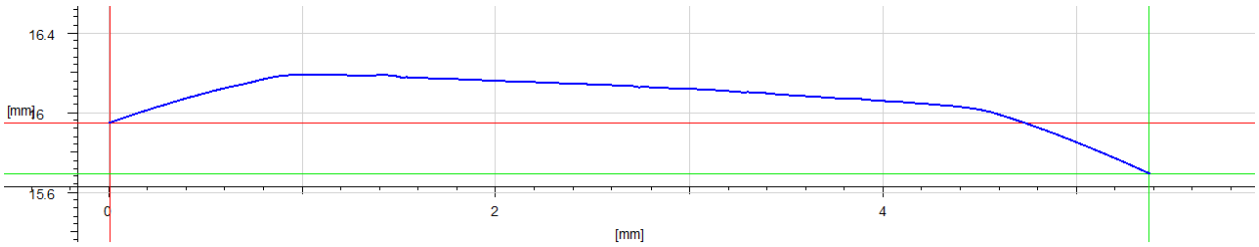

Figure 7.14 Wear profile for O-rings (PTFE) after reciprocating sliding wear

While for elastomer materials, the O-rings show signs of little to mild abrasion marks with respect to load, temperature and soot content. It also shows that particles are embedded on the surface of the O-rings and small cavities from fatigue crack occurred due to material properties of the material when subjected to cyclic loading during sliding against an elastomer material. Even though the wear volume is significantly higher than thermoplastic O-rings, it is not due to excessive material removal, but it is due to the deformation of the O-rings because of elastic deformation where they deform elastically when pressure applied and return back to its original shape and form. This is proven by the profile of the O-rings after a sliding test as shown in Figure 7.15.

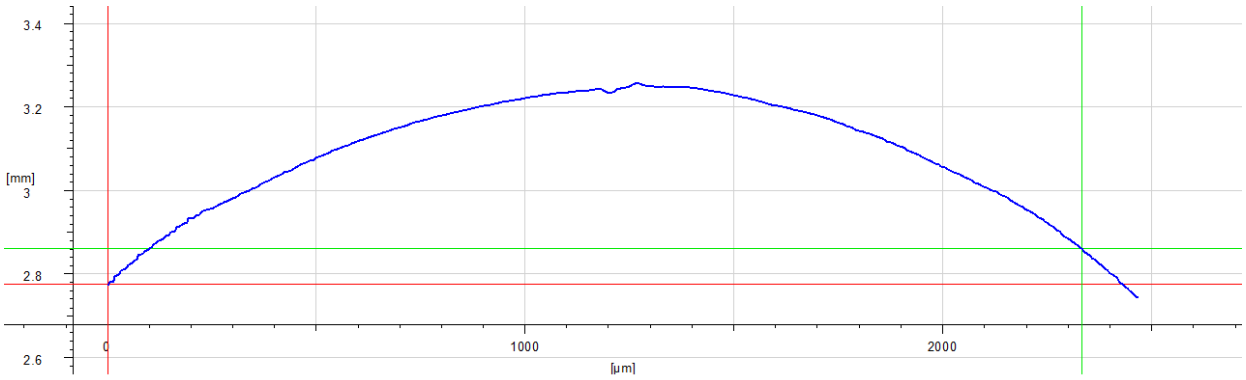

Figure 7.15 Wear profile for softer material (Silicone)

Figure 7.16 below shows the schematic diagram of the proposed wear mechanism for O-ring specimens. When harder O-rings slide in a lubricated environment, due to the load applied, the temperature of the lubricant and the soot content, the O-rings experienced high abrasive wear with signs of high material removal. Signs of high abrasive wear is due to the lubricant starvation that is caused by soot agglomerates preventing lubricant entering the contact area of the specimens. It is the same as for softer materials, but the wear mechanism is dominated by the material properties of the specimen whereby the O-rings experienced deformation with delayed recovery, little sign of abrasive wear, embedded particles on the surface and minor material removal (cavities) from fatigue crack when cyclic loaded during sliding against a harder material.

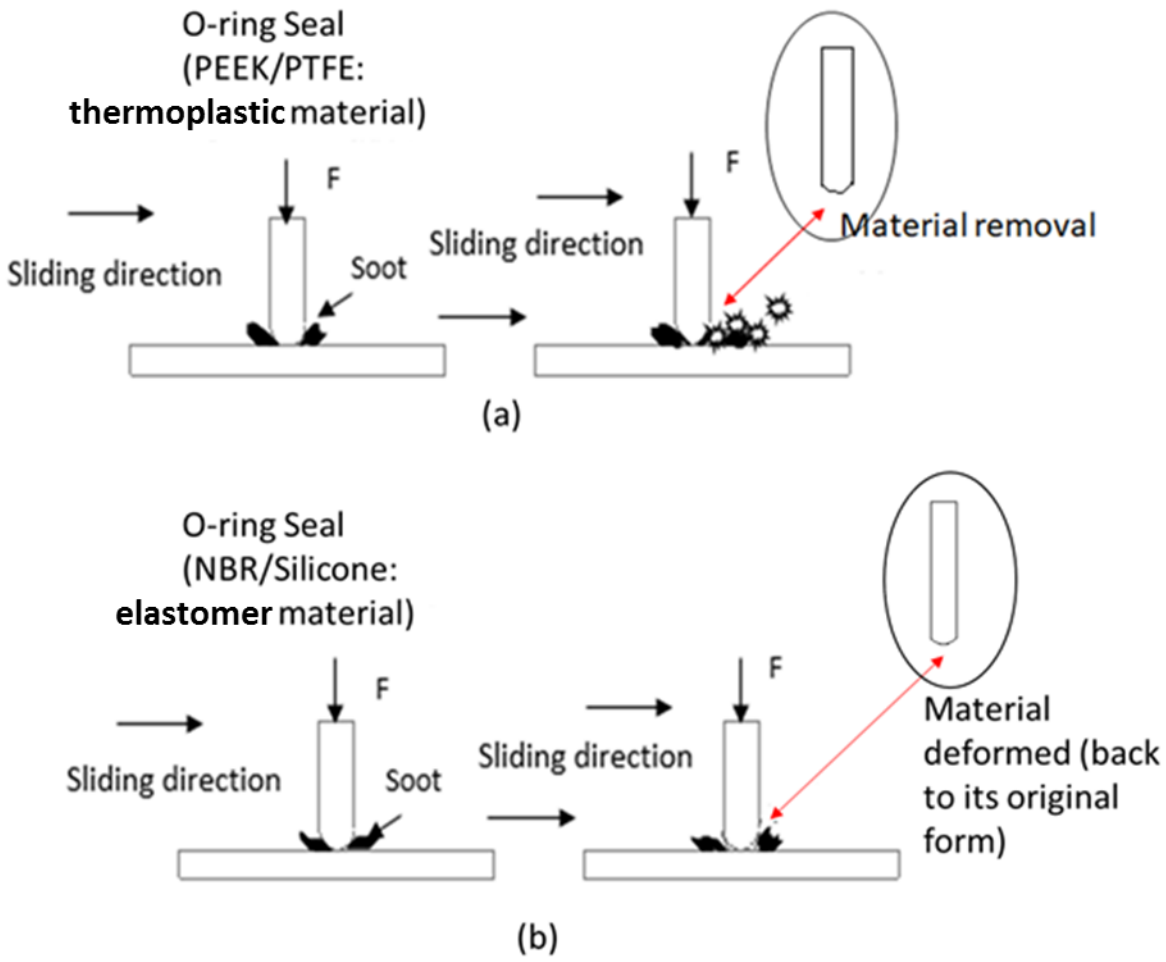

Figure 7.16 A schematic diagram of proposed wear mechanism for O-ring specimens

7.5.2.2 Final Contact Pressure

Due to the post wear scar which shows an elliptical shape (Figure 7.5), the final contact pressure were estimated using the equation below [86]. The contact became an ellipse when the bodies deformed after loading is applied.

$$P_{max} = \frac{F}{\pi ab} \tag{7.2}$$

where *F* is the force (*N*), *a* and *b* is the major and minor radius (*m*).

The final contact pressure was estimated using the elliptical wear scar dimensions. The results of this estimation in Figure 7.17 shows that the estimated contact pressure values reduced by an average of 6 times for both 20N and 30N normal load than the initial contact pressure as shown in Table 7.2.

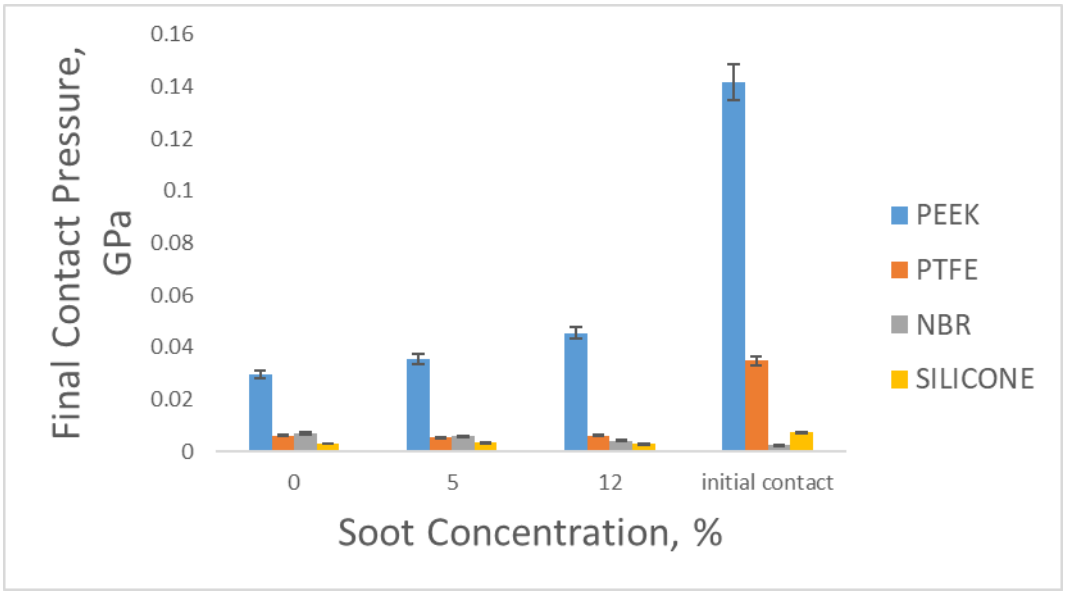

(a)

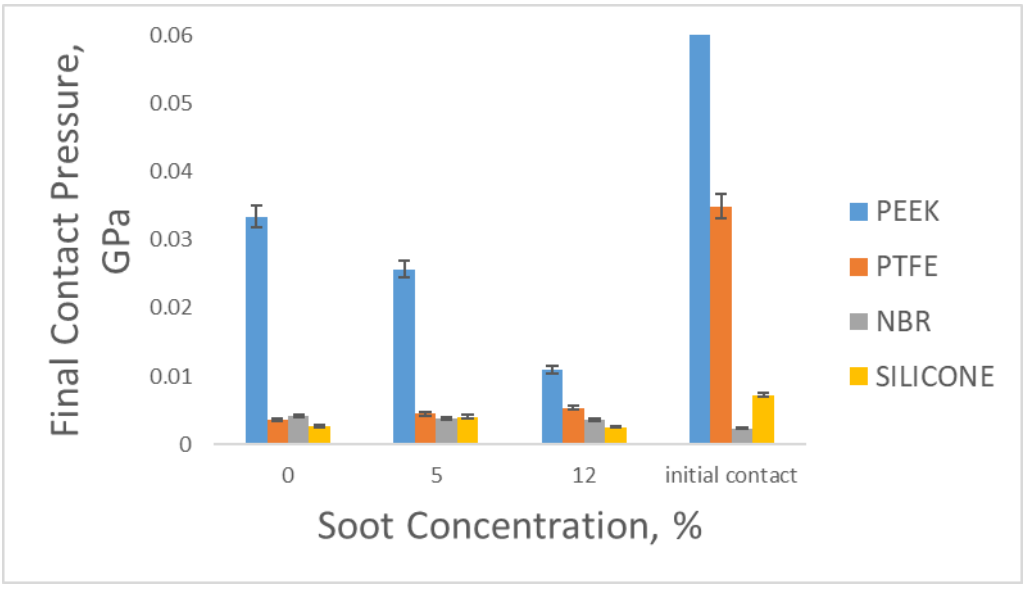

(b)

Figure 7.17 Final nominal contact pressure for different contact conditions (a) 30N at room temperature (b) 30N at 50°C

7.6 Summary

The experimental research summarized in this chapter examines the role of selected parameters on the friction and wear of four different O-ring seals against a harder material contact. More specifically, the experiments were designed to understand the effects of soot on elastomer/thermoplastic O-rings. From the results and discussion it can be concluded that:

- The soot greatly influenced the friction and wear properties of the O-rings, however, it had no significant effect on the friction. Different materials presented different wear mechanisms with soot content and other parameters. For thermoplastic materials, the increase in soot accelerated wear where it acted as a third body thus aggravating the surface wear of the materials with abrasive wear and material removal with respect to applied load and temperature. While for elastomer materials, the wear is dominated by material properties where it experienced deformation and small cavities formed through the embedded soot particles in the materials.

- Knowingly that the friction and wear properties were highly dependent on the parameters, such as load, applied temperature and soot content level, this work provides valuable results to understand the effects of soot on elastomer/polymer seals in helping to provide a fundamental basis to designing tool that can aid in reducing wear. This is seen when increasing soot content at high temperature for thermoplastic materials, the soot abrasively wears the surface of the material above the *Tg* value, whereas for elastomer materials even above the *Tg* value, the soot does not play a major role on the deformation of the material after sliding occur.

- Wear volume is over estimated for elastomer materials because of the elliptical wear area on the material as shown in Figure 7.8 and Figure 7.9 but looking at the profile there is no sign of material removal. Thus the volume calculation is over estimated. For thermoplastic materials, the volume loss is very small, but it does show volume loss by looking at the wear profile of the O-rings.

Chapter 8 Elastomer and Polymer Wear

A block-on-ring test was conducted using a Plint TE 99 BICERI Universal Wear Machine in a lubricated medium; this is to simulate tribological parameters (load, speed, temperature and geometry) as close as possible to valve stem tip sliding relatively to the guide in the intake valve. This is to reveal the behaviour of sooty-oil surrogate against an actual O-ring component in a non-conformal contact. Using a block-on-ring configuration, it is also expected that the volume of wear could be achieved as the O-ring rotates during sliding thus wear track could be determined to estimate the wear loss of the O-ring where from the previous test, the wear volume could not be determined as the wear are significantly small. This study is only focusing on the wear of an O-ring from four different types of elastomer/polymers in a lubricated contact at different temperature and different carbon black concentration.

8.1 Test equipment and specimens

The TE99 Universal Wear Machine (BICERI) Figure 8.1 (a), is a sliding type tribometer having a stationary block made of Aluminum 6082 forming a non-conformal elliptical contact with the O-ring seals (NBR, Silicone VMQ, PTFE and PEEK).

Figure 8.2 shows the modified ring with a groove to fit the O-ring seal. The rotational speed is manually controlled and set by measuring the ring rotational speed, normal load (W) on the block is applied via the hanger attached to the load frame and a block holder which can slide through the arm lever locates over the top face of the block to ensure alignment to the ring in a line contact as shown in Figure 8.1(b). An external oil bath is used to store and heat the lubricant to a pre-heated temperature. The heated lubricant is fed directly into the contact region and then allowed to drain into the oil bath for recirculation.

The size of each O-rings used for the BICERI test are selected based on the size of the specimen holder of the TE99 as shown in Figure 8.2. The O-rings specimen was fixed on the ring that was specifically designed to fit with the existing tribometer (Plint TE99). The dimension and mechanical properties for the block and O-rings can be seen in Table 8.1. The O-rings average surface roughness for each material before test is shown in Table 8.2 below.

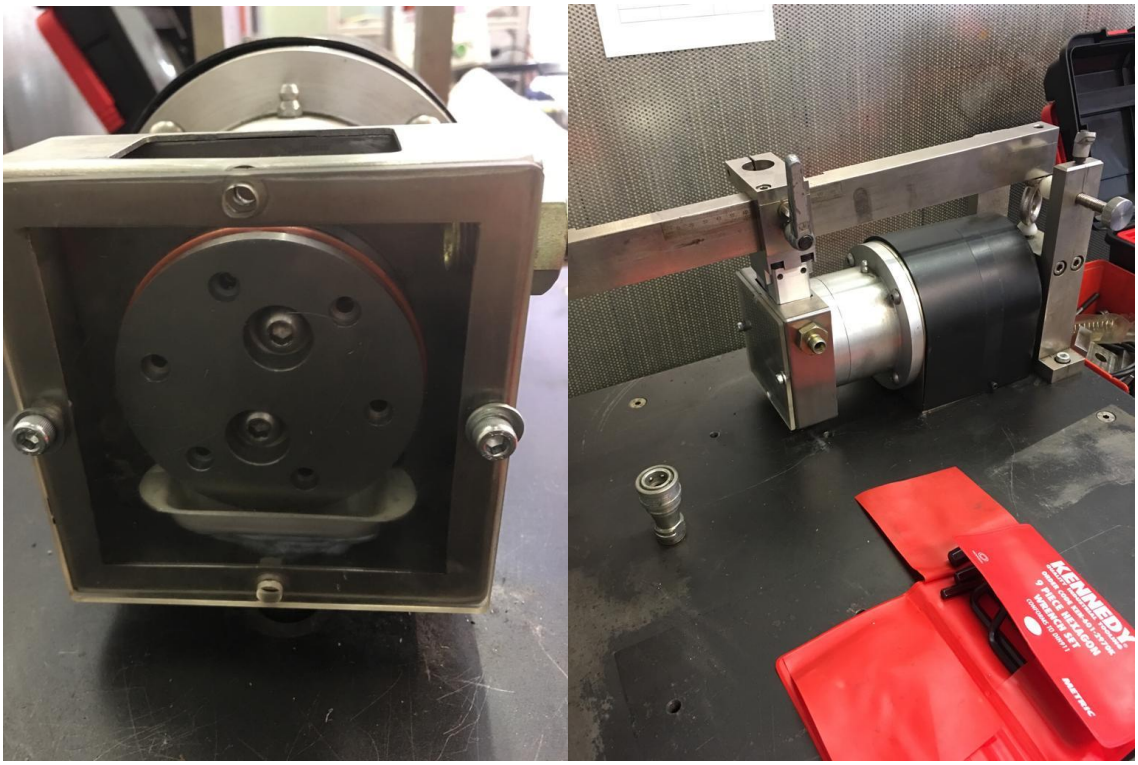

(a)

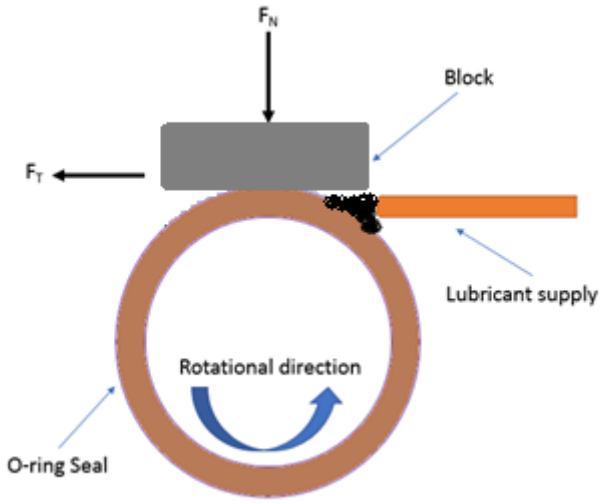

(b)

Figure 8.1 (a) Block-on-ring tribometer (b) Schematic Block-on-ring configuration

Table 8.1 Mechanical properties of O-rings and flat specimens

	Block specimen	**Non-ferrous material (O-ring)**			
Material	**Alloy 6082T6**	**NBR**	**silicone**	**PTFE**	**PEEK**
Tensile Strength (MPa)	340	14	6.1	29.5	82.7
Young Modulus, GPa	70	0.00102	0.05	3.075	4.2
Average Hardness (HV – Hardness Vickers) and Shore Hardness A	225 HV	76.1 (A)	95 (A)	6.1 HV	28.5 HV
Poisson's Ratio, υ	0.33	0.5	0.49	0.46	0.39
Dimension (mm)	(10.15x15.7x6.35)	71 ID x 2.5 CS	71 ID x 2.5 CS	71.12 ID x 2.62 CS	71 ID x 2.5 CS
*Source of information on above data were taken from respective supplier and compared with CES edupack	aalco.co.uk	Polymax	Polymax	Polymax	M Barnwell Services

Table 8.2 O-rings average surface roughness before test

O-rings	**Average Surface Roughness, µm**
NBR	1.31
silicone	1.26
PEEK	0.82
PTFE	1.61

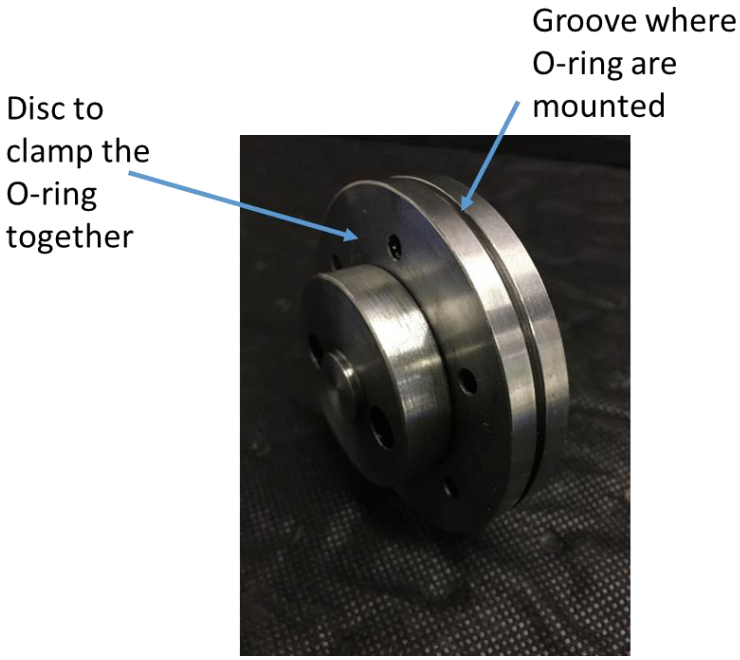

Figure 8.2 A specifically designed ring to fixed the O-rings to the tribometer

8.2 Calculation of contact parameters

8.2.1 Hertzian contact pressure

The initial contact pressures for BICERI test are shown in Table 8.3. The contact configuration for block-on-ring is assume to take the shape of an elliptical form after the sliding test. The contact pressure values shown are different due to the varying material properties even though the nominal load is the same throughout all tests. All contact operates under soft-elastohydrodynamic lubrication for all materials (NBR, silicone, PEEK and PTFE) [75]. The initial contact pressures estimation is expected to reduce when contact area increases due to progressive wear. The maximum initial contact pressure, p_0 can be determined by using Hertz's contact formulae (Equation 5.2) which is assume to follow the Hertz theory of a point contact.

Table 8.3 Contact pressure for various materials at 20N

Specimen Materials	Nominal Load, P (N)	Maximum Contact Pressure P_o (MPa)
PEEK	20	38.3
PTFE	20	33.2
NBR	20	0.17
silicone	20	0.49

8.2.2 Film thickness

In order to determine the tribological behaviour for a lubricated non-conformal contact, the oil film thickness of the sooty oil surrogates is determined for all elastomer/polymer materials. The film thickness for the non-conformal contact follows the equation for soft materials (Equations 5.3 till 5.7). The values of viscosity and density is taken from Table 6.5 as it was assumed that the values of the lubricant were the same as measured for a previous study [69]. The calculated minimum film thickness' are presented in Table 8.4 and the lubrication regime is determined from the mapping of the predicted film thickness on the regime map as shown Figure 8.14. From the table, it can be seen that the film thickness increases with carbon black content.

Table 8.4 Minimum film thickness for O-ring specimens (Block-on-ring wear test)

Specimen Material	Sooty Oils	Minimum Film Thickness at 25°C (μm)	Minimum Film Thickness at 100°C (μm)
NBR	0% CB	0.417	0.039
	5% CB	0.489	0.169
	12% CB	1.309	0.599
silicone	0% CB	0.209	0.019
	5% CB	0.246	0.084
	12% CB	0.657	0.299
PEEK	0% CB	0.012	0.002
	5% CB	0.014	0.008
	12% CB	0.037	0.029
PTFE	0% CB	0.013	0.002
	5% CB	0.016	0.009
	12% CB	0.042	0.033

8.3 Experimental procedures

The test conditions for all types of O-rings are shown in Table 8.5. They were selected in order to achieve measurable wear scars on all samples. These test conditions were used for non-conformal contact. The sliding speed was kept constant at 3.18m/s to replicate valve stem tip sliding relatively to the guide in the intake valve. A load of 2kg was used to simulate contact pressure for soft material in the range of 1MPa. The initial and post-contact pressures after test were estimated using Hertz theory for elastic elliptical contacts. The lubricant used was similar to that used in Chapter 5 and 6 with 0% CB for uncontaminated lubricant and 5% and 12% of carbon black mixture with engine oil and the temperature of 25°C and 100°C was selected in order to simulate a realistic operating temperature for O-rings on the valve guide.

Table 8.5 General BICERI test conditions for O-rings

Parameter	**Test Conditions**		
Temperature [°C]	25	100	
Load [N]	20		
Sliding velocity [m/s]	3.18		
Test Duration [min]	60		
Soot Concentration [%]	0	5	12

8.3.1 Wear analysis

Because of the unquantified mass loss analysis of the O-rings, a sequence of wear measurements before and after each test was carried out using Alicona 3D Profilometry and Scanning Electron Microscopy (SEM) where data is generated for numerical analysis of the wear scar and scanning electron images were used to interpret the wear mechanisms for each O-rings. Before profiling and SEM images is taken, all O-rings were gold coated to provide a conductive layer for better images.

8.4 Experimental results

8.4.1 Final contact pressure

The final Hertzian contact pressures (maximum) were theoretically calculated for a load 20N for all O-rings equations 8.1 and 8.2 for block-on-ring configuration [93] and presented in Table 8.6.

The maximum contact pressure, p_0 can be determined by using Hertz's contact formulae for block-on-ring configuration in Equation 8.2;

$$P_o = \frac{2W}{\pi L b} \tag{8.1}$$

where, *W* is the contact load in *N*, *L* is the contact length in *m* and *b* is the half contact width in *m*

The half-contact width *b,* is,

$$b = \sqrt{\frac{2PR}{\pi E^*}} \tag{8.2}$$

where, *E'* is the elastic modulus in *Pa, R* is the contact radius in *m* and *P* is the contact load in *N*

Table 8.6 Post-test Hertzian contact pressures (MPa)

Specimen Materials	**Nominal Load, P (N)**	**Maximum Contact Pressure p_o (MPa)**
PEEK	20	0.78
PTFE	20	0.70
NBR	20	0.013
silicone	20	0.030

From the final contact pressure, it is known that the contact operates under soft-elasto hydrodynamics lubrication. This confirms to the theory where for isoviscous elastic contact pressure value is 1MPa. The contact pressure is dependent on the area of contact, thus intensify the ability to propose and predict the wear mechanisms of the soot induced wear on these materials.

8.4.2 Wear scar roughness profiles

To determine the different soot concentration effect on the roughness, post-test roughness of the wear scars on the O-rings was measured using a 3D Alicona profilometer. This was done by scanning the wear scar using the Alicona and measuring the roughness longitudinally in the direction of the sliding operation. The results obtained for various carbon black contents at room temperature, 25°C and high temperature 100°C are presented in Figure 8.3. The values for all roughness test are

lower than the pre-roughness of all materials. The post-test surface roughness shows that the roughness decreases as soot content increases at low temperature for all material and vice versa when the temperature increases. The increase in roughness when at high temperature is probably due to the increase in friction resulting from adhesion where contact area increases and contact between the material and carbon black asperities indicates severe contact. This can be seen from the smooth surfaces of the materials which shows high wear with polishing effects, especially with PEEK, and thus lower roughness.

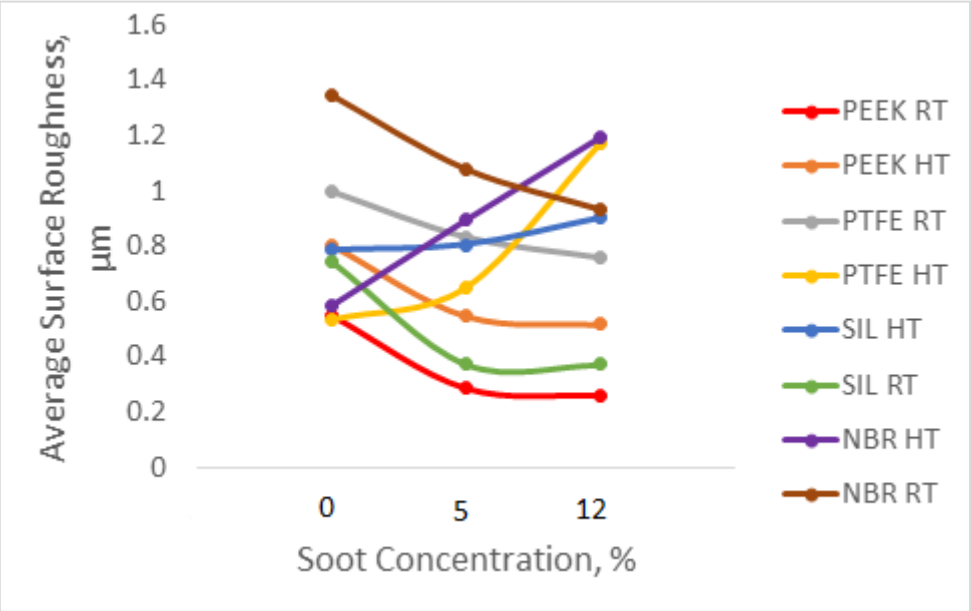

Figure 8.3 Post-test surface roughness at 25°C (RT) and 100°C (HT)

8.4.3 Wear scar profiles

The wear scar profiles were measured using a 3D confocal microscope (Alicona Infinite Focus SL) by measuring the geometry of the wear scar since the volume loss is insignificant to measured using analytical balance. Figure 8.4 shows the 2-D Image of the wear profile on the O-rings for silicone. It shows that the profile before and after does not change. It could be that the silicone deforms back after the test thus the profile remains unchanged. Figure 8.5 shows the 2-D Image of the wear profile for harder materials (PEEK), and it shows that the O-rings exhibit a small amount of material removal compared to before test were done. The profile results are similar to softer material NBR and harder material PTFE, where the softer material shows an unchanged profile and the latter shows a small amount of material removal.

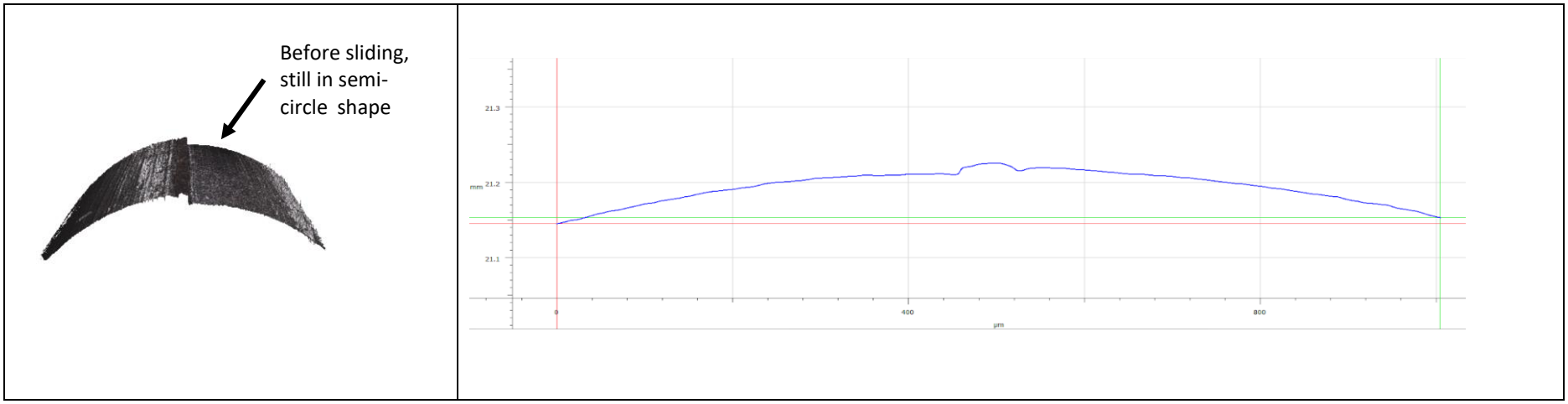

(a)

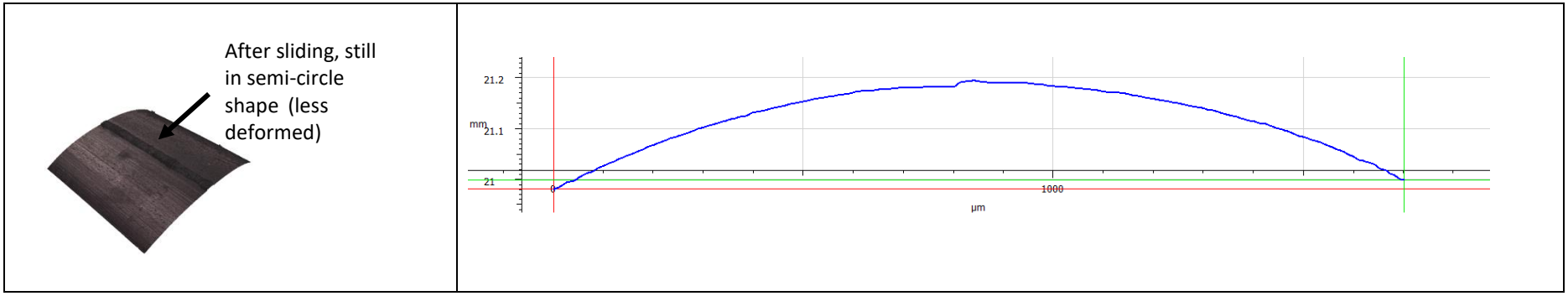

(b)

Figure 8.4 (a) 2-D Image of profile silicone before test (b) 2-D Image of profile wear scar for Silicone

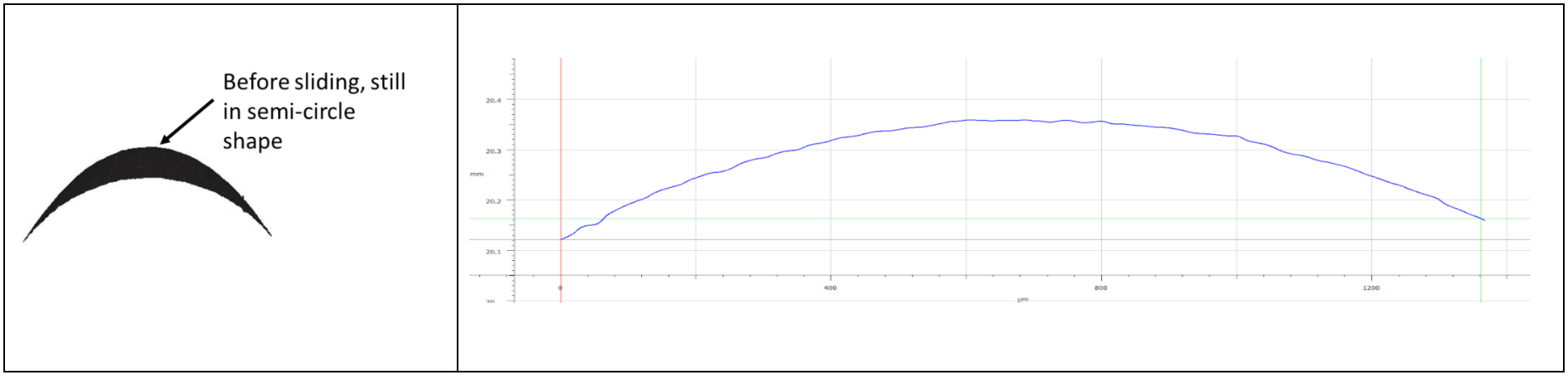

(a)

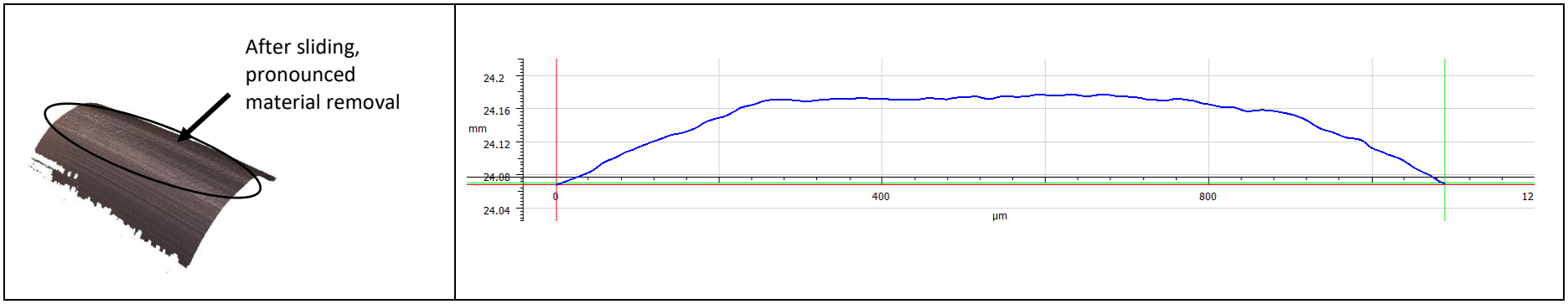

(b)

Figure 8.5 (a) 2-D Image of profile PEEK before test (b) 2-D Image of profile wear scar for PEEK

8.4.4 Wear scar scanning electron microscope (SEM) images

Figure 8.6 and Figure 8.7 show the SEM images of unused NBR and silicone O-rings respectively. Figure 8.8 shows the wear scar images for NBR at room temperature and high temperature for various carbon black contents. The observed wear mechanisms move from lubricate sliding wear at 0%CB for both temperatures to abrasive wear with material removal observed for 5%CB and 12%CB at both temperature and also particles embedment at the contact area for 5%CB and 12%CB. The sign of articles is possibly either from oil contaminants or wear debris.

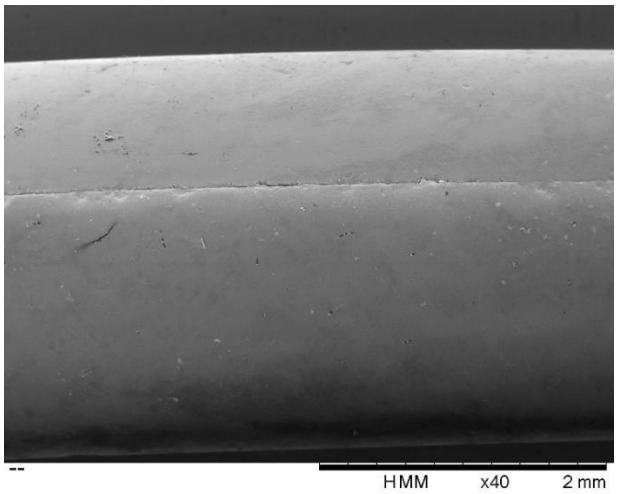

Figure 8.6 SEM image of unused NBR O-rings showing a smooth surface

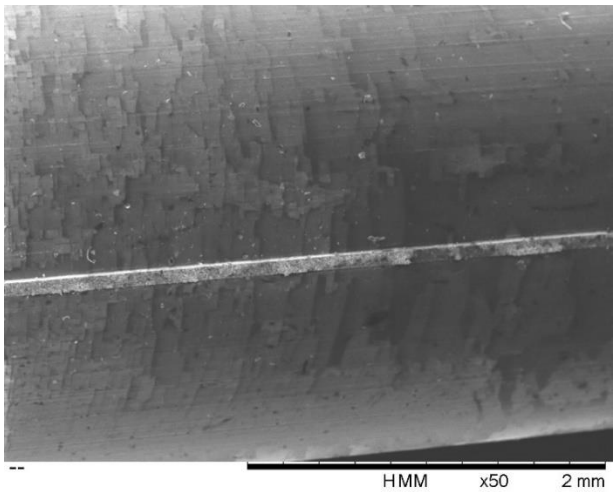

Figure 8.7 SEM image of unused silicone O-rings showing a smooth surface with compression molding marks on the surface

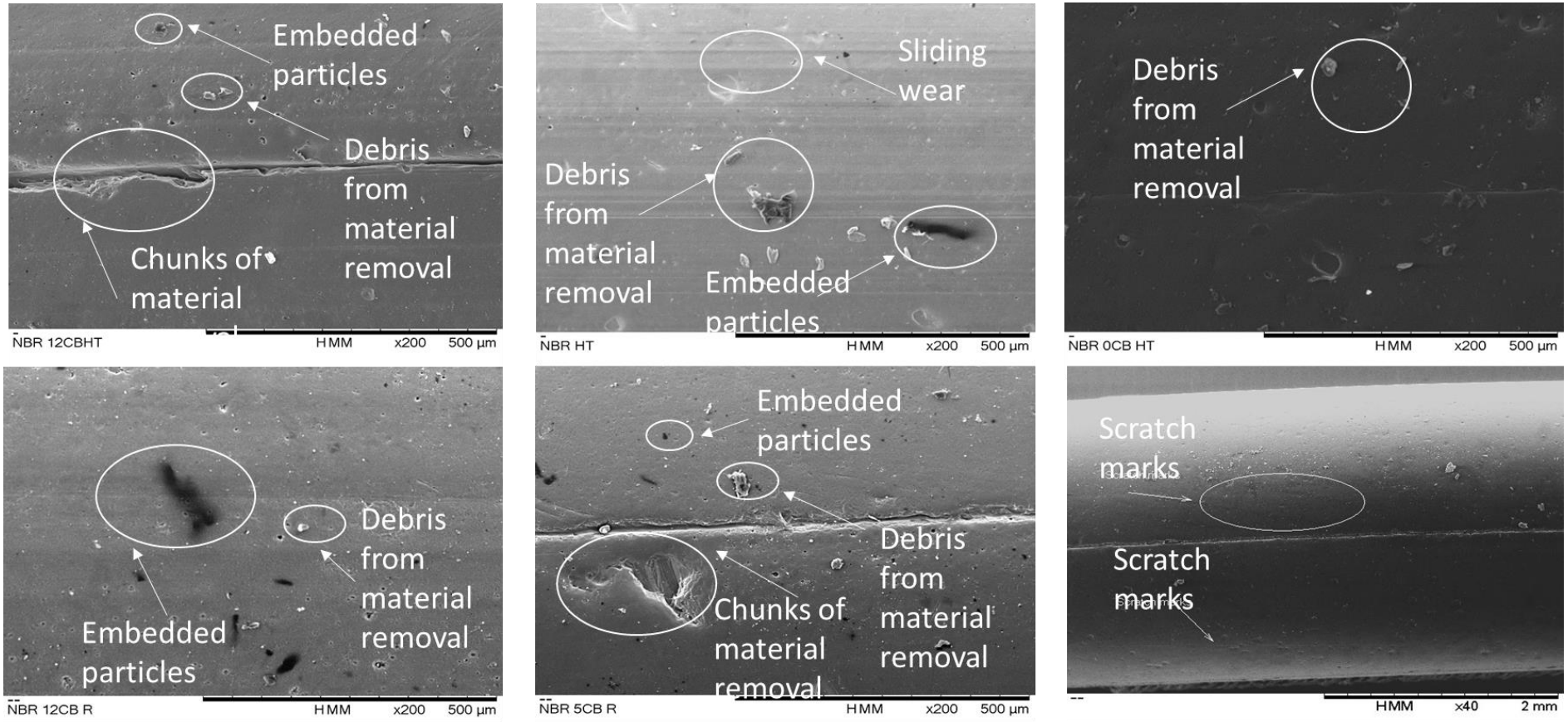

Figure 8.8 Wear scar images for NBR at 25°C (RT) and 100°C (HT)

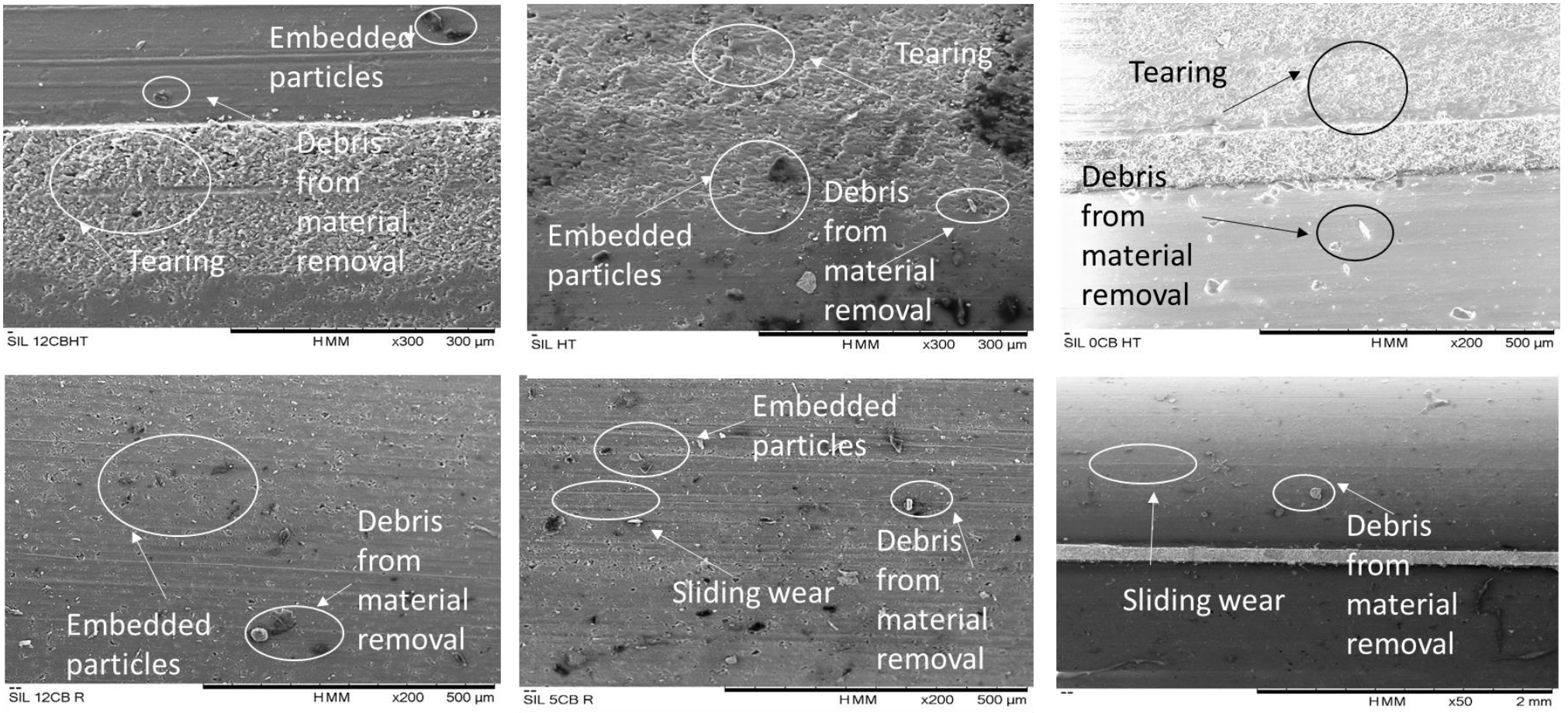

Figure 8.9 Wear scar images for silicone at 25°C (RT) and 100°C (HT)

Figure 8.9 show the unused O-rings and wear scar SEM images for used silicone o-rings at room temperature and high temperature for various carbon black contents. The sign of particles from material removal could be wear debris or soot contamination. And also particles that were embedded were also seen on the wear scar. Increasing scratches along the sliding direction were also visible on the used O-rings and can be related to abrasive wear from 0% CB to 12% CB. Figure 8.10 and Figure 8.11 show the SEM wear images for unused PEEK and PTFE O-rings respectively.

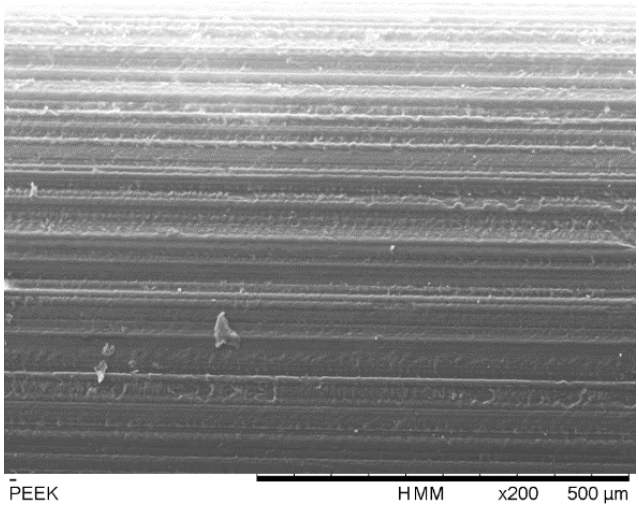

Figure 8.10 SEM image of unused PEEK O-rings showing a smooth surface with extrusion machining marks on the surface

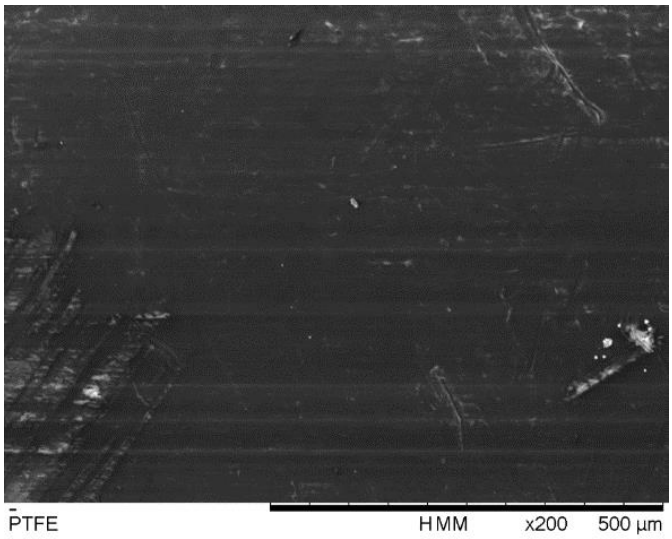

Figure 8.11 SEM image of unused PTFE O-rings showing a relatively smooth surface

Figure 8.12 shows the wear images of PEEK at room temperature and high temperature for uncontaminated lubricant and contaminated lubricant with 5% and 12% carbon black content. The wear mechanisms observed here are lubricated sliding wear with minimal material removal at 0%CB for both temperatures to abrasive wear with more material removal, ridges and furrows of the material observed for 5%CB and 12%CB at both temperatures and also soot particle embedment at the contact area for 5%CB and 12%CB.

Figure 8.13 shows the wear scar SEM images for PTFE used O-rings at room temperature and high temperature for various carbon black contents. The observed wear mechanisms are lubricated sliding wear at 0%CB for both temperatures to abrasive wear with more material removal and also peeling of the material observed for 5%CB and 12%CB at both temperatures and also soot particles embedment at the contact area for 5%CB and 12%CB.

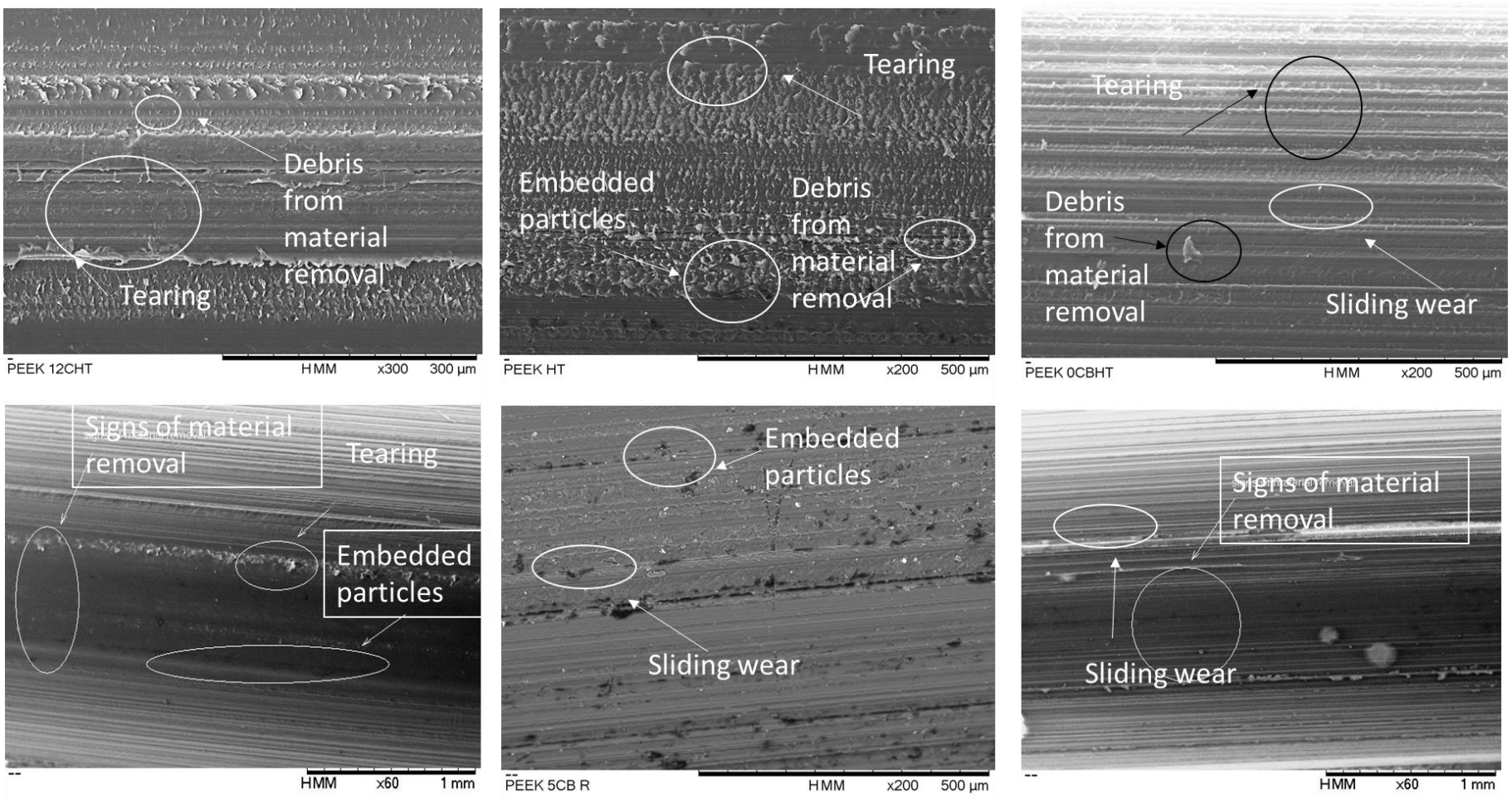

Figure 8.12 Wear scar images for PEEK at 25°C (RT) and 100°C (HT)

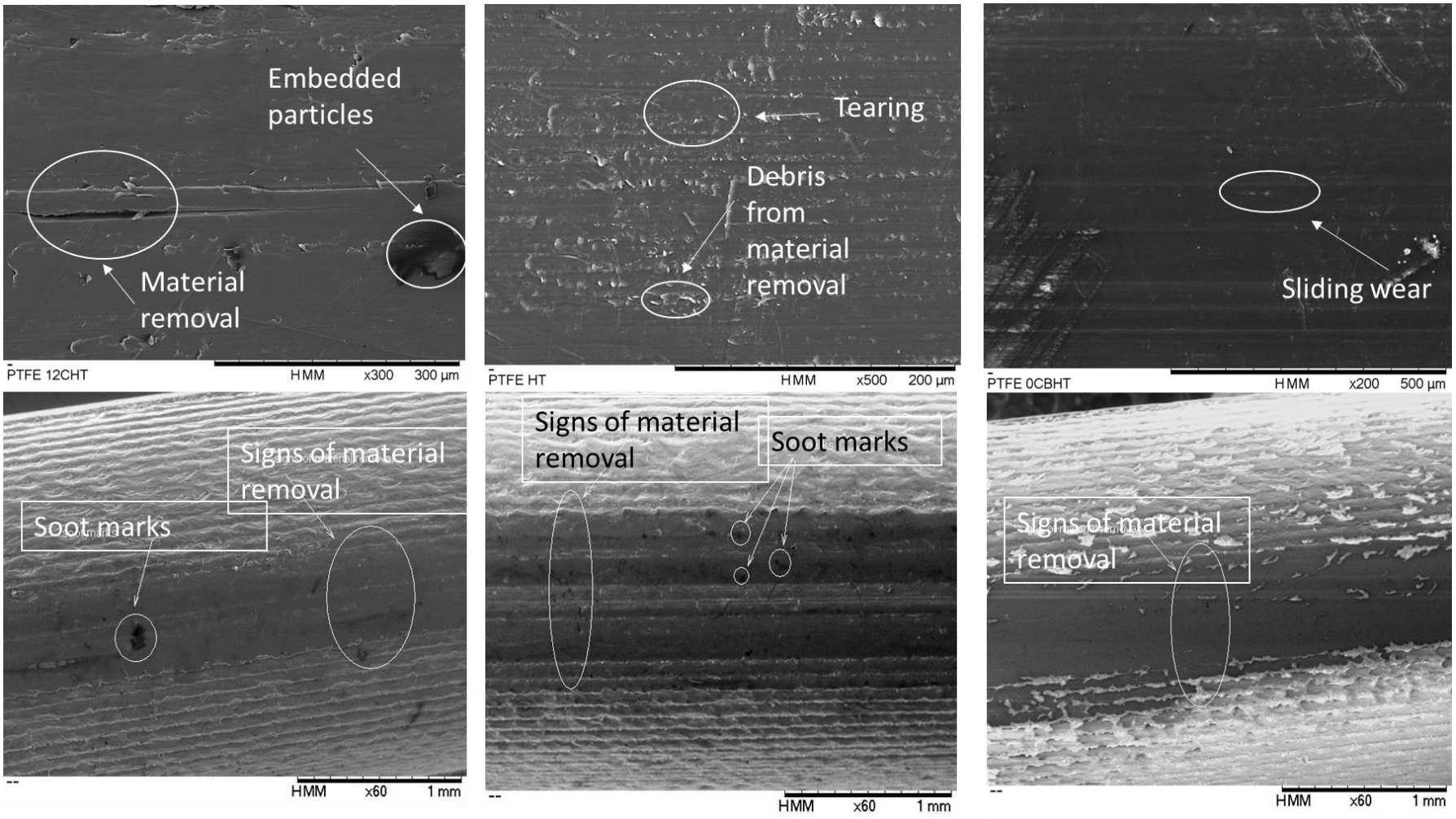

Figure 8.13 Wear scar images for PTFE at 25°C (RT) and 100°C (HT)

8.5 Discussion

8.5.1 Contact parameters

From Table 8.3, the contact pressure shows that the contact operates in isoviscous-elastic hydrodynamic lubrication (EHL) for all materials. As the block continues to slide on the ring, the contact area increases due to progressive wear thus the contact pressure reduces as shown in Table 8.6 and also from the wear scar images. The post-test contact pressure still shows that the contact operates in an isoviscous-elastic hydrodynamic lubrication regime. This can be related to the film thickness calculated which confirms to the lubrication regime.

By referring to Figure 8.14, it can be determined that for elastomers the contact operates in an isoviscous-elastic hydrodynamic lubrication regime or known as soft-elastohydrodynamic lubrication (EHL), however, for thermoplastic materials most of the contact operates in piezoviscous-elastic hydrodynamic lubrication regime of known as hard-elastohydrodynamic lubrication (EHL). This can be proven by the post-contact pressure calculated in Table 8.6 where all contact pressure is below 1MPa. As mentioned in the literature review, the estimated size of soot particles is similar to the size of carbon black used in this study which is between 0.2 µm and 0.5 µm. When this is compared to the film thickness calculated in Table 8.4, it is expected that the carbon black particles (being larger) can abrade through the film thickness when at lower and higher temperature thus causing wear to PEEK and PTFE. However, the film thickness for NBR and silicone have thickest film compared to the size of the soot surrogates at 25^{o}C thus will not influence the amount of wear on the specimens. However at 100°C, soot can abrade NBR and silicone at 0%CB and 5%CB due to thin film thickness compared to the size of soot surrogates.

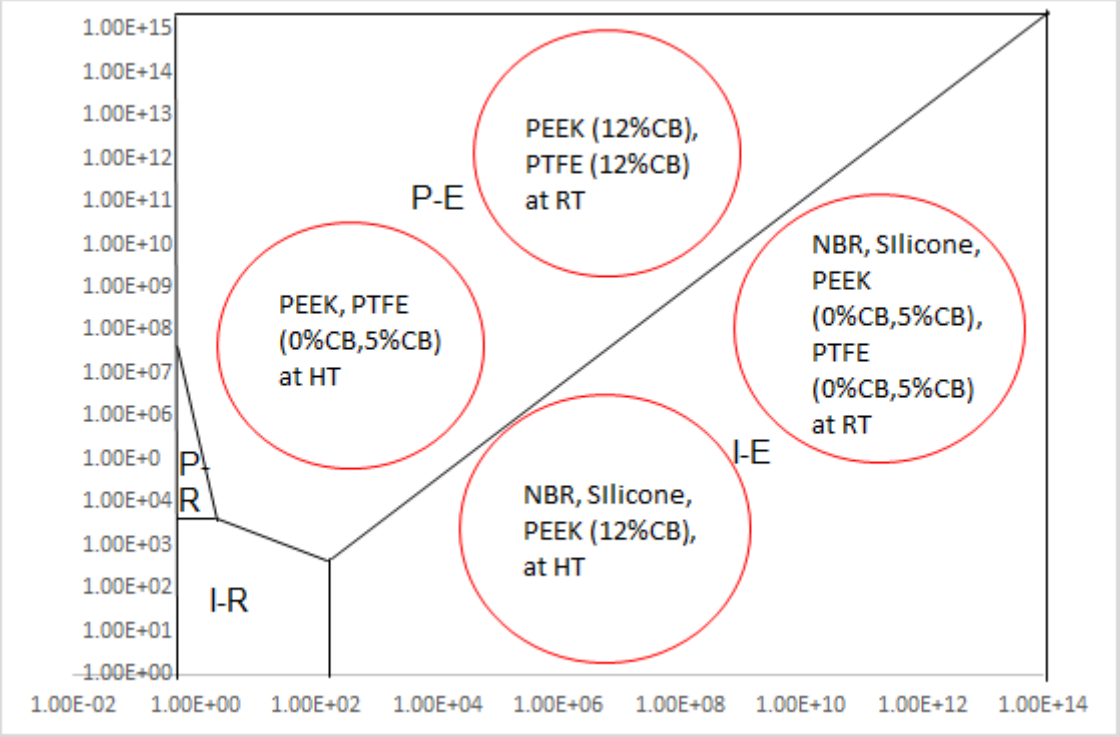

Figure 8.14 Hydrodynamic regime map for Block-on-ring contact

8.5.2 Wear analysis

8.5.2.1 Wear images and wear mechanisms

The scanning electron microscopic images for higher carbon black contents depict severe wear especially for thermoplastic materials (PEEK and PTFE) where signs of abrasion, tearing of surface and carbon black particles on the surface of the O-rings are visible. This, obviously may be because of the lubricant entrainment into the contact were restrained thus the agglomerates of carbon black get squeezed within the contact and embedded into the surfaces, thus creating three-body abrasion where the particles abrade through the contact surface. The schematic depiction of the abrasion mechanism of carbon black particles is shown in Figure 8.15.

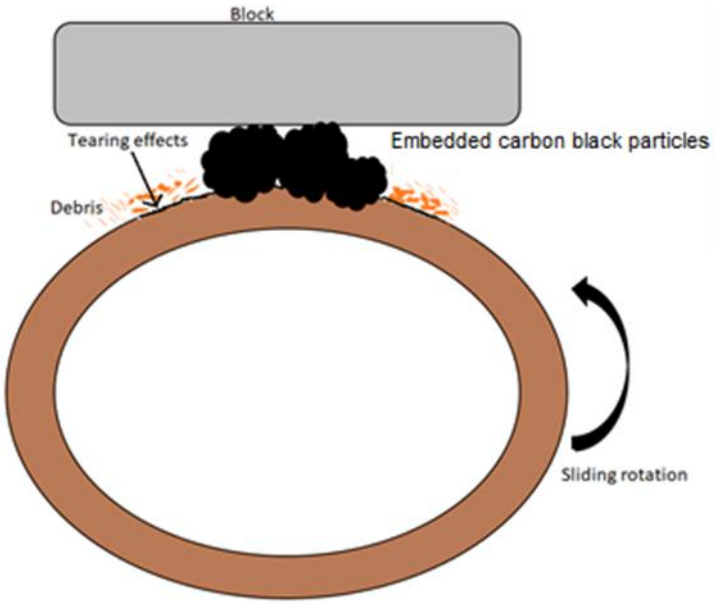

Figure 8.15 Wear mechanisms resulting in tearing effects on thermoplastic materials

However, for elastomer materials, NBR and silicone images depict scratch marks with pure diesel engine oil to more pronounced abrasive wear with small amount of material removal on both surfaces at 5% and 12% carbon black content due to ploughing action of softer materials when rub against harder material. The mechanism schematic diagram for the ploughing action is depicted in Figure 8.16. This also correlates to the estimated film thickness of the contact surfaces where the size of carbon black particles are bigger than the film thickness, and thus can abrade the surface [36].

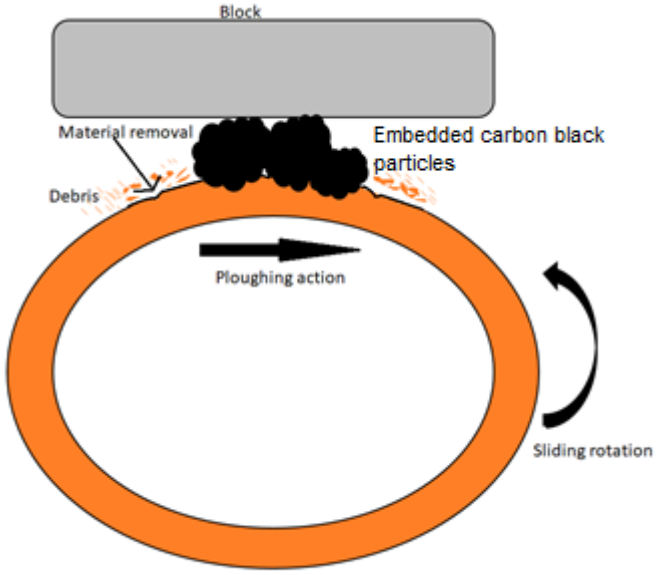

Figure 8.16 Ploughing action due to embedded carbon black particles when rubbed against thermoplastic material causing material removal

8.6 Summary

The non-conformal contact test using the designed block-on-ring rig was carried out to give a basic understanding on how carbon black causes wear in non-conformal contact in simulating the valve guide. The following conclusions can be drawn from the results presented in this study:

- The wear mechanism varies from lubricated wear at no contamination to more pronounced abrasive wear for elastomer materials with increasing carbon black content. For all materials, third-body abrasion was observed that was caused by the entraining lubricant with suspended carbon black particles at both carbon black content (5% and 12%) which either was due to lubricant starvation or/and particles embedding in the material surfaces.

- The wear mechanisms are dependent on various factors including temperature (oil film thickness), carbon black content and the material properties.

- The surface profile analysis also demonstrates that after sliding test, the elastomer materials deforms back to its original form. While thermoplastic materials show material removal which is consistent with scar images captured.

Chapter 9 Oil Film Thickness Measurement on Polymer/Elastomer Specimens

In this chapter, a novel approach using an ultrasonic technique was utilised in determining the oil film thickness measurement of thermoplastic/elastomer specimens in contact with steel. This study was conducted in order to determine how the film thickness of the lubricant behaves with softer materials during sliding. The test specimens were designed and manufactured, where eight embedded sensors were fitted to a liner specimen on the Plint and connected to the FMS-100 to capture the ultrasound signal. The sample O-rings tested were from NBR and PEEK and the lubricant with carbon black contamination was tested at 0%CB and 12%CB.

9.1 Principles of ultrasound

Ultrasound is a sound wave energy that has a higher frequency than the audible limit of human hearing range; which operates from 20kHz and above [94]. The ultrasound wave is the same as sound, which propagates through a medium. This medium consists of particles which are balanced by the elastic forces and can perform elastic oscillations assuming that no tension or compression force is applied beyond the elastic limits. The waves that can be generated by ultrasonic transducers can be distinguished by two main modes of propagation, which are longitudinal waves and shear waves. In longitudinal waves the particles move parallel to the wave direction, where if the particles are closer together; compression occurs and vice versa when the particles are further apart. The distance between one particle to another is called the wavelength, λ. While for shear waves, the particles move perpendicular to the wave direction. This wave needs a shear force and a solid medium to propagate with [95].

9.1.1 Speed of sound

The speed of sound which is the velocity that sound travels at through materials, varies due to the constituent of the particles inside a material. The product of a speed of sound is the multiplier of frequency and the wavelength the ultrasound waves go through. The equation is shown in Equation 9.1. A transducer is used to produce an ultrasonic impulse to detect echoes in a material. The time for the ultrasonic waves travels through the materials and the speed of sound can be calculated using a simple time-of-flight equation with a known thickness.

$$c = f\lambda \tag{9.1}$$

where f is the frequency in Hz and λ is the wavelength

9.1.2 Acoustic impedance

A sound wave that travels between two materials will partially transfer the acoustic energy through the material and the rest will be reflected. The ratio of reflected to transmitted signal is known as the reflection coefficient, *R*.

The reflection coefficient can be determined if the acoustic impedance, *z* is known. The acoustic impedance, *z*, is the resistance to sound wave propagation within the material and is defined as:

$$z = \rho c \tag{9.2}$$

where, ρ is the density of the material in kg/m^3 and *c* is the speed of sound in m/s.

If two materials have a major difference of acoustic impedance, the greater the amount of wave is reflected. If two materials have the same acoustic impedance than the wave reflection will be at minimal or no reflection at all. The reflection coefficient is defined by:

$$R = \frac{z_2 - z_1}{z_1 + z_2} \tag{9.3}$$

9.2 Oil film thickness measurement using Ultrasound

An established method for determining the oil film thickness is the spring model, whereby the lubricant layer is treated as a spring with a definable stiffness. Theoretically, to achieve a greater coefficient, a thinner film has greater stiffness compared to thicker film. The following equation derivation is outlined by Dwyer Joyce, Drinkwater & Donohoe [94].

$$h = \frac{\rho c^2}{\pi f z_1 z_2} \sqrt{\left(\frac{R^2 (z_1 + z_2)^2 - (z_1 - z_2)^2}{1 - R^2} \right)} \tag{9.4}$$

where *f* is frequency, ρ is the density in kg/m^3, *c* is the speed of sound in m/s, *z* is the acoustic impedance and *R* is the reflection coefficient.

For this method, a reference measurement is needed to reflect that the surface is cleaned and free from lubricant. The first measurement and A-scan test is captured and compared.

9.3 Calculation of contact pressure

The ring-liner contact configuration in this test, which is a ring on a concave surface (Figure 9.1), is similar to a contact between two parallel cylinders (line contact) as shown in Figure 9.2 where the contact pressure distribution is assumed to be acting on rectangular contact area of width *2b*.

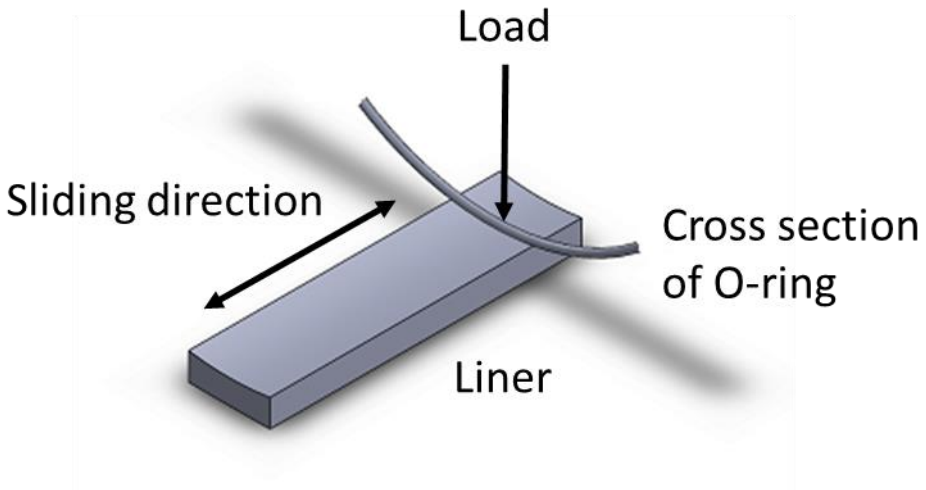

Figure 9.1 Schematic diagram of a conformal contact; representation of a ring-liner contact configuration

Thus the estimation of the maximum contact pressure, p_o was determined by using Hertz's line contact formula [12].

$$P_o = \frac{P}{\pi b} \tag{9.5}$$

$$b = \sqrt{\frac{4P'R'}{\pi E'}} \tag{9.6}$$

where *P* is the contact load *(N), b* is the half width of the contact rectangle *(m)* and *P'* is the load per unit length *(N/m)*.

While the mean contact pressure, p_m is determined using Equation 9.7.

$$P_m = \frac{P'}{2b} \tag{9.7}$$

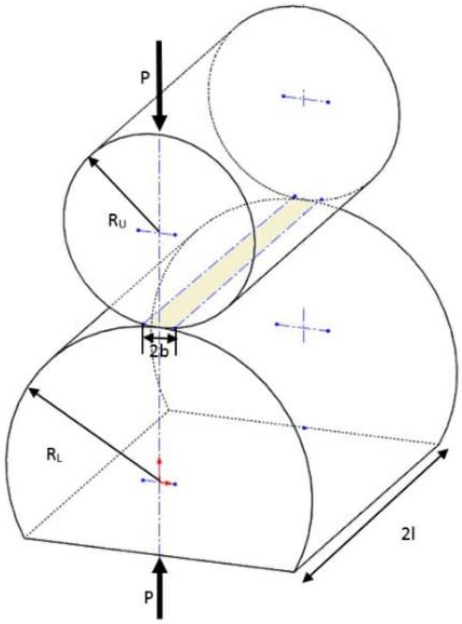

Figure 9.2 Schematic diagram of Hertzian contact pressure distribution between two parallel cylinders equating to a line contact

Table 9.1 below shows the estimated contact pressure for load of 20N and 30N for all tested materials.

Table 9.1 Estimated contact pressure for load 20N and 30N

	20N	**30N**
Contact pressure NBR (MPa)	0.012	0.029
Contact pressure PEEK (MPa)	1.399	1.715

9.4 Test equipment

The test was conducted by using Cameron Plint TE77 Reciprocating Rig as shown in Figure 9.3. The working system of the test rig is as described in Chapter 5. The film thickness is measured when the ring slides onto a liner as seen in Figure 9.4.

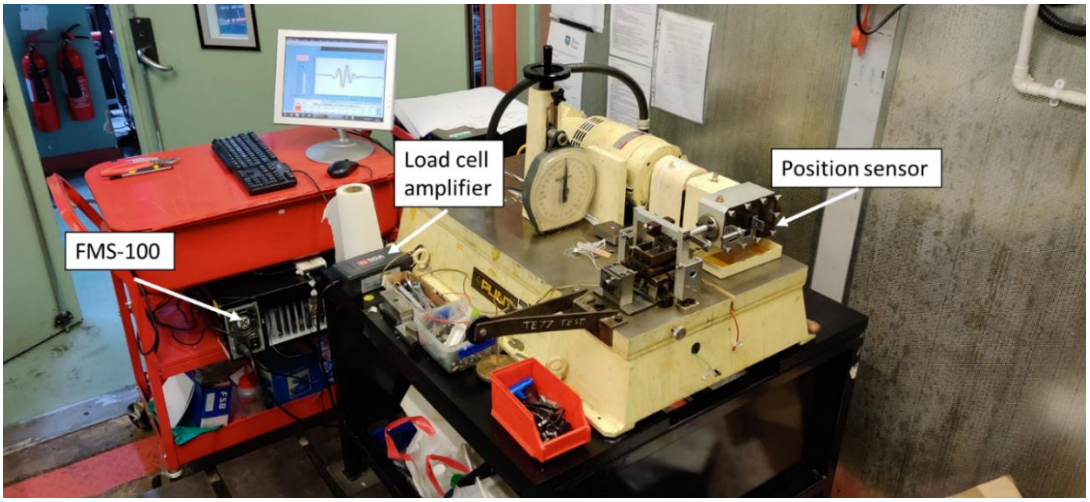

Figure 9.3 Labelled photograph of full test apparatus

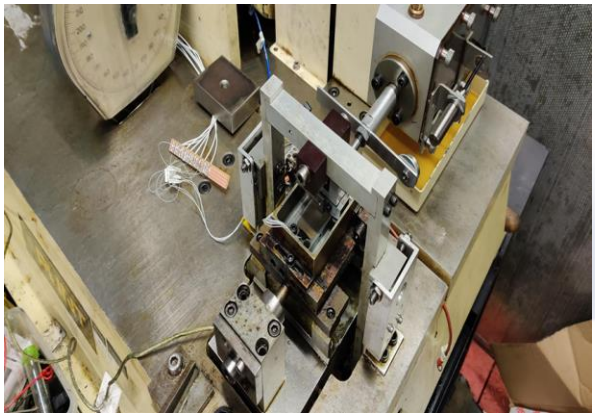

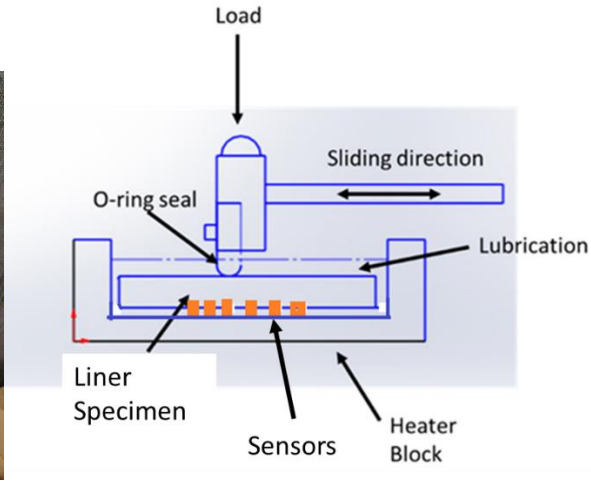

Figure 9.4 Zoomed view image of the test rig and schematic diagram of the reciprocating head

9.4.1 FMS-100

The FMS-100 is a PC based ultrasonic measurement system which allows the signal to be transmitted and received by the same sensors through a pulse/echo mode. The system also had a 100 ms/s digitiser which will digitised the reflected ultrasonic waves in real-time processing in order to determine the lubricant film thickness. The system also incorporates LabView to capture and store the test data.

9.4.2 Counterface liner specimen

The liner, made of cast iron with average hardness of 25HRC and Young's modulus of 103GPa was selected in order to replicate the ring and liner mechanism. The

acoustic impedance of cast iron liner is 34.9 MRayls. The thickness of the liner was carefully selected so that the lever arm of the TE77 remains level throughout the sliding stroke.

Eight 10Mhz sensors which are readily available and offers optimum resolution while still remaining in the measurement range were instrumented onto the liner specimen in this test. A photograph of the array layout is shown in Figure 9.5.

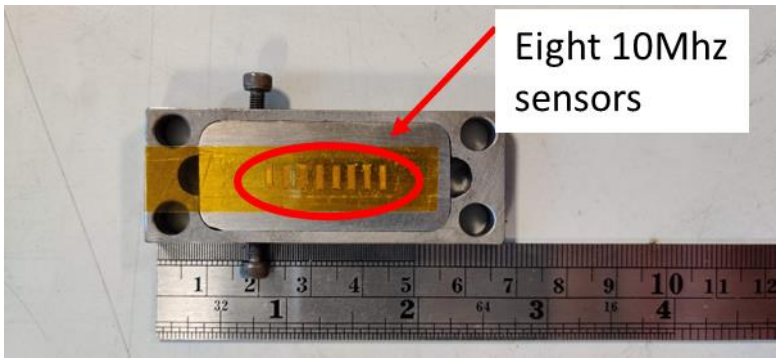

Figure 9.5 Photograph of liner specimen with sensors

9.4.3 O-ring specimen

The O-ring specimen (NBR and PEEK) is the key component in this study in order to investigate how the lubricant behave in elastomer/thermoplastic-to-metal contact. The O-ring is mounted and affixed on the head of the Plint TE77 with a screw; resemble a ring liner contact as shown in Figure 9.6.

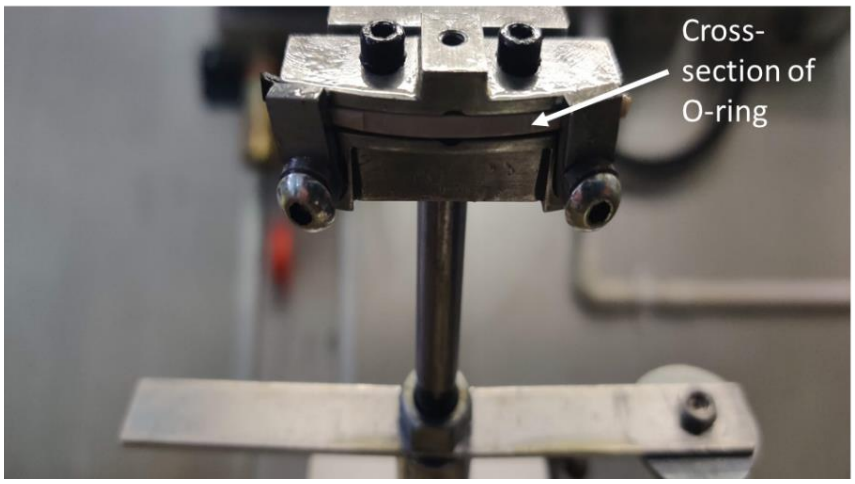

Figure 9.6 Cross section of an O-ring mounted on Plint TE77 head

9.4.4 Lubricant

The lubricant used in this study was Shell Helix HX5 (SAE15W40), a multi-grade synthetic motor oil with an additive package inside the lubricant. And another test was carried with 12% carbon black content blended in the lubricant oil to simulate used oil.

9.5 Experimental procedures

The cross section of the ring ran through a series of sliding tests against an instrumented liner. One set of tests was carried out where all the tests were run at varying load (20-30N) and varying temperature (25-50°C) with uncontaminated oil and contaminated oil (12% carbon black content) at speed of 10Hz. All the tests were conducted at sliding stroke of 15mm for 15 minutes. Table 9.2 shows the test conditions for the oil film thickness test for NBR and PEEK O-ring.

Table 9.2 General test conditions oil film thickness

Parameters	**Test Conditions**
Reciprocating Stroke	15mm
Speed	0.14 m/s
Normal Load (N)	20N and 30N
Temperature	25°C and 50°C
Lubricant	0% CB and 12% CB
Method of lubrication	Immersed
Lubricant viscosity	85.015 cSt (at 0% and 50°C) and 1066.6 cSt (at 12% and 50°C)
Lubricant density	0.866 kg/m^3 (at 0% and 15°C) and 0.928 kg/m^3 (at 12% and 15°C)

Table 9.3 summarises the various tests performed. Before the test was conducted, the luner surface was cleaned with acetone. Then a reference pulsed from the liner surface was recorded for each sensor which reflects all incident waves. Then the following tests using the simplified text matrix were conducted once the reference been taken.

Table 9.3 Simplified test matrix

Test Number	Soot Content	Material	Test Temperature (°C)	Load (N)
1	0%	PEEK	50	20
2	0%	PEEK	50	30
3	0%	PEEK	25	20
4	0%	PEEK	25	30
5	12%	PEEK	25	20
6	12%	PEEK	25	30
7	12%	PEEK	50	20
8	12%	PEEK	50	30
9	12%	NBR	50	20
10	12%	NBR	50	30

After testing, the data collected was post-processed using a LabView program created for this study [96]. This software uses the spring model method to measure the reflection coefficient for each sensor over time. The data is then analysed using Matlab code that were created by Beamish [96] by applying Equation 9.4 to convert reflection coefficient to lubricant film thickness.

9.6 Experimental results

Figure 9.7 and Figure 9.8 show the oil film thickness (OFT) for PEEK at 0% and 12% carbon black content. It shows that the trend of the film thickness is similar throughout the test from sensor 1 to 8, however, at 0% carbon black content, the ultrasound signal captured is higher when the O-rings slides pass the liner than at 12% carbon black content. This could probably due to the lubricant easily flow inside the contact. While at 12% carbon black content and 30N, shows thinner OFT compared at 20N as shown in Figure 9.9.

Thicker OFT is observed when at lower temperature as shown in Figure 9.8 when compared to higher temperature in Figure 9.10 for PEEK. When comparing elastomer material, NBR (Figure 9.11) with thermoplastic material, PEEK, the OFT is thinner with PEEK. This can be related to the wear scar images obtained in Figure 9.13. the summary of this oil film thickness can be seen in Figure 9.12.

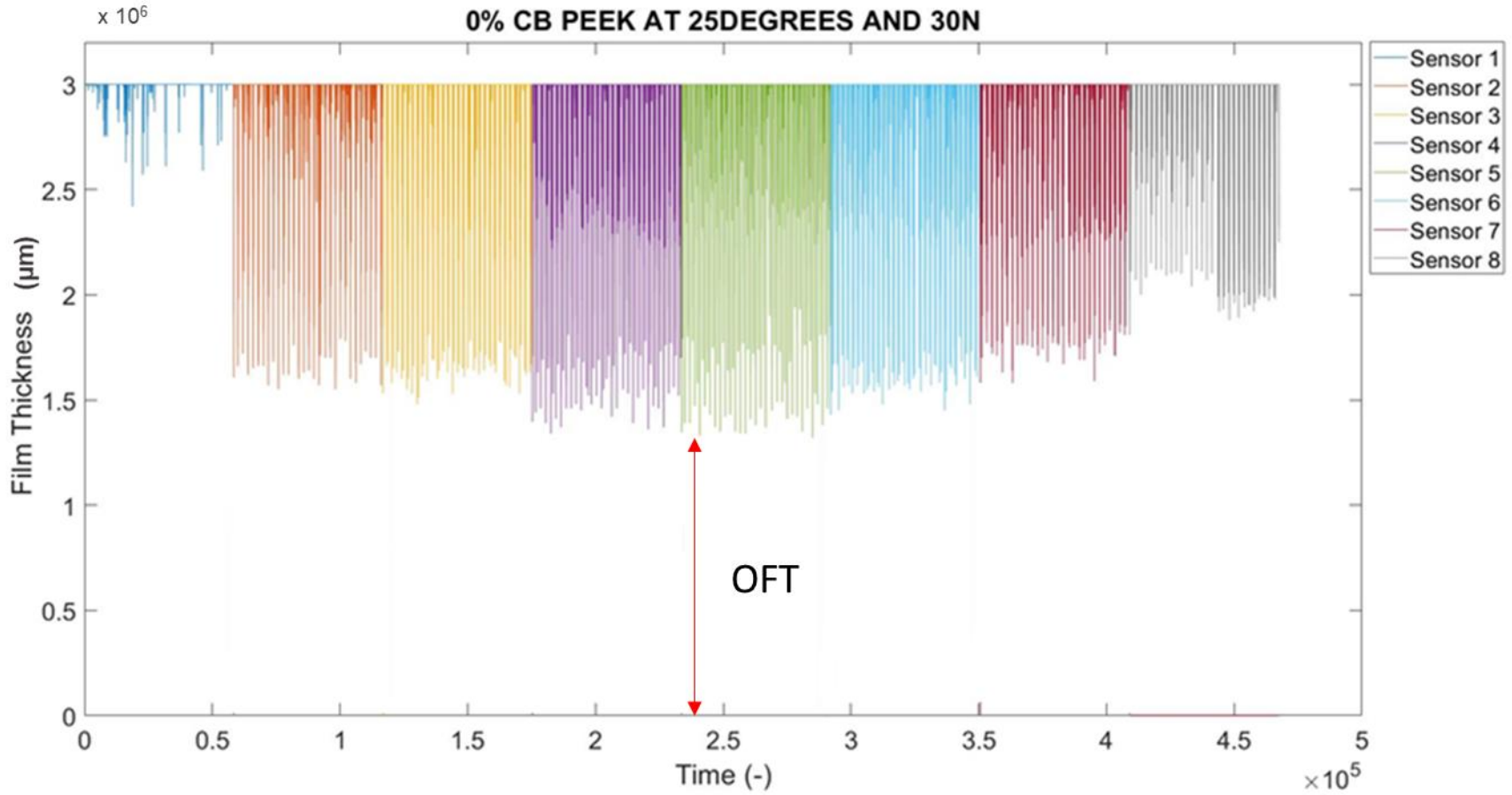

Figure 9.7 Oil film thickness for PEEK at 0% carbon black content, 25°C and 30N for the first 15seconds

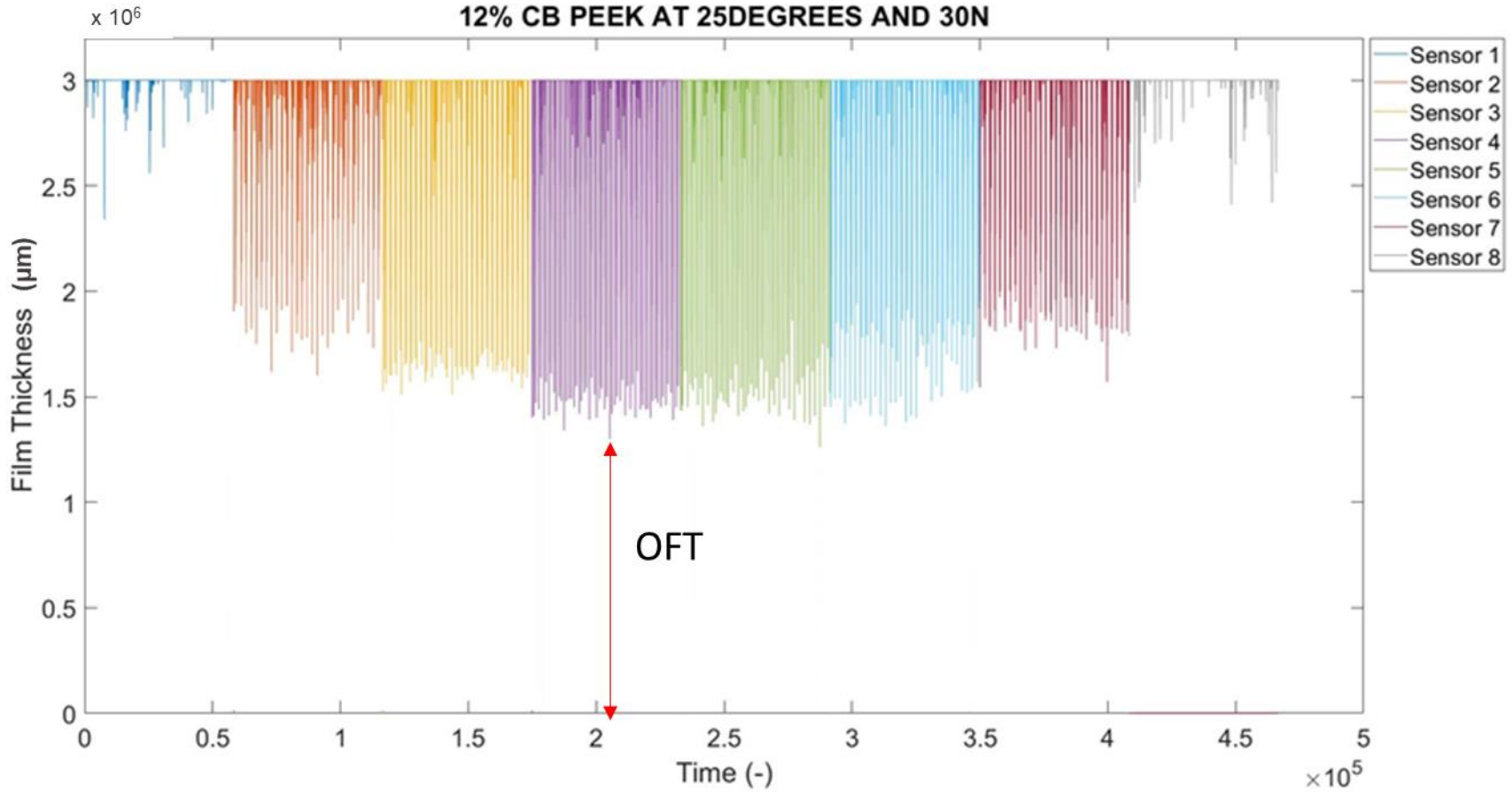

Figure 9.8 Oil film thickness for PEEK at 12% carbon black content, 25°C and 30N for the first 15seconds

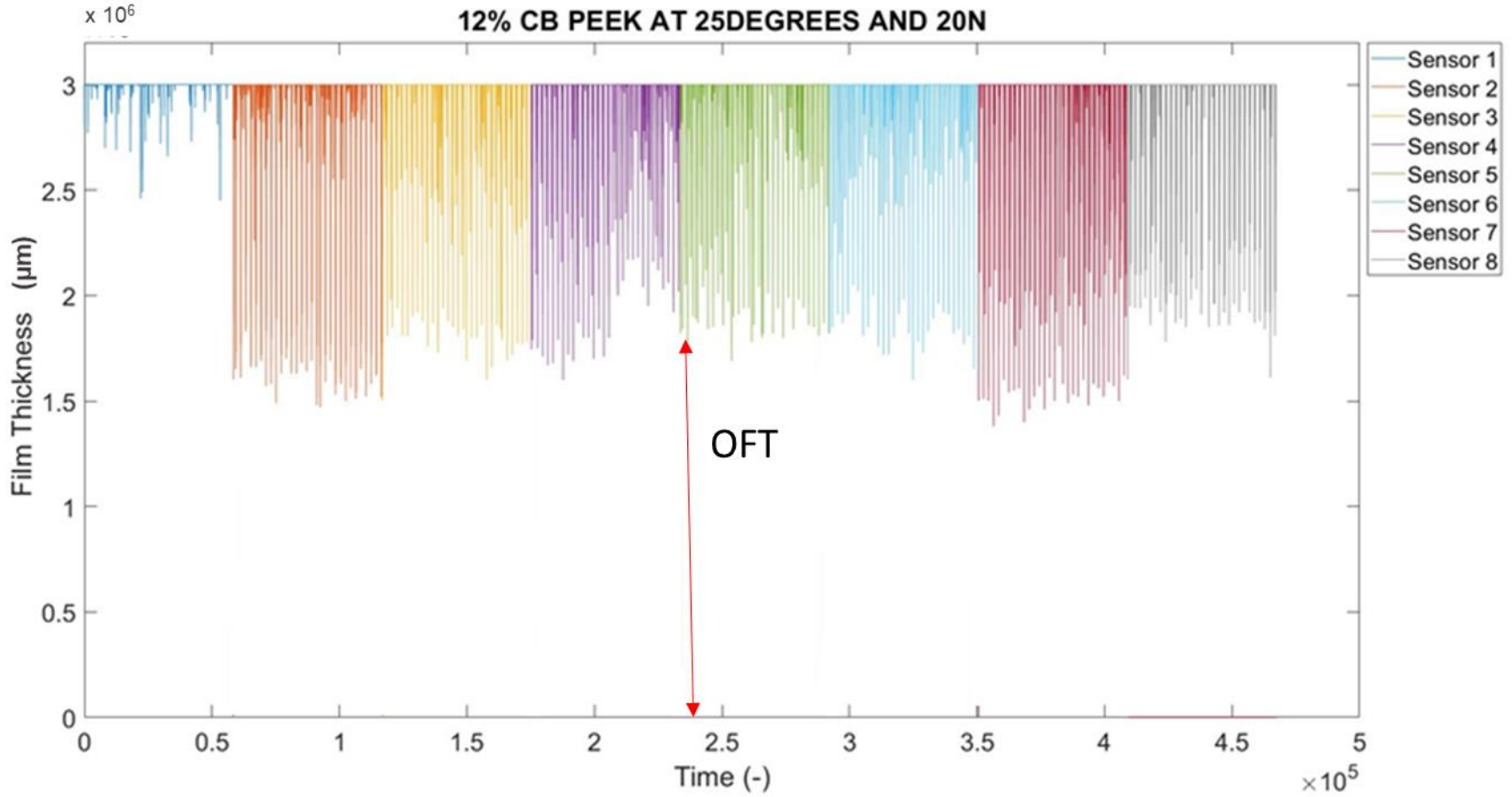

Figure 9.9 Oil film thickness for PEEK at 12% carbon black content, 25°C and 20N for the first 15seconds

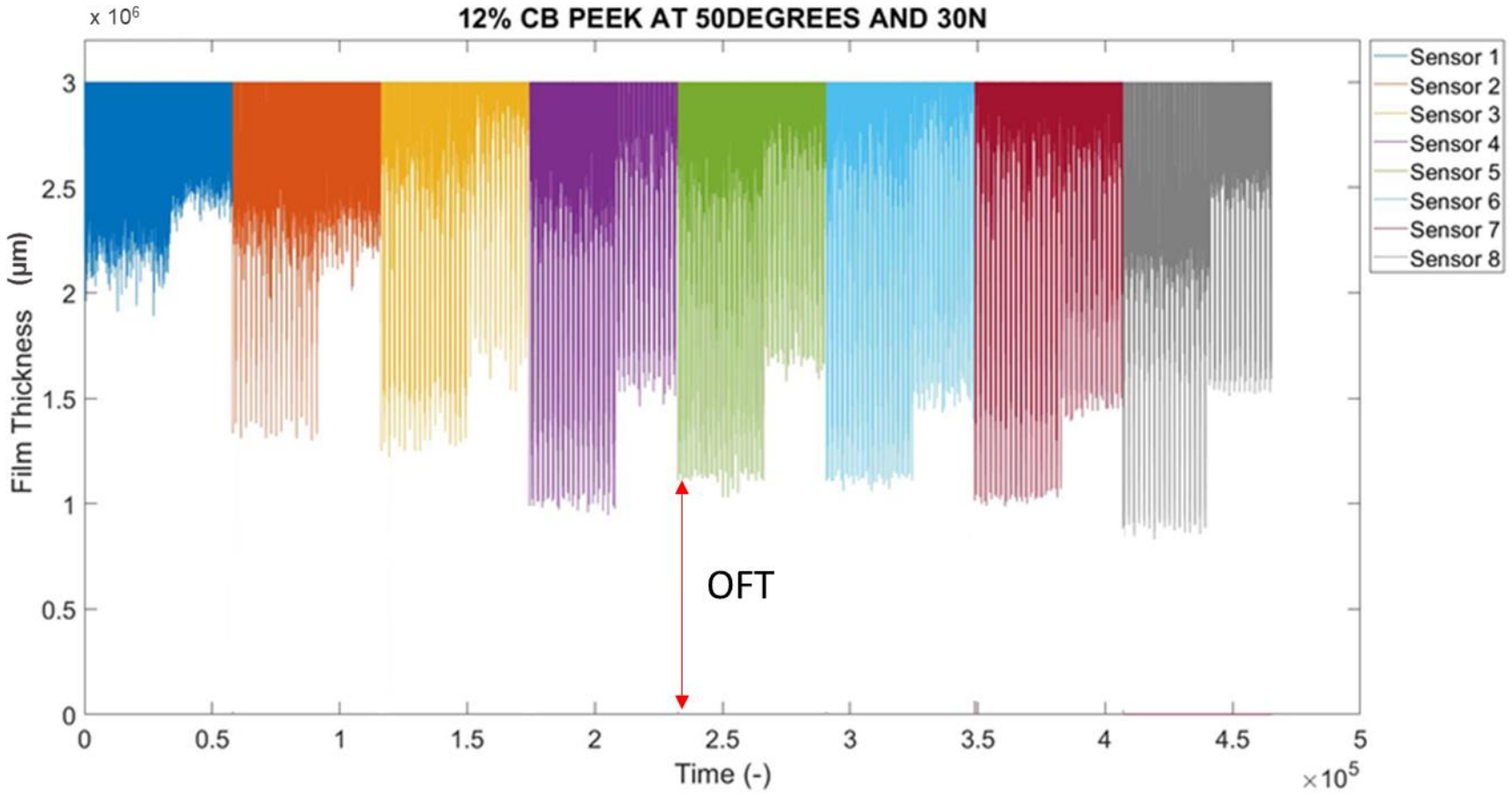

Figure 9.10 Oil film thickness for PEEK at 12% carbon black content, 50°C and 30N for the first 15seconds

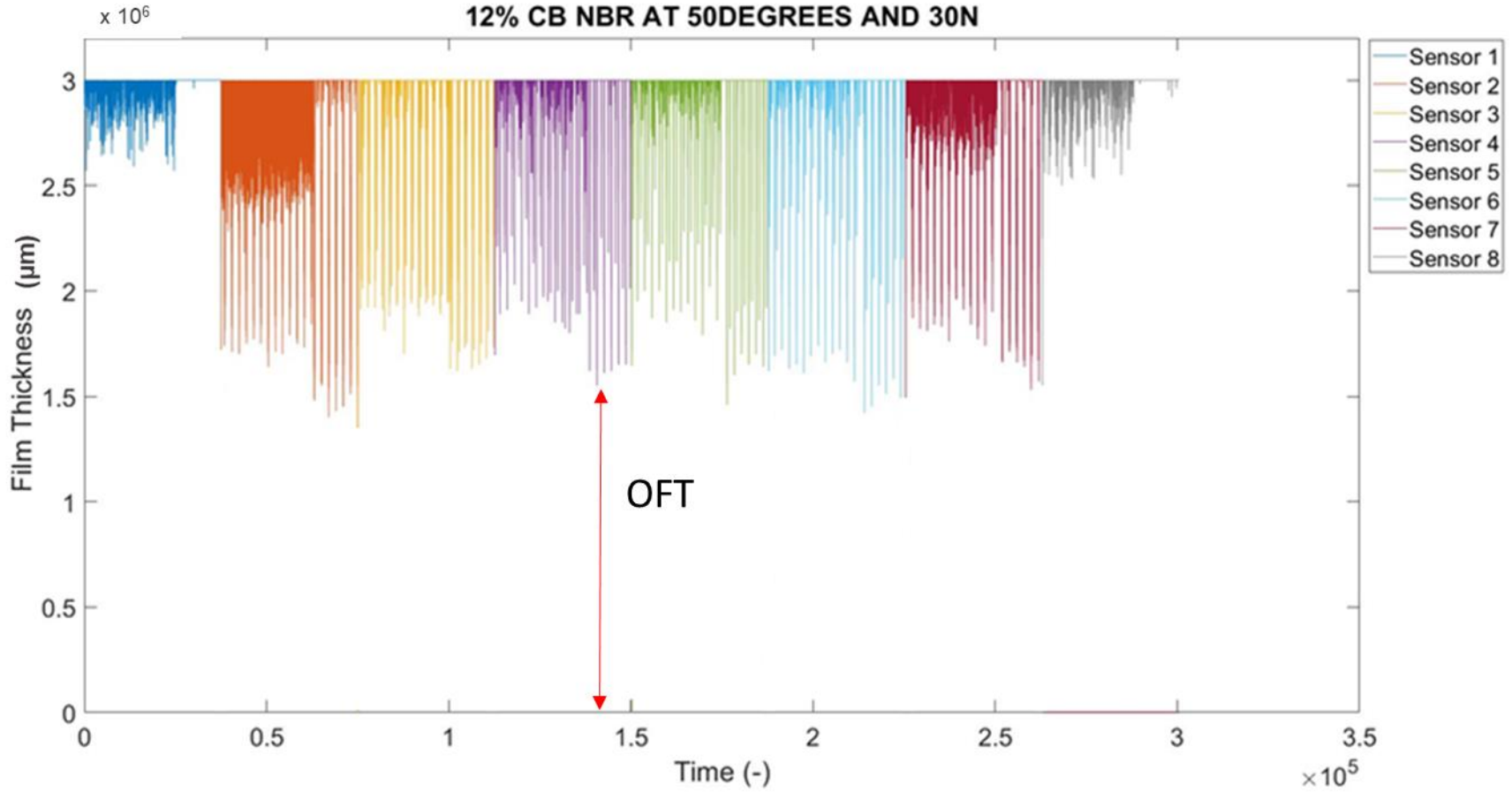

Figure 9.11 Oil film thickness for NBR at 12% carbon black content, 50°C and 30N for the first 15seconds

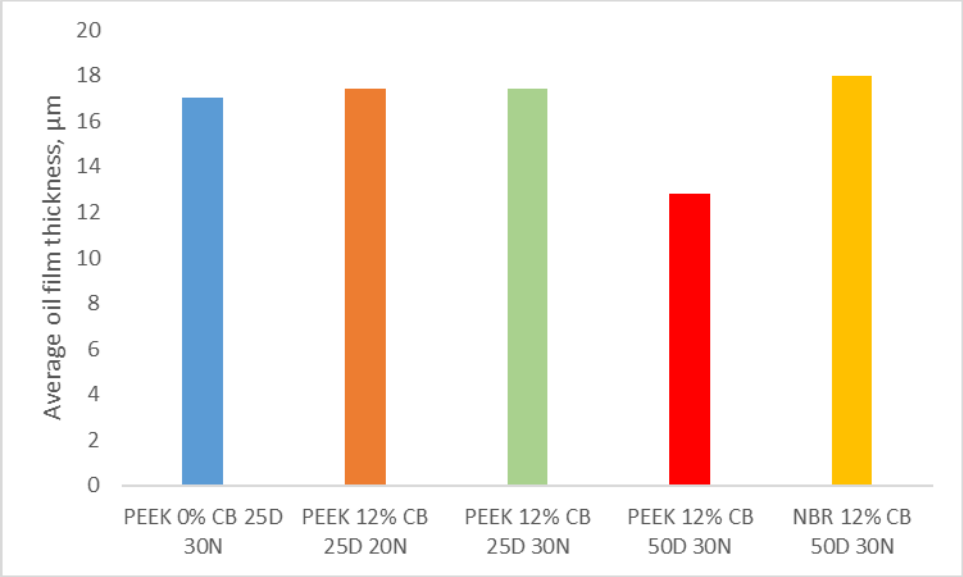

Figure 9.12 Average oil film thickness for all test

Figure 9.13 Worn PEEK after test

Figure 9.14 and Figure 9.15 showed the visible wear scars on the liner surface where carbon black could be seen adhering to the surface. The profile of the worn and unworn section of the liner is shown in Figure 9.16 where the roughness does not vary significantly, where the range is from 1.5 - 2µm.

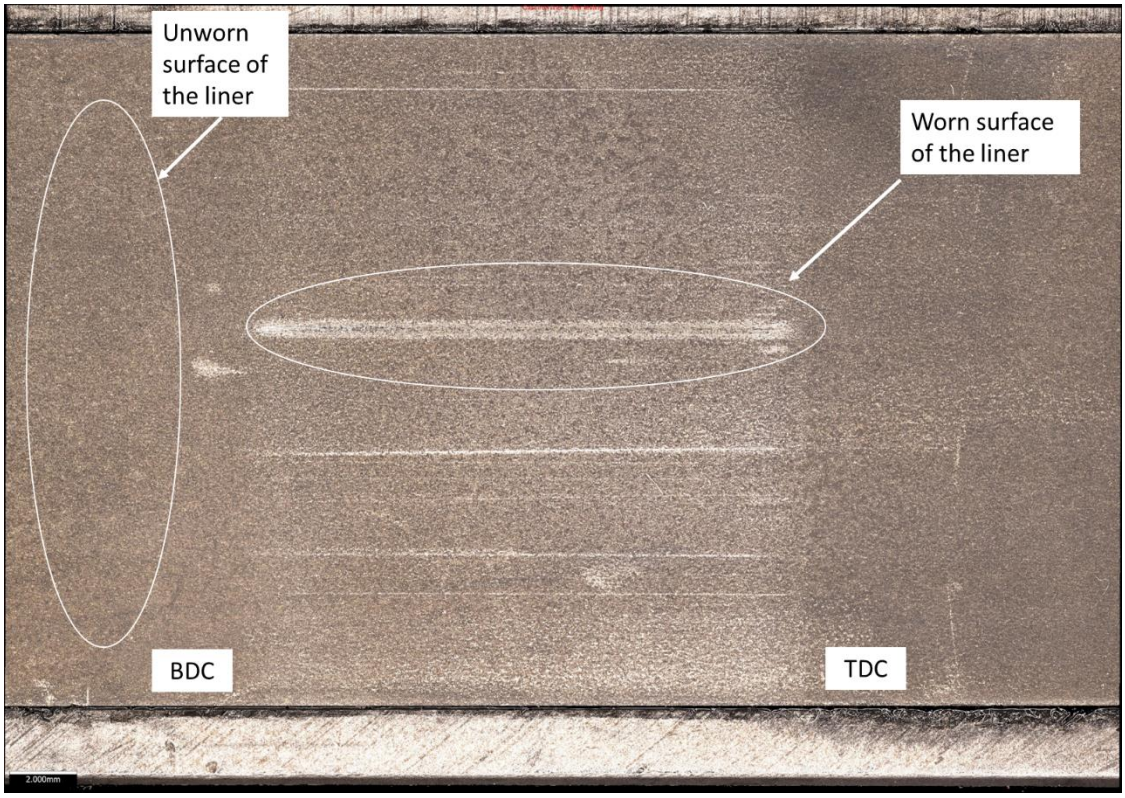

Figure 9.14 Wear scar of liner specimen used in test with worn and unworn profiles shown in Figure 9.16

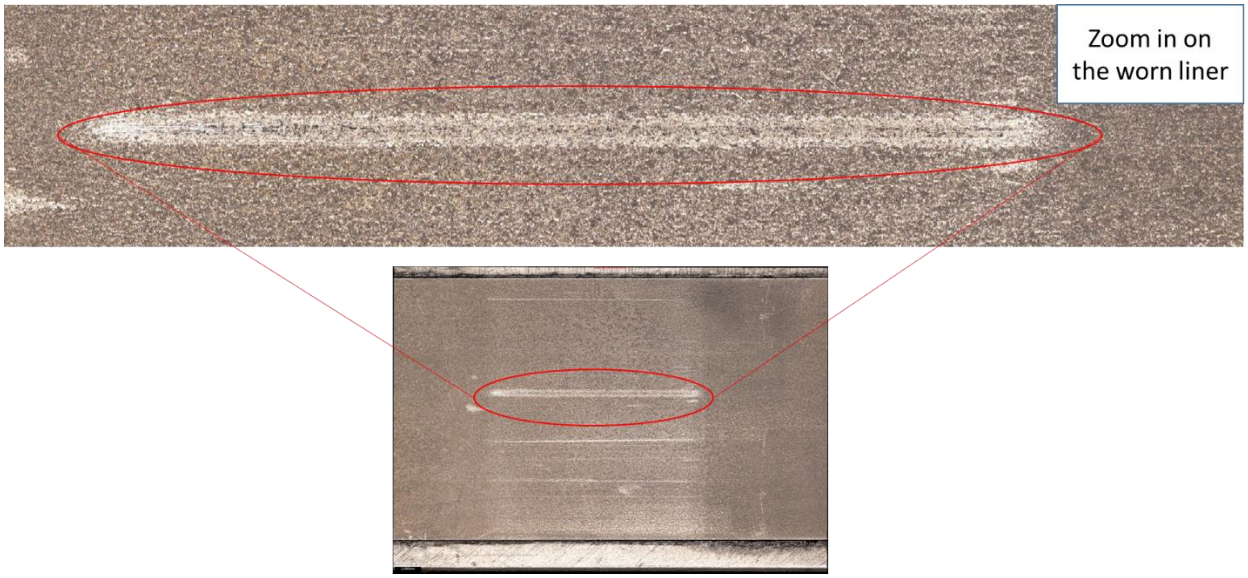

Figure 9.15 Zoomed in image on the wear scar due to the reciprocating sliding showing carbon black adhering on the surface

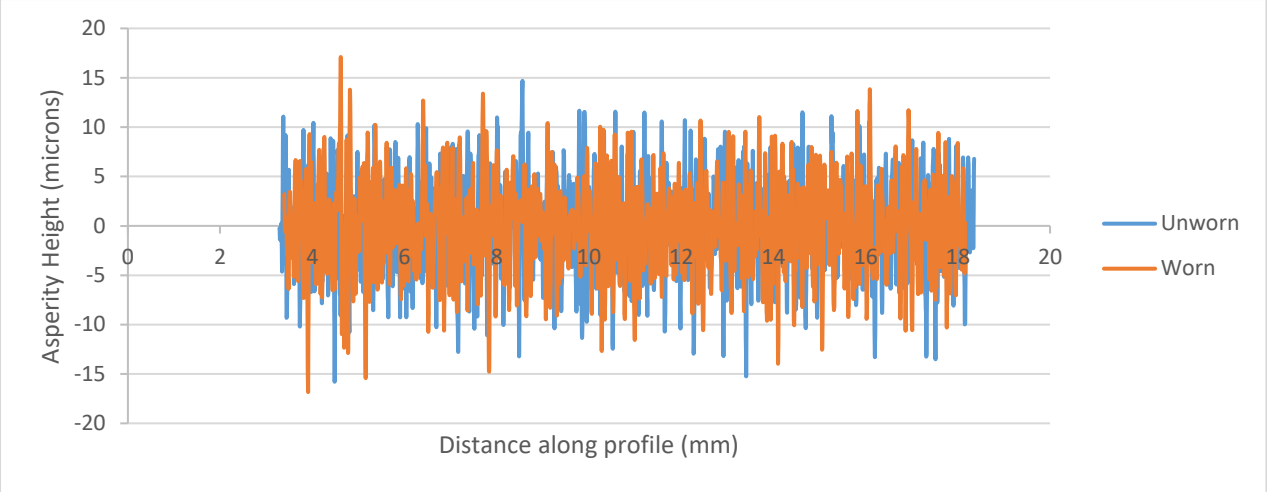

Figure 9.16 Profile of worn and unworn sections of the counterface liner used in this test

9.7 Discussion

The following discusses the findings obtained in these results of the oil film thickness measurements, wear scar images and comparison with analytical results from previous tests.

9.7.1 Varying load

As shown in Figure 9.7, higher load leads to a thinner film. This is due to the higher contact pressure when the ring pushes onto the liner though the changes in the OFT is not that significant. Therefore, a higher change in magnitude could be tested in order to give significant changes when load is varied.

9.7.2 Varying temperature

Thinner film due to the temperature increase is observed in Figure 9.10 when compared to Figure 9.9. This conforms to the theory that oil viscosity is inversely proportional to temperature [44].

The thicker films at lower temperature shows adequate separation between the reflected wave from the ring to the liner. At higher temperature, more ultrasound wave is captured due to the thinner films, when focusing on Sensor 4 (Figure 9.17) which is located at the middle of the liner, the OFT shows thinner films at 50°C compared with a low temperature (Figure 9.18).

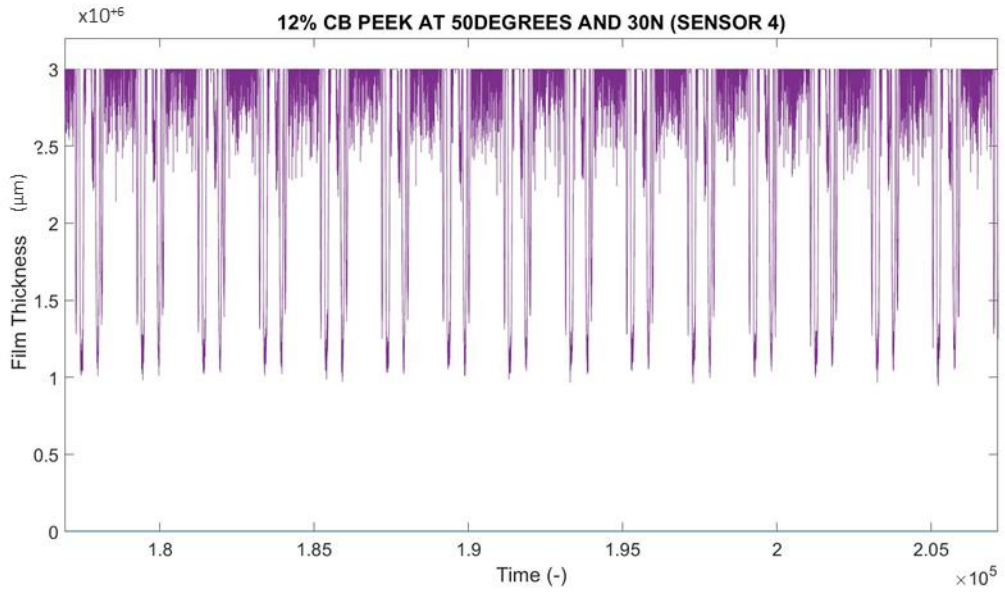

Figure 9.17 OFT Sensor 4 for PEEK at 12%CB, 50°C and 30N after 15seconds

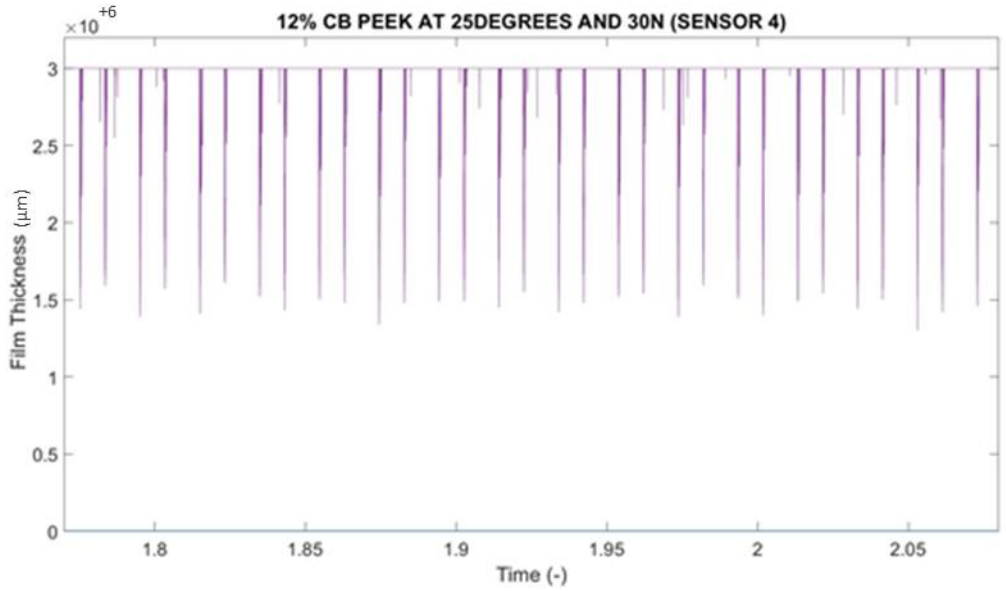

Figure 9.18 OFT Sensor 4 for PEEK at 12%CB, 25°C and 30N after 15seconds

9.7.3 Varying soot content

As can be seen in Figure 9.7 and Figure 9.9 , changes due to soot content do not vary significantly from Sensor 2 to Sensor 7, however, it varies significantly with Sensor 1 and Sensor 8. The first and last sensor shows thicker films compared to sensor 2 to 7, which shows thinner films. This could be seen from the mechanism shown in Figure

9.19 where the ring slides against the liner, the oil is pushed from front to back causing thicker film. And as the soot particles slides into the contact, thinner film is observed where the particles start to abrade the surface of the liner.

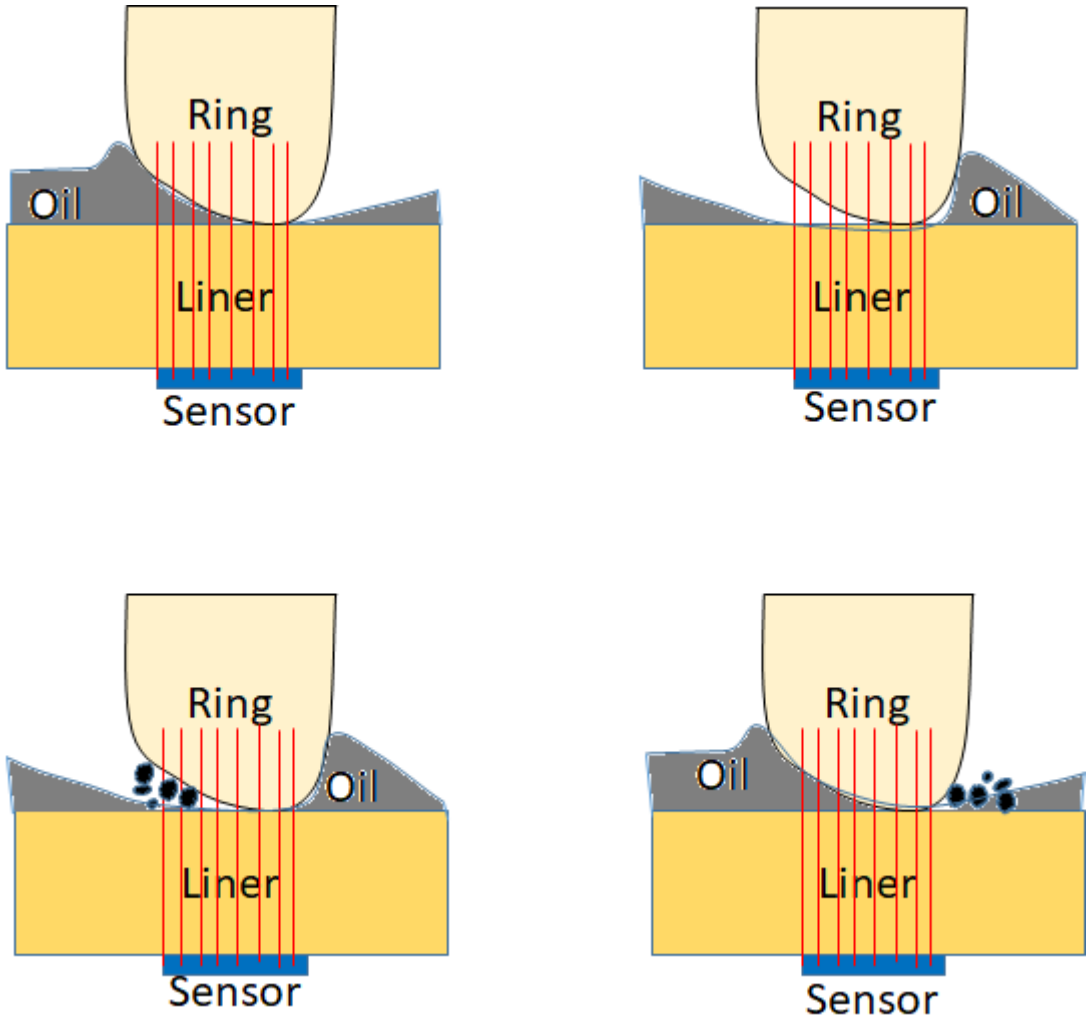

Figure 9.19 Mechanism showing the sliding of the ring on a liner with presence of carbon black content

9.7.4 Varying ring material

The wear image of worn PEEK as shown in Figure 9.13 shows that thinner film occurred when the ring slides against the liner where it also conforms to Figure 9.10. While Figure 9.11 and Figure 9.20 shows thicker film for NBR and less wear is shown on the ring. This shows that PEEK is more Hertzian than NBR because PEEK is stiffer than NBR. From the raw data of the ultrasound wave, it also shows that the PEEK is more consistent than NBR because PEEK is stiffer than NBR, where when sliding against the liner, the rubber tends to deform back to its shape.

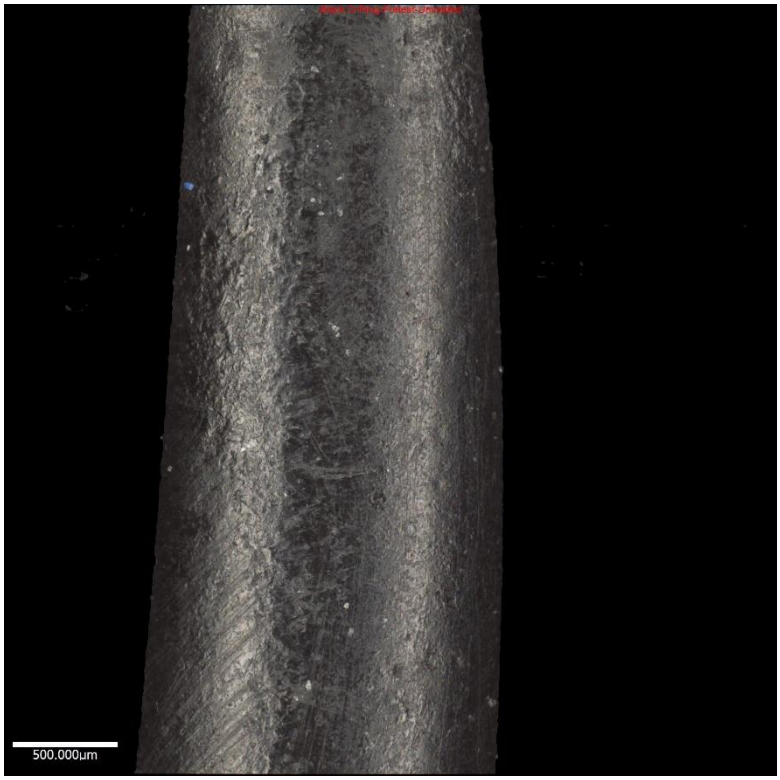

Figure 9.20 Worn NBR ring after test

9.8 Summary

The novel ultrasound technique approach has been used in determining the OFT for two different materials with two different lubricants (uncontaminated & contaminated). This method was developed by using a cross section of an O-ring sliding against a liner. The coding was developed by using the spring model approach to find the OFT for the non-metallic material. The following conclusions can be drawn from the results presented in this study:

- All sensors show a consistent trend throughout the test with most of the test showing that sensor 1 and 8 have thicker film than other sensors which could probably due to the agglomerates of the soot at either end of the contact. The OFT is thicker at low temperature and low load. Varying soot content also plays a role where visible soot content is found on the abraded surface of the liner.

- The OFT is also thicker with softer materials compared to stiffer material where worn surface of PEEK is more significant than rubber.

- This technique is still in development. It still needs improvement where more robust results can be obtained when determining the OFT especially for softer materials.

Chapter 10 General Discussion

10.1 Soot build-up

Due to the stringent emission legislations that are reviewed regularly, automotive industries need to improve and develop new formulations of lubricants and engine parts made from other materials that could increase the performance of an engine while reducing tribological performance, because of the resultant soot build-up in automotive engines.

There has been no agreement on the mechanism responsible for wear in soot contaminated lubricant for elastomer/polymer-to-metal contact, thus, the need for further fundamental studies on the wear mechanisms for elastomer materials.

10.2 Soot effects on elastomer/thermoplastic materials

From all the tests conducted in this research, it is observed that soot does effect the surface of the materials during sliding. The particles are either embedded on the surface due to the material properties or act as a three body abrasive that ploughs into the rubbing contact and removes parts of the sliding surface material. The soot particle content inside the lubricant does not affect the friction sliding of the elastomer/thermoplastic material, probably due to the hysteresis loss of the elastomer/thermoplastic surface that generates deformation of the surface. Soot inside the lubricant could also starve the lubricating contact thus reducing the film thickness between rubbing surfaces resulting in material removal during sliding.

10.3 Wear mechanisms induced by carbon black

Various forms of wear mechanisms were observed throughout the tests in this research work such as abrasive wear, adhesive wear and ploughing that causes material removal; however, the dominating wear mechanism that occurs throughout all tests is abrasive wear as dictated by the carbon black (CB) content at all operating conditions.

For 0% CB content, the wear mechanism was mild abrasion with some material removal for polymer material and also deformation of the sliding surface for elastomer material. For moderate carbon black content (5%), the observed wear was three-body abrasion where the carbon black particles infiltrate the area between both surfaces along with the entraining lubricant with removal of material as they slide against each other and also deformation of the sliding surfaces which occurs on elastomer materials. At higher carbon black content (12%), both wear mechanisms occur. The carbon black agglomerates tend to adhere more to the elastomer materials, but do not wear it abrasively. These hard particles can also get into the contact and abrade the

surface as observed under SEM for the PEEK O-ring. The carbon black agglomerates could also starve the contact by restricting the lubricant, resulting in elastomer/thermoplastic contact as the asperities of the specimens come into direct contact as shown in Figure 7.16.

10.4 Ultrasound film thickness

This study uses a novel approach of using an ultrasound technique to measure the oil film thickness between a section cut from an O-ring and a cylinder liner. This technique is a pilot test which was trialled on the Plint TE77 reciprocating test rig where 8 strips of sensors was placed on the back of the liner and the film thickness of the lubricant (fresh lubricant oil and 12% carbon black blended oil) were determined by using the spring model approach. The findings from the trialled test using were that:

- All sensors shows consistent trend of measured film thickness for all materials and different load and temperature and carbon black content.
- At 30N, the film thickness decreases compared to 20N due to higher contact pressure but the variation is minimal.
- When compared to temperature of 25°C and 50°C the film thickness is higher when at low temperature. The more viscous the lubricant, the thicker films in the contact.
- Two lubricant samples with different viscosity were tested using the liner specimen with two different materials. The film thickness shows consistent trend of film thickness. However, more wave is obtained for 0% lubricant. This could be due to the acoustic impedance of the lubricant where z value for 12% carbon black is higher than 0%.
- By focusing on a middle sensor (sensor 4), the film thickness is higher for NBR compared to PEEK at 50°C and less consistent compared to PEEK. This is because softer materials tend to deform more than PEEK resulting in the consistency of the wave captured.
- The effect of liner surface finish after the test were analysed. Moreover, the worn surfaces with visible carbon black detainment could be seen. The O-ring especially PEEK are also worn out when at higher load and temperature while for elastomer material, NBR the surface has not change significantly compared to before test were conducted.

This trialled pilot test is to build confidence in measuring the O-ring film thickness and comparing it with the previous tests using BICERI test rig and Plint TE77 test rig. The knowledge gained from these tests could provide help in improving the design and development of the film thickness measurements using ultrasound technique especially for elastomer materials.

One of the limitations from this trial pilot test is insufficient repeated tests to compare for other elastomer materials and at other contact parameters such as at higher load and sliding speed.

Chapter 11 Conclusions & Future Work

11.1 Conclusions

This chapter summarises the conclusions from various works conducted in this thesis. This study has provided an in-depth understanding of the effects of soot contaminated oil in elastomer/thermoplastic contacts specifically on seals. Finally, future work on this subject is also presented here.

The major findings of this research are presented in the following sections.

11.1.1 Wear analysis

For tests using the Plint TE77, as the temperature and carbon black content increases, the wear scar also increases. Elastomer material (NBR and Silicone shows a larger wear volume with a less abrasive scar compared to thermoplastic material (PEEK and PTFE) where thermoplastic material shows a lower wear volume, but a pronounced abrasive scar and material removal especially at higher temperature. This is because of the material properties of elastomer materials, where elastomer material deforms when sliding force is applied and recovers back to its original form or has delayed recovery after sliding has occurred. This indicates a direct relationship between wear and carbon black content, load and temperature. An increase in level of wear with respect to increase in carbon black content and temperature was also observed for the block-on-ring test configuration. The dominant form of wear found on the O-rings was abrasive wear and ploughing that causes material removal.

11.1.2 Coefficient of friction

The specimen tests using the Plint TE77, showed that the variation of friction with respect to temperature was not that significant with increase of carbon black content contamination for all materials. However, at higher soot concentration, the friction slightly increased. This is likely due to the agglomeration and thickening of oil. All tests on the Plint TE77 operate under a soft-elastohydrodynamic lubrication regime while for block-on-ring tests, harder materials operate under a hard-elastohydrodynamic lubrication regime. All of these regimes correlate with the calculated film thickness obtained in this study.

The study used a realistic approach whereby, a representative engine contact is used with realistic engine test conditions to help in producing reliable data. All the tests are laboratory-based; however, as said before, the engine contact were tested using suitable materials. From the results and analysis conducted, it can be concluded that the contact geometry and determination of lubrication regime where the O-rings are

operated will influence the level of wear they are experiencing from soot contamination.

11.1.3 Ultrasonic film thickness measurement

The spring model approached is used in determining the oil film thickness (OFT) of the softer materials when sliding against a liner. It was found that the OFT for PEEK is thinner thus causing the PEEK to wear and also contributes to the wear found on the surface of the liner, while NBR shows insignificant wear on the surface of the ring, this could probably be because the nature of rubber that could deform back when sliding on harder material.

All sensors also showed consistent trends throughout the test for all materials at different load, temperature and carbon black content. However, the OFT differs significantly with previous tests using the block-on-ring and O-ring-on-flat specimens. Thus more development and improvement of this technique should be done in order to validate with other experimental work done before. This study is a pilot trial test to ensure that this technique can be used to determine the OFT for elastomer materials.

11.2 Recommendations for future works

A quite number of variables and parameters in this study such as carbon black concentration, lubricant, friction, wear, viscosity, material properties of polymeric materials and film thickness. Detailed study of the combined effect of all these parameters can be very complex and time consuming. There are still various aspects of this study that were not investigated thoroughly, mainly due to time constraints. Possible future works for this study that can be investigated are as proposed below:

11.2.1 A follow-up on soot characterisation

This work has investigated soot characterisation in terms of roughness and size of soot on flat polished specimens. The simple test could be improved with the possibility of determining the hardness of real soot engine and also determining the structure and chemical properties of soot and particles size and compare it with soot surrogates therefore wear mechanism effects on elastomer/thermoplastic materials could be predicted. This would require a more established procedure in determining the hardness of soot. HRTEM can be used to measure the soot hardness using plasmon energy and hardness of carbon, graphite and diamond-like carbons.

11.2.2 Modelling of soot wear mechanism

Numerical simulation and modelling of automotive soot has not been studied intensively because they are still not fully understood. The soot wear study is complex which makes the simulation and predicting wear behaviour difficult. This is not only for metal-to-metal contact, but also on polymer-to-metal contact. With this soot modelling on polymer contact, it could verify the experimental works that previous and current research had done.

11.2.3 Visualisation of the soot movement in a contact

Leading from this study, an in-situ visualisation of soot movement in a contact is also a possible study that could give the conformity if the soot does abrade the surface of a contact, or does it block the lubricant from going into the contact. This future study is important for elastomer/thermoplastic materials in order to verify the post-test sliding effects in a contact with presence of soot.

A pin-on-disc test rig consists of a transparent disc and rubber ball with endoscopic system equipped with CCD camera could be develop to help understand the effects of soot especially on polymeric materials.

11.2.4 Investigate the viscoelastic properties on frictional heating

Study on viscoelastic properties of a contact on frictional heating with presence of soot is also important in order to predict failure mechanisms associated with excessive thermal effects caused by sliding friction. This could be done experimentally using an infrared thermal image system that helps measuring the surface temperature distribution when in sliding. This could then be verified with a proposed temperature model where it could determine the contact surface temperature in lubricated sliding system with presence of soot inside the lubricant especially for cases where the sliding contact area repeatedly sweeps over the same area on the contacting bodies.

11.2.5 Improvement on seal rig

It should be noted that the O-ring in this study is based on specimen/component contact; this is one of the limitations of the design. A continuation to this study is that it is suggested to upgrade/design a new test rig that could simulate real engine arrangement with O-ring as its subject of test.

11.2.6 Development of the ultrasound film thickness approach

More repeated test on the film thickness using ultrasound technique to see the changes in view of material and load. It could also help if the tests were conducted over a long period of time in order to investigate the running-in effects. This would improve the understanding of soot effects on wear of polymeric materials. A transparent liner could also be used in the test rig, to further understand what is happening in polymeric materials especially for elastomer materials. If this can be better characterised, then a comparison of the soot effects for polymeric materials between experimental and simulation can be made.

References

[1] C. Knauder, H. Allmaier, D. E. Sander, and T. Sams, “Investigations of the friction losses of different engine concepts. Part 1: A combined approach for applying subassembly-resolved friction loss analysis on a modern passenger-car diesel engine,” *Lubricants*, vol. 7, no. 5, pp. 1–35, 2019.

[2] R. Lewis and D.A. Green, “The effects of soot-contaminated engine oil on wear and friction: A review,” *J. Automob. Eng.*, vol. 222, pp. 1669–1689, 2008.

[3] D. A. Green, R. Lewis, and R. S. Dwyer-Joyce, “Wear effects and mechanisms of soot-contaminated automotive lubricants,” *Proc. Inst. Mech. Eng. Part J J. Eng. Tribol.*, vol. 220, no. 3, pp. 159–169, 2006.

[4] H. Nagai, I., Endo, H., Nakamura, H. and Yano, “Soot and Valve Train Wear in Passenger Car Diesel Engines,” *SAE Pap.*, no. 831757, 1983.

[5] S. Aldajah, O. O. Ajayi, G. R. Fenske, and I. L. Goldblatt, “Effect of exhaust gas recirculation (EGR) contamination of diesel engine oil on wear,” *Wear*, vol. 263, no. 1-6 SPEC. ISS., pp. 93–98, 2007.

[6] M. Gautam, K. Chitoor, M. Durbha, and J. C. Summers, “Effect of diesel soot contaminated oil on engine wear — investigation of novel oil formulations,” *Tribol. Int.*, vol. 32, pp. 687–699, 1999.

[7] B. Jayashankara and V. Ganesan, “Effect of fuel injection timing and intake pressure on the performance of a di diesel engine - A parametric study using CFD,” *Energy Convers. Manag.*, vol. 51, no. 10, pp. 1835–1848, 2010.

[8] M. A. Zuber, W. Mohd, F. W. Mahmood, Z. Z. Abidin, and Z. Harun, “In-Cylinder Soot Particle Distribution in Squish Region of a Direct Injection Diesel Engine,” no. 05, 2014.

[9] C. Automotive, “Worldwide Emission Standards and Related Regulations - Passenger Cars / Light and Medium Duty Vehicles.”

[10] T. G. Vlachos, P. Bonnel, A. Perujo, M. Weiss, P. Mendoza Villafuerte, and F. Riccobono, “In-Use Emissions Testing with Portable Emissions Measurement Systems (PEMS) in the Current and Future European Vehicle Emissions Legislation: Overview, Underlying Principles and Expected Benefits,” *SAE International Journal of Commercial Vehicles*, vol. 7, no. 1. SAE International, pp. 199–215, 2014.

[11] H. Spikes, “Tribology research in the twenty-first century,” *Tribol. Int.*, vol. 34, no. 12, pp. 789–799, 2001.

[12] G. Stachowiak and A. W. Batchelor, *Engineering Tribology*. Butterworth-Heinemann, 2013.

[13] V. W. Wong and S. C. Tung, “Overview of automotive engine friction and reduction trends–Effects of surface, material, and lubricant-additive technologies,” *Friction*, vol. 4, no. 1, pp. 1–28, 2016.

[14] P. Nagendramma and S. Kaul, “Development of ecofriendly/biodegradable lubricants: An overview,” *Renew. Sustain. Energy Rev.*, vol. 16, no. 1, pp. 764–774, 2012.

[15] C. J. Reeves, P. L. Menezes, T.-C. Jen, and M. R. Lovell, “The effect of surface roughness on the tribological performance of environmentally friendly bio-based lubricants with varying particle size,” in *STLE Annual Meeting and Exhibition, Detroit, MI, May*, 2013, pp. 5–9.

[16] P. G. Nikolakopoulos and D. A. Bompos, “Experimental measurements of journal bearing friction using mineral, synthetic, and bio-based lubricants,” *Lubricants*, vol. 3, no. 2, pp. 155–163, 2015.

[17] N. Salih, J. Salimon, and E. Yousif, “The physicochemical and tribological properties of oleic acid based triester biolubricants,” *Ind. Crops Prod.*, vol. 34, no. 1, pp. 1089–1096, 2011.

[18] L. R. Rudnick, *Lubricant Additives: Chemistry and Applications, Second Edition*. CRC Press, 2009.

[19] J. Williams, Ed., “Contact between surfaces,” in *Engineering Tribology*, Cambridge: Cambridge University Press, 2005, pp. 73–131.

[20] C. Delprete and A. Razavykia, “Piston dynamics, lubrication and tribological performance evaluation: A review,” *Int. J. Engine Res.*, Jun. 2018.

[21] A. Thate, W. Mach, and J. Bölter, “Soot in Used Oils,” in *Encyclopedia of Lubricants and Lubrication*, T. Mang, Ed. Berlin, Heidelberg: Springer Berlin Heidelberg, 2014, pp. 1930–1942.

[22] Y. Yan, “7 - Tribology and tribo-corrosion testing and analysis of metallic biomaterials,” in *Metals for Biomedical Devices*, Woodhead Publishing Limited, 2010, pp. 178–201.

[23] G. Wang and X. Nie, “Effect of Surface Roughness and Sliding Velocity on Tribological Properties of an Oxide-Coated Aluminum Alloy,” *SAE Tech. Pap.*, no. 2014-01–0957, 2014.

[24] P. J. Blau, B. Dumont, D. N. Braski, T. Jenkins, E. S. Zanoria, and M. C. Long, “Reciprocating friction and wear behavior of a ceramic-matrix graphite composite for possible use in diesel engine valve guides,” *Wear*, vol. 225–229, no. PART II, pp. 1338–1349, 1999.

[25] Gwidon W. Stachowiak, *Wear: Materials, Mechanisms and Practice*. John Wiley & Sons, Ltd, 2006.

[26] Kenneth C Ludema, *Friction, Wear, Lubrication: A Textbook in Tribology*. CRC Press, 1996.

[27] S. Zhang, *Tribology of Elastomers*. Elsevier Science, 2004.

[28] A. Abdelbary, “Wear of Polymers and Composites,” in *Wear of Polymers and Composites*, Woodhead Publishing Limited, 2015, pp. 1–223.

[29] D. H. Buckley, *Surface effects in adhesion, friction, wear and lubrication*. Elsevier, 1981.

[30] B. Bhushan, *Introduction to Tribology, Second Edition*, 2nd Editio. John Wiley & Sons, Ltd, 2013.

[31] B. Briscoe and S. K. Sinha, “Wear of polymers,” *Proc. Inst. Mech. Eng. Part J J. Eng. Tribol.*, vol. 216, no. 6, pp. 401–413, 2002.

[32] W. Wieleba, “The Mechanism of Tribological Wear of Thermoplastic Materials,”

Arch. Civ. Mech. Eng., vol. 7, no. 4, pp. 185–199, 2007.

[33] A. D. . Clague, J. . Donnet, T. . Wang, and J. C. . Peng, “A comparison of diesel engine soot with carbon black,” *Carbon*, vol. 37, no. 10. pp. 1553–1565, 1999.

[34] D. R. Snelling *et al.*, “Particulate Matter Measurements in a Diesel Engine Exhaust by Laser-Induced Incandescence and the Standard Gravimetric Procedure,” *SAE Trans. - J. Fuels Lubr.*, vol. 108–4, 1999.

[35] S. Li, A. A. Csontos, B. M. Gable, C. A. Passut, and T. Jao, “Wear in Cummins M-11 / EGR Test Engines,” *SAE Trans.*, vol. 111, pp. 2258–2271, 2002.

[36] K. et al. Kawatani, T., Mori, K., Fukano, I., Sugawara, “Technology for Meeting the 1994 USA Exhaust Emission Regulations on Heavy-Duty Diesel Engine,” *SAE Pap.*, no. 932654, 1993.

[37] E. Hu, X. Hu, T. Liu, R. Song, K. D. Dearn, and H. Xu, “Effect of TiF3 catalyst on the tribological properties of carbon black-contaminated engine oils,” *Wear*, vol. 305, no. 1–2, pp. 166–176, 2013.

[38] F. Chinas-Castillo and H. a. Spikes, “The behavior of diluted sooted oils in lubricated contacts,” *Tribol. Lett.*, vol. 16, no. 4, pp. 317–322, 2004.

[39] M. Gautam, M. Durbha, K. Chitoor, M. Jaraiedi, N. Mariwalla, and D. Ripple, “Contribution of soot contaminated oils to wear,” in *Proceedings of the 1998 SAE International Spring Fuels and Lubricants Meeting and Exposition*, 1998, pp. 55–67.

[40] S. George, S. Balla, and M. Gautam, “Effect of diesel soot contaminated oil on engine wear,” *Wear*, vol. 262, no. 9–10, pp. 1113–1122, 2007.

[41] R. Penchaliah, T. J. Harvey, R. J. K. Wood, K. Nelson, and H. E. G. Powrie, “The effects of diesel contaminants on tribological performance on sliding steel on steel contacts,” *Proc. IMechE Part J J.Engineering Tribol.*, vol. 225, pp. 779–797, 2011.

[42] S. Antusch, M. Dienwiebel, E. Nold, P. Albers, U. Spicher, and M. Scherge, “On the tribochemical action of engine soot,” *Wear*, vol. 269, no. 1–2, pp. 1–12, 2010.

[43] D. a. Green, R. Lewis, and R. S. Dwyer-Joyce, “Wear of Valve Train Components Due to Soot Contaminated Lubricant,” *SAE Tech. Pap. 2006-01-1098*, no. 724, 2006.

[44] D. A. Green and R. Lewis, “Effect of soot on oil properties and wear of engine components,” *Journal of Physics D: Applied Physics*, vol. 40, no. 18. pp. 5488–5501, 2007.

[45] C. Kuo Cheng, A. Passut Charles, C. Jao Tze, A. Csontos Aladar, and M. Howe James, “Wear mechanism in Cummins M-11 high soot diesel test engines1. Kuo Cheng, C., Passut Charles, a, Jao Tze, C., Csontos Aladar, a & Howe James, M. Wear mechanism in Cummins M-11 high soot diesel test engines. Proc. 1998 SAE Int. Spring Fuels Lubr. Meet. Exp,” *Proc. 1998 SAE Int. Spring Fuels Lubr. Meet. Expo.*, vol. 1368, no. 724, pp. 21–32, 1998.

[46] D. J. Growney *et al.*, “Is Carbon Black a Suitable Model Colloidal Substrate for Diesel Soot?,” *Langmuir*, vol. 31, no. 38, pp. 10358–10369, 2015.

[47] I. Berbezier, J. M. Martin, and P. Kapsa, “The role of carbon in lubricated mild wear,” *Tribol. Int.*, vol. 19, no. 3, pp. 115–122, 1986.

[48] M. Kawamura, T. Ishiguro, K. Fujita, and H. Morimoto, “Deterioration of antiwear properties of diesel engine oils during use,” *Wear*, vol. 123, pp. 269–280, 1988.

[49] M. Soejima, Y. Ejima, K. Uemori, and M. Kawasaki, “Studies on friction and wear characteristics of cam and follower: Influences of soot contamination in engine oil,” *JSAE Rev.*, vol. 23, no. 1, pp. 113–119, 2002.

[50] P. Ramkumar, L. Wang, T. J. Harvey, R. J. K. Wood, K. Nelson, and E. S. Yamaguchi, “The effect of diesel engine oil contamination on friction and wear,” in *Proceedings of WTC2005 World Tribology Congress III September 12-16, 2005, Washington, D.C., USA*, 2005, pp. 1–2.

[51] C. Liu, S. Nemoto, and S. Ogano, “Effect of Soot Properties in Diesel Engine Oils on Frictional Characteristics,” *Tribol. Trans.*, vol. 46, no. 1, pp. 12–18, 2003.

[52] J. J. Truhan, J. Qu, and P. J. Blau, “The effect of lubricating oil condition on the friction and wear of piston ring and cylinder liner materials in a reciprocating bench test,” *Wear*, vol. 259, no. 7–12, pp. 1048–1055, 2005.

[53] S. George, S. Balla, V. Gautam, and M. Gautam, “Effect of diesel soot on lubricant oil viscosity,” *Tribol. Int.*, vol. 40, no. 5, pp. 809–818, 2007.

[54] M. J. Souza de Carvalho, P. Rudolf Seidl, C. R. Pereira Belchior, and J. Ricardo Sodré, “Lubricant viscosity and viscosity improver additive effects on diesel fuel economy,” *Tribol. Int.*, vol. 43, no. 12, pp. 2298–2302, 2010.

[55] H. Sato, N. Tokuoka, H. Yamamoto, and M. Sasaki, “Study on Wear Mechanism by Soot Contaminated in Engine Oil (First Report: Relation Between Characteristics of Used Oil and Wear),” *SAE Tech. Pap.*, no. 724, pp. 1–7, 1999.

[56] E. Hu, X. Hu, T. Liu, L. Fang, K. D. Dearn, and H. Xu, “The role of soot particles in the tribological behavior of engine lubricating oils,” *Wear*, vol. 304, no. 1–2, pp. 152–161, 2013.

[57] M. Ã. Kaneta, T. Irie, H. Nishikawa, and K. Matsuda, “Effects of soot on wear in elastohydrodynamic lubrication contacts,” *Engineering*, vol. 220, pp. 307–317, 2006.

[58] P. Ramkumar, T. J. Harvey, R. J. K. Wood, A. D. Rose, D. C. Woods, and S. M. Lewis, “Factorial study of diesel engine oil contamination effects on steel and ceramic sliding contacts,” *Proc. Inst. Mech. Eng. Part J J. Eng. Tribol.*, vol. 233, no. 5, pp. 726–740, 2019.

[59] E. S. Yamaguchi, M. Untermann, S. H. Roby, P. R. Ryason, and S. W. Yeh, “Soot Wear in Diesel Engines,” *Proc. Inst. Mech. Eng. Part J J. Eng. Tribol.*, vol. 220, pp. 463–469, 2006.

[60] K. Ishiki, S. Oshida, M. Takiguchi, and M. Urabe, “A Study of Abnormal Wear in Power Cylinder of Diesel Engine with EGR - Wear Mechanism of Soot Contaminated in Lubricating Oil,” *SAE Tech. Pap.*, no. 2000-01–0925, 2000.

[61] E. Feyzullaho lu, “Abrasive wear, thermal and viscoelastic behaviors of rubber

seal materials used in different working conditions," *Proc. Inst. Mech. Eng. Part J J. Eng. Tribol.*, vol. 229, no. 1, pp. 64–73, 2014.

[62] S. H. Lee, S. S. Yoo, D. E. Kim, B. S. Kang, and H. E. Kim, "Accelerated wear test of FKM elastomer for life prediction of seals," *Polym. Test.*, vol. 31, no. 8, pp. 993–1000, 2012.

[63] S.-M. PARK, T.-Y. WON, G.-H. KIM, D.-S. KIM, and Y.-Z. LEE, "Effect of Dust Particle Inflow on the Wear of Rubber Seal Material in Automobile Chassis System," *Tribol. Trans.*, vol. 54, no. 1, pp. 87–95, 2010.

[64] H. M. Ayala, D. P. Hart, O. C. Yeh, and M. C. Boyce, "Wear of Elastomeric Seals in Abrasive," *Wear*, vol. 220, no. 1, pp. 9–21, 1998.

[65] M. Mofidi and B. Prakash, "The Influence of Lubrication on Two-body Abrasive Wear of Sealing Elastomers Under Reciprocating Sliding Conditions," *J. Elastomers Plast.*, vol. 43, no. 1, pp. 19–31, 2011.

[66] M. Harmon and R. Lewis, "Review of top of rail friction modifier tribology Review of top of rail friction modifier tribology," *Tribol. - Mater. Surfaces Interfaces*, vol. 10, no. 3, pp. 150–162, 2016.

[67] L. B. Abdulqadir, N. F. Mohd Nor, R. Lewis, and T. Slatter, "Contemporary challenges of soot build-up in IC engine and their tribological implications," *Tribol. - Mater. Surfaces Interfaces*, vol. 12, no. 3, pp. 115–129, 2018.

[68] R. S. Dwyer-Joyce, "Tribological Design Data," *Contact Mechanics*, 1997. [Online]. Available: http://www.leonardocentre.co.uk/media/default/documents/book_3_contact_mechanics.pdf.

[69] L. B. Abdulqadir, "Investigation of the effects of soot on the wear of automotive engine components," 2015.

[70] B. J. Hamrock, B. J. Schmid, and B. O. Jacobson, *Fundamentals of Fluid Film Lubrication*. CRC Press, 2004.

[71] D. A. Green and R. Lewis, "The effects of soot-contaminated engine oil on wear and friction: a review," *Proceedings of the Institution of Mechanical Engineers, Part D: Journal of Automobile Engineering*, vol. 222, no. 9. pp. 1669–1689, 2008.

[72] R. Lewis and T. Slatter, "Design for Reduced Wear ," *Automotive Lubricants and Testing* . pp. 293–315, 01-Nov-2012.

[73] P. A. Schweitzer, *Mechanical and Corrosion-Resistant Properties of Plastics and Elastomers*. CRC Press, 2000.

[74] G.-03 ASTM, "Scratch Hardness of Materials Using a Diamond Stylus," 2017.

[75] B. Bhushan, *Fundamentals of Tribology and Bridging the Gap Between the Macro- and Micro / Nanoscales*, 1st ed. Springer Netherlands, 2001.

[76] B. J. Hamrock and D. Dowson, "Minimum film thickness in elliptical contacts for different regimes of fluid-film lubrication," *NASA Tech. Pap.*, 1978.

[77] M. Esfahanian and B. J. Hamrock, "Fluid-Film Lubrication Regimes Revisited," *Tribol. Trans.*, vol. 34, no. 4, pp. 628–632, Jan. 1991.

[78] N. Marx, J. Guegan, and H. A. Spikes, "Elastohydrodynamic film thickness of

soft EHL contacts using optical interferometry," *Tribol. Int.*, vol. 99, pp. 267–277, 2016.

[79] G. Zhang, H. Yu, C. Zhang, H. Liao, and C. Coddet, "Temperature dependence of the tribological mechanisms of amorphous PEEK (polyetheretherketone) under dry sliding conditions," *Acta Mater.*, vol. 56, no. 10, pp. 2182–2190, 2008.

[80] F. E. Kennedy, "Frictional heating and contact temperatures," *Mod. Tribol. Handb.*, vol. 1, pp. 235–272, 2001.

[81] L. I. Farfán-Cabrera, E. A. Gallardo-Hernández, C. D. Reséndiz-Calderón, and C. Sedano de la Rosa, "Physical and Tribological Properties Degradation of Silicone Rubber Using Jatropha Biolubricant," *Tribol. Trans.*, vol. 61, no. 4, pp. 640–647, Jul. 2018.

[82] L. I. F. Cabrera, E. A. G. Hernandez, and C. D. R. Calderon, "Abrasive wear study of a nitrile butadiene rubber (NBR) rotary seal in dry and muddy contact s using a micro-abrasion tester," *Superf. y vacío*, vol. 30, no. 1, pp. 1–5, 2017.

[83] B. Bhushan, *MODERN TRIBOLOGY HANDOOK VOLUME ONE*. CRC Press, 2001.

[84] B. J. Briscoe and S. K. Sinha, "Tribological applications of polymers and their composites: Past , present and future prospects," *Tribol. Interface Eng. Ser.*, vol. 55, pp. 1–14, 2008.

[85] V. L. Popov, "Viscoelastic Properties of Elastomers," in *Contact Mechanics and Friction*, Springer, 2017, pp. 255–281.

[86] O. O. Ajayi and R. A. Erck, "Variation of nominal contact pressure with time during sliding wear," *International Joint Tribology Conference*. pp. 1–17, 2001.

[87] J. Khedkar, I. Negulescu, and E. I. Meletis, "Sliding wear behavior of PTFE composites," *Wear*, vol. 252, no. 5–6, pp. 361–369, 2002.

[88] V. Rodriguez, J. Sukumaran, A. K. Schlarb, and P. De Baets, "Influence of solid lubricants on tribological properties of polyetheretherketone (PEEK)," *Tribol. Int.*, vol. 103, pp. 45–57, 2016.

[89] R. Lewis and R. S. Dwyer-Joyce, "Wear of diesel engine inlet valves and seat inserts," *Proc. Inst. Mech. Eng. part D J. Automob. Eng.*, vol. 216, no. 3, pp. 205–216, 2002.

[90] G. F. Simmons, M. Mofidi, and B. Prakash, "Friction evaluation of elastomers in lubricated contact," *Lubr. Sci.*, vol. 21, no. 10, pp. 427–440, Nov. 2009.

[91] D.-H. Kim, S.-S. Yoo, H.-J. Kim, and D.-E. Kim, "Surface damage behavior of polyurethane O-rings in automated material handling system for glass panels," *Int. J. Precis. Eng. Manuf.*, vol. 17, no. 1, pp. 43–50, 2016.

[92] N. Argibay and W. G. Sawyer, "Low wear metal sliding electrical contacts at high current density," *Wear*, vol. 274–275, pp. 229–237, 2012.

[93] R. Roshan *et al.*, "Friction Modelling in Boundary Lubrication Considering the Effect of MoDTC and ZDDP in Engine Oils," *Tribol. Online*, vol. 6, no. 7, pp. 301–310, 2011.

[94] R. Dwyer-Joyce, B. W. Drinkwater, and C. J. Donohoe, "The measurement of

lubricant-film thickness using ultrasound," *Proc. R. Soc. A Math. Phys. Eng. Sci.*, vol. 459, Apr. 2003.

[95] E. Avan, A. Spencer, R. Dwyer-Joyce, A. Almqvist, and R. Larsson, "Experimental and numerical investigations of oil film formation and friction in a piston ring–liner contact," *Proc. Inst. Mech. Eng. Part J J. Eng. Tribol.*, vol. 227, pp. 126–140, Feb. 2013.

[96] S. Beamish, "Oil Film Thickness Measurement Program." 2019.

Appendices

Appendix A-1 Hertzian Point Contact Pressure

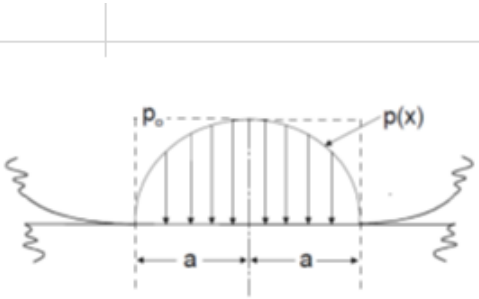

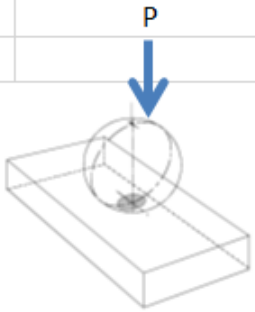

$$p_0 = \frac{3P}{2\pi a^2}$$

	Cast Iron EN1351	EN24	
Load, P	50	50	N
Radius, R_1	3	3	mm
Radius, R_2	1.00E+100	1.00E+100	mm
1/R	0.333333333	0.3333333	
R	3	3	mm
v_1	0.3	0.3	
v_2	0.26	0.3	
E_1	215	215	GPa
E_2	103	210	GPa
1/E*	0.013284985	0.0085659	
E*	75.27294729	116.74208	GPa
a	0.000114333	9.877E-05	m
a	0.114332895	0.0987738	mm
Maximum contact pressure, p_o	**1.82628684**	**2.4469664**	GPa
Average contact pressure, p_m	**1.21752456**	**1.6313109**	GPa

Appendix A-2 Hertzian Point Contact Pressure

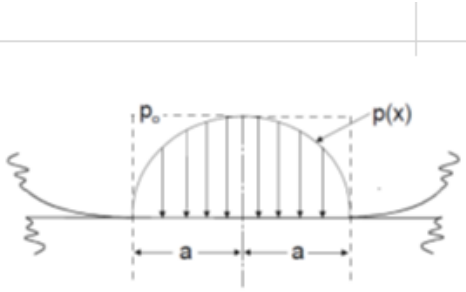

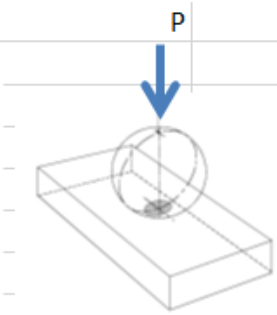

$$p_0 = \frac{3P}{2\pi a^2}$$

	PEEK	PTFE	NBR	Silicone	
Load, P	10	10	10	10	N
Radius, R_1	3	3	3	3	mm
Radius, R_2	1.00E+100	1.00E+100	1E+100	1E+100	mm
1/R	0.333333333	0.3333333	0.33333	0.33333	
R	3	3	3	3	mm
v_1	0.3	0.3	0.3	0.3	
v_2	0.37	0.46	0.5	0.49	
E_1	215	215	215	215	GPa
E_2	4.2	2.8	0.00102	0.005	GPa
1/E*	0.209732558	0.285804	735.298	151.984	
E*	4.767976936	3.4989015	0.00136	0.00658	GPa
a	0.000167732	0.000186	0.00255	0.00151	m
a	0.167732077	0.1859589	2.54809	1.50659	mm
Maximum contact pressure, p_o	**0.169710666**	**0.1380726**	**0.00074**	**0.0021**	GPa
Average contact pressure, p_m	**0.113140444**	**0.0920484**	**0.00049**	**0.0014**	GPa

Appendix B-1 Minimum Oil Film Thickness Calculation (Example for EN24)

Film Thickness Calculation

Lubricant Temperature, T	100	°C
Load, w	50	N
Ball Radius	3	mm
Sliding speed	0.133	m/s
Modulus of elasticity of Ball Specimen	215	Gpa
Modulus of elasticity of Flat Specimen	260	GPa
Poisson ratio of Ball Specimen	0.3	
Poisson ratio of Flat Specimen	0.3	
Effective Radius in x direction, Rx	0.0015	m
Mean surface velocity, u	0.0665	m/s
Effective Modulus of Elasticity, E'	2.59E+11	Pa
Dimensionless Load Parameter, W	8.59E-05	
Elipticity Parameter, k	1.034	
r.m.s roughness, σ*	6.53E-07	m

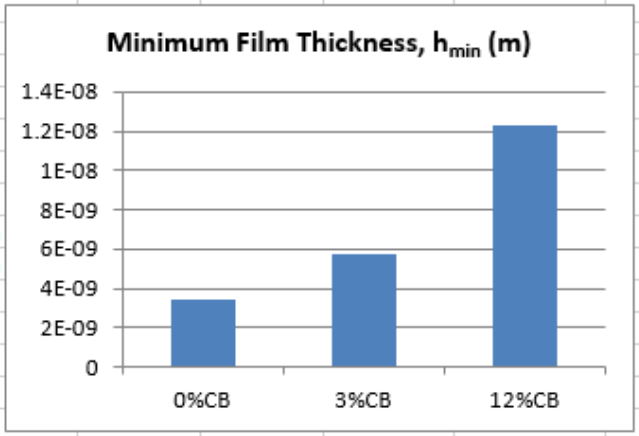

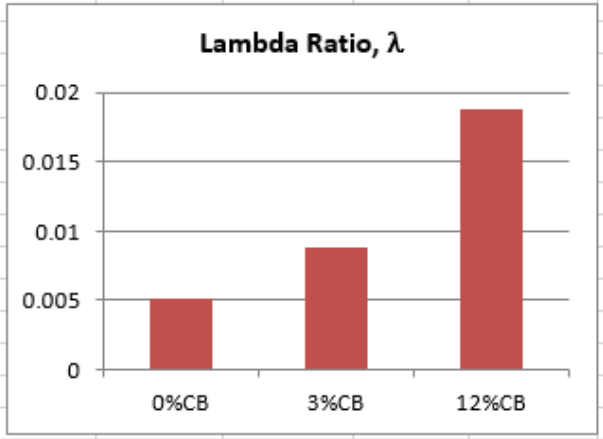

$$H_{min} = 3.63U^{0.68}G^{0.49}W^{-0.073}\left(1 - e^{-0.68k}\right)$$

Sooty oil	Kinematic Viscosity @40°C (cSt)	Kinematic Viscosity @100°C (cSt)	Density at 15°C (g/cm^3)	Density at T°C (g/cm^3)	Dynamic viscosity at temperature T & atm pressure, (Pa.s)	Pressure Viscosity-coefficient, αEHL (Pa^{-1})	Dimensionless Material Parameter, G	Dimensionless Speed Parameter, U	Dimensionless Minimum Film Thickness, H_{min}	**Minimum Film Thickness, h_{min} (m)**	**Lambda Ratio, λ**
0%CB	106	14.27	0.866	0.819626	0.0116961	1.43E-08	3707.1561	2E-12	2.261E-06	**3.39E-09**	**0.0051927**
3%CB	184.17	50.874	0.881	0.833822	0.0424199	7.04E-09	1820.7506	7.27E-12	3.832E-06	**5.75E-09**	**0.0088016**
12%CB	1156.1	888.07	0.928	0.878306	0.7799969	5.82E-10	150.49974	1.34E-10	8.18E-06	**1.23E-08**	**0.0187892**

Appendix B-2 Minimum Oil Film Thickness Calculation (Example for NBR)

Film Thickness Calculation

Lubricant Temperature, T	25	°C
Load, w	10	N
Ball Radius	3	mm
Sliding speed	0.14	m/s
Modulus of elasticity of Ball Specimen	215	Gpa
Modulus of elasticity of Flat Specimen	0.0049	GPa
Poisson ratio of Ball Specimen	0.3	
Poisson ratio of Flat Specimen	0.48	
Effective Radius in x direction, Rx	0.0015	m
Mean surface velocity, u	0.07	m/s
Effective Modulus of Elasticity, E'	12733545	Pa
Dimensionless Load Parameter, W	0.349034	
Elipticity Parameter, k	1.034	
r.m.s roughness, σ*	3.25E-06	m

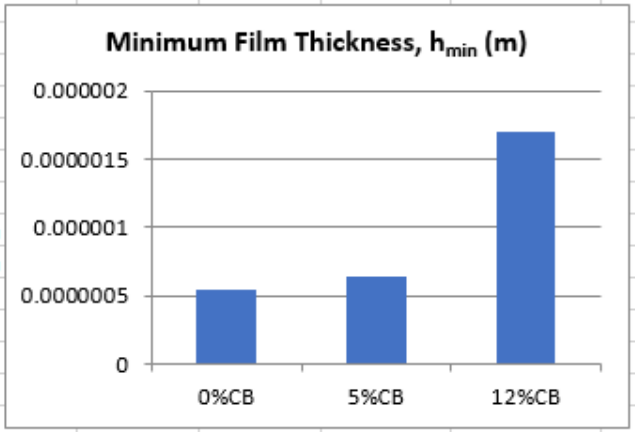

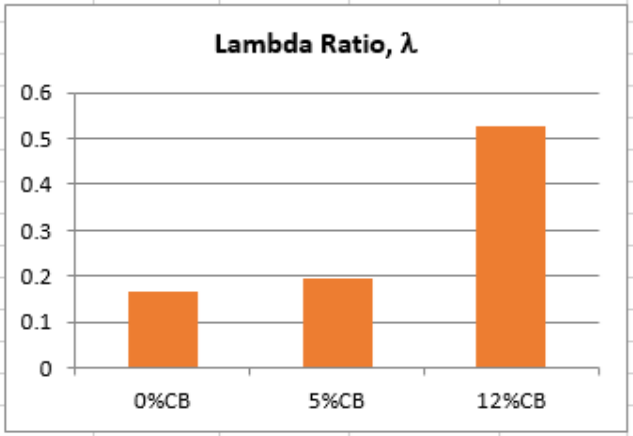

$$H_{min} = 3.63U^{0.68}G^{0.49}W^{-0.073}\left(1 - e^{-0.68k}\right)$$

Sooty oil	Kinematic Viscosity @40°C (cSt)	Kinematic Viscosity @100°C (cSt)	Density at 15°C (g/cm^3)	Density at T°C (g/cm^3)	Dynamic viscosity at temperature T & atm pressure, (Pa.s)	Pressure Viscosity-coefficient, αEHL (Pa^{-1})	Dimensionless Material Parameter, G	Dimensionless Speed Parameter, U	Dimensionless Minimum Film Thickness, H_{min}	**Minimum Film Thickness, h_{min} (m)**	**Lambda Ratio, λ**
0%CB	106	14.27	0.866	0.860544	0.1979003	2.21E-08	0.2813744	7.25E-07	0.0003628	**5.4416E-07**	**0.1674022**
5%CB	239.35	131.86	0.891	0.885387	0.2535407	2.29E-09	0.0291473	9.29E-07	0.0004262	**6.3924E-07**	**0.1966537**
12%CB	1156.1	888.07	0.928	0.922154	1.1499	5.82E-10	0.0074093	4.21E-06	0.0011386	**1.7079E-06**	**0.5254121**

Appendix C Raw Data for Wear Profile

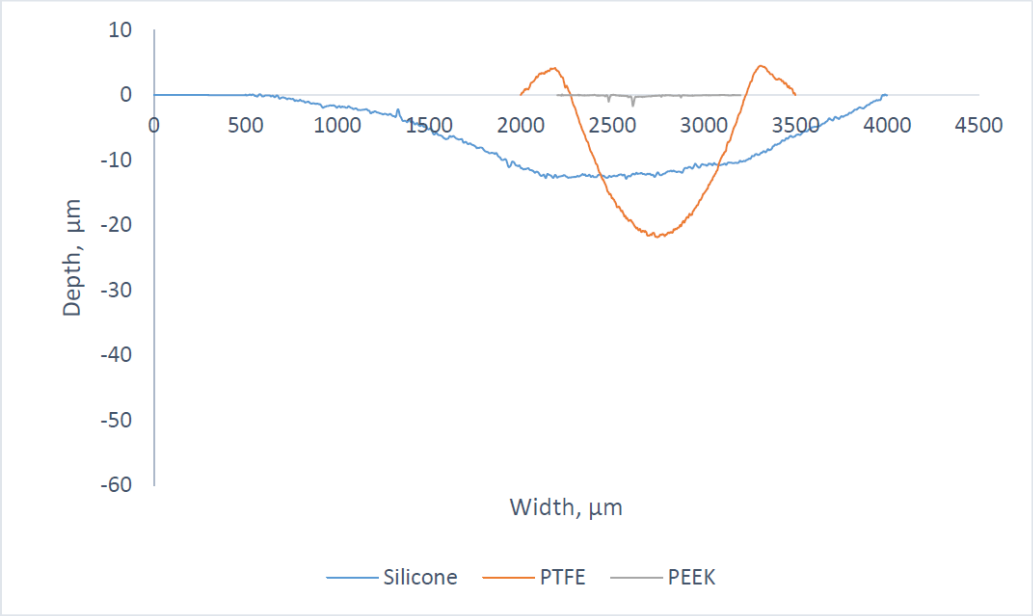

Figure 1 Wear scar profiles for Silicone, PTFE and PEEK at 100°C, 10N

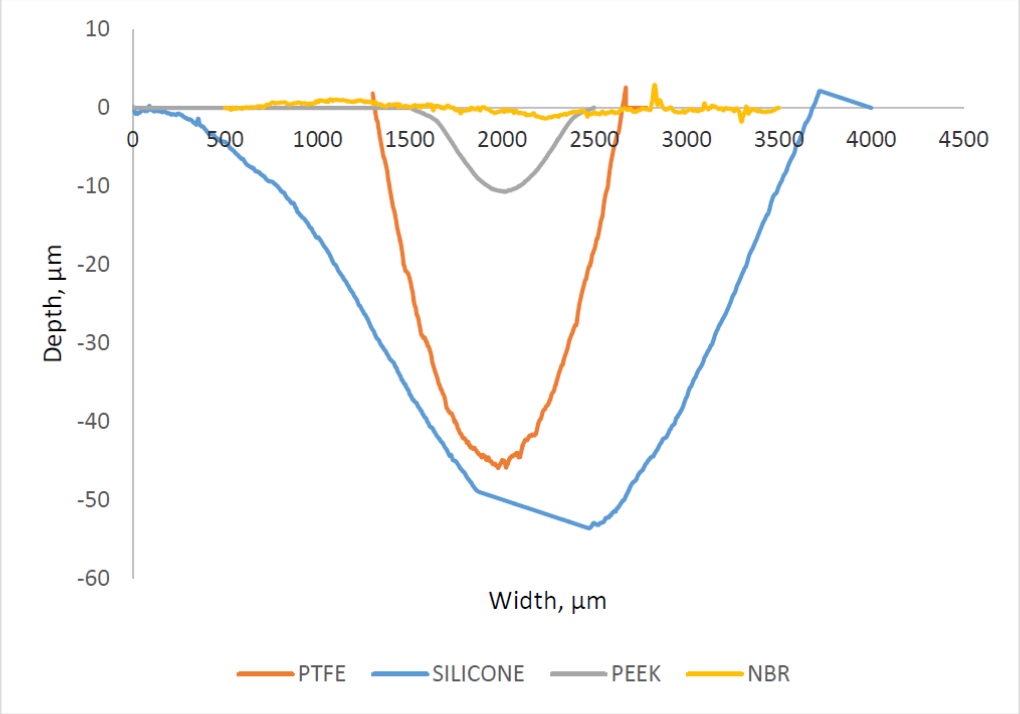

Figure 2 Wear scar profiles for all polymers at 5% Carbon Black, 100°C and 30N

Appendix D Raw Data for OFT using Ultrasound Technique

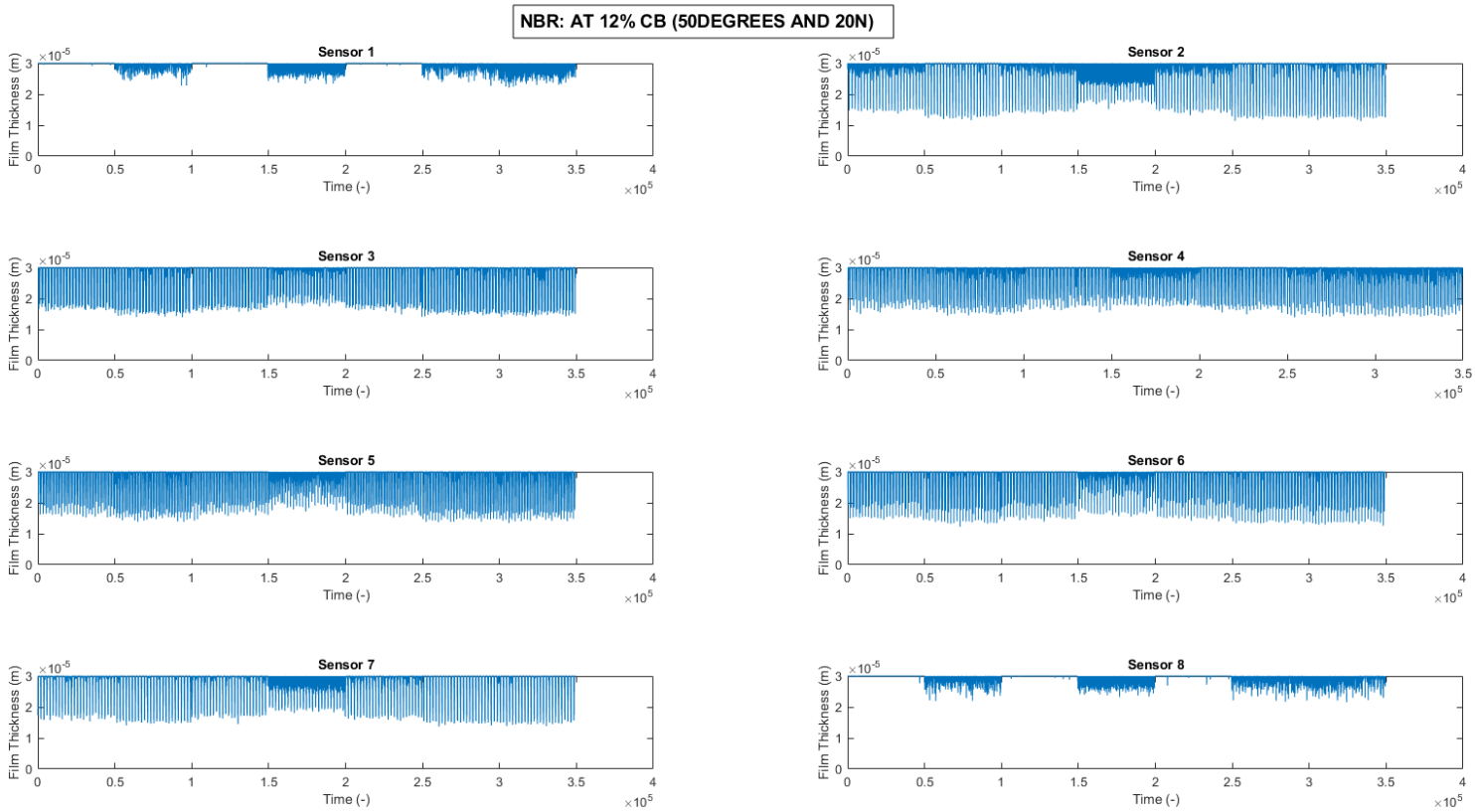

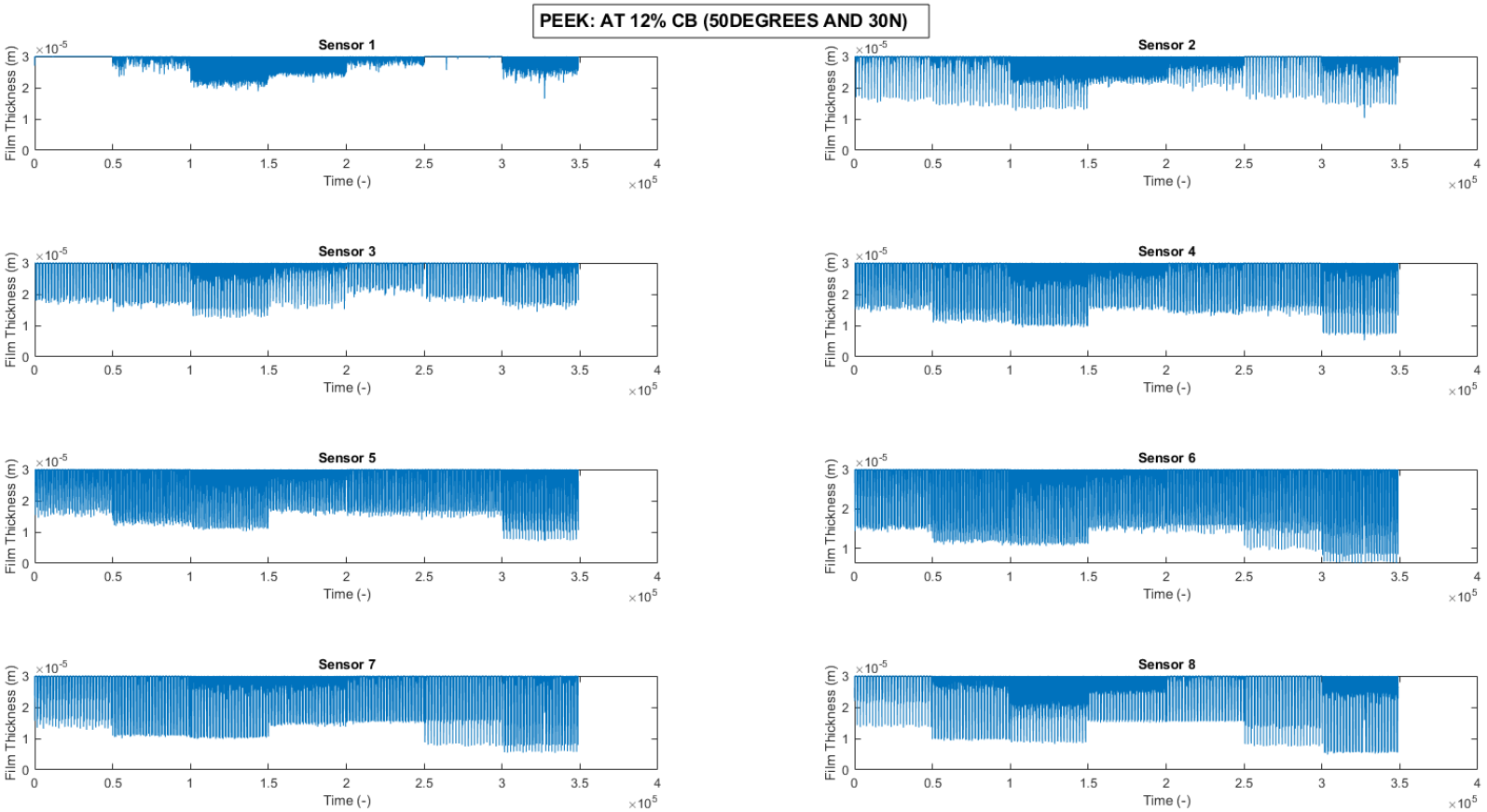
PEEK: AT 12% CB (50DEGREES AND 30N)
Sensor 1
Sensor 2
Sensor 3
Sensor 4
Sensor 5
Sensor 6
Sensor 7
Sensor 8
Film Thickness (m)
Time (-)
×10^-5
×10^5

PEEK: AT 12% CB (50DEGREES AND 20N)

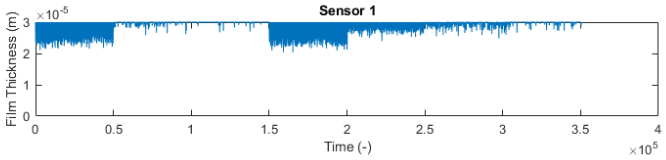

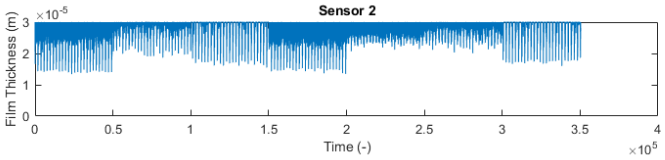

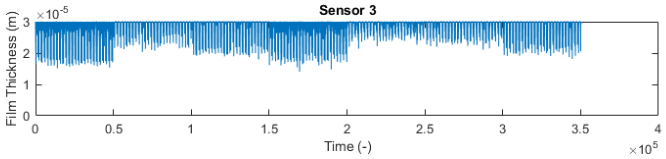

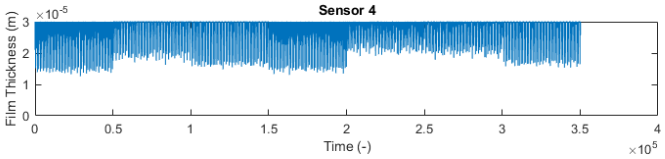

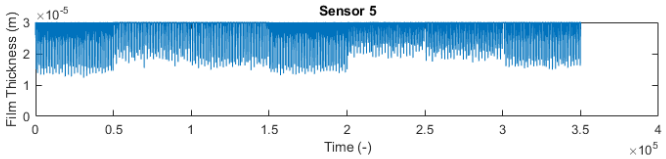

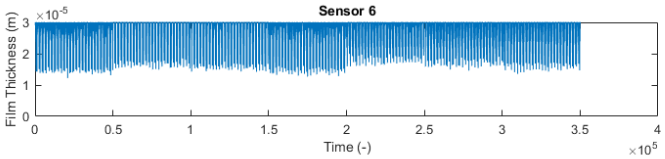

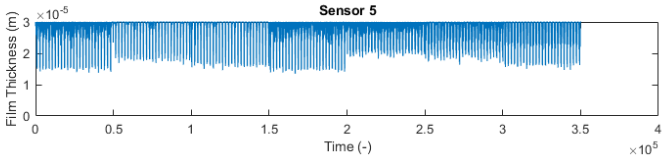

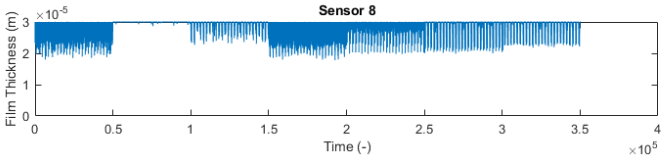

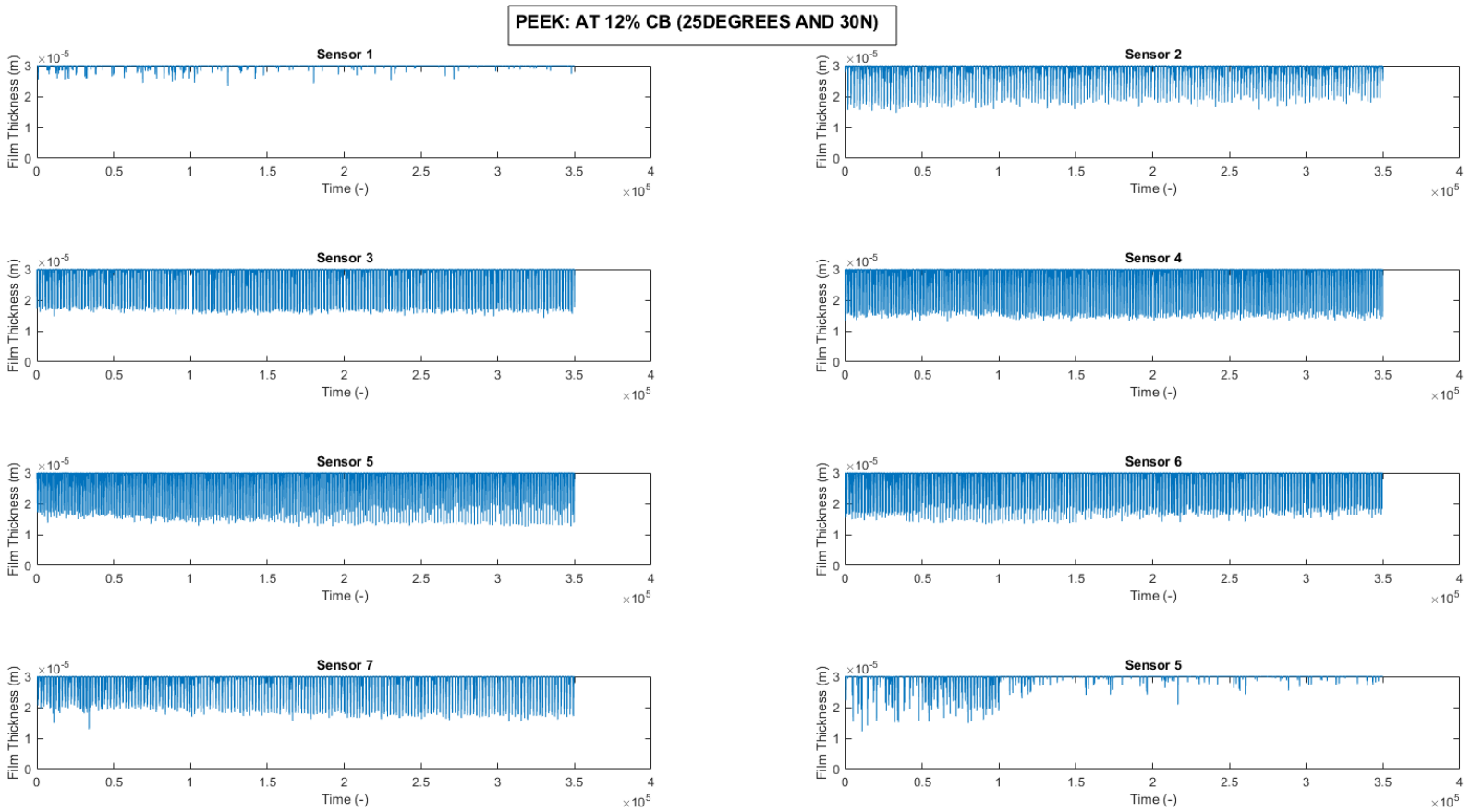
PEEK: AT 12% CB (25DEGREES AND 30N)
Sensor 1
Sensor 2
Sensor 3
Sensor 4
Sensor 5
Sensor 6
Sensor 7
Sensor 5
Film Thickness (m)
Time (-)
×10^-5
×10^5

PEEK: AT 12% CB (25DEGREES AND 20N)

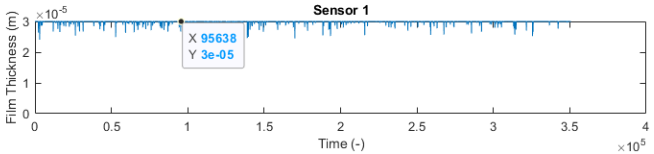

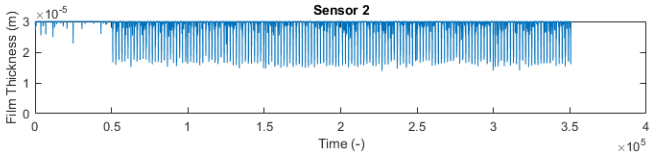

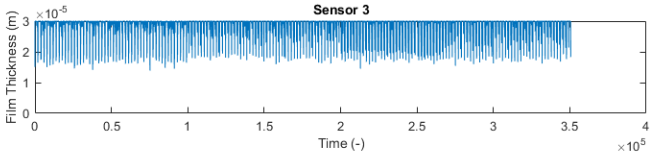

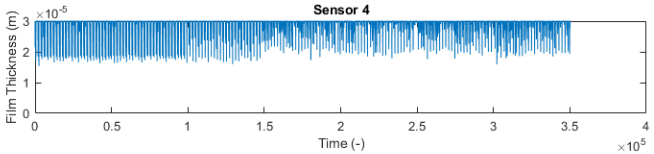

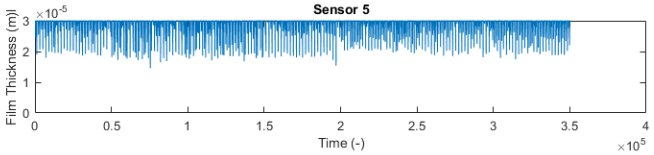

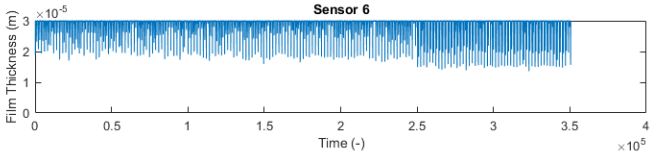

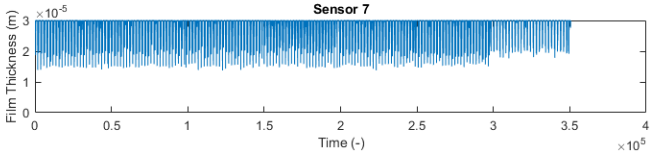

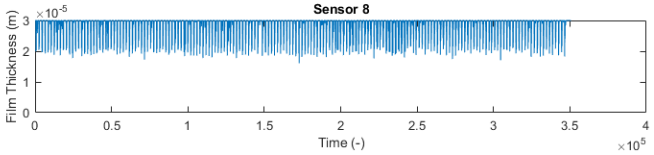

PEEK: AT 0% CB (25DEGREES AND 30N)

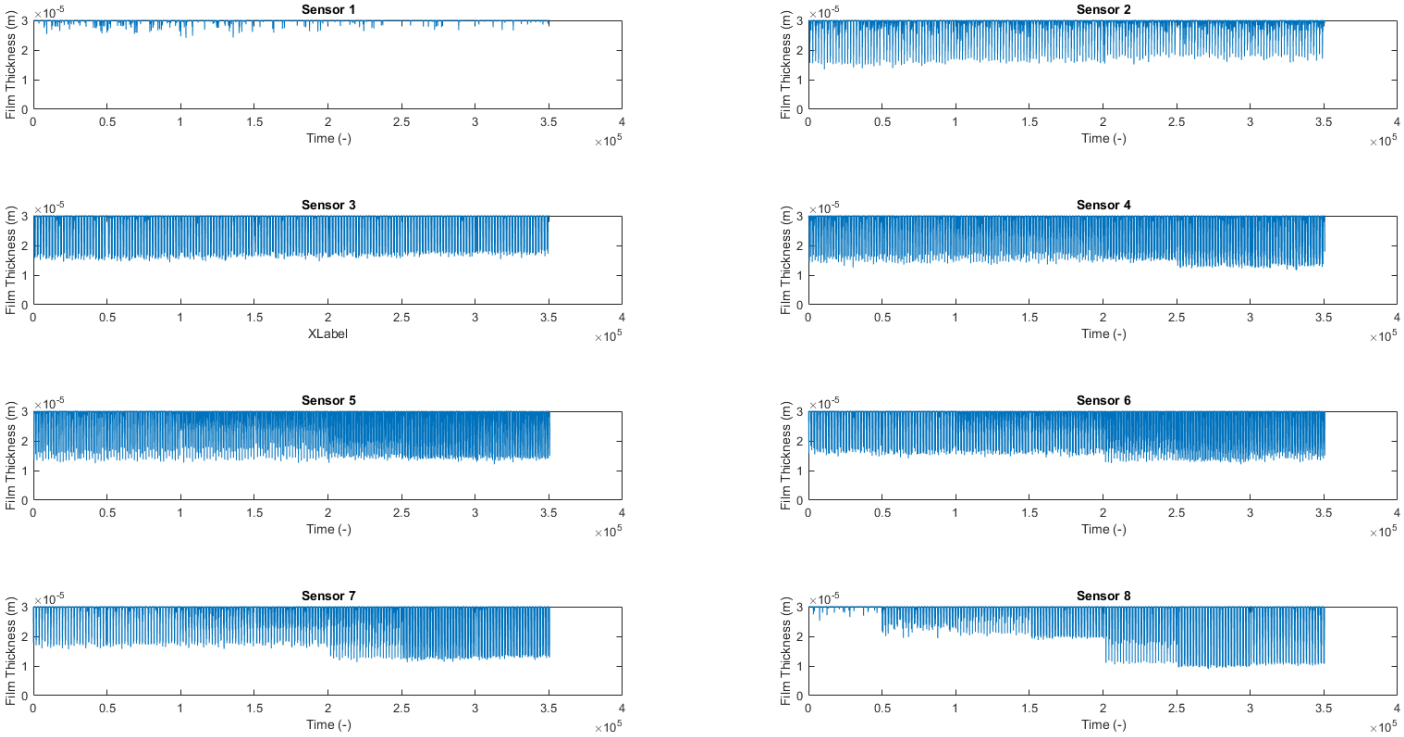

PEEK: 0% CB (25DEGREES AND 20N)

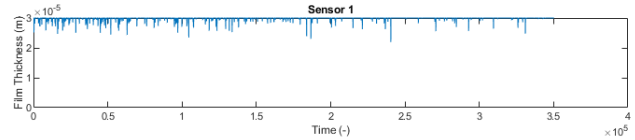

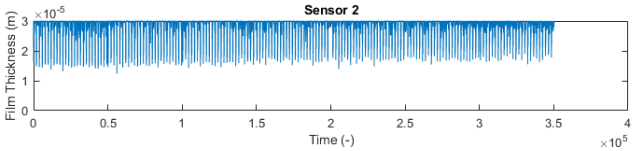

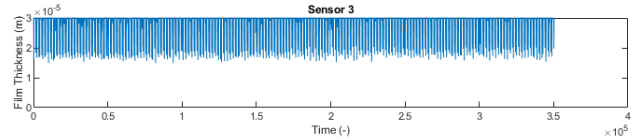

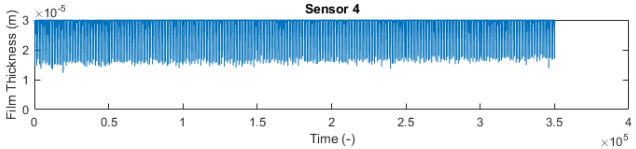

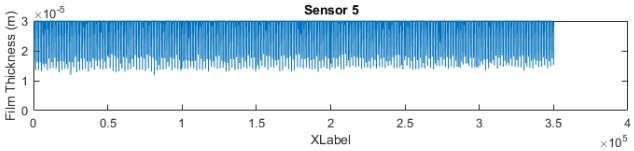

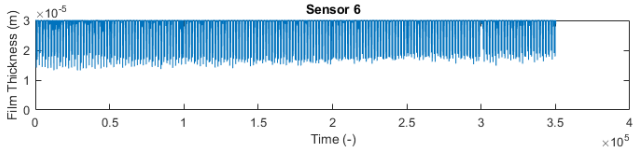

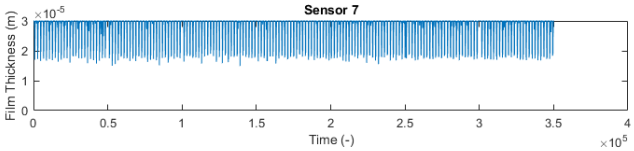

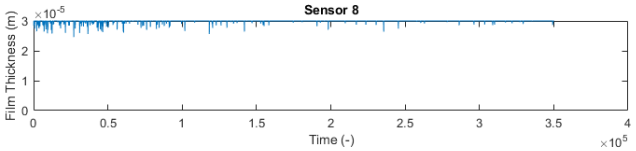

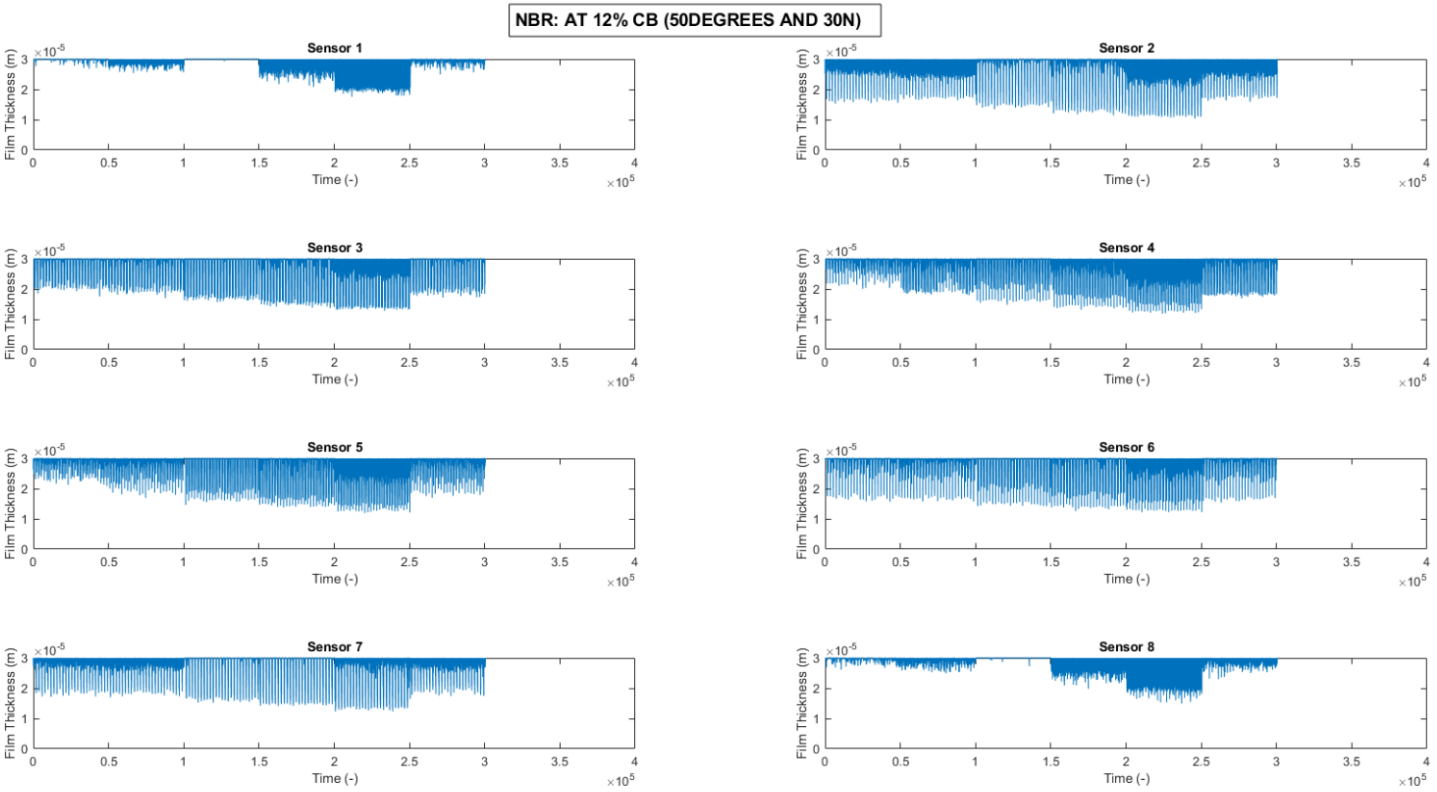
NBR: AT 12% CB (50DEGREES AND 30N)
Sensor 1
Sensor 2
Sensor 3
Sensor 4
Sensor 5
Sensor 6
Sensor 7
Sensor 8
Film Thickness (m)
Time (-)
×10^-5
×10^5